University of
Strathclyde
Glasgow

Department of Pure and Applied Chemistry

Fabricating Protein Arrays using Dip-pen Nanolithography Techniques for Improved Sensitivity of Biomarker Detection

by

Eleanore Jane Irvine

A thesis is presented to the Department of Pure and Applied Chemistry, University of Strathclyde, in fulfilment of the requirements for the degree of Doctor of Philosophy.

2012

Acknowledgements

First and foremost I would like to thank my supervisors Prof. Duncan Graham and Dr Karen Faulds, who gave me the opportunity to work in their research group. The experience over the last 3 and a half years has been invaluable to my future as a researcher and their advice and guidance is much appreciated.

In terms of funding and sponsorship, I would like to acknowledge Nanoink Inc. as they provided financial support and extensive training throughout the studentship. Individuals from Nanoink Inc. who committed time to my skill development include Sergey Rozhok, Donato Ceres, Nabil Amro, Deany Delaney, Bruce Dudzik and Mike Nelson.

Thank you to members of the Raman group, for the technical and moral support throughout my research. The numerous discussions about 'non-specific binding' will never be forgotten. Specifically Dr Aaron Hernandez, Dr Rob Stokes and Stacey Laing, as members of team DPN, their guidance and technical support has help produced much of the work in this thesis. It was a truly 'combined' effort. Other members who deserve a mention for their help and feedback include Dr Alastair Wark, Dr Jen 'lather, rinse, repeat' Dougan, Dr Iain Larmour, Sarah McAughtrie, Alan Hutton and David Blatchford.

I would like to thank my friends and family for support and generally putting up with me, especially as I neared the end of my research. Finally, thank you to Scott for his input and support.

Abstract

Dip-pen Nanolithography (DPN) was first established as a fabrication technique in 1999, as an alternative method for printing various small molecules and biomolecules on the low nanoscale. Thirteen years on, DPN plays a far more prominent role in nanotechnology investigations. Early studies demonstrated that a single tip can place a series of molecules on a surface, which have lead to robust, consistent printing methods that are currently applicable in electronics, biosensing and cell interactions.

In the present study, DPN was used to develop a platform for the detection of the biomarker, prostate-specific antigen (PSA), using optical microscopy techniques. Investigations into creating a faster patterning method, with reduced feature sizes of antibodies are first detailed. The aim was to develop a diagnostic system that competes with current biomarker detection formats such as ELISA and microarray formats produced by alternative printing techniques. DPN methods were optimised to create PSA immunoassay arrays, which were detected by fluorescence microscopy and gave good limits of detection (LOD). Furthermore, the assay method proved adaptable, as consistent results were obtained from two different functional glass substrates.

To improve the sensitivity of PSA detection, the assay was modified to render it compatible with SERS analysis. Two different approaches were investigated. It was shown that reproducible results could be achieved through a conjugate based system, giving an improved calculated LOD compared to that of the fluorescence assay.

Finally, the optimised method for printing proteins was used for an alternative application, enzymatically generating a novel SE(R)RS active substrate by DPN. Arrays of streptavidin conjugated horseradish peroxidase (HRP) were fabricated, acting as enzymatic templates for the reaction of a silver crystal growth kit, namely, EnzMet™. The development of the first DPN-made SERS active substrate is discussed.

Ultimately this research has optimised a high-throughput protein array printing method using the DPN technique that can be used for creating both a biomarker detection platform and SERS enhancing metal micro-structures. It highlights the importance of combining DPN with a sensitive optical detection method (SERS) for improved biomarker detection.

Abbreviations

μCP	Micro-contact printing
ABTS	2,2'-Azino-bis(3-ethylbenzothiazoline-6-sulfonic acid)
AFM	Atomic force microscopy
APTMS	3'-Aminopropyltrimethoxysilane
BSA	Bovine serum albumin
cDPN	Conductive dip-pen nanolithography
DEPC	Diethylpyrocarbonate
DNA	Deoxyribonucleic acid
DPN	Dip-pen nanolithography
EDC	*N*- (3-Dimethylaminopropyl)-*N*'-ethylcarbodiimide hydrochloride
eDPN	Electrochemical dip-pen nanolithography
ELISA	Enzyme-linked immunosorbent assay
HRP	Horseradish peroxidase
IHC	Immunohistochemistry
iSPR	Imaging surface plasmon resonance
LbL	Layer by layer
LFM	Lateral force microscopy
LOD	Limit of detection
MHA	16-Mercaptohexadecanoic acid
NA	Numerical Aperture

NBT	4-Nitrobenzene thiol
NHS	Sulfo *N*-hydroxysuccinimide
NIL	Nanoimprint Lithography
NLP 2000	Nanolithography platform 2000
NSL	Nanosphere lithography
ODT	1-Octadecanethiol
OPA	Octadecylphosphonic acid
PAA	Poly-(acrylic acid)
PBS	Phosphate buffered saline
PDDT	Poly(3-dodecylthiophene)
PEG	Polyethylene glycol
PNIPAAm	Poly(N-isopropylacrylamide)
PPB	Protein print buffer
PSA	Prostate-specific antigen
PSA Cap Ab	PSA capture antibody
PVD	Physical Vapour Deposition
PVP	Poly (4-vinylpyridine)
R&D	Research & Diagnostics
RH	Relative Humidity
RRM	Raman reporter molecule
SEF	Surface enhanced fluorescence
SAM	Self-assembled monolayer
SEM	Scanning electron microscope

SERRS	Surface enhanced resonance Raman scattering
SERS	Surface enhanced Raman scattering
STM	Scanning tunneling microscopy
Strep-BT	Streptavidin-BT dye linker conjugate
TA	Thioctic acid
tDPN	Thermal dip-pen nanolithography

Contents

---

1. Introduction

New nanofabrication techniques are constantly being developed to benefit numerous areas of scientific research.[1] These techniques are underpinned by the ability to print molecules and biological entities on a surface, creating a platform for biological investigations. Applications include disease diagnosis or treatment through the creation of biosensor arrays[2,3] and research-based studies of DNA,[4] proteins[5,6] and cell interactions.[7,8] Reducing the size of biosensor arrays to the low-micron and nanoscale can be valuable, as high density arrays can provide more information and with sensitive detection methods, lower detection limits for more efficient disease screening is possible. To achieve nanoscale fabrication, lithography techniques such as e-beam[9] and photolithography[10,11] can be employed, but the extreme laser-based conditions required to pattern surfaces limit the use of such techniques to non-biological environments, such as electronics.

Current methods used to print proteins and other biomolecular compounds tend toward either high-throughput, stamp-based printing such as micro-contact[12,13] or ink jet printing.[14,15] Whilst these tools have been shown to create effective platforms for immunoassay arrays, they are limited in terms of flexible patterning (where stamp shape pre-determines the pattern) and minimal array feature resolution. Inkjet methods are limited to typically 100 μm features.[5] Such a scale of feature production limits the array density per single chip, reducing screening efficiency and increases reagent consumption in biodiagnostic processes.

Dip-pen Nanolithography (DPN), a technique inspired by the high resolution analysis method of atomic force microscopy (AFM), overcomes many of the issues addressed above. It has been utilised to pattern a variety of compounds on the nanoscale. Small molecule,[16,17] biomolecule,[18] metal[19] and polymer patterning,[20] highlight its applicability in both the biotechnology and electronic device industry. DPN technology also requires temperature and humidity control during printing,[21] allowing the user to maintain mild conditions that are favourable in order to retain biomolecular activity. Furthermore, DPN is capable of producing sub-50 nm features; with the smallest feature size (line width) produced being just 15 nm.[22] E-beam and photolithography techniques are also capable of achieving this resolution of feature scale with regards to electrical device application, but this low scale feature production is a great advancement in terms of printing biological moieties.[5] Miniaturising the size of biosensor arrays and exploring alternative biomolecule patterns creates an opportunity to advance the understanding of biomolecular interactions at the scale they are occurring *in vivo*. As a result, the use of DPN has brought a new perspective to important biological systems, for example, DNA morphology and the ability to control its coiling shape through surface templates;[23] single virus attachment and conformation in the presence of functional surface group arrays[24] and self assembly of biological structures at the nanoscale.[25] More recently, the technique has presented the opportunity to investigate how sensitive control over changes to an environment can affect the adhesion and growth of cells at a surface.[26]

1.1 Biosensor Arrays and Alternative Nano-patterning Techniques

As researchers strive to achieve nanoscale resolution patterning capabilities, various alternative techniques have been adopted. These can generally be categorised into laser and tip based methods.

Laser based methods include such techniques as photolithography[10] and e-beam lithography.[9] Photolithography is popular in microelectronics and the micro fabrication process for solid-state materials. This technique involves the surface being coated with a polymer photoresist layer. A specific region on this layer is then exposed to a UV light through a photolithographic mask. The UV light either breaks or strengthens the molecular bonding in the polymer layer and the exposed or unexposed resist layer is removed when substrate is immersed in a specific solvent, leaving the resist patterned on a specific area of the substrate.[10] Photolithography can be a fast patterning method where a large surface area is exposed simultaneously through a photogenic mask. It is a high-throughput, low cost, technique and has been frequently used in the semi-conductor industry in the last 40 years. However, the resolution capabilities of the technique are limited, with the smallest feature sizes achieved being 65 nm.[27] E-beam lithography is designed for achieving extreme low nanoscale patterns as it can etch patterns directly on to the surface using a single electron beam.[9] This gives it an additional flexibility as a technique when considering pattern choice (photolithography patterns will always be limited by mask design). However, it takes longer to pattern surfaces in comparison to photolithography; it has very limited use of materials and is an expensive technique to use. Pattern sizes using e-beam lithography can be sub 50 nm.

Tip-based patterning methods alternative to DPN include the likes of nanoshaving/ nanografting.[28] [29] [30] This technique utilises the tip to simultaneously expose nanometre areas of a monolayer coated surface and deposit a new ink in place of that exposed area. This is performed by immersing a self-assembled monolayer (SAM) coated surface in a liquid containg a different SAM which the user requires a nanoscale pattern of. An AFM tip is then used at high force to mechanically break the bonds linking the SAM bonds to the surface.[30] As this occurs in the area contacted by the tip, the molecules will enter the solvent phase present and the exposed area of the surface will be replaced with the other molecule present in the solvent. While this has been shown to produce nanoscale patterns of various thiol,[30] silane[29] and DNA molecules,[28] it is a complicated technique that requires careful consideration of the solvent/ monolayer interface. In the case of high affinity surface SAM molecules, long-term exposure of that interface could result in molecular exchange at surface areas separate from the shaving or grafting occurring at the tip.[31]

A combinatorial technique has been created that uses the advantages of both tip and laser method as a means to achieve nanopatterns. Leggett *et al.* use scanning near-field photolithography (SNP), where they overcome the optical limitations often found with photolithography, by using a scanning near-field optical microscope (SNOM) coupled to a UV laser. [32] [33] [34] This offers nanometer precision by directing UV light at a functional thiol monolayer, oxidizing the strong alkylthiolates in to a weak alkyl sulfonate, and therefore creating a weak patterned area that allows for a new thiol molecule to be brought in to replace the weakened alkylsulfonate. This alternative technique has produced patterns, as small as 20 nm in size,[35] however, as with all the techniques described, there is a lacking ability to directly print a thiol or protein on the nanometer scale.

1.2 Atomic Force Microscopy (AFM)

1.2.1 Instrumental Setup

AFM was first reported by Binnig *et al.* in 1986 as a method for generating images of surfaces based on forces present on a modified substrate.[36] An AFM instrument consists of a sharp, soft-spring cantilever often made from silicon nitride (micro fabricated through photolithography techniques) which repeatedly scans back and forth across a surface. As the scanning motion occurs, varying forces are felt between the cantilever and substrate. These forces can be due to tip-substrate interaction or interactions of any chemical or physical forces occurring on the substrate.[36] Such forces cause bending and deflections of the cantilever which are monitored by a laser beam focused on the end of the cantilever.[37] The cantilever deflects the diode laser in the direction of a photo detector, which measures changes in the positioning of the reflected beam due to movement of the cantilever (figure 1.1). The tip deflection is used by the AFM feedback system to control the deflection, via adjustment of the z-piezo voltage, and used to gain accurate and quantitative data from the forces acting at the cantilever tip.[36] A display system then converts the measurements acquired during scanning into a high resolution image of the surface features.[38]

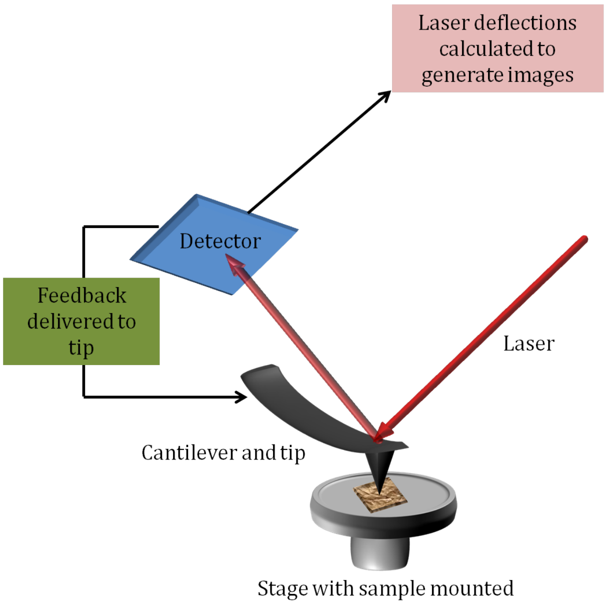

Figure 1.1: *Schematic of the basic AFM functions and feedback system*

The cantilever (deflection) is highly sensitive to minute changes in both topography and surface functionality, allowing images of various surface nanostructures, both insulating and conducting in nature, to be generated. It therefore proves advantageous over scanning tunneling microscopy (STM)[39] and other nanoscale imaging techniques which require samples that are conducting in nature. The successful use of AFM in samples under gas[40] or liquid[41] exemplifies its versatility. A range of molecules and surface topographies can be analysed, with notable results including monolayer self-assembly and structure,[42] metallic substrates[37] and biological systems like DNA and proteins.[43]

1.2.2 Scanning Modes

Three scanning modes can be employed for AFM analysis: contact mode, non-contact mode and tapping mode. Contact mode requires the tip to make physical contact with the substrate as it scans the surface.[38] It is highly effective as it generates stable, quantitative topography images with high resolution.[38] However, the images produced do not reproduce long-range forces and there is risk of damaging the sample surface due to contact of the tip.[43] As a result, this mode is unsuitable for scanning ‘soft’ substrate features like biomolecules, which are highly sensitive to their environment.

Non-contact mode operates through oscillating the tip at a high frequency, nanometres above the surface, without coming into contact with the surface. This greatly increases the sensitivity of the AFM scan, in terms of determining force interactions between the surface and AFM tip.[43] As a force is felt, the vibration of the tip will decrease the resonant frequency which in turn is detected by the deflected laser. This allows for long-range magnetic, electrostatic and Van der Waals forces to be considered in the imaging and eliminates the possibility of damaging the surface.[38] Despite these attributes, non-contact mode is rarely used. The tip is often captured easily by adhesive forces resulting in poor resolution. Furthermore, due to the high sensitivity, this mode is not applicable under liquid environments, where long range forces are greatly detrimental to imaging quality.[43]

Tapping mode is a compromise between contact and non-contact modes. The tip is oscillated under larger amplitudes, bringing the tip into contact with the surface briefly enough to allow imaging, but avoiding damage to the surface. Due to constant oscillation, images are still produced based on long range forces felt by the tip.[43] A larger amplitude and use of rigid cantilevers overcomes issues of the adhesive forces caused by the surface in non-contact mode.[44] This mode gives good resolution, little surface damage and is applicable in biological environments.

As a result, AFM is a technique that can obtain high resolution images, showing features on the nanoscale. It is this capability that makes the technique a basis for the development of DPN. Functionalising the tip with various molecular inks has proved effective in patterning surfaces. As a result, DPN and AFM go hand-in-hand, with AFM allowing for DPN patterns to then be imaged, creating a new scale of surface patterning to be discovered in mild, biologically friendly, atmospheres.

1.3 Dip-pen Nanolithography (DPN)

1.3.1 Establishing the Technique

The DPN technique was first reported by Mirkin *et al.* at Northwestern University, IL in 1999.[16] Inspired by the concept of a fountain pen loaded with an ink, writing on paper, they recreated this at the nanoscale using an Atomic Force Microscope (AFM)[36] cantilever as the 'pen'. Utilising the well known self-assembly system of alkanethiols (as the 'ink') on a gold surface (the 'paper') through covalent chemisorption, they successfully patterned nanoscale features of 1-octadecanethiol (ODT) and 16-mercaptohexadecanoic acid (MHA) on gold (figure 1.2).[16]

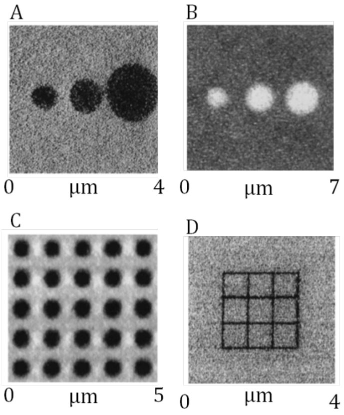

Figure 1.2: *Lateral force microscopy (LFM) images of three DPN produced spots of ODT (A) and MHA (B) on gold using different tip contact times for each spot. A 5 x 5 spot array of ODT using 20 seconds tip contact time (C) and a line grid image showing line widths of just 100 nm (D). All images captured by fast 'rastering' of the tip immediately after DPN printing with the same tip*[16]

Initial dip-pen publications utilised an AFM tip coated with an alkanethiol (usually MHA or ODT). By contacting the tip with the surface, humidity from the air forms a water meniscus interface between the tip and surface, acting as a transport bridge for the ink to immobilise on the surface. A further advantage of DPN is that the tip, after printing a pattern, can then be utilised as an AFM imaging tool, by "rastering" the tip quickly over the area of choice, giving the user rapid feedback and an image of what feature sizes are capable with the ink of choice.

DPN quickly emerged as an effective combinatorial nanopatterning and analysis technique, offering a viable alternative lithography method. In turn, this resulted in more diverse applications and ink choices.

1.3.1.1 Discovering New DPN Inks

Over the last decade, the creation of functional surface templates using alkanethiols on gold has proven a popular use of DPN. However, since the first DPN publication, a plethora of alternative inks have be investigated for DPN compatibility including metals,[19] inorganic salts,[45] collagen,[46] DNA,[47] proteins[48,49] and various monomer/ polymer formulations.[20,50] As novel ink formats were optimised for DPN applications, key studies showed that control of experimental conditions such as temperature,[21] humidity[21,47] and surface wettability[49] are more important because such factors greatly affect the transport properties of the ink and, in turn, influence the uniformity of DPN structures. Interactions between tip and ink, and ink and surface have been thoroughly discussed, recognising that the ink's affinity for the tip is vital for good ink loading.[51] Yet, the ink's affinity for the surface must overcome that of the ink-tip interactions to ensure efficient transport to the surface of the substrate.[21] In order to maintain this system, new approaches to the DPN technique have revolutionised efficient biomolecule printing, pushing DPN to the forefront of biomolecular array patterning on the low micro to nanoscale.

1.3.1.2 Modified DPN Systems for Improved Ink Compatibility

Modification of DPN instrumentation has been explored in order to print specific molecular structures. One modification that was established in 2004 is called thermal DPN (tDPN).[52] This was introduced as a means of directly printing solid structures or molecules with high melting points that were difficult to deposit at room temperature.

The DPN tips had integrated heaters which could be used to apply a temperature capable of melting the chosen ink and thus causing it to deposit at the surface.[52] Simply contacting the heated tip with the metal/ compound will eventually melt and coat the tip.[53] The work carried out by Sheehan *et al.,* is summarised in figure 1.3. They found that by continuing to heat the tip upon contact with the surface of choice, the ink is deposited as required. Results show that tDPN has been successfully used to print molecules such as octadecylphosphonic acid (OPA),[52] poly(3-dodecylthiophene) (PDDT),[54] poly(N-isopropylacrylamide) (PNIPAAm)[55] and Indium.[53]

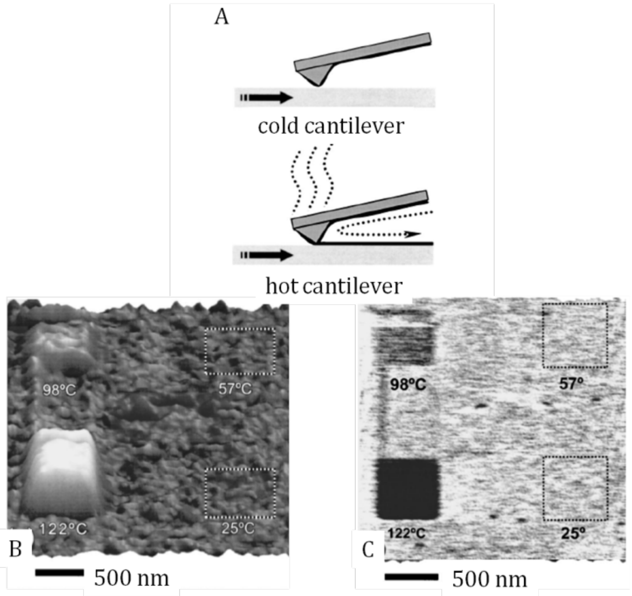

Figure 1.3: *Schematic demonstrating the tDPN mechanism (A). A topographic (B) and LFM (C) image of a surface scanned with a heated OPA coated DPN cantilever for 256 seconds in each of four 500 nm squares. The cantilever tip temperature is shown for each of the four scans*[52]

A further modified DPN concept, electrochemical DPN (eDPN), can be used to create solid metal nanostructures at a surface.[56] In this case, inorganic salts and semiconductors are coated on the tip and an electric field is applied, acting as a driving force to form metal features at the surface using the water meniscus as a reaction vessel.[56] Similarly, conductive DPN (cDPN) uses an applied bias at the tip. Inks used in this scenario are often small molecules[57] or buffers which are used to change the pH and charge properties of the tip,[58] causing local oxidation or reduction of functional surfaces to etch/ develop nanostructures.[59] While various researchers have attempted to give unique names to the two techniques, eDPN and cDPN use the same concept of applied voltage at the tip. While in both cases the water meniscus is used to assist localised surface reactions, changes in ink choice can yield completely different processes, e.g. deposition,[60] desorption[58] and chemical reactions.[56] E/cDPN's ability to influence surface functionality has also been applied to the immobilisation of proteins.[61]

1.3.1.3 Overcoming Large Scale Printing Limitations

Despite the ground-breaking capabilities of DPN, a major limitation of the technique is the limited array size that can be fabricated by a single DPN tip. The AFM scanner on which the tip is mounted has a limited range no greater than a 100 x 100 μm area,[62] and the use of a single tip to cover larger areas of patterning can be time consuming. This hinders the use of DPN in high-throughput array printing, making it difficult to rival current methods used for large scale array preparation like micro-contact printing (μCP).[63] In order to improve the capacity to print over larger areas, multi-pen probe arrays have been developed. In the case of passive pen arrays, they are designed for printing identical patterns simultaneously.[62,64] No complicated electronics or modifications to instrumentation are required. Consistent patterning from tip-to-tip is achieved simply by appropriate levelling of the tips, while AFM control is possible through laser focus on a single tip representative of the others on the probe.[62] Thus far, reports of fabricated 1D passive pen arrays range from 8 up to 32 tip on a single probe.[64] Additionally, an innovative 2D pen array has been developed with 55,000 tips (figure 1.4 (A)) on a single chip.[65] These multi-pen probes have produced nanoarrays of ODT and MHA[66] with minimal pattern variation from tip-to-tip. In more recent studies, passive probe tips have been used in various applications like protein printing for assay development and fabricating sensor chips for pH detection.[67]

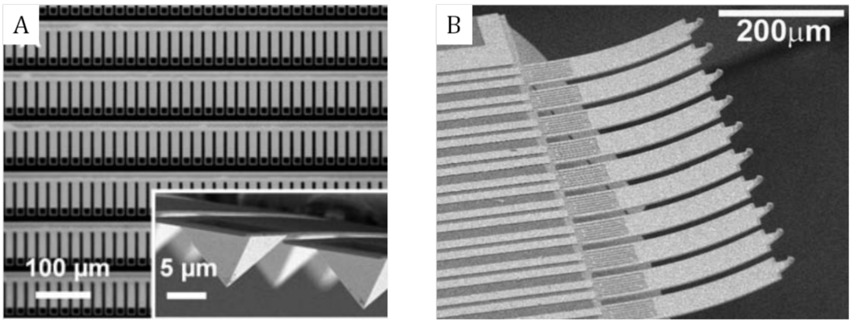

Figure 1.4: *Optical micrograph of section of 2D 55,000 tip array probe (A) with inset scanning electron microscopy (SEM) image zoom on cantilevers.* [65] *Image of thermally actuated probe array with 10 individually addressable cantilevers (B)*[68]

A recent development has seen production of multi-pen probe arrays with individually addressable cantilevers (figure 1.4 (B)).[68] This allows the user to control which tips are contacting the surface for printing at any one time. They are usually controlled by thermal bimorph actuators, whereby a heat is applied through the actuator to an individual tip, lifting it from the surface whilst another pen is in contact and printing.[69] Active pen probes make for a valuable addition as a DPN consumable since it is now possible to create large scale nano-sized features with flexible high precision patterning capabilities.

1.3.1.4 Nanoink Inc.: System Developments and Consumables

DPN instruments and many of the passive and active probes that have been developed by research groups are now commercialised products made by Nanoink Inc., based in Skokie, IL. They are the first company to manufacture systems designed specifically for DPN printing and analysis. Their first DPN system, NScriptor™,[70] has been upgraded and new systems have been developed. The DPN 5000 and nanolithography platform 2000 (NLP 2000) are both DPN-based systems but are tailored for different purposes.

The DPN 5000 uses a standard AFM feedback system for printing and the chip holder is designed to accommodate to both single tip and multiple passive and active pens. The system is fitted with an e-chamber for humidity control while system modifications, such as a heating/ cooling stage and other devices for eDPN and tDPN experiments can be added. Ultimately, it is designed for nanoscale printing and analysis for new ink discoveries and complex patterns. The NLP 2000, however, is designed for high-throughput, large scale array production. The system has no AFM feedback and the DPN tip(s) are held stationary on a chip holder while the substrate platform movement is controlled by a series of piezoelectric stacks situated under the platform, giving larger patterning range capabilities of the tip. A high resolution microscope is coupled to the system to visualise tip deflection as the tip contacts the surface. The tip is manually landed in a series of locations on the surface. These contact points are calculated, allowing the system to recognise how the platform shall move to contact the substrate with the tips for printing. The NLP 2000 is limited to printing arrays of dots and lines. Additionally, passive probe multi-pens and Nanoink Inc.'s microfluidic inkwells are compatible with the system, allowing a different ink to be distributed to each of the pens in a single probe. This makes it possible to fast pattern arrays on a whole slide in a multiplexed format.

1.3.2 DPN Transport Mechanisms

1.3.2.1 Water Meniscus Transport Model

Feature size of DPN patterns are often controlled by dwell time, i.e. the length of time the tip is in contact with the surface.[16] Decreasing dwell time shortens the transport window that a given molecule has to transfer through the water meniscus and assemble on the surface, thereby limiting the size of the ink deposit.[16] However, transport rates will differ between inks and for efficient patterning, shorter dwell times are favourable. Therefore, it is important to consider all other variables that influence either water meniscus formation or the ink's molecular behaviour in order to control the transport rate of the ink for effective printing as required by the user. A schematic representation of the water meniscus transport model is given in figure 1.5.

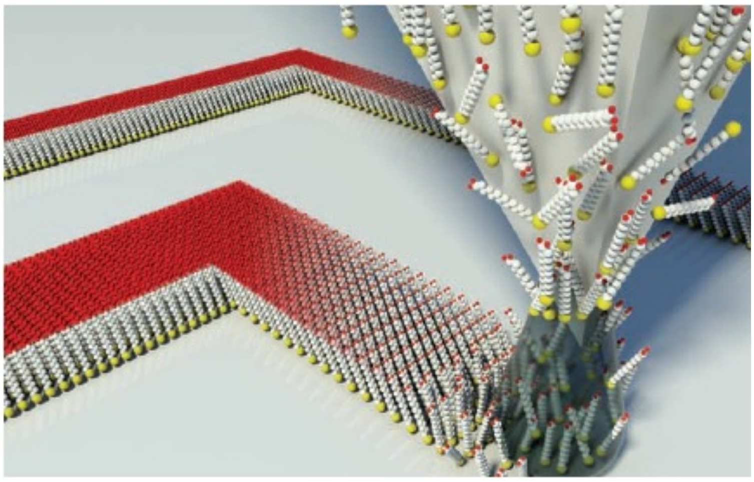

Figure 1.5: *Schematic of a DPN coated tip depositing self assembly molecules using the water meniscus for transport to the substrate*[71]

Printing alkanethiols on gold continues to be a favourable ink-substrate combination when utilising DPN for nanoscale printing. Alkanethiols are stable molecules[72] (under biological conditions) that readily transport from the DPN tip into uniform features on gold.[22] Due to the diverse functional groups possible on long chain thiols, it is possible to use DPN to create alkanethiol nano-templates for biomolecule attachment via simple surface reactions,[73,74] though, detailed studies have be carried out to understand the role of the water meniscus in the deposition of alkanethiols. DPN transport mechanisms for new inks are often discussed based on the fundamental studies of alkanethiol transport from a DPN tip, an example of this being DPN of dendrimers on silicon surfaces.[75]

It is widely recognised that alkanethiols have a high affinity for gold and readily form self-assembled monolayers (SAMs) via chemisorption.[72,76] Although this explains their predisposition to transfer from the tip to the surface, literature concerning the role of the water meniscus for alkanethiol transport has been fraught with contradictions. This has resulted in a closer study of the molecular properties of specific alkanethiols in order to determine factors that affect transport rate from the tip.

1.3.2.1.1 Humidity effects

MHA and ODT are the most commonly used and studied alkanethiol inks for DPN. They are similar in length but differ greatly in functionality. ODT is hydrophobic and therefore insoluble in water, whereas MHA is hydrophilic in nature and dissolves in water.[21,77,78] To coat the tip, both molecules (and other thermally stable inks) can be coated either by heated vapour coating or by dipping the tip in a saturated solution of the molecules in solvents like ethanol.[77,79] Both methods result in the inks being dried onto the tip. Due to ODT's insolubility in water, it has been hypothesised that the water meniscus has no influence over the deposition of ODT on gold. This was first suggested by Sheehan *et al.* when they removed all the water vapour in the DPN chamber thereby precluding meniscus formation.[80] Despite this, ODT was still successfully written. It was later shown that even with humidity reduced to 0 %, a small volume of water can still condense at the tip-surface interface.[21] Nevertheless, further research continued to back up this initial idea of the water meniscus having no influence over ODT transport.

Rozhok *et al.* performed a gradual humidity change to study the effects on MHA and ODT transport rates, shown in figure 1.6.[21] Results indicated that an increase in humidity increases the water collected at the tip-surface interface, forming a larger water meniscus.[81] In addition to Rozhok's humidity study, other research has demonstrated that an increase in humidity can accelerate the transport rate of MHA (figure 1.6B) and growth of the SAM on the gold from the point of tip contact.[21,79,82] Alternatively, increasing the water meniscus size was found to have little influence over the transport rate of ODT (figure 1.6A) and in fact caused a very slight decrease in transport rate.[21] The theory rationalised from these trends is that the water meniscus can improve the inking rate in some respects, but impede it in others. In one sense, an increase in humidity will result in a larger water meniscus interface between the surfaces and tip. In the case of water soluble inks like MHA, this will dissolve more ink into the meniscus and transport the molecules to the surface more rapidly. However, the water meniscus can also act as a surface-resist. This effect is pronounced for water insoluble inks like ODT, where the molecules will not dissolve through the meniscus and thus with an increased meniscus size, ink transport rate will decrease slightly as the water blocks the adsorption of the molecule to the surface.[21]

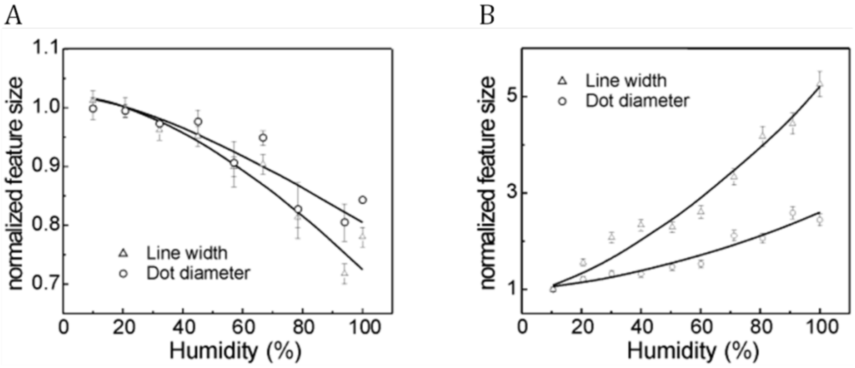

Figure 1.6: *The relative humidity (RH) dependencies of SAM growth at a gold surface for inks ODT (A) and MHA (B) when depositing lines and dot patterns. Dot dwell times and line speeds remained constant for each RH applied.*[21]

Humidity control can further be used to make new inks assemble at a surface without the use of more complicated instrumentation. An excellent example of this is DPN of OPA on gold.[83] Sheehan *et al.* have used tDPN to print OPA (figure 1.3), since the compound was required in molten form to allow patterning.[52] Huang *et al.* have since discovered that by increasing the humidity to 45 %, they were able to produce nanoscale features of OPA at room temperature.[83] It is important to recognise that the reduction of humidity to negligible amounts could benefit the use of water sensitive inks, minimising molecular breakdowns of the ink during printing.

Another interesting effect of humidity control has been demonstrated by DPN deposition of alkanethiol mixtures.[84,85] Nafday *et al.* coated a tip using a mixed ODT and MHA solution. By conducting a humidity study (results shown in figure 1.7), they found that MHA always occupied the middle section of the spot, whilst the ODT formed a SAM around the periphery of the spot feature (figure 1.7A and C), and increasing humidity eventually suppressed ODT deposition (figure 1.7B). This level of specific ink control is explained by the dissolution kinetics of the two inks in the presence of the water meniscus. MHA will dissolve through the meniscus occupying the centre area of the spot feature, whereas ODT will adsorb onto the remaining outer bare gold surface where there is less of a water surface resist effect from the meniscus. Finally, as humidity increases, the transport rate of MHA becomes so rapid that no spaces are available for ODT to deposit around the feature, completely suppressing the deposition of ODT.[85]

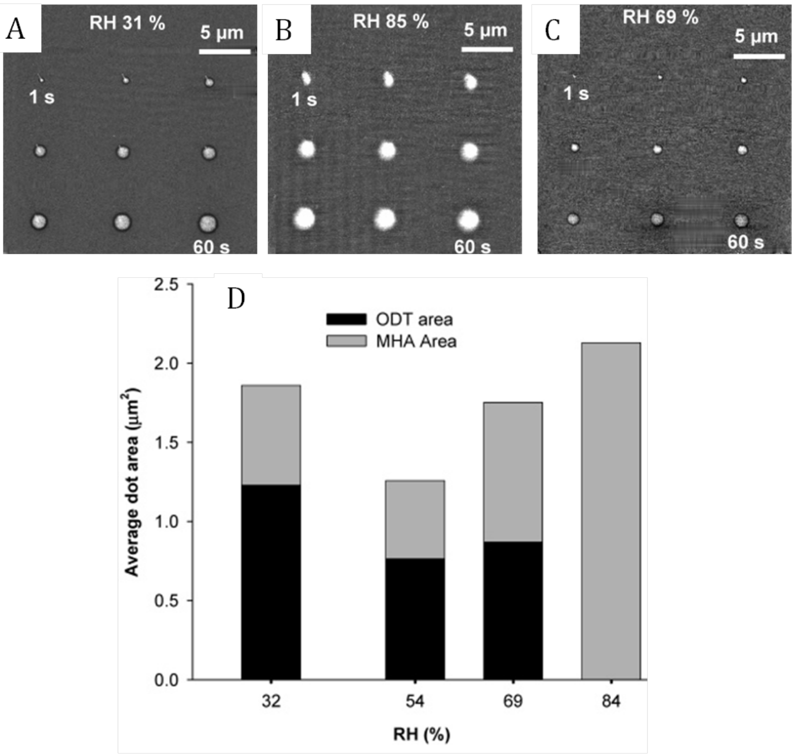

Figure 1.7: *LFM images of phase-separated dots formed consisting of MHA (inner, light contrast) and ODT (outer, dark contrast) regions observed for dwell times of 1-60 seconds range at RH of 31 % (A), 85 % (B) and 69 %. Bar chart plot (D) of average MHA and ODT dot areas vs. RH for 40 seconds dwell time spots*[85]

1.3.2.1.2 Temperature Effects

Temperature is another important variable that can influence ink transport rate, but the level of control induced by temperature is related to molecular behaviour as opposed to influencing water meniscus formation.[21,77] It is generally found that increasing temperatures will increase transport rate for both ODT and MHA.[21] Higher temperatures provide more enthalpy for desorption/ dissolution processes of the ink at the tip-surface interface, allowing more molecules to solvate in the water meniscus.[21] In the case of MHA, this matches well with its polarity and its ability to dissolve in water. However, this molecular behaviour appears to be true for ODT too, despite its lack of affinity for water meniscus assistance during DPN printing.[21] These trends were reported by Rozhok *et al.* and are shown in figure 1.8.

It is important to recognise that this kind of temperature effect is not mistaken for tDPN, as the temperatures reached with these types of experiments will never exceed that of the melting point of the ink - it is simply used to influence the molecular interaction at the meniscus interface for improved printing.

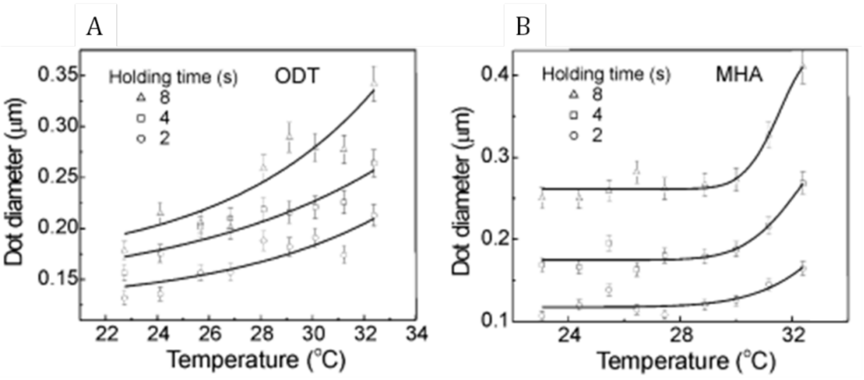

Figure 1.8: *Plot of temperature range vs. dot diameter size for ODT (A) and MHA (B) at dwell times of 2, 4 and 8 seconds*[21]

1.3.2.1.3 Other Factors that Influence Ink Transport Rates

In addition to temperature and humidity, other factors can be used to influence ink transport. Increasing the number of ink coatings to a tip has been found to increase the deposition rate of MHA.[86] Dip coating the tip appears to print molecules faster than vapour coating despite less molecules being available at the surface using the dip coat method. It has been hypothesised that this is due to solvent effects.[79] Alternatively, effects of different organic vapours used in the printing environment have been studied. Organic vapour doping results in meniscus composition mimicking that of the solvent chosen. Vapours of ethanol, methanol, hexane and dichloromethane were all found to significantly increase the transport rate of both MHA and ODT. This phenomenon is still poorly understood.[87]

It is clear that in order to print new inks by DPN that there are numerous variables that can be used to encourage molecular flow from the pen tip to the surface. The mechanism itself is intricate and highly sensitive, as demonstrated by thorough alkanethiol DPN studies which have shown that slight tip or surface contamination can adversely affect printing.[21] These initial alkanethiol based investigations, which explored the fundamentals of DPN transport using the water meniscus transport model are the basis of new ink discovery for DPN applications.

1.3.2.2 Tip Modification for Improved Biomolecule Deposition

The effect of water meniscus transport on different inks has so far been discussed. In the case of biomolecule printing directly from the tip, a water meniscus will always be a necessity in order to reduce the risk of the biomolecule denaturing on the tip before deposition at the surface. This is borne out by the few attempts made to directly print biomolecules by DPN with no tip modification.[46,88,89,90] In most cases, high humidities were used, sometimes reaching 75 %.[88] An additional example is the method used by Lynch *et al.* whereby the DPN system was modified to release regular bursts of humidified air, in order to maintain a highly humid environment throughout printing.[90] Biomolecule modification has also been employed to encourage deposition at the surface, for example, linking a thiol group to collagen for compatible immobilisation on gold.[46] Regardless of these optimisation attempts, coating untreated DPN tips with biomolecules will always risk drying out of the ink at the tip and with no pre-functionalisation, a significant proportion of the biomolecules taken up onto the tip are likely to denature.

Tip modification involves coating procedures that greatly improve the ability to print biomolecules. The material used for modification depends on the specific biomolecule being applied to the tip. Two types of modification – functional SAMs[47] and polymer-based coatings[91] – have so far been utilised. Both work very differently but are ultimately used for the same purposes of improved ink loading at the tip,[91] reduced denaturing of biomolecules[18] and maintenance of systems where the biomolecule has a greater affinity for the surface upon contact with the tip for transport.[48]

1.3.2.2.1 Tip Modification using Self-assembly Systems

Functional SAMs have previously been used for tip modification to improve direct printing of functionalised oligonucleotides[47] and proteins.[18] Many commercially available DPN tips are made of silicon nitride with the back side of the cantilever coated in gold. As a result, modification often requires the use of alkanethiols with polyethylene glycol (PEG) groups to block adsorption of the biomolecule on the gold areas.[18] Alkylsilane at the silicon nitride tip expose a specific functional group at the tip surface. The choice of functional alkylsilane is specific to that of the biomolecular ink in order to increase the tip hydrophilicity and encourage better ink loading.[47,92] An effective example of this specificity is from Demers *et al.* who functionalised a tip with 3'-aminopropyltrimethoxysilane (APTMS) to improve ink uptake of hexanethiol modified oligonucleotides. This facilitated successful nanoscale printing of DNA on gold with features as small as 50 nm.[47] They then hybridised the DNA arrays with a fluorescently-tagged complementary strand, confirming that the DNA retained its activity throughout the DPN process.[47] In the case of protein printing, figure 1.9 summarises the work carried out by Lee *et al.*, where both lysozyme (figure 1.9B) and IgG proteins (figure 1.9C) were printed using the same tip modification procedure, showing that the modification can be applied to uptake of a variety of proteins. They initially blocked the backside of the cantilever with PEG-thiol before coating the tip with gold and functionalising with thioctic acid (figure 1.9A). Again, protein array function was confirmed by attaching complementary antibodies conjugated to gold nanoparticles (figure 1.9D and E), resulting in a large increase of array height, imaged by AFM.[18] Both research groups found that biomolecule DPN transport was similar to that of alkanethiol diffusion on gold. An increased feature size with longer dwell times was found and in the case of DNA deposition, changing humidity also influenced ink transport rate.[47]

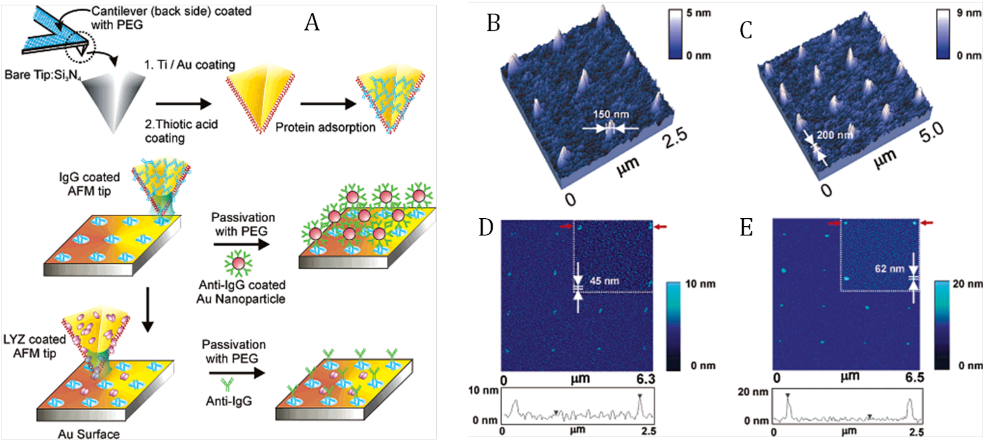

Figure 1.9: *Schematic of tip functionalisation using thiol SAMs (A). 3D topography AFM images of lysozyme nanodot arrays using 20 seconds dwell time (B) and IgG nanodot arrays using 30 seconds dwell time (C). 2D topography AFM images with corresponding height profiles for IgG nanodot array before (D) and after (E) treatment with a solution of anti-IgG coated gold nanoparticles*[18]

1.3.2.2.2 Tip Modification using Polymer Coating Methods

Two different approaches have been applied to the modification of tips using polymers. A layer by layer (LbL) approach was developed by Wu *et al.,* to create alternating polymer films of poly (4-vinylpyridine) (PVP) and poly-(acrylic acid) (PAA) that range between 20-30 nm in thickness.[91] Alternatively Shin *et al.* used a silane initiator to polymerise a nano-porous network of $PMeO_x$ which can also offer control over polymer thickness at the tip.[93] Nano-porous polymer networks are designed to retain protein activity and increase ink loading. Interestingly, dwell time is found to have little control over spot size and it appears a stamping effect is adopted.[91,93] This is due to the small diffusion barrier of the hydrogel compared with the large barrier of the water meniscus diffusion model. This key difference explains DPN diffusion of alkanethiols on gold. Furthermore, it was recognised that the diffusion of the large adeno-assisted virus particles printed on the surface is driven by the electrostatic attraction of the virus to the bare SiO_x substrate.[93] Polymer modification has allowed users to overcome the issue of poor ink uptake by the tip with large biomolecules.[93] Additionally, alternative variables can be used to control feature sizes such as variation of polymer thickness at the tip.[93]

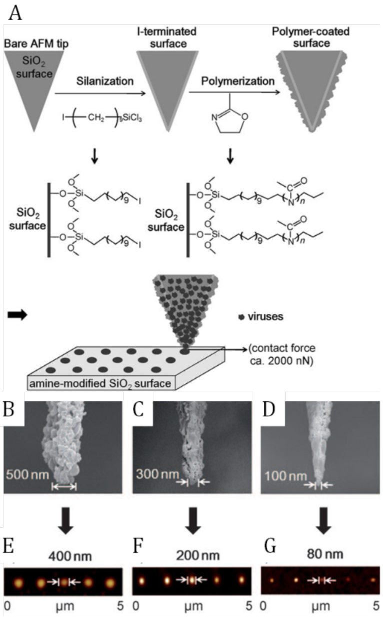

Figure 1.10: *Schematic for fabrication of a nanoporous PMeOx-coated tip (A). SEM images of the PMeOx-coated tips prepared under decreasing incubation times of 2 hours (B), 30 minutes (C), and 10 minutes (D). Corresponding AFM images (E-G) of dot patterns of virus molecules are shown, all produced by a dwell time of 1 second*[93]

1.3.2.3 Liquid inks: An Alternative Transport Model

As DPN research continues to expand, liquid carrier inks have become an increasingly popular method for direct printing of biomolecules, polymers and metals.[20,94,95] It involves simply mixing (or dissolving) the ink of choice with a liquid that will maintain a hydrated form whilst ink is on the tip and after deposition at the surface (figure 1.11). This method has some advantages similar to those found with tip modification including retention of biomolecule activity and improved printing consistency,[96] for instance. Liquid inks are also highly compatible with microfluidic inkwells, thus creating an opportunity for multiplex printing with multi-pen arrays.[97] The kinetics and deposition influencing factors are very different from the water meniscus model, resulting in the requirement for much shorter dwell times and the ability to print the same ink on a variety of substrates.[98] Liquid inks have ultimately revolutionised fast, large scale nanopatterning by DPN.

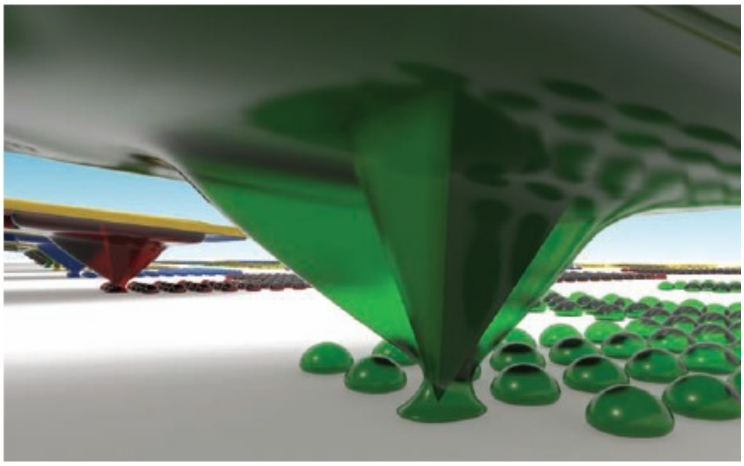

Figure 1.11: *Schematic of liquid carrier ink meniscus formation and transport simulation*[71]

1.3.2.3.1 Liquid Carrier Ink to Assist Biomolecule Printing

For biomolecular printing, tip modification alone does not always eliminate the requirement for high humidities during printing.[18,48,51] However, by adding small amounts of viscous liquids such as Tween® 20 or glycerol, it is possible to retain a liquid ink state throughout the whole printing process, preventing denaturing of the biomolecules. These carrier surfactants improve the wettability of a surface; the carrier ink takes on the role of the water meniscus and forms its own tip-surface bridge, wetting the surface to transfer the carrier ink and biomolecule.[49] This was reported by

Jung *et al.* who studied the use of Tween® 20 as a carrier to print thiol-functionalised biotin.[49] They observed not only that addition of Tween® 20 to the protein solution successfully deposited the biotin whilst maintaining its biomolecular activity, but that high humidities were not required and printing consistency was improved and could be controlled based on the percentage of Tween® 20 applied. Furthermore, Tween® 20 alone printed very effectively, indicating that the biomolecule itself had no influence over the transport mechanism.[49] Further investigations into the use of carrier liquids concluded that physical adsorption is the dominant deposition influence when using liquid carrier inks with biomolecules.[96] A study of agarose-assisted DPN found that agarose plays the role of the carrier and the use of tricine as an 'initiator' can increase transport rate of the biomolecule.[96] Examples of these 'initiator' effects are illustrated in figure 1.12.

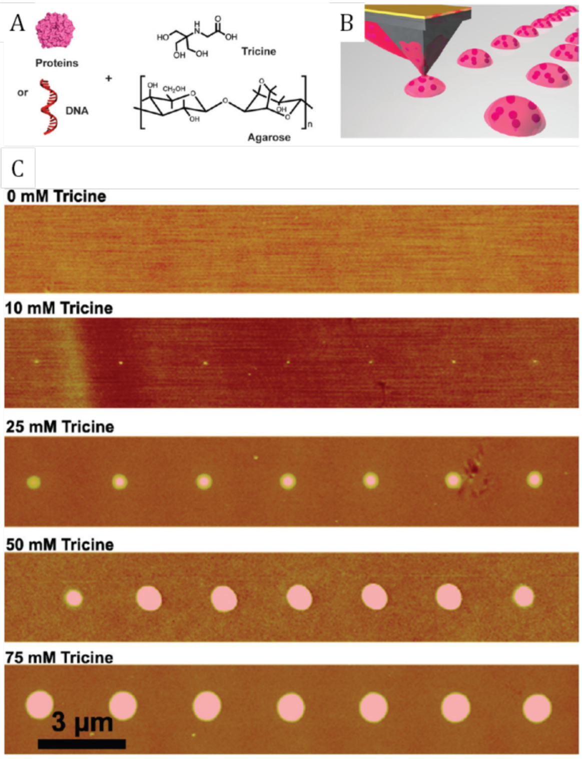

Figure 1.12: *A schematic representation of ink and matrix components (A); an illustration showing the process of agarose-assisted DPN (B); 2D AFM images of spots generated by agarose-assisted DPN (C) with increasing tricine concentration from 0 - 75 mM at 0.5 second dwell time and 50 % humidity*[96]

Generally, it is accepted that due to the dominating force of physical adsorption, liquid inks have faster transport rates than those of the ink transport dictated by the water meniscus diffusion model.[96] Larger feature sizes are achieved with increased dwell times but the spot feature limit is achieved at much shorter dwell times than that of alkanethiol diffusion on gold.[96] In terms of fast deposition, water meniscus diffusion of biomolecules is less reliable than deposition from the carrier liquids. The latter are able to maintain a hydrated atmosphere for biomolecules throughout the whole DPN experiment and even after deposition so that within a sessile drop, biomolecules have time to react and bind to the surface in a concentrated area before the spot dries out. Ink carrier liquids can also be used to influence specific environmental factors to reduce issues that discourage biomolecule deposition. Examples of this include alteration of the pH of the carrier ink to reduce self-assembly of peptides during the DPN process, suppression of self-assembly until peptides are at the surface, and the use of glycerin as a carrier to increase viscosity in order to slow down inter-biomolecular reactions before deposition from the tip.[25]

1.3.2.3.2 DPN of Polymers

Early examples of polymer printing follow the water meniscus diffusion model, where the polymer ink used is water soluble. The rate of deposition and feature size was sensitive to various factors including dwell time,[99] molecular weight[75] and electrostatic interactions with the surface.[100] However, this model limits DPN printing of polymers to specific substrates and water soluble polymers only. In some cases, this transport model produces very irregularly shaped features, thereby limiting the user's control over the feature shape.[99] More recent examples used the liquid ink model for polymer deposition, with the polymer completing the composition of the meniscus at the tip-surface interface.[20,101] The advantages of this method of deposition are again attributed to the fact that physical adsorption is the predominant factor in the molecular transport to the surface.[20,101]

Surface tension exerts great influence over feature size when liquid ink formulations are used.[20] Therefore it is possible to limit feature size based on changes to surface functionality or choice of substrate. Varying surface tensions determines the spreading of a polymer ink drop upon deposition. An increased dwell time for polymer liquid printing results in an increase in feature width and height,[20] whereas polymers that are deposited through water meniscus transport only vary in width with dwell time.[99]

Direct DPN of liquid polymers is often hindered by relatively slow polymerisation reactions and high viscosity during printing processes. Various approaches have been used to combat these issues. Hernandez *et al.,* used DPN to print PDMS in a high-throughput fashion using multi-pen array probes and microfluidic inkwells.[20] Initially the PDMS itself was too viscous to be printed since the polymer did not flow through the microfluidic channels of the inkwells. By diluting it in hexane, optimal conditions were realised and allowed fast, consistent array printing before the polymer cured (figure 1.13). The PDMS features were then cross linked to the substrate, creating a micro-structured chip that could be applied as a mould of PDMS printing stamps.[20] This work was published in Chemical Science in 2011, the full article can be found in the appendix.

Another notable example of an alternative approach to polymer deposition by DPN is the printing of the monomer ink and using additives to slow down polymerisation time until printing has finished, preventing polymerisation until after deposition.[50] Currently, polymer printing using DPN is accessible, with a good understanding of how to maintain a liquid polymer state during the DPN process.

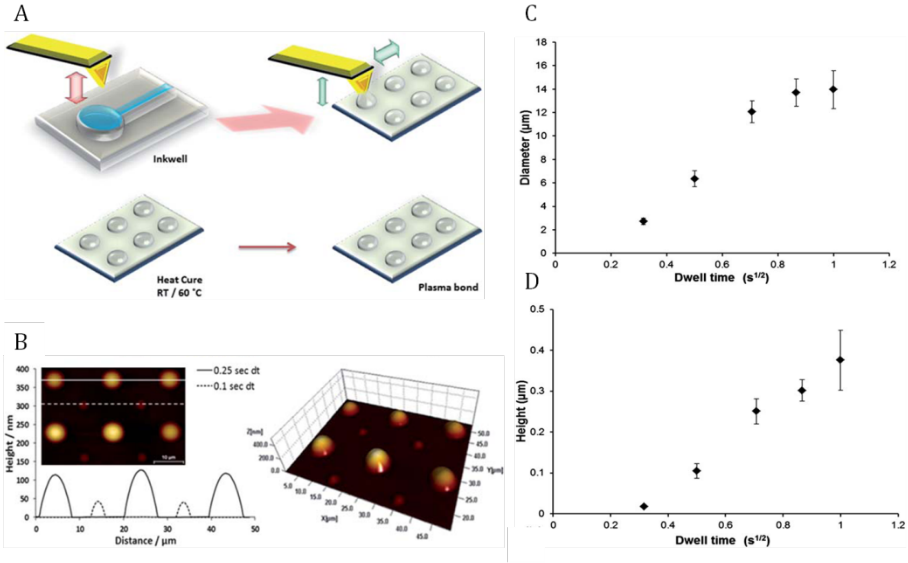

Figure 12: *Example of polymer printing using liquid ink transport. Schematic representation of the DPN procedure used to pattern PDMS on a silicon dioxide substrate (A). 2D and 3D AFM topography images of programmable patterning of PDMS structure with overlaid height profile of PDMS spots created by using alternating dwell times of 0.25 and 0.1 seconds (B). Plot of dwell time vs. spot diameter (C) and plot of dwell time vs. feature height (D)*[20]

1.3.2.3.3 Direct Write of Metal Inks

Approaches to produce metal nanostructures by DPN differ greatly including the use of alkanethiol arrays as etch resists,[102] eDPN and printing metal salts that later require treatment to form nanoscale metal features.[103] Although recent attempts are limited, direct metal printing by DPN has been successful in creating silver conductive traces using liquid carrier molecules.[95,98] Again, physical adsorption and surface tension influences deposition and consistent printing across two different surface materials is possible,[98] further emphasising that carrier liquids can be used as a universal printing buffer that have greatly improved DPN's compatibility and flexibility in applications.

1.3.3 Applications of DPN in Biosensing

1.3.3.1 Biomolecule Immobilisation for Biological Research and Biomarker Detection

Throughout the last decade, DPN of alkanethiols has continued to be used for immobilisation of biomolecules.[74,104] This indirect method of fabricating protein arrays has always been advantageous in the case of inks like MHA and AUT which are easy to control by DPN in terms of nanoscale printing. Their functionality has proven to be compatible with immobilising proteins[74] or oligonucleotides[104] either directly through the functional moiety exposed on the gold surface[105] or through simple 1-ethyl-3-(3-dimethylaminopropyl)carbodiimide (EDC) coupling reactions.[104] It has also been demonstrated that SAM templates can be adapted to suit other surfaces; printing alkylsilanes to immobilise proteins on glass substrates, for example.[17] In all cases, these SAMs retain the immobilised DNA or protein activity and there have been numerous examples where simple antibody-antigen binding and DNA hybridisations have occurred on these nanoscale templates.[73,106,107]

Earlier publications of this nature used only AFM for analysis of biomolecular binding of the arrays.[104,105,106] While AFM remains a very useful and detailed analysis tool - especially in terms of DPN nanoarrays - it is time consuming and cannot be used to collect fast quantitative data in the same way as optical microscopy techniques like fluorescence.[108] However, Borrebaeck *et al.* highlighted that conventional fluorescence scanners tend to have a resolution limit of just 1 μm. This means that nanoscale biomolecule arrays would remain difficult to analyse and therefore, for fast analysis of

DPN produced assays, it is important to create features in the 1-10 µm range.[5] Indeed, as more biomolecule array binding studies were carried out using DPN alkanethiol templates, both AFM and fluorescence microscopy analyses were utilised, with the fluorescent arrays designed on the low micron scale (figure 1.14).[17,73,109]

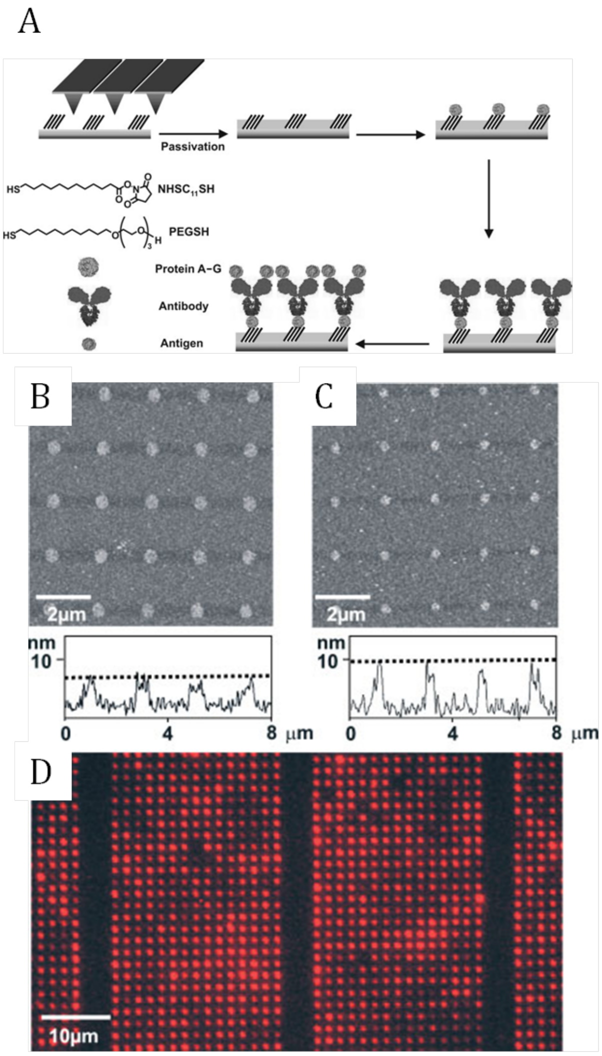

Figure 1.14: *Example of fluorescence detectable protein interaction arrays. Schematic representation of the process used to obtain biologically active antibodies on the protein A/ G (A). AFM topography images and their corresponding height profiles of anti-b-galactosidase nanoarrays immobilized on protein A/ G templates before (B) and after (C) incubation in a b-galactosidase protein solution. High resolution fluorescence microscopy image of the Alexa 594-labeled b-galactosidase complex nanoarrays (D)*[109]

Further developments in DPN fabrication for protein assays involved multi-pen probes for faster and larger area printing.[109] However, to compete with other fabricating techniques like inkjet printing[14,15] and alternative immunoassay based methods such as

ELISA,[110,111,112] the need for surface functionalisation using alkanethiol arrays should be eliminated, as the reaction steps required to immobilise biomolecules, adding time to the assay development process. This problem was addressed by the development of tip modification and use of carrier liquid methods in order to directly print proteins on pre-functionalised surfaces. Despite these developments using direct DPN of biomolecules, examples of utilising the arrays as a quantitative detection platform are limited.[3,113]

With miniaturised array feature sizes, biochip dimensions are reduced and more assays can be performed per chip, thus improving disease detection efficiency. The next stage for future development is to match these miniaturised arrays with more sensitive detection techniques. Key examples of new detection techniques being utilised in conjunction with DPN are detection of DNA hybridisation arrays via surface enhanced resonance Raman scattering (SERRS)[94] and quantitative analysis of protein-protein interactions using imaging surface plasmon resonance (iSPR).[113] These alternative detection methods allow more efficient use of DPN biomolecule arrays and therefore an opportunity for improved sensitivity for disease detection.

Lipid-based materials have been shown to be highly compatible as a DPN ink. In some instances, nanoscale printing of the lipids allows for detailed studies of membrane surface layer structures, providing useful insight into the structural formations of phospholipids and their functional relations.[114] They have also been used in studies which demonstrate the ability to print inks under water using DPN[115] and have enabled determination of the number of molecules deposited within a DPN droplet at a surface.[116] Lipid-based materials have also been used as nanomaterial carriers and a basis for attaching proteins which influence cell activation and adhesion.[97] Use of lipids is relatively new in the field of DPN, but could have numerous bio-based applications in the future.

Producing biomolecule arrays by DPN has created the opportunity to miniaturise features to scales comparable with fabrication techniques such as e-beam and photolithography. Working with biomolecules at the low micron to nanoscale could help improve biosensing platforms for more efficient disease diagnosis, drug candidate screening and better the understanding of biological pathways.

1.3.3.2 DPN in Cell Applications

A variety of DPN approaches have been used to influence cell adhesion and activity. Studies have proven to be biomolecule - or functional group - specific, for example, direct printing of fibronectin to immobilise fibroblast cells[117] or MHA templates functionalised with poly-l-lysine to immobilised bacterial cells.[118] However, Stokes *et al.* achieved adhesion and controlled differentiation of mesenchymal stem cells through alkanethiol DPN arrays. They produced nanoarrays on gold using a variety of functional thiols and by altering the array pitch (space between each feature within an array), they were able to investigate what formats best influence stem cell differentiation (figure 1.15). They concluded that both functional group and pitch could induce different levels of cell adhesion and control the growth of cells towards various cell types.[26] This body of work was published in Lab on a chip in 2010 and full article can be found in the appendix.

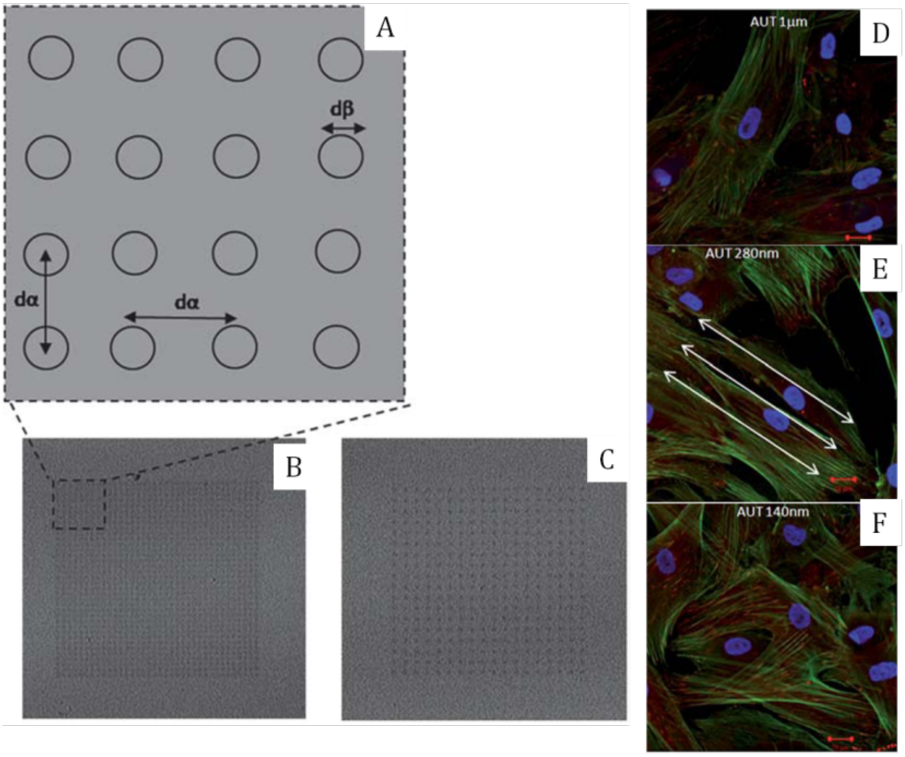

Figure 1.15: *Nano-patterned surface design model used for stem cell control and differentiation showing dot to dot pitch (da) and dot diameter (db) (A), LFM image of small area 140 nm pitch array (B) and 140 nm pitch array (C). Fluorescence image of stained stem cells were cultured in contact with* $-NH_2$ *modified surfaces of varying pitch for 24 hours (D-F)*[26]

This use of DPN to produce nanoscale features could have a breakthrough effect on cell studies and the stem cell industry, with an onset advance in regenerative medicine research.[26]

1.3.3.3 Opportunities in future Biosensing Applications using DPN

It is clear from the extensive examples of DPN capabilities in biomolecular array fabrication, that DPN could play a major part in the development of new assay formats for better diagnostic platforms. The work detailed in this thesis will be carried out with this intention in mind. In order to prove that DPN methods are an attractive route for fabrication, the technique needs to be applied to formats used for detection of relevant biomarkers, while processing of the detection platform must include fast fabrication of arrays to maintain a high throughput array system processing. As much research has considered DPN to be useful in gaining increased sensitivity of quantitative biomolecule detection, it is important to recognise detection techniques that are capable of analysing miniaturised biomarker arrays, giving good sensitivity limits and include compatible array recognition technology.

1.4 Optical Microscopies Applicable in Biosensing

AFM is an effective method of analysis for imaging small scale patterns at a surface. However, it is limited in terms of fast analysis and true quantitative imaging that details target biomolecule concentrations captured at a surface array. In order to determine quantitative information about biosensor array capabilities in capturing low levels of target molecules, optical microscopies are a popular choice.

1.4.1 Fluorescence Microscopy

1.4.1.1 Fluorescence Theory[119]

When a molecule is excited by light of a certain wavelength the molecule absorbs energy from the light, causing the molecule to move to an excited electronic state from its ground electronic state. As this state is unstable, the molecule naturally returns to a ground state through energy dissipation. The molecule moves down the vibrational transitions within the excited state through radiationless decay (energy that is lost through the release of heat). However, in order to return to the ground state, the molecule will give out a greater level of energy than that resulting from radiationless decay (but lower in energy than that of the exciting light); one process by which this can occur is fluorescence.

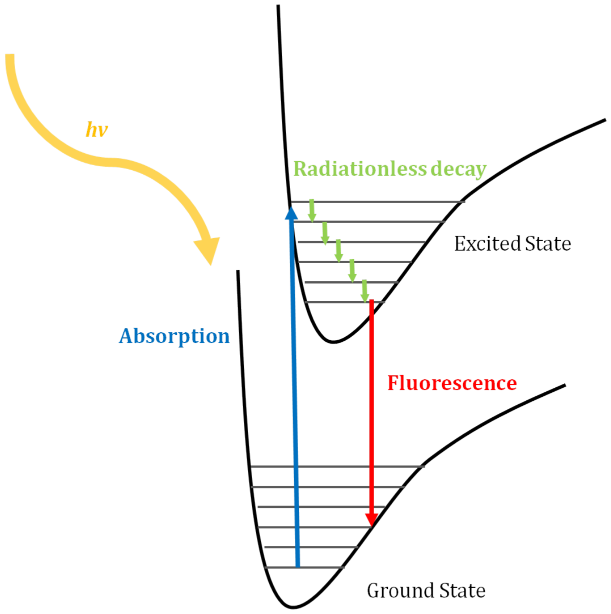

Figure 1.16: *Schematic of molecular states involved in fluorescence excitation and emission*

Fluorophore molecules will vary in terms of wavelength (energy) required to excite them. As energy is also lost through other processes (radiationless decay), the fluorescence emission is slightly reduced in energy, resulting in an emission spectrum further towards the visible region (red-shifted) than the excitation spectrum. The various molecular states and processes that result in fluorescence are schematically represented in figure 1.16.

In order to collect data for the fluorescence properties of a molecule, various setups can be employed. In the case of biosensor arrays, fluorescence microscopy is often favourable. A fluorescence microscope allows the user to collect the colourful light emitted by fluorescent arrays in a photographic image. The microscope focuses light on the sample at the excitation wavelength required and emitted light is collected back through the microscope objective. For this to be possible, two filters are applied to the microscope. One filters through the correct wavelength for excitation of the sample and another filter blocks any excitation light that could interfere with the emission light that is processed into a fluorescence image.

1.4.1.2 Fluorescence used in Biosensing Applications

The use of fluorescence for both qualitative and quantitative analysis extends to numerous biological research avenues including cell imaging,[120,121,122] biomolecule detection assays[123,124] and protein/sugar pathway monitoring.[125,126]

Biomarker analysis is usually approached using one of two methods. Either the analyte is tagged directly by the fluorophore or it interacts with the fluorophore in an indirect manner.[123, 127] The latter is a more common method used in array formats, whereby the fluorophore is usually conjugated to a biomolecule known to interact readily with the biomarker in question. This is particularly prominent in 'sandwich' immunoassay array platforms. Commonly, a biomarker is initially captured by an antibody immobilised on a substrate. This interaction is then sandwiched by a detection antibody. These detection antibodies are often conjugated with a fluorescent dye, or with a biotin group that can readily bind with dye-conjugated streptavidin. This approach gives a fluorescence readout representative of the biomarker present and is used very often for diagnostic mircoarrays.[128] Sandwich assays and fluorescence detection are often combined in microarray formats for fast quantitative detection of biomarkers.

1.4.2 Raman and Surface Enhanced Resonance Raman Spectroscopy (SERRS)

1.4.2.1 Raman Theory[129]

Unlike other spectroscopic techniques such as infrared (IR), where molecules are identified by light absorption, Raman scattering identifies molecules by the manner in which the incident light is scattered. The light scattering is observed by detecting the scattered photons at an angle to the incident beam being focused on the sample.

The Raman excitation beam is of a single wavelength. If the energy of the incident photons is not sufficient for molecular excitation into a higher electronic state, then scattering can occur. The photons distort the cloud of electrons around a nucleus, distorting them to virtual excited states. As this is an unstable state, photons are then re-radiated, allowing the molecule to relax into a lower state. Most commonly the photons undergo Rayleigh scattering, where no energy change occurs. Raman scattering occurs when an energy change occurs in the photon on returning to a lower state. For energy change to occur, the photons must cause nuclear motion.

Two types of Raman scattering are possible, namely Stokes and anti-Stokes scattering. Stokes scattering occurs when the molecule is excited to the virtual state from a ground state and absorbs energy from the photon to then return to an excited vibrational state which is higher than the original ground state. When thermal energy is available, some molecules are already in a higher excited vibrational state and when excited to a virtual state, the molecule releases energy that transfers to the photon and the electron of the molecule returns to a ground state, anti-Stokes scattering occurs. A diagram showing the three forms of scattering is shown in figure 1.17. Stokes scattering is more common than anti-Stokes scattering since most analysis is performed at room temperature. However, as the temperature is increased, more molecules will be in the excited state resulting in an increase in anti-Stokes scattering.

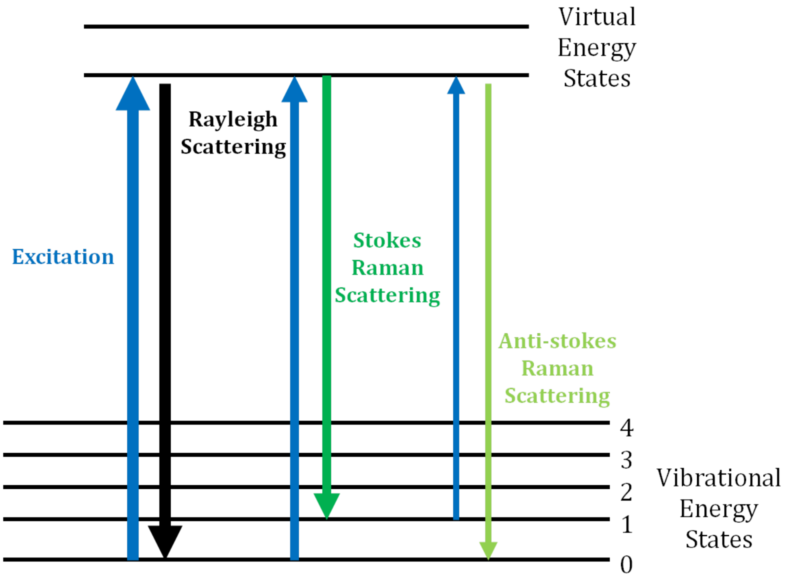

***Figure 1.17**: Diagram showing Rayleigh, Stokes and anti-Stokes scattering*

One of the major advantages of Raman is that there is virtually no sample preparation required. Solids and aqueous solutions can be analysed through glass containers with no interference. However, despite improvements in laser and machine quality, the technique still has the disadvantages of sample degradation, fluorescence interference and a great lack of sensitivity.

1.4.2.2 Surface Enhanced (Resonance) Raman Scattering (SE(R)RS)[129,130,131]

Surface Enhanced Raman scattering (SERS) was introduced as a method to overcome the sensitivity issues that are often encountered with Raman scattering. SERS requires that the Raman active molecule (chromophore) is adsorbed onto a roughened metal surface, yielding a possible 10^6 enhancement of scattering efficiency compared to when the molecules are bound to a flat substrate. This enhancement is often rationalised by the electromagnetic theory, where it is thought localised surface plasmons in the roughened metal are excited when hit by the incident light. This increases the local optical field intensity, giving an enhanced signal of the sample present. However, for effective scattering to occur, these plasmon oscillations must be perpendicular to that of the surface.

Further enhancement is achieved when the Raman chromophore is resonant with that of the incident laser wavelength and metal surface chosen. Accordingly, the technique is called SERRS. It provides greater enhancement than SERS alone and, in some cases, higher sensitivity compared to fluorescence. The improved enhancement from resonance of the laser frequency and chromophore results in the electrons being promoted to a real vibrational excited state rather than a virtual state. This causes greater energy transfer from the photon and so upon returning to a lower energy state, an enhanced signal of the spectrum is produced.

In the case of resonance Raman alone, the issue of background fluorescence can occur due to the intensity of the vibrational state, so both scattering and photon absorption can occur. Such an effect causes a broad fluorescence spectrum which overlays the Raman spectra peaks and masks sample information. The use of SERRS in this regard can have a marked effect. When a molecule with a fluorophore is attached to a roughened metal surface (commonly gold or silver), the fluorescence of the molecule is quenched, yielding an enhanced SERRS signal. This means that identification of the molecule is more reliable and a wider range of molecules can be identified.

1.4.2.3 Biosensing Applications using SE(R)RS Analysis

While fluorescence is a well established and reliable technique used in biosensor applications, there is a growing level of research aimed towards the use of SE(R)RS for detection of low levels of DNA[131,132,133] protein interactions[134,135,136] and for tracking functions related to the biology of cell function.[137,138] A variety of roughened metal substrates have been used and developed but gold and silver nanoparticles are popularly utilised in the case of biosensing. The choice to use SE(R)RS over fluorescence has proven popular given the advantages outlined in section 1.3.2.2. Fluorescence peaks are often very broad so multiplexing for detection of a variety of labelled biomolecules is difficult since fluorescence peaks for different fluorophores can overlap. Various studies of SE(R)RS as a multiplexed technique,[139,140] demonstrated that in some diagnostic situations, it is a more effective analytical technique than fluorescence.[130]

In the present work, SE(R)RS has been investigated as a compatible detection method for use in analysing biosensor arrays created by DPN.

1.4.3 Dark Field Microscopy[141,142]

Dark field microscopy is a useful technique for improving the illumination of objects that are normally difficult to visualise by standard bright field microscopy. When light is focused on a transparent sample, the objects present at the sample surface scatter the light in various directions, while the light that hits the area surrounding any sample artifacts will remain unscattered. Dark field microscopy only collects scattered light, thus illuminating the object very brightly against a dark background. This has proven useful for materials which are highly transparent against a clear background, or very low nanoscale features that scatter light efficiently. An excellent example of the advantages of dark field microscopy is shown in figure 1.18, where a more detailed image of nylon fibres are given, compared with that of a bright field illumination image.

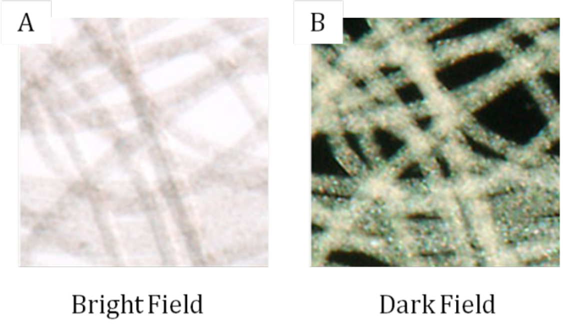

Figure 1.18: *Example of bright field (A) vs. Dark field (B) image of nylon fibres mounted on microscope glass cover slip* [141]

Nanoparticles are highly compatible for dark field microscopy imaging. As discussed previously, in relation to Raman and SE(R)RS theory (section 1.3.3), the majority of light scattered by an object does not result in an overall energy change from excitation of light (Rayleigh scattering). Metal nanoparticles are far more efficient light scatterers due to the localised electron oscillations that undergo excitation on the metal surface. Dark field collects this Rayleigh scattering and as a result, bright colourful images are often produced. Furthermore, these colours can give further details about particle shapes, sizes and whether clusters or single particles have formed at a surface. As a result, dark field microscopy often plays a role in biosensing through its ability to clearly track nanoparticle presence and behaviour under various conditions, such as nanoparticle protein conjugate interactions and cellular imaging.

Based on current applications, it was considered that dark field microscopy would be a useful analysis and imaging tool for DPN based work in this thesis. This is in context of nanoparticles and metal substrate development for SE(R)RS related biosensing studies.

It is clear that DPN as a technique has advanced greatly, with evidence of it being utilised for high-throughput printing of biomolecule arrays, improving upon current microarrays platforms through feature size miniaturisation. However, thus far there is little evidence of DPN arrays being used for quantitative biomarker detection or the development of DPN biomolecule arrays that are compatible with SE(R)RS detection.

The work in this thesis aims to address these areas of research that DPN has yet to be applied to. As a result, a high-throughput protein array print method was optimised for detection of a relevant biomarker, namely, prostate specific antigen (PSA). Investigation into biomarker detection using optical techniques fluorescence microscopy and SERS was performed in addition to the use of protein array templates for designing metal structures for SERS active substrate production.

1.5 Key Concepts of Biosensing

The concept of biosensing encompasses any given setup or device that is designed to detect a biological analyte, making it visible via a given signal transduction method. It plays a role in various different industries including medical research for disease detection and diagnosis,[143] or to detect expiry of food products.[144] Three major concepts to consider when designing a biosensing device are the platform, the detection technique and the binding efficacy of the analyte to the overall system.

Platform designs for biosensing varies greatly from biosensor arrays[15] and microfluidics[145] to lateral flow assays.[146] Platform design will always be determined by the purpose of the application. Microfluidic and array based platforms are a result of this interest in miniaturisation to benefit new applications, e.g hand-held drug testing devices.

While platform design will be determined by the use of the biosensor, it can also be influenced by the choice of detection method implemented. The choice is often determined by the sensitivity required in order to research the lowest level of analyte required in order to decide between a positive and negative result. For example, in the case of a hand held device such as a pregnancy test, the detection method must be able to detect the minimal level of analyte found in the urine, in order to determine if a woman is or is not pregnant, yet the method should also be able to fit within the small hand held size of a pregnancy test, further emphasising how the choice of detection is influenced by the platform choice and purpose of the biosensing tool.

Finally, the efficacy of detecting the analyte will be fully determined by the binding activity of the analyte within the system it is captured in. Equilibrium constant, K, is often used to explain the association of a reaction. An example is shown in equation 1, where the equilibrium is shown for a given analyte (A) and ligand (L) binding together to give an analyte-ligand complex (AL).

$$A + L \rightleftharpoons AL \qquad \textbf{Eq. 1}$$

Equations 2 and 3 show how the association constant (K_a) and dissociation constant (K_d) is determined, where $[A]$, $[L]$ and $[AL]$ represent concentrations of analyte, ligand and analyte-ligand complex.

$$K_a = \frac{[AL]}{[A][L]} \qquad \textbf{Eq. 2}$$

$$K_d = \frac{[A][L]}{[AL]} \qquad \textbf{Eq. 3}$$

The dissociation constant K_d is the value most often used to describe the binding efficiency of a protein in biosensing assays. As this represents the ease at which the analyte can come apart from the bound complex that any given assay is trying to induce, the lower the value of K_d, the more effectively it will bind to the complex. An excellent example of this is the commonly used biotin-streptavidin complex, which is often used in immunoassays in order to attach the detectable fluorophore to the analyte complex of interest. K_d for biotin-streptavidin complex is 10^{-14} mol/ L. It is well known that biotin and streptavidin have a high affinity for each other, hence the very low K_d value.

Ultimately, the K_d value of an analyte in any biosensing tool will determine its applicability of the technique. The work in this thesis looks at the miniaturisation of bioarrays via DPN, i.e. reduced platform size and coupling of SERS as an alternative detection technique for improved sensitivity. Therefore, choice of immunoassay to study must be carefully chosen. This thesis will explore the adaptation of an ELISA PSA immunoassay into miniaturised bioarrays. This is appropriate as PSA is found have a K_d value of approximately 10^{-10}.[147]

2. Aims and Objectives

The objective of this work was to explore the applicability of DPN in printing biomolecules for improved diagnostic purposes.

The initial focus was aimed at adapting an ELISA method used for the detection of PSA into an array format. Objectives for this work included:

1. To developing and optimise a fast patterning method for DPN of PSA capture antibody for immunoassay array templates.
2. To create fluorescently detectable PSA immunoassay arrays with comparable sensitivity to that of the ELISA kit.
3. To investigate compatible surfaces for the immunoassay array method.

Upon success of PSA immunoassay array adaptation, the next stage was to improve upon the sensitivity by altering the immunoassay for compatibility with SERS detection methods. Objectives were:

1. To investigate the ideal approach for assay alteration for SERS detection of arrays using nanoparticle based methods.
2. Improve upon the sensitivity gained by fluorescence based methods using SERS.

Finally, use of protein printing methods was applied in an alternative application to enzymatically create a SERS active substrate using a HRP reaction with silver growth media EnzMet™. The objectives considered here included:

1. To determine ideal patterns of streptavidin-HRP and optimum EnzMet™ conditions to dictate silver crystal growth.
2. To test SERS enhancement effects of silver substrate.

3. Experimental

3.1 Materials and Technology

3.1.1 Instrumentation and Apparatus

Alpha300 R, confocal Raman microscope fitted with lasers of λ_{ex} = 532, 633 and 785 nm (WITech, Ulm, Germany)

DPN 5000® (NanoInk Inc, Skokie, IL)

Leitz DMRB fluorescence (with TRITC filter)/ dark field microscope (Wetzlar, Germany)

Nanolithography Platform (NLP) 2000 (NanoInk Inc, Skokie, IL)

Nexterion® 16-well incubation chamber (Schott, Jena, Germany)

Nikon Coolpix 5400 camera (Japan)

Plasma cleaner (Diener electronic, Nagold, Germany)

3.1.2 Consumables

Centrifugal filter units (Millipore ™, UK)

DPN multi-pen M-type probes (M-1 end comprises of 12 "diving board" shape writing pens 100 μm apart and M-2 end has 12 "A-frame" writing pens 66 μm apart) (Nanoink Inc., Skokie, IL)

Inkwell arrays (M-6MW) (Nanoink Inc., Skokie, IL)

Nexterion® Slide E, epoxysilane coated glass (Jena, Germany)

PATH™ nitrocellulose slides (Gentel Biosciences Inc, Madison, WI)

Tapping mode AFM tip (AppNano, Santa Clara, CA)

3.1.3 Chemicals

All chemicals were purchased from Sigma Aldrich (Dorset, UK) unless otherwise stated.

Benzotriazole (BT) dye linker (synthesised in house by Anna Robson)

Biotin-dPEG$_3$®-Lipoic acid (Quanta Biodesign Ltd, Powell, OH)

EnzMet ™ western blot HRP detection kit (Nanoprobes, Yaphank, NY)

16-Mercaptohexadecanoic acid (MHA)

4-Nitrobenzene thiol (NBT)

N- (3-Dimethylaminopropyl)-*N*'-ethylcarbodiimide hydrochloride (EDC)

Sulfo *N*-hydroxysuccinimide (NHS)

Thioctic acid (TA)

Tween® 20

UltraPure ™ diethylpyrocarbonate (DEPC)-treated Water (Invitrogen ™, NY)

3.1.4 Proteins

Bovine serine albumin (BSA) (Sigma Aldrich, Dorset, UK)

Monoclonal mouse anti-human 3/PSA capture antibody (PSA Cap Ab) (Research & Diagnostics (R&D) systems, Abingdon, UK)

Recombinant human Kalikrein PSA (PSA standard) (R&D systems, Abingdon, UK)

Biotinylated goat anti-human Kalikrein PSA detection antibody (PSA Det Ab) (R&D systems, Abingdon, UK)

Streptavidin (Thermo Scientific, Northumberland, UK)

Steptavidin Dylight™ 549 (Thermo Scientific, Northumberland, UK)

Streptavidin horseradish peroxidise (HRP) conjugate (strep-HRP) (R&D systems, Abingdon, UK)

3.1.5 Buffers

4-(2-Hydroxyethyl)piperazine-1-ethanesulfonic acid (HEPES) buffer – 300 mM HEPES in deionised water, pH 7.6

Phosphate buffer – 10 mM Sodium dihydrogen phosphate and 10 mM disodium hydrogen phosphate, pH 7.

Phosphate buffered saline (PBS) - 137 mM sodium chloride, 2.7 mM potassium chloride, 8.1 mM disodium hydrogen phosphate and 1.5 mM potassium dihydrogen phosphate, pH 7.2-7.4, 0.4 μm filtered.

Protein printing buffer (Nanoink Inc., Skokie, IL)

Reagent diluent (RD) – 1 % BSA in PBS, pH 7.2-7.4.

Wash buffer (WB) – 0.05 % Tween® 20 in PBS, pH 7.2-7.4.

3.2 Nanoparticle Synthesis

Prior to preparation, all glassware was soaked in *aqua regia* and left for at least 4 hours. *Aqua regia* was then removed and all glassware was thoroughly rinsed with deionised water.

3.2.1 Gold Nanoparticles

The Turkevich method[148] was utilised for the synthesis of gold nanoparticles sized in the range of 10-20 nm. Sodium tetrachloroaurate (III) (50 mg, 0.14 mM) was dissolved in 500 mL of deionised water and this solution was then heated to boiling with continuous stirring. At the point of boiling, 1.5 mL (1 % (w/v)) of sodium citrate was added and the solution was left to boil for a further 15 minutes. The heat was removed and the solution was left to cool to room temperature.

λ_{max} = 521 nm

3.2.2 Silver Nanoparticles

The Lee and Meisel method[149] was adopted for the synthesis of 40-50 nm sized silver nanoparticles. 480 mL of deionised water was heated to 45 ˚C before the addition of 90 mg (0.5 mM) of silver nitrate in 10 mL of deionised water and continuous stirring was maintained throughout. Further heating was applied to the solution to bring it to a temperature of 98 ˚C and then 110 mg of trisodium citrate dissolved in 10 mL of deionised water was added. The temperature was maintained at 98 ˚C for 90 minutes before allowing the solution to cool back to room temperature.

λ_{max} = 401 nm; Particle size = 45 ± 4.3 nm (determined by dynamic light scattering, using the mean of 3 measurements)

3.3 Conjugate Preparation

3.3.1 Thiolated Streptavidin Dylight ™ 549

Solutions of NHS (2 mg/ mL) and EDC (2 mg/ mL) were separately prepared in deionised water. In an eppendorf, 50 µL of HEPES buffer (300 mM) was added and mixed with 10 µL of the EDC and NHS solutions followed by 10 µL of MHA (10 mM) in ethanol. The solution was mixed thoroughly and kept at 4 ˚C for 30 minutes. 20 µL of streptavidin Dylight™ 549 (1 mg/ mL in PBS) was added to 30 µL of UltraPure™ DEPC-treated water before incorporation with the EDC activated MHA solution. All chemicals and protein were well mixed and left for 4 hours to react at 4 ˚C.

The solution was placed in a centrifugal filter unit and 50 µL of HEPES buffer (300 mM) was added. The solution was then centrifuged at 13.4 rate per minute (rpm) for 5 minutes. This was repeated twice more and after each centrifugation 50 µL of HEPES buffer was added. The newly thiolated streptavidin Dylight™ 549 solution was stored at 4 ˚C until required.

3.3.2 Conjugation of Benzotriazole (BT) Dye Linker to Streptavidin

Solutions of NHS (2 mg/ mL) and EDC (2 mg/ mL) in deionised water were prepared. In an eppendorf, 50 µL of HEPES buffer (300 mM, pH 7.6) was added and mixed with 10 µL of the EDC and NHS solutions, and finally 10 µL of BT dye linker in ethanol (10^{-4} M) was added. The solution was mixed thoroughly and kept at 4 °C for 30 minutes. 2 µL of streptavidin (10 mg/ mL in PBS) was then added to 48 µL of UltraPure™ DEPC-treated water before incorporation with the EDC activated BT dye linker solution. All chemicals and protein were well mixed and left for 4 hours to react at 4 °C.

The solution was then placed in a 0.5 mL centrifugal filter unit and 50 µL of HEPES buffer (300 mM, pH 7.6) was added. The solution was then centrifuged at 13.4 rpm for 5 minutes. This was repeated twice more and after each centrifugation, 50 µL of HEPES buffer was added. The streptavidin-BT dye linker conjugate (strep-BT) solution was stored at 4 °C until required.

3.3.3 Streptavidin Nanoparticle Conjugates

The following method was applied to both thiolated streptavidin Dylight™ 549 and strep-BT prepared in section 3.3.1 and 3.3.2.

1 mL of silver nanoparticles (see section 3.2.2 for synthesis) was centrifuged at 5 rpm for 10 minutes. The loose pellet formed was shaken back into solution and nanoparticle solution was removed and placed in a fresh eppendorf, separate from those undesired nanoparticles that fell out of solution. The entire streptavidin modified solution was then added to the silver nanoparticles, mixed thoroughly and agitated overnight. The conjugates were centrifuged at 3.5 rpm for 20 minutes. The surfactant was removed leaving the streptavidin-nanoparticle conjugate pellet. The pellet was reconstituted in 1 mL of phosphate buffer (10 mM) and thoroughly mixed. Streptavidin-nanoparticle conjugates were stored at 4 °C until required for use.

Particle size after conjugate addition = 52 ± 5.5 nm (determined by dynamic light scattering, using the mean of 3 measurements)

3.4 Fabrication of Protein Arrays

3.4.1 Inkwell and Protein Preparation

M-type probes were cleaned using oxygen plasma for 40 seconds (50 % power, 72 cm^3/ min) prior to use. Protein print solution was prepared by adding 5 parts of the chosen protein in the required buffer to 3 parts protein printing buffer. 0.3 µl of the prepared protein print solution was then added to each of the 6 ink reservoirs on the inkwell arrays.

3.4.2 NLP 2000 Setup

A screen capture image of the NLP 2000 software windows are depicted in figure 3.1. The platform maximum co-ordinate limits were calculated using the "home" function. The substrate of choice was then mounted on the platform alongside inkwell arrays and the M-type tip was mounted on the chip holder with the M-2 pens exposed for microscope view and printing. Using the platform directing arrows, the stage was moved to contact the clean tips with the substrate. The "TY" co-ordinates were adjusted until tips were level and all tips were in contact with the substrate simultaneously. The platform was then manoeuvred to contact the tips in 3 separate locations around the area to be printed. These locations were saved as 'P1,' 'P2' and 'P3' and then the 'calculate' command was input. Array dimensions and dwell times were input on the pattern design screen (figure 3.1B) and assigned a pattern number. A location outside of the print area was assigned for tip 'bleeding'. The 6 tips furthest to the left were landed in the inkwell channels and saved as inkwell location A, followed by the 6 tips to the right of the probe, being landed in the channels and saved as inkwell location B. Finally, 'DC mode' was selected from the 'configure' drop down menu.

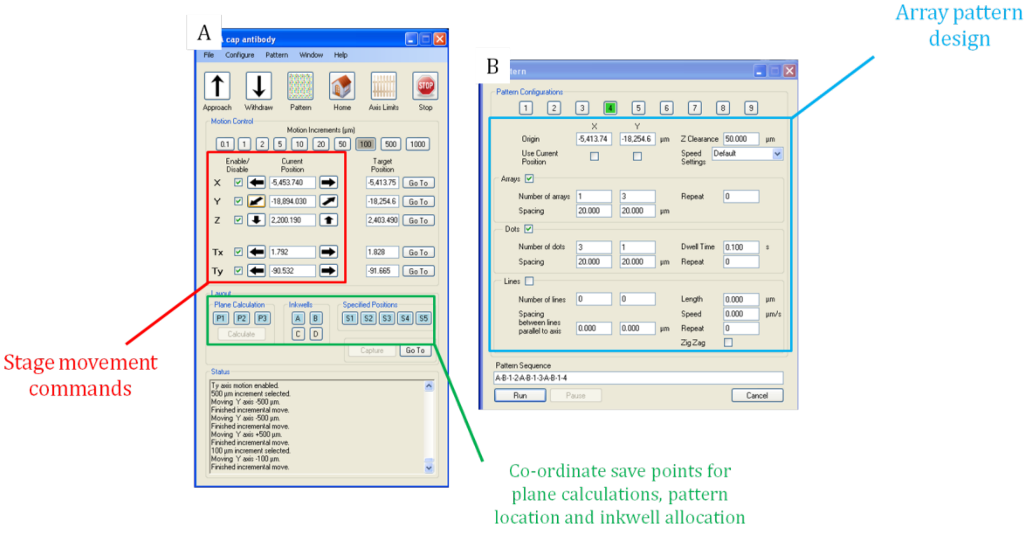

X ☑ -5,453.740 → Target -5,413.75
Y ☑ -18,894.030 → Target -18,254.6
Z ☑ 2,200.190 → Target 2,403.490
Tx ☑ 1.792 → Target 1.828
Ty ☑ -90.532 → Target -91.665

```
Ty axis motion enabled.
500 µm increment selected.
Moving Y axis -500 µm.
Finished incremental move.
Moving Y axis -500 µm.
Finished incremental move.
Moving Y axis +500 µm.
Finished incremental move.
100 µm increment selected.
Moving Y axis -100 µm.
Finished incremental move.
```

Origin X -5,413.74 Y -18,254.6 µm
Use Current Position ☐ ☐
Z Clearance 50.000 µm
Speed Settings Default
Arrays ☑
Number of arrays 1 3
Spacing 20.000 20.000 µm
Repeat 0
Dots ☑
Number of dots 3 1
Spacing 20.000 20.000 µm
Dwell Time 0.100 s
Repeat 0
Lines ☐
Number of lines 0 0
Spacing between lines parallel to axis 0.000 0.000 µm
Length 0.000 µm
Speed 0.000 µm/s
Repeat 0
Zig Zag ☐
Pattern Sequence A-B-1-2-A-B-1-3-A-B-1-4

Figure 3.1: *Screen capture of NLP 2000 software used for stage control (A) and pattern design (B)*

3.4.3 Pattern Programming (figure 3.1B)

In all experiments, pattern allocation 1 was always setup for the bleeding step. Each tip was programmed to deposit either a 2 x 2 dot, using a 1 second dwell time and a 33 µm pitch, or, a vertical and horizontal line, 66 µm in length at 20 µm/ s. Pattern allocations 2-9 were used for printing patterns that were for experimental studies and analysis and varied as per experiment. At the bottom of the pattern design window a text box was used for input of pattern order. While the order of pattern and pattern design varied for each experiment, any design input to allocations 2-9 were preceded by the functions 'A-B-1'. Patterning was started by initiation the 'run' command which landed the two sets of 6 tips on the probe in the inkwell channels; this was immediately followed by the bleed array function. The system continued to print whatever pattern function was input as per the given sequence for that experiment.

All experiments performed on the NLP 2000 were carried out at room temperature (19-21 ˚C) and a relative humidity of 40-60 %. Once the desired arrays were fabricated, the substrates were left to incubate overnight at 4 ˚C.

3.5 PSA Immunoassay Array Protocol

3.5.1 Printing Capture Antibody Arrays

The monoclonal mouse anti-human 3/PSA capture antibody (PSA Cap Ab) was reconstituted in PBS to a concentration of 3.2 ng/ mL and mixed with protein print buffer (section 3.4.1) to give a total PSA Cap Ab concentration of 2 mg/ mL. This solution was then applied to inkwell arrays (section 3.4.1). The NLP 2000 was set up with an epoxysilane or nitrocellulose functionalised glass slide mounted on the platform. Arrays were printed based on the designated experimental study and in areas of the slides that are exposed to the wells of the 16-well incubation chamber. Once printing was complete, the printed slide was incubated overnight at 4 °C.

3.5.2 PSA Immunoassay Attachment

After overnight incubation, the slide was removed from such conditions and allowed to return to room temperature for 1 hour. The slide was then washed in wash buffer (WB) before being applied to the 16-well incubation chamber. Wells that contained printed arrays were blocked by adding 100 µL of reagent diluent (RD) to the well. The slide was left to further incubate at room temperature for 1 hour. Recombinant human Kalikrein PSA (PSA standard) was reconstituted in RD to a concentration of 1030 ng/ mL. A range of PSA standard dilutions (60 ng/ mL to 0.24 ng/ mL in RD) were prepared based on the specifications of the experiment carried out at the time. A wash step was then performed on the slide whereby 3 x 100 µL of WB was added and removed from each well. 100 µL of the PSA standard dilution series was then added to the appropriate wells of the slide in the incubation chamber. A control array was prepared by adding 100 µL of RD to a well. The slide was then incubated for 2 hours with agitation. Biotinylated goat anti-human Kalikrein PSA detection antibody (PSA Det Ab) was reconstituted in RD at 200 ng/ mL. The slide was then washed (x3) with WB before adding 100 µL of PSA Det Ab to each of the wells. The slide was once again incubated for 2 hours with agitation. In preparation for the detection step, PSA Det Ab was removed and a wash step was carried out.

3.6 Detection of PSA Immunoassay Arrays

3.6.1 Fluorescence Detection

100 µL of streptavidin Dylight™ 549 (5 µg/ mL in RD) was added to each array set and incubated for 30 minutes while agitating. Finally, the slide was removed from the incubation chamber and washed in WB for 10 minutes. This was followed by de-ionised water and then the slide was blown dry with nitrogen. The processed slides were analysed by fluorescence microscopy using a TRITC filter (Ex. 543/ 40, Emm. 593/ 40) and a 50x objective (numerical aperture (NA) 0.5). Exposure time of 10 seconds was used for all images taken using either Leica QWin or MetaMorph software. Images were processed using Image J software.

3.6.2 Layer by Layer (LbL) Approach for SERS Detection

Streptavidin was diluted to a working concentration of 500 µg/ mL in RD. 100 µL of this solution was added to each array set and shaken for 30 minutes. A solution of biotin-dPEG$_3$®-lipoic acid was then prepared in RD at a working concentration of 1 mM. The streptavidin solution was removed from the arrays and a wash step (x3) was applied before adding 100 µL of biotin-dPEG$_3$®-lipoic acid solution to each array set for 1 hour (shaking). A further wash step (x3) was carried out before adding the gold nanoparticles (section 3.2.1). The nanoparticles were then incubated for 1 hour while agitating. Finally, the slide was removed from the incubation chamber and washed in WB for 10 minutes. This was followed by de-ionised water and then the slide was blown dry with nitrogen.

On the day of analysis, a 1 mM solution of 4-nitrobenzene thiol (NBT) in water was prepared (first prepared at 10 mM in ethanol then diluted further with water to 1 mM). The slide was again setup in an incubation chamber and 100 µL of NBT solution was added to each array set for 30 minutes. The slide was then removed, rinsed with water and once again dried under nitrogen.

False colour SERS map images of the arrays were then collected using a λ_{ex} = 633 nm, laser power 1 % - 250 mW, 1 µm resolution, 0.1 seconds integration time and a 50x objective (NA 0.5). Maps of a 3 x 3 spot section were taken and processed using WITech Project 2.02 software.

3.6.3 Streptavidin-Nanoparticle Conjugate Attachment for SERRS and Enhanced Fluorescence Detection

Streptavidin-nanoparticle conjugates were prepared as per section 3.3.3. To each array set, 100 μL of streptavidin-nanoparticle conjugate solution was added. Incubation times varied depending on the experiment to which they were applied. The solution was then removed from arrays and the slide was taken out of incubation chamber. It was finally washed in WB for 10 minutes with agitation, followed by 10 seconds in deionised water. The slide was fixed once blown dry with nitrogen.

Fluorescence images of arrays were captured using a TRITC filter (Ex. 543/40, Emm. 593/40) and a 50x objective (NA 0.5). Gain and exposure times remained constant for all images taken using MetaMorph software. Images were processed using Image J software.

False colour SERS map images of the arrays were then collected using a λ_{ex} = 532 nm, laser power 1 % - 500 mW, 1 μm resolution, 0.1 seconds integration time and a 50x objective (NA 0.5). Maps of a 3 x 3 spot section were taken and processed using WITech Project 2.02 software.

3.6.4 AFM analysis

All images were collected using a tapping mode AFM cantilever on the DPN 5000. The scan rate used was 0.5 Hz and a 512 pixel image resolution was collected. Raw images were processed using SPIP software.

3.6.5 Dark Field Microscopy Imaging of Arrays

Coloured images of nanoparticle based PSA immunoassay arrays were captured using dark field microscopy. A Leitz DMRB microscope with a 50x objective (N.A 0.5) was used to locate the arrays. Images were captured with a Nikon Coolpix 5400 camera that was connected to the microscope using reflection geometry. Automatic camera settings were used for image capture.

3.7 EnzMet™ Substrate Production Protocol

3.7.1 Preparation and Printing of Streptavdin-HRP Arrays

Streptavidin-HRP (strep-HRP) was provided in liquid form at a high but unknown concentration. Six solutions of strep-HRP in protein print buffer were prepared, utilising various concentrations and ratios of strep-HRP and protein printing buffer (PPB). The ratios and concentrations used were as follows:

1. 5:3 ratio of strep-HRP at 100 %: PPB
2. 5:3 ratio of strep-HRP at 50 % in PBS: PPB
3. 5:3 ratio of strep-HRP at 25 % in PBS: PPB
4. 1:1 ratio of strep-HRP at 100 %: PPB
5. 5:2 ratio of step-HRP at 100 %: PPB
6. 5:1 ratio of strep-HRP at 100 %: PPB

Solutions were applied to inkwell arrays as per section 3.4.1 in a format dependent on the experimental parameter being studied. The NLP 2000 was set up (section 3.4.1) whereby an epoxysilane functionalised glass slide was mounted on the platform. Arrays were printed based on designated experimental study and in areas of the slides that were exposed to the wells of the 16-well incubation chamber. Once printing was complete, the printed slide was incubated overnight at 4 °C.

3.7.2 Application of EnzMet™ Solution to Arrays

EnzMet™ western blot HRP detection kit comprises of three solutions; EnzMet™ solutions A, B and C. Both the kit and slide with strep-HRP arrays printed on it were firstly removed from 4 °C conditions and left for 1 hour to return to room temperature. The slide was rinsed with WB and shaken for 10 seconds before being immersed in water and left for 5 minutes with gentle agitation. The water wash step was repeated (2x) before excess water was removed and the slide was secured in the incubation chamber. To those wells in which strep-HRP arrays were present, 60 µL of EnzMet™

solution A was added for 4 minutes. Following this, 20 µL of EnzMet™ solution B was added and mixed thoroughly within each well. The solution was left to react with the slide for a further 4 minutes before 20 µL of EnzMet™ solution C was added to each well and mixed. Depending on the experimental parameters applied, the solution was incubated on the surface for times ranging from 5-25 minutes. Each stage of the EnzMet™ solution incubation required the application of agitation. At the end of each set time period the solution mixture (comprising all 3 EnzMet™ solutions) was removed from the surface and the slide was washed (3x) with deionised water for a period of 5 minutes. Finally the slide was dried under nitrogen and stored at room temperature for further applications.

3.7.3 Dark Field Imaging of EnzMet™ Substrate Arrays

Images of the EnzMet™ substrate arrays were captured using dark field microscopy. A Leitz DMRB microscope with a 50x objective (N.A 0.5) was used to locate the arrays. Images were captured with a Nikon Coolpix 5400 camera that was connected to the microscope. Automatic camera settings were used for image capture.

3.7.4 Application of NBT to EnzMet™ Array Substrate

A 1 mM solution of NBT in water was prepared (10 mM in ethanol then diluted further with water to 1 mM). The slide was setup in the incubation chamber and 100 µL of NBT solution was added to each well containing an EnzMet™ array substrate. The solution was applied for 30 minutes before being removed, and the slide was rinsed with water and dried under nitrogen.

False colour SERS map images of the arrays were then collected using a λ_{ex} = 532 nm, laser power 1 % - 500 mW, 1 µm resolution, 0.1 seconds integration time and a 50x objective (NA 0.5). Map dimensions varied in order to capture differing patterns. Images were processed using WITech Project 2.02 software.

4. Fluorescent PSA Immunoassay Arrays Fabricated by DPN

As reviewed earlier, there is an incentive to adapt current biomarker detection methods toward an array format, replacing the common disease screening method, enzyme-linked immunosorbent assay (ELISA).[2,3,112,150,151] Immunoassay microarrays have the advantages of multiplexing ability,[2,14] increased sample throughput[152] and reduced sample and reagent consumption.[151] Current printing techniques utilised for microarray printing include the likes of ink jet printers[14,15] or micro-contact printing,[12,13] which directly deposit the capture proteins on a functionalised glass substrate. Such techniques are found to produce feature sizes in the region of 100-200 μm.[5] Therefore, there is an opportunity to reduce this feature size using DPN. Results from miniaturisation of arrays could include increased array density per chip, improving experimental efficiency, reduced sample and reagent volumes and ultimately lower the cost of screening methods.

Substrate surface chemistry plays a vital role in both retaining activity of the printed capture protein and efficacy of assay detection, i.e. minimal background signal. There are a variety of surface chemistries which are commercially available as functionalised glass substrates for protein array attachment. Such functional surface groups including epoxy, aldehyde and NHS-activated glass surfaces have been reviewed extensively in the literature.[153,154] These substrates are found to covalently bind to the capture proteins, immobilising them on the substrate and the binding mechanism is well understood.

Nitrocellulose is a polymer matrix often coated on glass slides which has been used as a functional substrate for fabricating protein microarrays for various applications.[151,155,156] It is a common surface of choice in protein array applications due to its protein binding properties and high capacity. However, the exact mechanism that acts to retain protein functionality is not completely understood.[157] There has been speculation as to how the nitrocellulose functions and binds to the capture protein. Some literature suggests that it has a hydrophobic, non-covalent binding nature and it acts in a 'sponge like' manner, with electrostatic interactions playing a role in retaining protein function at the substrate surface.[157,158]

Recently, DPN has been found to be an effective method for printing arrays with micro-scale features on epoxysilane coated glass, resulting in the commercialised cytokine immunoassay kit that Nanoink Inc. now provide. However, DPN has yet to be used for printing on nitrocellulose, a substrate that is favourable to those in the disease screening field. Spot sizes produced on nitrocellulose using other methods, thus far, have been no smaller than 200 µm.[159]

Prostate-specific antigen (PSA) is a protein marker commonly used for the diagnosis of prostate cancer in men. PSA is present in both serum and blood plasma and is found both in complex and free form.[160,161] The concentration of free PSA in the body is measured, and used as an indicator for the development of prostate cancer. Therefore, creating a highly sensitive detection platform to determine levels of PSA in the body is of great interest in medical research.[161] Immunoassay approaches to the detection of PSA have already shown potential. Currently there are a variety of PSA detection kits including an ELISA kit supplied by R&D systems. This kit utilises a sandwich assay format whereby streptavidin-HRP is bound to the captured analyte and reacts with a substrate solution for colorimetric detection of the PSA.

In this work, the sandwich immunoassay format from the R&D systems ELISA kit was adapted into a microarray format using DPN. Printing of the PSA capture antibody (PSA Cap Ab) was investigated for compatibility with nitrocellulose and the printing process was optimised. The aim was to develop a fast patterning method to fabricate PSA immunoassay arrays on spin-coated nitrocellulose slides that were compatible with fluorescence detection, giving a comparable limit of detection (LOD) with that of the ELISA kit. Adaptability of the immunoassay arrays was further tested by comparing the nitrocellulose substrate with epoxysilane coated glass. Finally, with miniaturised spot sizes achieved, analysis of the arrays on the nitrocellulose was performed to gain some insight into the nitrocellulose function.

4.1 Adapting the Sandwich Assay Format

For fast patterning of the functionalised glass substrates, the NLP 2000 was used for all experiments. The tip-substrate contact is controlled through a series of plane calculations where the surface is moved to contact with the tips and contact can be visualised through a bright field microscope. Further to this, the NLP 2000 has the ability to print over a larger area range and at higher speeds than conventional DPN, as the tips are held stationary while the stage movement is controlled by a series of piezoelectric stacks located under the platform which the substrate is placed on. This is ideal for printing on the substrates of interest as both nitrocellulose and epoxysilane glass slides are 2.54 x 7.62 cm in size.

The capability to preset patterns and automated re-inking through inkwells was also favourable, as a semi-automated printing system could be designed. Up to 9 different patterns, in separate locations, can be printed in any one printing sequence input to the system. In this study, the M-2 side of the multi pen M-type probe was used, as the distance between each tip aligns with that of the inkwells channels, so that 6 tips at any one time can be coated with the PSA Cap Ab solution (see section 3.4.1 for inkwell preparation). Use of passive multi-pens and inkwell delivery was vital for the fast fabrication process as it allowed for automated reloading of ink between each array printed without having to manually recoat the tips by removing them from the system.

Figure 4.1 shows the successive steps taken to build the immunoassay arrays. The tips were first coated with PSA Cap Ab print solution by contacting the tips with the inkwell. Once coated, the capture antibody is deposited onto nitrocellulose by placing the tip in contact with the surface using the NLP 2000 (full procedure found in section 3.4.1, 3.4.2, 3.5.1).

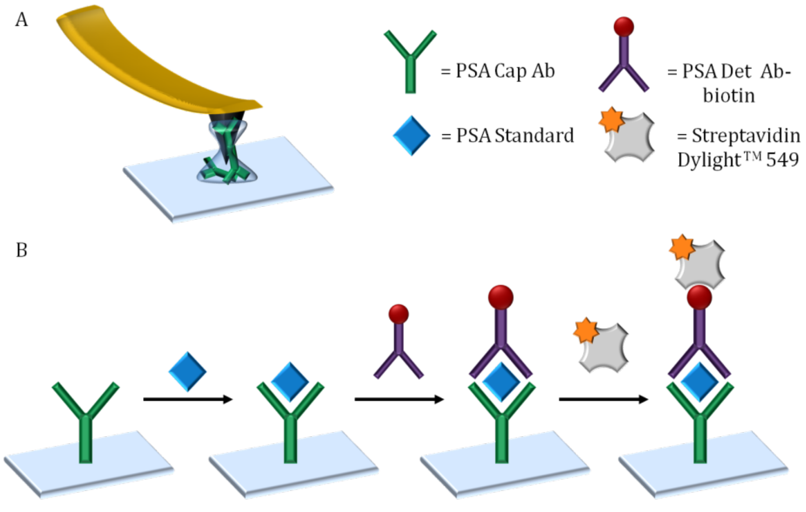

Figure 4.1: *Schematic of PSA immunoassay array development. DPN is used to pattern the surface with PSA Cap Ab (A) followed by the exposure to PSA standard, biotinylated PSA Det Ab and finally fluorescently tagged streptavidin Dylight™ 549 (B)*

The PSA Cap Ab solution was delivered to the substrates in array format at a concentration of 2 mg/ mL. This was a large increase in concentration from that of the ELISA kit protocol (0.1 mg/ mL), due to the large decrease in volumes used for the array assay. The ELISA kit applies 100 µL of PSA Cap Ab to each well in order to coat the bottom of the ELISA plate which is up to 6 mm in diameter, whereas a total of only 1.8 µL of Cap Ab is distributed in the inkwell reservoirs for DPN printing. Further to this, with the microarray spots being miniaturised to such a degree, it is important that a high concentration of antibody is used in order to ensure the surface area of the spot is well coated in the PSA Cap Ab.

Blocking of the slide and binding of the PSA standard and the biotinylated PSA detection antibody (PSA Det Ab) was carried out using the same concentrations, volumes and incubation times as the ELISA protocol, such as detailed in section 3.5.2. The streptavidin-HRP and colorimetric enzymatic detection method was replaced simply by adding streptavidin Dylight™ 549, which attaches to the assay through the biotinylated moiety on the PSA Det Ab. This gives a quantitative based PSA detection method through identifying the arrays by fluorescence, with varying PSA standard concentrations representing different spot intensities. Section 3.6.1 details the protocols for array preparation for fluorescence compatibility and analysis conditions used.

4.2 Parameters that Influence Spot Size and Shape

4.2.1 Effects of Dwell Time on Spot Size

Initial investigations were carried out to determine how dwell time would affect the feature size, as it is often a highly influential factor in the control of spot size. For a fair analysis of how each tip writes individually, a 4 x 4 feature array with 10 µm pitch (distance between spots) was printed by each of the 12 pens simultaneously, using inkwells filled with PSA Cap Ab solution (an example of four PSA immunoassay arrays printed by four of the tips is shown in figure 4.2A). Five sets of these 12 arrays were printed, each using a different dwell time for the features, ranging from 0.01 to 1 second. Dwell times greater than 1 second were of no interest as the aim was to develop a fast patterning technique. 0.01 second was the lowest tested contact time as it was the limited speed of the NLP 2000. The second parameter studied for influence of feature size and shape was the use of repeat printing. For this, the various contact times were repeated again but with repeat deposition over the same array after re-inking. This method of fabrication was of interest for investigating if further inking the spots would improve spot intensity or influence the feature shape. Therefore in total, there were 10 sets of arrays that each of the 12 tips produced.

PSA immunoassay protocol (section 3.5.2) and streptavidin Dylight ™ 549 array attachment (section 3.6.1) was carried out on the arrays using a PSA standard concentration of 60 ng/ mL and images of the arrays were captured using a fluorescence microscope (details of analysis conditions are found in section 3.6.1). Average spot size for each contact time was determined by measuring the diameter of 4 spots from the second row of 4 arrays (example image shown in figure 4.2A) using Image J software. Graphs were then plotted for average spot diameter vs. the square root of contact time for both single and repeat print arrays and are shown in figure 4.2B.

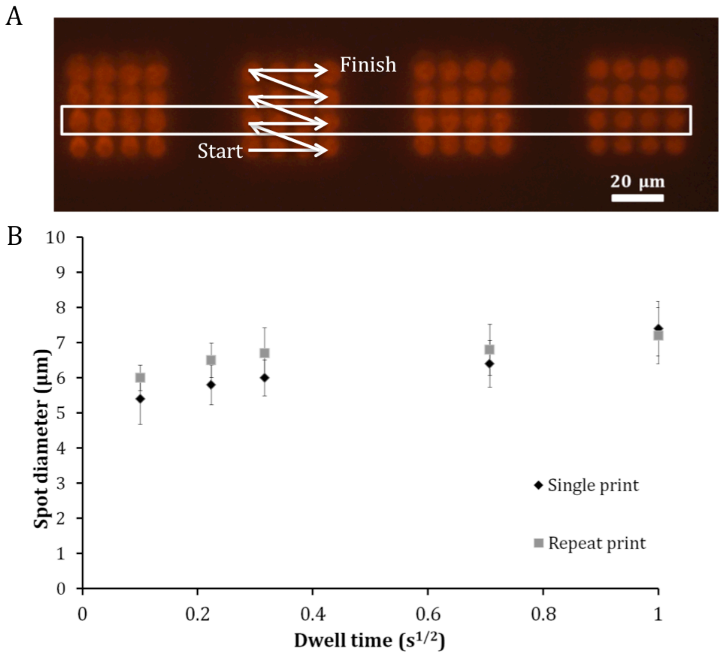

Figure 4.2: *A fluorescence image of PSA immunoassay arrays with a PSA standard concentration of 60 ng/ mL produced by a 1 second dwell time, single print (A), white box represents spots used for spot size analysis and arrows show direction and order of spot printed by tip. Plot of average spot diameter vs. square root of dwell time for single print and repeat print (B)*

A decrease in dwell time resulted in a reduction of feature size for both printing methods, the smallest being 5.4 ± 0.7 μm (0.01 second dwell time) and the largest being 7.4 ± 0.8 μm (1 second dwell time). However, the reduction is minimal as there is only a 2 μm difference between using the longest and shortest contact time. The factors that influence the lack of reduction are likely to be the physical nature of the protein printing buffer. Before addition to the inkwells, the PSA Cap Ab solution was mixed with a protein print buffer. The addition of this buffer facilitates effective ink deposition at the surface throughout the DPN printing process. It acts as a liquid ink carrier and has a low vapour pressure that prevents drying out of the ink in the inkwells. It also adds viscosity to the ink, aiding good uptake of Cap Ab onto the tip to allow efficient transfer to the surface. More importantly, it retains the activity of the antibody during the printing process. Further to this, publications evidenced that the use of carrier inks resulted in a liquid ink transport model being adopted, giving much faster ink deposition rates and therefore requiring shorter dwell times, much like the results found here.[96] Little change in spot size occurred with dwell time and larger features are spotted at much faster dwell times. It is likely that these trends are from the protein print buffer improving the wettability of the surface and tip and this facilitates deposition, physisorption being the dominating factor. This would make sense, as nitrocellulose is thought to be hydrophobic in nature, so deposition of a hydrophilic ink from a hydrophilic tip would be difficult. However, this protein print buffer overcomes this issue, creating a meniscus bridge upon tip-surface contact and allowing PSA Cap Ab arrays to be printed. Finally, since the protein carrier buffer has a low vapour pressure, the spots will take time to dry at the surface, so continued spreading of the features can occur while the spot is still hydrated i.e. whilst they dry slowly overnight.

Repeat printing of the arrays influenced both the feature size and homogeneity of the features. Comparing the data in figure 4.2B, it is clear that the decrease in spot diameter for the repeat print arrays is less than that of the single print arrays. This is due to the repeat printing adding more liquid to the spot and the repeat contact spreading the spot wider resulting in larger feature sizes. Again, these increases are not significant. From the data compiled in figure 4.2B and from general observations of the NLP 2000, the optimal dwell time to use was 0.1 seconds. This is due to the significant increase in speed over that of 0.5 and 1 second dwell time. Further to this, the difference in spot diameter between 0.1 and 0.01 seconds is only a 0.5 μm difference. Observations made during printing also found that, although dwell times as low as 0.01 seconds can be input to the NLP pattern design, the reality of this dwell time being achieved by the instrument (and for 0.05 seconds dwell time) was not the case. The only difference really in dwell time was between 1, 0.5 and 0.1 seconds dwell time, therefore, 0.1s dwell time was chosen for fast patterning.

4.2.2 Effects of Repeat Print on Spot Homogeneity

It was decided that single vs. repeat print methods would be compared again for 0.1 seconds dwell time as it is important to confirm the optimum settings to gain the best methods. Although speed of patterning is important, spot shape consistency is also vital for good accurate array analysis.

As dwell time was no longer in question, a new array format was adopted, in order to create a single array from all 12 tips. As a result, two arrays, using 0.1 seconds dwell time, were printed with the dimensions of 24 x 8 features and a pitch of 33 µm. This meant that each pen on the probe contributed 2 x 8 spots within the overall array, with the order of patterning for each pen working from left to right (i.e. two spots side by side) followed by the pens moving in an upwards direction to print next row. A 33 µm pitch was used because the distance between each pen was 66 µm so it produced even distances between each feature. Only 16 spots per pen were printed since the ink volume and the consistency of the spot size depleted greatly beyond this point. One array set was designated to single printing whilst the other was repeat printed. PSA immunoassay arrays bound to streptavidin Dylight™ 549 were produced. An example of the resulting array patterns are shown in figure 4.3. Both images depict an 8 x 5 spot area of the single and double print arrays.

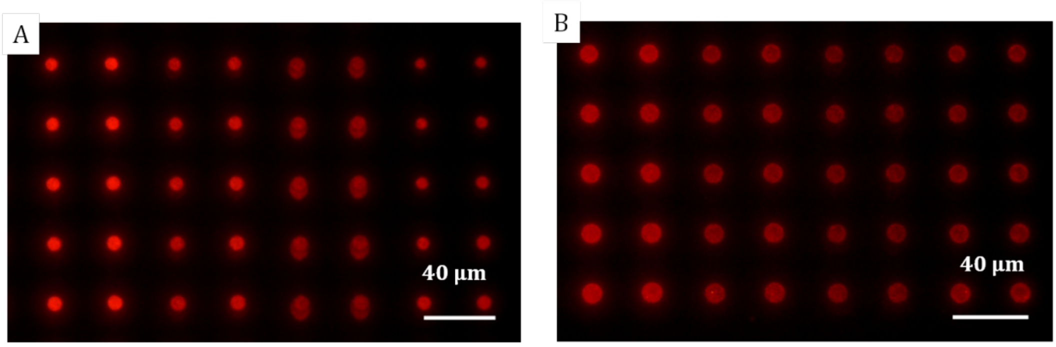

Figure 4.3: *Fluorescence images of an 8 x 5 feature area of single (A) and repeat (B) print array of PSA immunoassay arrays with a PSA concentration of 60 ng/ mL. Contrast for images have been modified to optimise spot shape definition*

The fabrication of each array made use of all twelve pens printing simultaneously, therefore issues of feature size variation from pen to pen are possible. Reasons for this occurring include bending of the pens to produce variable contact points with the surface from pen to pen, surface plane shifts whilst printing and defects or tip damage. This variability is shown in figure 4.3A where single printing has been used, resulting in the four columns of spots to the right of the image varying in size to the other columns in the image. The two columns produced by the third tip is this area maybe bent downwards out of the plane from the rest of the tips, resulting in a larger spot size compared with that of the others. In the case of the furthest two columns to the right, the pen appears to have run out of ink. This is likely as it can be seen that the spot size reduces in size as the printing continues toward the top of the image. Again simple defects could explain this tip's behaviour.

These spot size variations appear to be reduced greatly when repeat printing is performed (figure 4.3B). The process re-deposits extra ink and therefore gives the area a fuller spot and improves any poor printing that may have occurred from the first deposition. The lack of increase in intensity for the repeat print is likely due to the high concentration of PSA Cap Ab used. At 2 mg/ mL concentration, large quantities of PSA Cap Ab will be deposited onto the nitrocellulose in the small volume of ink. Therefore, unless the first deposition was unsuccessful, there will be no available binding sites in the area as the high concentration of antibody from the first deposition will saturate the surface. It is likely that any excess capture antibody within the feature array is removed in the first wash step.

From these results it was concluded that 0.1 seconds dwell time and repeat print is required for fast patterning of PSA Cap Ab arrays, with good feature size consistency and shape. The optimised conditions are ideal in terms of increased patterning speeds through use of liquid ink transport, inkwells and multi-pens. Further to this, the low micro-scale in which the arrays are produced means that they are highly compatible with conventional detection microscopies, a requirement that was highlighted previously.

4.3 Sensitivity Limits of PSA Immunoassay Arrays

Having optimised the printing, the next step was to use the arrays for a PSA concentration study, to compare with that of the ELISA kit.

Using a dwell time of 0.1 second and the same array dimensions as described in section 4.2.2, 8 arrays were printed on a nitrocellulose slide. PSA immunoassay arrays tagged with streptavidin Dylight™ 549 were developed such that each array corresponded to a different concentration of a PSA standard. PSA standard concentrations ranged from 60-0.94 ng/ mL plus a control array was prepared where only reagent diluent was added in place of PSA standard. Fluorescence microscopy images were taken of each array and the images were processed.

The mean fluorescence intensity for 20 spots was measured to give an average spot intensity (average background was subtracted from each spot values) for each array representing a different PSA standard concentration. This was calculated for 20 spots in an array and averaged to get the total average spot intensity for a set PSA standard concentration. A plot of average spot intensity vs. PSA concentration is shown in figure 4.4.

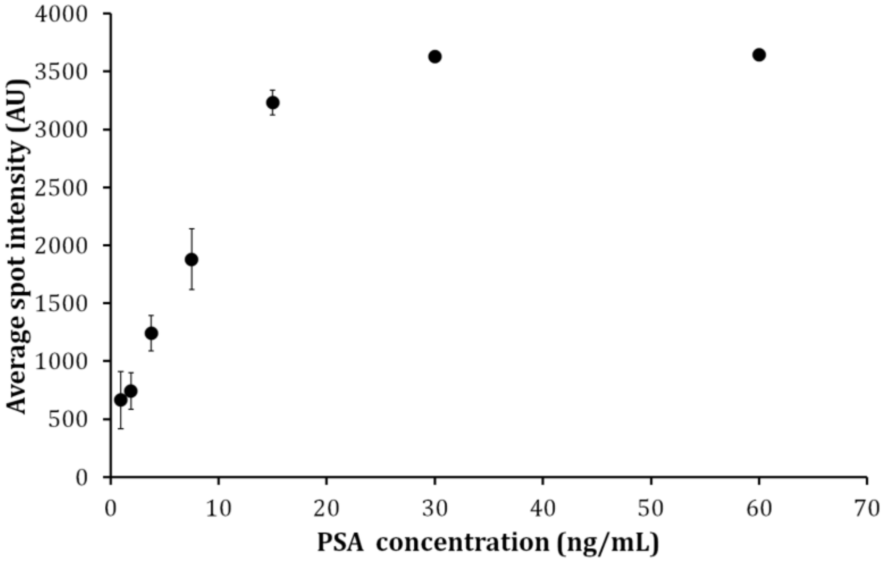

Figure 4.4: *Plot of average spot intensity vs. PSA concentration for limit of detection PSA immunoassay arrays*

The concentration study was effective as an increase in intensity occurs as PSA concentration increases. Saturation of PSA binding to the capture antibody arrays occurred at concentrations between 30 and 60 ng/ mL of PSA standard which resulted in no further increase in fluorescence intensity from the arrays as PSA concentration increased. Furthermore, no fluorescence spots were imaged in the control assay, only some low fluorescence background which proves minimal non-specific binding was achieved. The concentration study was repeated twice more, giving similar results to that shown in figure 4.4. The limit of detection (LOD) was calculated by multiplying the standard deviation of the control assay intensity by 3 and dividing the resulting number by the gradient of the slope given from the data points in the concentration range of 15-0.94 ng/ mL i.e. the linear concentration range. The calculated LOD was found to be 0.098 ng/ mL. This was comparable with the PSA ELISA kit provided by R&D systems which states that their calculated LOD is in the region of 0.030 ng/ mL. This proves that the immunoassay method transfers to nitrocellulose surface chemistry easily, making it a sensitive detection method with a more flexible and faster processing opportunity especially through fabricating the arrays using DPN.

4.4 Analysis of Nitrocellulose Surface

As discussed earlier, nitrocellulose is a popular choice of substrate in microarray platforms despite the lack of understanding about its true function to retain protein activity at the surface. Nitrocellulose can be coated onto glass in the form of a 3D porous matrix and in the case of the PATH® slides used here, it is spin-coated into a film of only 200 nm in thickness. This was ideal for the scale of the arrays printed, using DPN, since the surface is flat and claims to be non-porous.

AFM studies are often carried out on protein micro/ nano arrays printed by DPN when working with flat surfaces such as glass or gold which show increasing heights that correlate with the size of the proteins present on the surface.[51] The aim here was to determine how the PSA immunoassay arrays appears on the nitrocellulose surface in order to gain a better understanding of how the matrix functions to maintain protein function for the full assay to be carried out. To this end, the assay was inspected at different stages to observe how each additional step affected the nitrocellulose surface topography. Seven sets of arrays were printed using 24 x 8 features layout with 33 μm pitch and a 0.1 seconds dwell time. Five of the arrays were printed with PSA Cap Ab print solution and each array was developed to various stages of the immunoassay. One array was simply washed with wash buffer (0.05 % Tween 20 in PBS), the next was washed and blocked with reagent diluent (1 % BSA in PBS). The other three arrays were treated as per the assay protocol with one being the full fluorescent assay, another lacking the streptavidin Dylight™ 549 and the final one had both streptavidin Dylight™ 549 and the biotinylated detection antibody absent. To further test that spots were present due to the presence of protein in the ink, another two set of arrays were printed simply with PBS and protein carrier buffer combined. One array was washed with wash buffer whilst the other was blocked with reagent diluent.

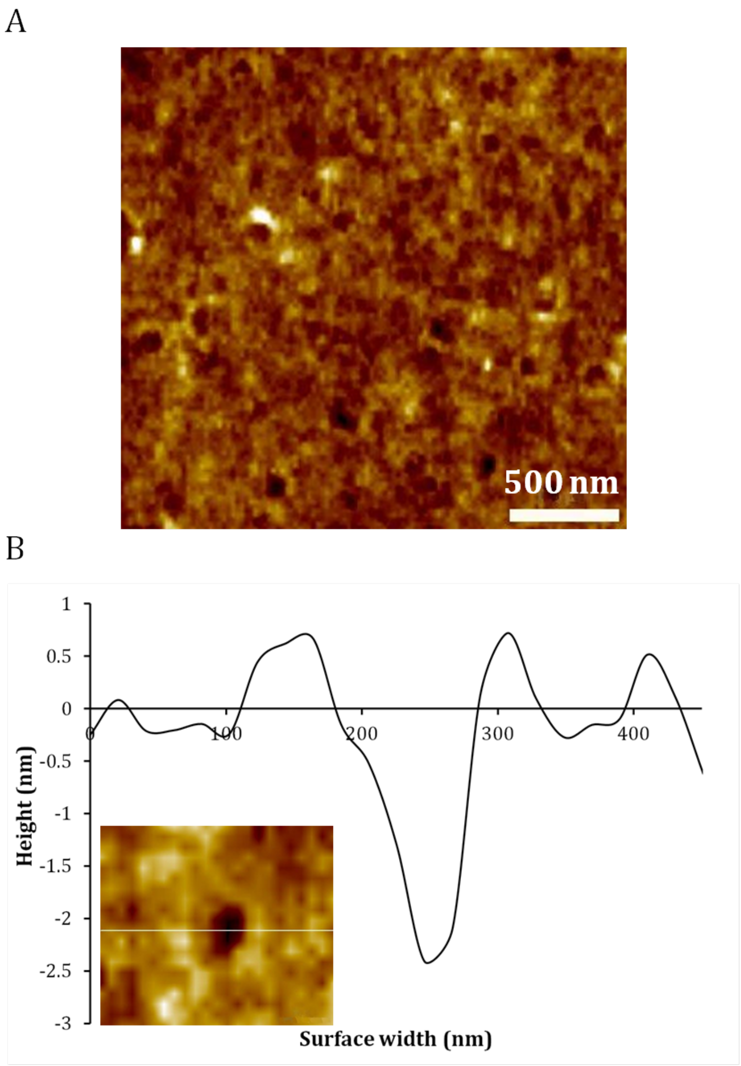

Figure 4.5: *AFM topography image of a hydrated nitrocellulose surface with no proteins present (A) and height profile across a pore (B) with AFM image of analysed pore on inset*

It was initially found that a porous matrix forms upon hydration of the nitrocellulose as shown in figure 4.5. Here, the nitrocellulose PATH® slide was hydrated with wash buffer then dried under nitrogen before being analysed by AFM. Pores can be seen in the AFM image in figure 4.5A and the example used in the surface profile (figure 4.5B) shows that the pores are roughly 144 ± 21 nm in width. This suggests that spin coated nitrocellulose becomes porous upon hydration which allows for the matrix to absorb protein into the surface to bind and retain protein function.

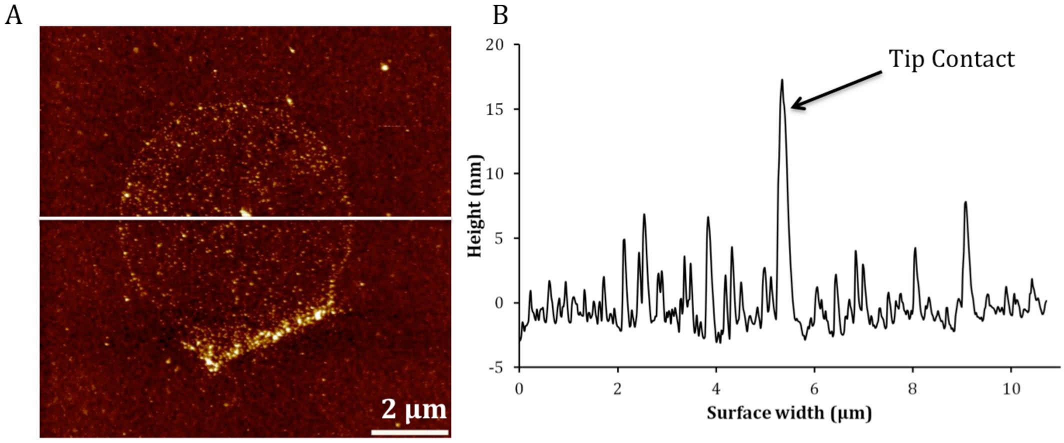

Figure 4.6: *AFM topography image of a single spot from 60 ng/ mL PSA immunoassay array (A) and surface profile through middle of the spot (B)*

A topographical AFM image of a spot representative of the full immunoassay is shown in figure 4.6A. The full assay involves four different protein interactions within the feature, yet the spot remains flat and low in height across the surface. This further confirms the concept that the nitrocellulose absorbs the proteins through its porous nature, upon wetting of the material. Images gained from the other arrays representing different stages of the assay all gave a similar resulting image. As can be seen in figure 4.6B, there is some change in the surface profile across the area where the spot is, however, as this was consistent for all arrays at various stages of the assay, it confirms that the proteins and antibodies are absorbed into the nitrocellulose matrix to bind as part of the assay as opposed to building up on the surface (which would cause an increase in height of the surface profile of the spot) as would occur on modified glass surfaces.[51] Furthermore, in figure 4.6B, and all other scans of the arrays, a small feature in the centre of the spot can be seen. This is from the contact of the tip with the surface, slightly piercing it. This confirms that when AFM scans were performed on an assay spot, it was in fact the nitrocellulose that the tip was in contact with as the image is scanned. Therefore, the nitrocellulose material functions effectively by allowing protein binding and function to be maintained by absorbing the protein into thesurfaces through the pores and the protein interactions occur within the thin nitrocellulose layer as opposed to the exposed surface where initial protein contact happens. Finally the control arrays printed, with no capture antibody present in the printing solution, were not found to be present at the surface after washing, i.e. no spots could be imaged by AFM showing the presence of any printing buffer having been used. This concludes that PSA Cap Ab (or in general, a functional biomolecule) must be present in the printing solution for array spots to be imaged by AFM. It further suggests that the printing solution really does just act as a protein carrier and that upon washing the surface, the protein print buffer is removed while the protein or antibody is captured by the nitrocellulose surface.

4.5 Adaptability of the PSA Immunoassay Arrays to Alternative Substrates

4.5.1 PSA Concentration Study on Epoxysilane Substrate

Previous publications related to DPN have shown that in the case of protein binding, the conditions and materials used are highly specific to the experiment carried out at the time. However, it is advantageous to be able to develop a printing method that is adaptable. Some researchers have found that molecules printed via liquid carrier inks can often be adapted to different surfaces, as the dominating effect of physisorption facilitates deposition and therefore would improve the wettability of any surface; however, this has only really been explored for metal patterning.[98] In any case, this should mean that it is possible to adapt the printing method for PSA Cap Ab arrays to other surfaces, which is important in terms of immunoassay arrays, as a whole variety of surface chemistries are available for using as microarray platforms. Therefore, it was of interest to see if the same immunoassay array protocol could be adapted to epoxysilane coated glass, in order to achieve consistent or even better results, in terms of PSA standard sensitivity and calculated LOD.

PSA immunoassay arrays were printed and developed on epoxysilane coated glass, for a PSA concentration study using the same methods and array design as in section 4.3.

PSA standard concentration range of 15-0.94 ng/ mL was studied, as it was clear from the nitrocellulose immunoassay array work that this concentration range made up the linear part that determined the sensitivity of the assay. This substrate differs greatly to that of nitrocellulose as the epoxy groups covalently bind to the protein applied at the surface during printing. It is also a hard substrate and all binding interactions occurring within the arrays will happen on the substrate surface as opposed to the absorbing nature of the nitrocellulose matrix.

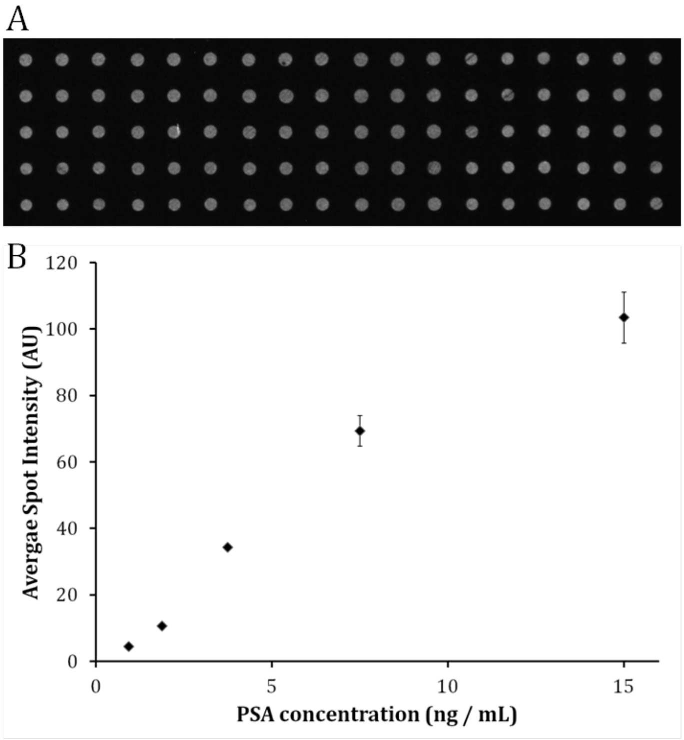

Figure 4.7: *Fluorescence image of PSA immunoassay arrays at 15 ng/ mL PSA standard concentration (A) and a plot of average spot intensity vs. PSA concentration (B)*

Figure 4.7 shows both a fluorescence microscopy image of an example array representing 9 of the 12 tips used (figure 4.7A). Spots show good uniformity and minimal intensity variation (further shown by the small error bars found for each point in the graph in figure 4.7B). A calculated LOD of 0.067 ng/ mL was found (using same calculation method as in section 4.3) in this case for the epoxy based substrate arrays, giving an improvement upon the calculated LOD for the nitrocellulose arrays. This further highlights the importance of immunoassay array methods being adaptable, as it is proven that certain substrate platforms may give better reduced background signal or improved protein binding, resulting in more sensitive results.

An observation was made in that the spots on the epoxy substrates were calculated to have an average diameter of 9.8 ± 0.6 µm. This is interesting as the same tip design, dwell times and distances were used as they were for nitrocellulose yet the feature dimensions are almost twice the size. This supports the theory of how surface tension has an influence over feature size when using liquid carrier meniscus deposition. The epoxy substrate may have a lesser surface tension and greater wettability effect on the ink therefore the spot spreads more across the surface than with nitrocellulose. Another possible theory could be related to the larger difference in the two substrates functionality. As the nitrocellulose is a porous network, when the protein solution is deposited in a spot, the diffusion of proteins into the matrix and well as spreading of ink at the surface occurs, unlike with epoxy glass, where spreading will only occur at the surface, therefore only being pushed outwards across the surface, possibly resulting an increase in spot size width.

4.5.2 AFM Analysis of PSA Immunoassay Arrays on Epoxysilane Coated Glass

AFM analysis of the arrays on epoxy glass was carried out, in order to fully determine the difference in protein interaction with epoxy compared with nitrocellulose functionalised glass. An example AFM analysis of a PSA immunoassay spot on epoxysilane coated glass is show in figure 4.8.

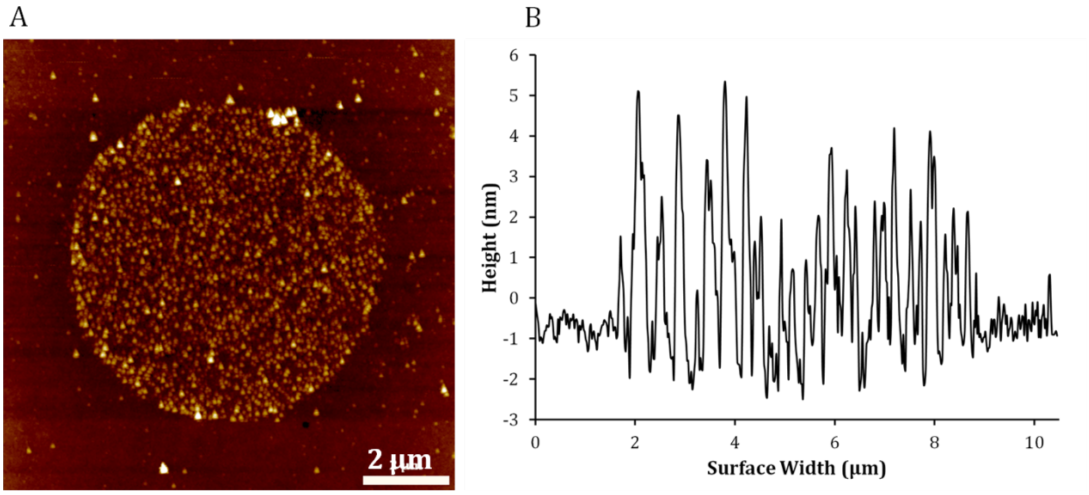

Figure 4.8: *AFM topography image of 60 ng/ mL PSA immunoassay spot on epoxysilane coated glass (A) and plot showing cross sectional height across the spot (B)*

It is clear from figure 4.8A that the epoxy surface is very flat and there is no evidence of porosity as found with nitrocellulose surfaces. Further to this, the spot contained various PSA immunoassay interactions and are found to be clearly immobilised on the surface of the glass as expected, giving a general increase in height across the area where the spot is present, as shown in the graph in figure 4.8B. Finally there is no evidence of tip damage at the epoxy surface in the middle of the spot, which was found with the nitrocellulose arrays. Therefore, the proteins are bound at the surface of the substrate and maintain their activity throughout the build up of the assay due to the epoxy group covalently binding to the initial PSA Cap Ab's that were printed.

4.6 Concluding Remarks

DPN was used to fabricate protein microarrays onto an alternative surface that was nitrocellulose. It produced features at least 20 times smaller than any features produced on nitrocellulose substrates using other printing techniques such as ink-jet printing. Furthermore, the use of the NLP 2000 system, multi-pen probe arrays and inkwells gave an opportunity to develop a high-throughput method of array fabrication, covering a large surface area print. Control of spot size and optimisation of feature morphology was possible through changing contact time between pen and surface and also repeat printing. Successful application of the arrays was further proven by creating PSA immunoassay arrays for a concentration study of PSA, whereby the arrays were detectable by fluorescence. The PSA immunoassay array method was found to be adaptable to other substrates and was also produced on epoxysilane coated glass. The array assay for both substrates gave a PSA LOD comparable with that of the standard commercial ELISA kit. This highlights that the DPN techniques are compatible for fast patterning of proteins for the detection of biomarkers at low micron scale on a single chip. With miniaturised arrays, this gives an opportunity to obtain more results within a smaller substrate area and therefore testing for diseases or conditions faster and accurately whilst consuming less materials and maintaining sensitivity of the assays tested.

AFM analysis of the immunoassay arrays gave great insight to the porous, absorbing nature of nitrocellulose. It was found that its absorbent nature is the key to retaining protein activity at the surface, in order for further binding to occur within the immunoassay. This differed greatly to the binding of proteins to the epoxy glass substrate, which form covalent bonds with surface proteins and immunoassay proteins built up on the external surface of the glass.

Much of this work resulted in publication in the journal Analyst in 2011 (E. Irvine *et al.*, *Analyst*, 2011, **136**, 2925. The full publication can be found in the appendix.

5. Developing PSA Immunoassay Arrays Optimised for SERS Detection

The work in this chapter focuses on improving upon the sensitivity of the PSA immunoassay microarrays achieved in the previous section through optimising the assay for SE(R)RS detection. As the PSA sandwich assay itself is currently optimised for compatibility with functionalised glass surfaces, nanoparticle approaches were considered for the SE(R)RS enhancement. Both a layer by layer (LbL) nanoparticle-dye assembly method and protein-nanoparticle conjugate approach were investigated in an attempted to gain the best PSA limit of detection via SE(R)RS.

A constant challenge in the field of biodiagnostics is improving upon the sensitivity of current methods for biomarker detection. There are numerous biomarkers that require improved sensitivity in order to monitor disease development or to diagnose a patient. This is still the case for the prostate cancer biomarker PSA. Current methods require that a patient serum sample produces an elevated PSA level in the range of 4-10 ng/ mL in order for that patient to be considered at risk.[162,163] However, elevated PSA levels can often be the result of other conditions such as prostatitis and benign prostatic hyperplasmia.[163] Therefore, attempts to diagnose prostate cancer at this stage based on PSA elevation can result in false positives leading to overtreatment of patients. Attempts to combat this issue include the likes of early stage monitoring of PSA elevations, where high risk patients are determined by an increase of PSA levels over the course of a year before reaching the 4 ng/ mL level,[163] leading to the possibility of earlier diagnosis which would be advantageous. As a result, the ability to detect lower levels of PSA is vital for improved diagnosis of prostate cancer but also to recognise failed treatment post-radical prostatectomy.[164] Further to this, it has recently been considered that elevated PSA levels in women could be used to detect early stage breast cancer; however, to determine this, picogram (pg) levels of detection must be achieved.[165]

To enhance the sensitivity of PSA detection, a variety of approaches have been attempted including photonic crystals or quantum dots for enhanced fluorescence,[143,166] electrogenerated chemiluminescence,[167] surface plasmon resonance

(SPR)[168] and microcantilever methods.[169,170] An alternative approach that has emerged is nanoparticle based enhancement for SE(R)RS related detection. However, other than examples of technique compatibility in PSA detection,[171] there is little evidence of SE(R)RS application for quantitative purposes. Stevenson *et al.*, proved that using gold nanoparticles to enhance the Raman signal of 2,2'-azino-bis(3-ethylbenzothiazoline-6-sulfonic acid) (ABTS), gave an increased sensitivity SERRS ELISA for PSA, improving upon that of the colorimetric detection method.[172] A further example includes the work of Porter *et al.*, who utilised functionalised gold films to immobilise PSA cap Ab's and successfully achieved femtomolar (fM) detection through use of a sandwich assay, where tracer antibodies attached to gold nanoparticles tagged with a Raman reporter molecule (RRM) gave a SERS response based on the level of PSA present.

Importantly, the methods described for quantitative SE(R)RS detection of PSA were carried out in large quantities like ELISA or, in the case of Marc Porter's work, the use of gold substrates that required extra steps for surface functionalisation, in order to make it compatible with antibody immobilisation. Ultimately, there have been no attempts to miniaturise the sandwich assay for SE(R)RS detection using microarray formats. Further to this, there is little evidence of SE(R)RS being utilised with DPN printed materials. Stokes *et al.*, appears to be the only case, where they used a plasmonic substrate, Klarite™, for the enhanced SERRS signal of DNA hybridisations at the surface. Using SE(R)RS and DPN together allows for the advantages of both techniques to be brought together with potential for miniaturised arrays from the DPN and improved sensitivity attributes from the SE(R)RS technique. Also with the numerous dyes available and the distinct SE(R)RS fingerprint often found for these dyes, multiplexed detection could be applied, so that essentially numerous biomarkers could be studied and detected within a single DPN printed array and distinguished clearly by the SE(R)RS spectra from the applied dyes.

5.1 Layer by Layer Nanoparticle-Dye Assembly for SERS Active PSA Immunoassay Arrays

5.1.1 Adapting the Assay Format for SERS

A schematic of the LbL nanoparticle-dye assembly approach is shown in figure 5.1. Based on the optimisation of the PSA immunoassay arrays (section 4), adapted from the PSA ELISA kit, it was clear that the current assay protocol was effective, as good limits of detection were obtained and there was minimal non-specific binding in the control arrays. Therefore, there was no disruption to the protocols used for forming the PSA immunoassay as far as the PSA Det Ab step.

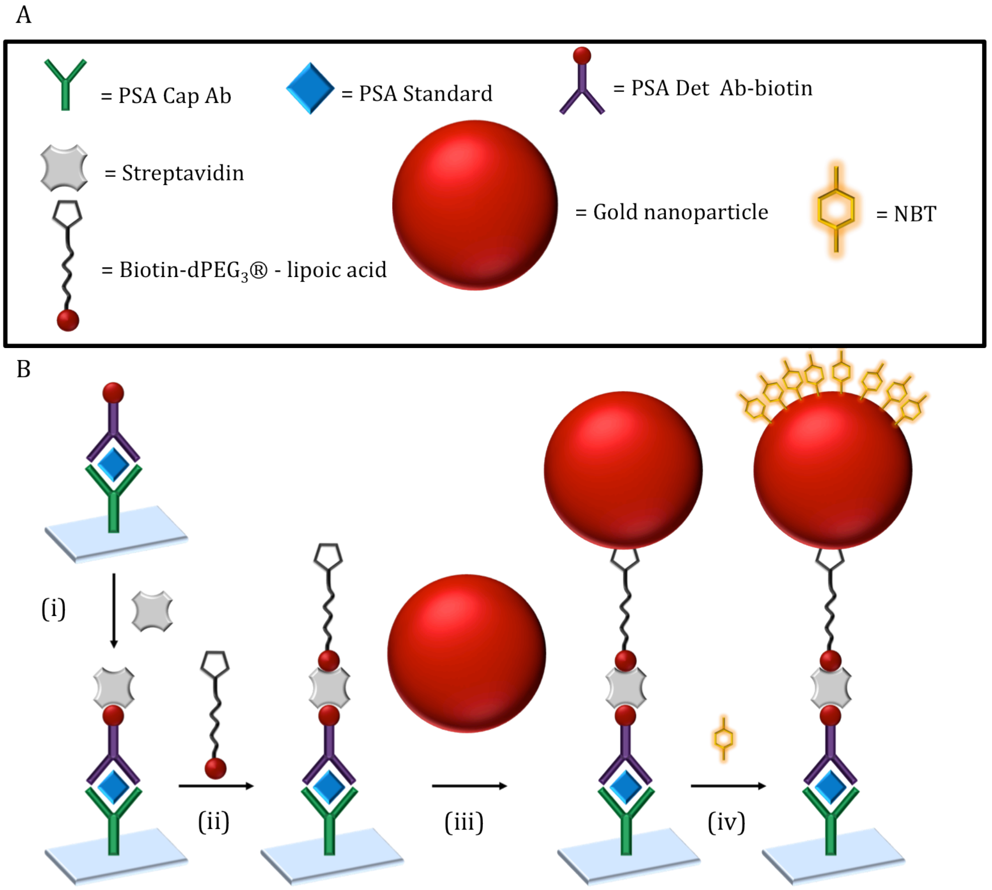

Figure 5.1: *Legend for new addition materials (A) and schematic representation of the LbL method for SERS detection of arrays (B). Immunoassay arrays carried out as far as PSA Det Ab step, streptavidin is then added (i), followed by biotin-dPEG®-lipoic acid linker (ii) and then gold nanoparticles (iii). On day of analysis, NBT dye is added (iv)*

For the LbL application, unlabelled streptavidin is added to the array in place of streptavidin Dylight™ 549. This change was made simply to ensure that no fluorescence background interferes with the SERS dye that was being applied to the arrays at a later stage. In order to first immobilise the gold nanoparticles, a linker was required. For this, a biotin-dPEG®-lipoic acid was used (chemical structure given in figure 5.2) as it was thought to bind to the streptavidin readily, exposing the lipoic acid for nanoparticle assembly.

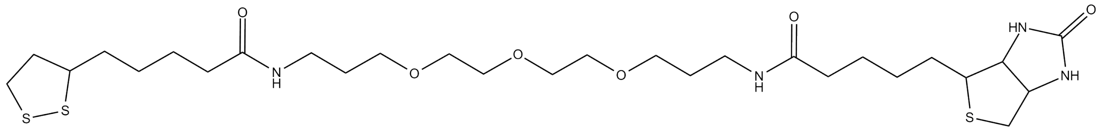

***Figure 5.2:** Chemical structure design of biotin-dPEG®-lipoic acid*

For LbL assembly, gold nanoparticles were prepare by the Turkevich method (synthesis found in section 3.2.1),[148] as it is a robust method that was found to produce stable gold nanoparticles. It was important to choose a nanoparticle that maintained a good level of stability as they were to be added to the assay in their raw state. Often nanoparticles are found to be highly sensitive to their surroundings and use of a less stable particle choice could risk aggregation upon addition to the array surface, resulting in non-specific deposition in the areas surrounding the arrays. Successful preparation of these gold nanoparticles was confirmed by ultraviolet-visible (UV/ vis) spectroscopy, as it is one way of determining the monodispersity and size of the particles made. The resulting spectrum for the gold nanoparticles used in the following experiments is shown in figure 5.3.

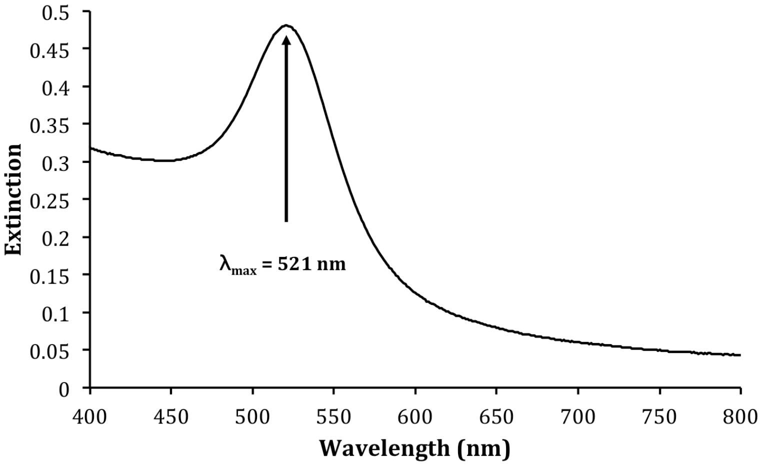

***Figure 5.3:** UV/ vis spectrum of gold nanoparticles used in LbL array application*

The UV/ vis results show the λ_{max} value to be 521 nm, which is in good agreement to what it should be for gold in the 10-20 nm range (520 nm).

Finally, a label is added to the assay that binds specifically to the gold nanoparticles and is SERS active. The dye chosen was 4-nitrobenzenethiol (NBT), a small aromatic molecule that is Raman active and often used in SERS studies as it readily binds to gold or silver via the thiol moiety present on the molecule (structure of NBT shown in figure 5.4).[173,174] In this case, the NBT is added to the substrate, binding to the exposed surface of the gold nanoparticles immobilised on the arrays. It was considered that with reducing PSA concentrations, a reduction in nanoparticle attachment would occur resulting in a reduced SERS signal, giving quantitative results from the PSA immunoassay arrays by SERS detection.

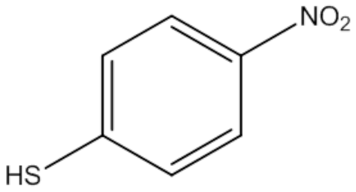

Figure 5.4: *Chemical structure of 4-nitrobenzenethiol (NBT)*

5.1.2 SERS PSA Immunoassay Array Concentration Study on Nitrocellulose

PSA Cap Ab arrays were fabricated on a nitrocellulose substrate using the NLP 2000 (see section 3.4 and 3.5.1 for details). Pattern format was altered to suit the Raman microscope stage capabilities, for efficient Raman mapping. As a result, each of the 12 pens were programmed to print a 3 x 3 array, with 20 µm pitch using a dwell time of 0.1 seconds and repeat printing i.e. the optimised print conditions that were confirmed in section 4.2. These 12-spot arrays were produced eight times on the substrate, for separate applications of PSA standard concentrations.

PSA immunoassay arrays were developed, applying a PSA concentration range of 60-0.94 ng/ mL to each of the 7 sets of arrays, leaving one as a control. The sandwich assay was completed as far as addition of the PSA Det Ab as per the protocol detailed in section 3.5.2. The LbL approach was then applied to each of the arrays whereby streptavidin was conjugated to the assay arrays followed by the biotin-dPEG®-lipoic acid linker and gold nanoparticles. The slide was finally washed and dried under nitrogen. The NBT label was not added until the day of mapping analysis, due to NBT's tendency to undergo photochemical reaction. Therefore by collecting all Raman maps of the arrays on the day the label was added, this reduces the risk of peak shifts, which could skew the analysis results (section 3.6.2).

SERS maps were collected for 3 sets of 3 x 3 array features for each of the applied PSA standard concentrations. A λ_{ex} = 633 nm laser was used as it was the most resonant excitation with that of the gold nanoparticles. As NBT does not have an electronic transition (i.e. no UV/ vis peak) it is considered to be a Raman active molecule that gives distinct Raman spectra at all laser wavelengths available on the spectrometer and is compatible with both silver and gold nanoparticle enhancement to give SERS enhanced spectra. Low integration times of 0.1 second were used to take point spectra across the arrays to generate the maps. This was to ensure maps of the arrays were collected in a suitable time here.

An example of a resulting SERS map from a 3 x 3 SERS PSA immunoassay array with 30 ng/ mL PSA applied is shown in figure 5.5. Both a bright field microscopy and corresponding SERS map image is given (figure 5.5A and B). The bright field image shows gold nanoparticle assembly on the PSA immunoassay arrays as intended. This is further highlighted by the bright spots of high NBT signal given in the SERS map which was generated using the intensity of the 1330 cm^{-1} peak in the NBT spectra which proves an enhanced signal generated by the gold nanoparticles that the NBT has assembled on. It is important to note that the NBT dye is commonly recognised by three distinctive peaks produced upon Raman scattering. These peaks are clear in the red spectrum found in figure 5.5C and are found at 1070, 1330 and 1565 cm^{-1}. The red spectrum represents an example of the level of SERS intensity coming from an array feature contrasting to the blue and green spectra which represent the varying signal coming from the areas surrounding the arrays. As is clear, the increased nanoparticle assembly on the array features has resulted in an increased SERS signal, giving a clear and defined SERS map of the 3 x 3 arrays. Further enhancement will have also been gained by the fact nanoparticle assembly occurs on a low micro-sized spot bringing the nanoparticles into close proximity to each other giving a collective further enhancement of the SERS signal from the NBT.

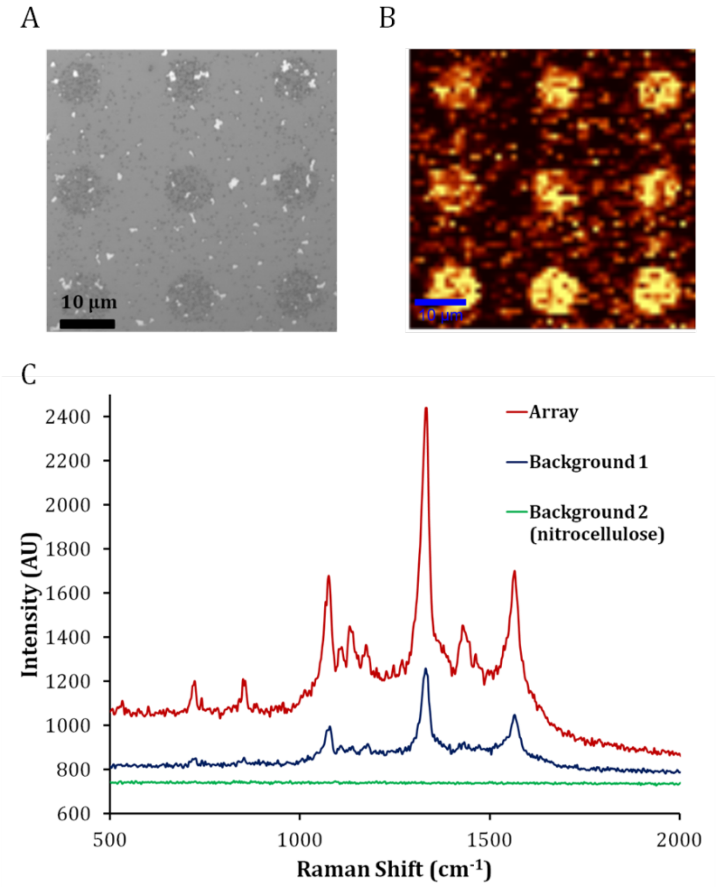

Figure 5.5: *A bright field microscopy (A) and corresponding SERS map (B) of a 3 x 3 SERS active PSA immunoassay array developed using the LbL method. SERS map generated from intensity given by NBT dye at around 1335 cm^{-1}, colour scale shows most intense peaks as yellow, lower intensity as red and lowest to negligible peak presence as black. A graph is plotted showing the spectra plotted of NBT (C) for that of areas on the array feature (red), and two sample areas from the background surrounding the arrays (blue and green)*

However, the blue spectrum in figure 5.5C does confirm that there is a level of non-specific binding to the areas surrounding the arrays. As it is likely that the NBT molecules will only assemble in areas where gold is present, this suggests that the non-specific binding is occurring at the nanoparticle addition stage. Therefore, upon NBT addition to the arrays, signal is given from the gold nanoparticles that have non-specifically immobilised on the substrate. This signal is reduced due to the lack of clustering, giving a weaker NBT SERS signal, hence why the arrays are still highly visible against the background. An example spectrum of the darkest areas on the map is shown in green, where no particles are present at all, therefore, no NBT spectrum is produced. Ideally, the arrays should be the only area giving the strong NBT signal and in fact, by reducing the non-specific binding surrounding the arrays, it would give greater spot definition – which is important for analysis of arrays with a lower PSA standard concentration.

The mean SERS intensity for 9 spots (3 from each map collected for a set PSA concentration) was measured to give an average spot intensity (average intensity from the background areas surrounding the spots was subtracted from each spot value) representative of each PSA standard concentration. This was carried out for each of the 3 main peaks in the NBT spectra and resulting intensities were plotted against PSA standard concentration. This plot and example maps for each concentration are given in figure 5.6.

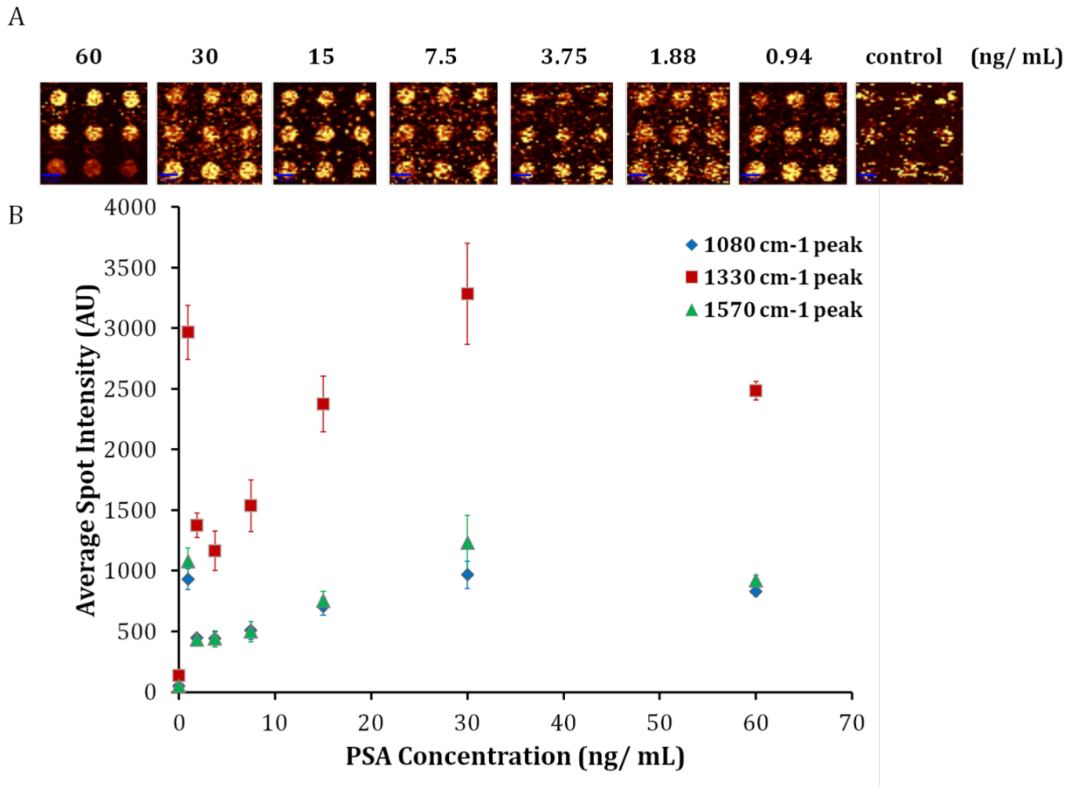

Figure 5.6: *SERS maps generated from the 1330 cm^{-1} peak of NBT for each PSA concentration (A), colour scale shows most intense peaks as yellow, lower intensity as red and lowest to negligible peak presence as black. Map colour scales are not relative to each other and are optimised for spot clarity in each case. A plot of average spot intensity vs. PSA concentration for three main peaks in the NBT spectrum (B)*

From both the map images and the graph, it is clear that there is variation in the nanoparticle assembly at the surface for each array with a different PSA standard concentration applied. Ideally, a decrease in spot intensity with decreasing concentration should be obtained, however, the graph shows that this only occurs for the points in the 30-3.75 ng/ mL range. The SERS maps (figure 5.6A) also show the large variation in background signal for each concentration due to nonspecific binding of the nanoparticles. For example, a comparison of the SERS maps for 1.88 and 0.94 ng/ mL arrays show how less non-specific binding of nanoparticles has occurred in the 0.94 ng/ mL arrays over that of 1.88 ng/ mL features. This non-specific binding will raise the background signal value, lowering the overall intensity value for the spots, whereas interference from this is far less in the 0.94 ng/ mL array therefore a higher value of average spot intensity is gained. This is likely a reason as to why the intensity plot for the 0.94 ng/ mL value is so high.

A positive attribute of this assay attempt is that there is a low value given for the control as these arrays produced less signal to that of any arrays where PSA was captured. The range between 30 ng/ mL and 3.75 ng/ mL follows the obvious trend of decreasing signal with that of PSA concentration; however, due to the anomalies that sit out with the trend, the quantitative aspect of the study is rendered void, as no reliable PSA LOD can be calculated here. This is due to the 60 ng/ mL arrays producing a lower SERS signal than that of 30 ng/ mL and both 1.88 ng/ mL and 0.94 ng/ mL arrays giving a sudden increase in signal, over that of all other arrays.

It was clear that from the fluorescence PSA immunoassay array study, that the PSA assay itself requires no alterations. Therefore, the change in assay format for SERS detection was likely to be the issue. The LbL nanoparticle assembly plus dye addition is problematic in terms of the signal intensity being unrepresentative of the amount of PSA present on the arrays. As shown earlier, the NBT molecule will only show signal where nanoparticles are present, therefore it is the presence of nanoparticles that will dictate the level of signal gained. One likely cause of the poor co-relation of signal intensity to concentration of PSA is the non-specific attachment of gold nanoparticles across the background areas surrounding the arrays. In both SERS and fluorescence assays, the background signal is subtracted from the mean intensity calculated for each spot within the array. Therefore, if background signal from the substrate is not generally consistent throughout the concentration study, it could have a manipulative effect on the assay, and possibly mask the true values of the arrays. This problem is emphasised in figure 5.7, which depicts a graph comparing the average background intensity for the fluorescent and SERS PSA immunoassay arrays at each PSA standard concentration. In the case of fluorescence, the background signal is generally the same for the area of the slide where the arrays were printed. In the case of fluorescence, a low level of background fluorescence will be produced from the substrate itself (this will vary for each substrate).

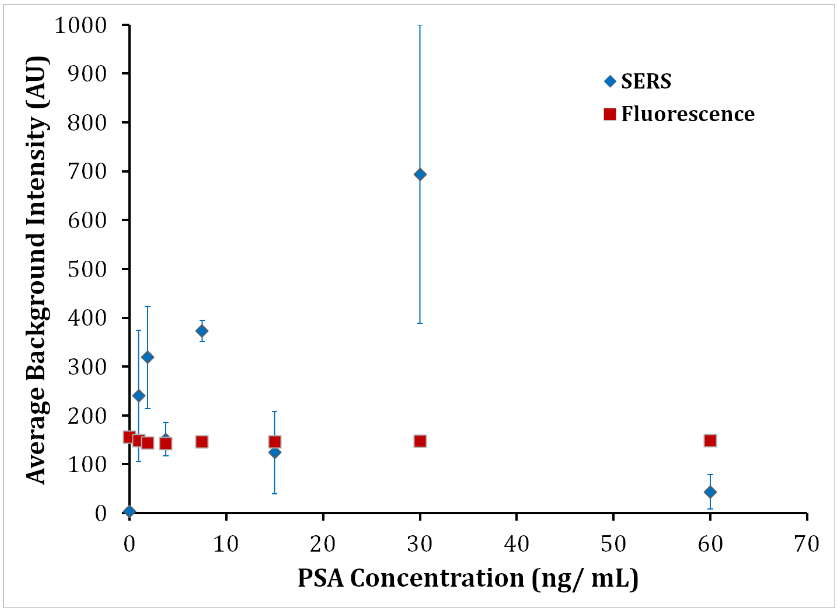

Figure 5.7: *Plot of average background intensity vs. PSA concentration for fluorescence and SERS (using 1335 cm^{-1} peak for NBT) PSA immunoassay arrays*

Observation of the average background intensity for the SERS assay proves to be quite different. The signal varies greatly for each area where different PSA concentrations were applied. Additionally, the error for majority of the points is substantially higher. While many glass substrates often have a low fluorescence background, in the case of SERS, this issue should be eliminated. Therefore the graph in figure 5.7, confirms that the gold nanoparticles are not specifically binding to the arrays and the level of this non-specific binding varies for each different application to the surface. This is interesting as each array is treated with the same volume and batch of gold nanoparticles, yet, for each area surrounding the arrays, a very different amount of non-specific nanoparticle binding is observed. This could be due to slight variations in the washings before the nanoparticles are added. For example, upon washing, residual wash buffer may remain in the wells and therefore excess salts present in the buffer could interfere with the stability of the nanoparticles upon application to the surface increasing the risk of aggregation and encouraging non-specific nanoparticle deposition.

5.1.3 SERS PSA Immunoassay Array Concentration Study on Epoxysilane Coated Glass

Before altering the assay protocol itself, the LbL nanoparticle assembly method was attempted on the epoxysilane coated glass. It is clear from the previous experiment that there was a variation in background deposition of nanoparticles across the surface due to non-specific binding. While this could be due to a variety of factors such as excess wash buffer causing aggregation or the lack of protective conjugation on the nanoparticles, it could also be the nature of the substrate that is disrupting the nanoparticle stability. As discussed in section 4.4, hydration of the nitrocellulose surface causes a porous form to be adopted, with pores of an average 144 nm in width. This will in turn create a roughened surface, more so than that of hard glass based substrates. It was considered that the porous nature of the nitrocellulose may also be an additional contribution to the uncontrolled attachment of gold nanoparticles across the surface, as the pores may trap the nanoparticles.

Therefore, the assay was prepared on epoxysilane coated glass. Epoxy substrates were used in the previous chapter simply to show the adaptability of the fluorescence assay arrays, meaning a dwell time comparison study was not carried out. Therefore, before preparing arrays for a PSA concentration study, a brief comparison of various dwell times was carried out. For this, 6 arrays of PSA Cap Ab were prepared with each pen producing a 3 x 3 array with 20 µm pitch. 3 array sets were prepared with dwell times of 0.1, 0.5 and 1 second. This was repeated for the other 3 array sets with repeat printing applied too. The arrays were then treated with the same LbL nanoparticle protocol for SERS detection using a high PSA standard concentration of 15 ng/ mL. As no fluorescent dye was present on the arrays, dark field microscopy was used to visualise the arrays.

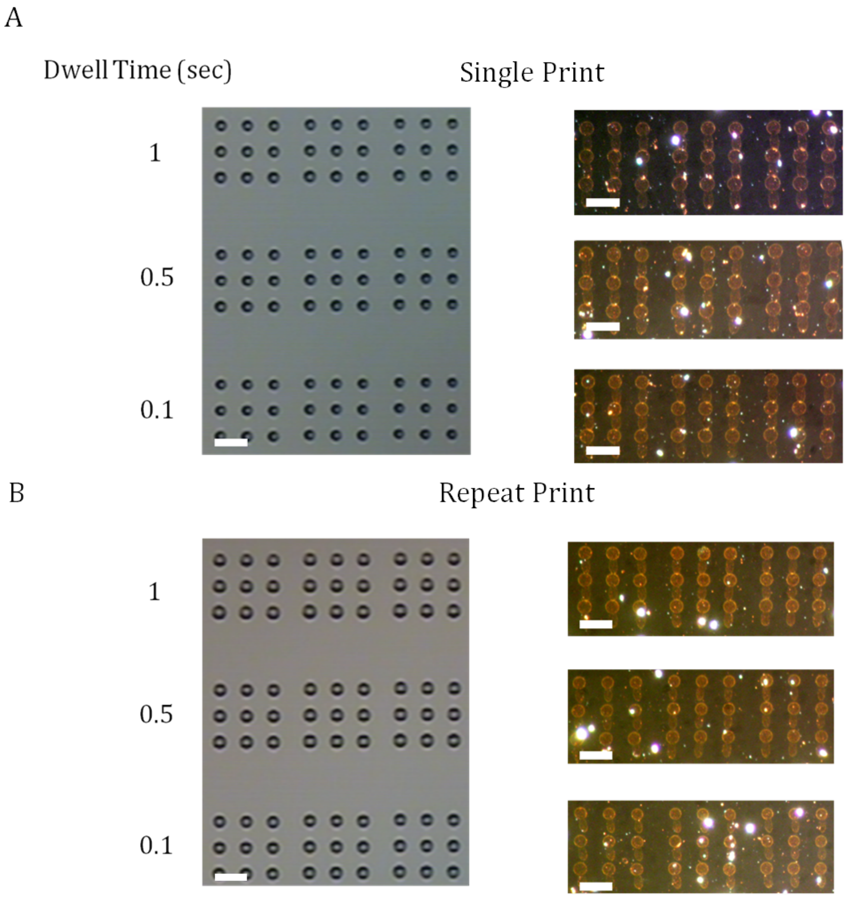

Figure 5.8: *Bright field microscopy images of PSA Cap Ab arrays after printing and corresponding dark field images for each array set after development of SERS PSA immunoassay arrays with 15 ng/ mL PSA concentration. Dwell times for single (A) and repeat print (B) are shown. Scale bar represents 20 µm. Over exposure of dark field images could not be control due to bright defects at surface.*

As observed previously (section 4.5), the spot sizes for PSA Cap Ab arrays printed on epoxy are generally found to be bigger than those when printing on nitrocellulose. This is likely due to the variation of wettability for the two surfaces. Interestingly, the images in figure 5.8 show that both single and double print give good spot size consistency and little tip-to-tip variation. While in the case of nitrocellulose, double printing was a necessity for improved spot size consistency throughout a whole array. As this was suggested to be due to tip defects, which is still a contributing factor, it is clear here that the nature of the nitrocellulose was also a factor of influence in the case of improved printing consistency. Throughout the time of printing on epoxy, it was found, generally, that repeat printing was not required on epoxy slides and was only used on the basis of the tips having been used frequently. Image J was used to determine the average spot size for each array set of different printing conditions using the dark field images in figure 5.8. As found for printing on nitrocellulose study, a minimal reduction in spot size occurred with decreasing spot size for both single (8.63-7.9 μm) and double print (9.9-9.4 μm). Also, the dark field images, which show the full PSA immunoassay developed for SERS compatibility via the LbL method, show some tailing occurs. This is likely due to washing of the arrays after printing and the excess PSA Cap Ab within the saturated spot binding to any exposed epoxy area surrounding the spot upon washing. Therefore, it was considered that in order to minimise spot tailing and maintain fast patterning methods, single print and 0.1 second dwell time would be applied in all cases for PSA Cap Ab printing on epoxysilane substrates.

Using the optimised printing methods, the LbL method was applied to 8 PSA immunoassay arrays, each corresponding to a different PSA standard concentration in the range of 15-0.24 ng/ mL. This was considered to be an essential change as the fluorescence assay proved that those PSA standard concentrations above 15 ng/ mL maxed out the signal and therefore the arrays were well saturated with PSA and the calculated LOD could only be determined from the points plotted in the range below 15 ng/ mL. Further to this, by investigating lower PSA standard concentrations it is possible to determine if SERS active arrays can be used for detecting lower levels of PSA visually and based on a calculated LOD. The first attempt at the SERS PSA immunoassay arrays on epoxy glass proved promising, the data is shown in figure 5.9.

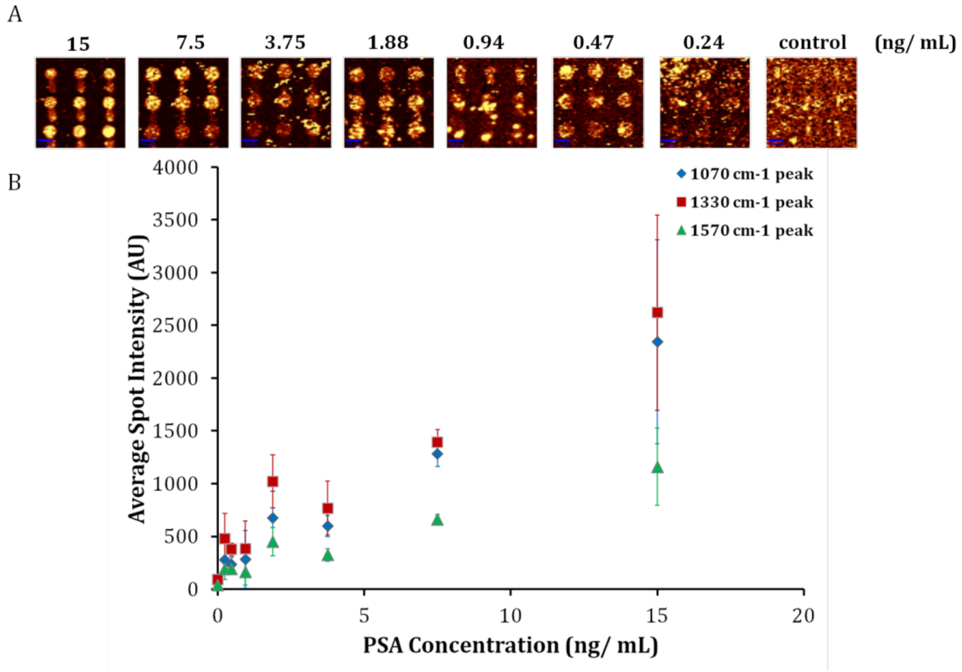

Figure 5.9: *SERS maps generated from the 1330 cm^{-1} peak of NBT for each PSA concentration (A), colour scale shows most intense peaks as yellow, lower intensity as red and lowest to negligible peak presence as black. SERS map colour scales are not relative to each other and are optimised for spot clarity in each case. Plot of average spot intensity (background corrected) vs. PSA concentration for the three main peaks in the NBT spectrum (B)*

A general trend of decreasing SERS intensity with decreasing PSA concentration was observed. Additionally, arrays were detected for the two lower PSA standard concentrations that were applied. Control arrays show some SERS signal but again it is minimal compared with that of the PSA applied arrays. There are several issues evidenced in figure 5.9 including anomalies to the decreasing intensity with PSA concentration trend. This applies to the 1.88 ng/ mL arrays, which show a slightly elevated intensity to that of 3.75 ng/ mL arrays. Plus, the three lowest PSA standard concentration arrays show an increasing intensity with decreasing concentration, although overall these are still reduced in comparison to 1.88 and 3.75 ng/ mL arrays.

Another advantage of moving to the epoxy substrate is the reduction in non-specific attachment of gold nanoparticles to the substrate surrounding the arrays. This is confirmed in figure 5.10, where the average background intensity is compared with the previous results from the nitrocellulose based arrays. Further to this, the low intensity is fairly consistent throughout each array of differing PSA concentration, with only 0.47 ng/ mL showing an increase in background signal.

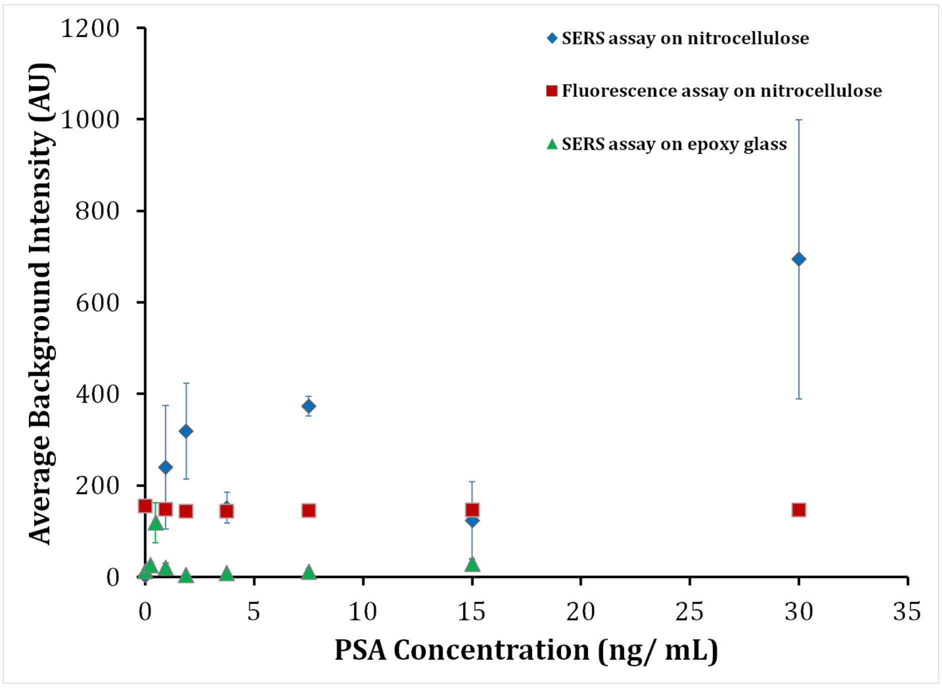

Figure 5.10: *Plot of background intensity vs. PSA concentration for fluorescence and SERS PSA immunoassay arrays*

This assay was replicated two more times and it quickly became evident that the results were not reproducible and that in fact, the assay showed poorly coordinated nanoparticle assembly in relation to level of PSA present in the arrays.

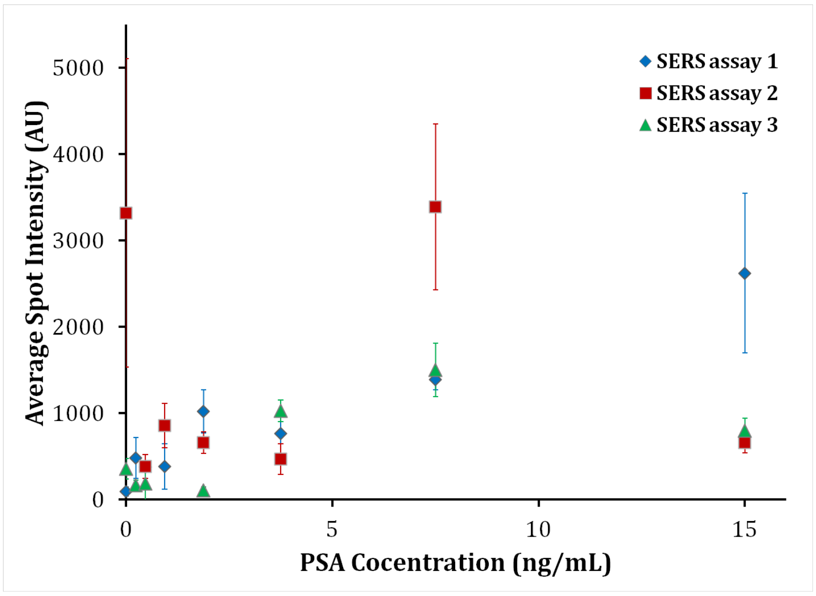

Figure 5.11: *Plot of average spot intensity vs. PSA concentration comparing all 3 SERS PSA immunoassay arrays printed on epoxysilane coated glass. Intensity based on SERS maps generated from the peak at 1330 cm^{-1} in the NBT spectrum*

As is clear in figure 5.11, the assays produced by the LbL nanoparticle assembly method are very inconsistent. The graph compares the three concentration studies for PSA using the same array printing and assay development protocols throughout. Average spot intensity was calculated based on the maps focusing on the three main peaks, however, figure 5.11 only shows the plots for the 1330 cm^{-1} peak of NBT. Not only do none of the concentration studies show a good linear decrease in SERS intensity with decreasing PSA concentration, but each assay gave a differing trend of intensities for each study, proving that the nanoparticle assembly of the arrays is in no way dictated by the levels of PSA present in the array. Further to this, although nanoparticle background attachment has been minimised in comparison to the attempt on nitrocellulose, it still occurs occasionally, i.e. mostly found to occur in assay 2 (comparison of background intensity for all 3 assays are shown in figure 5.12). While positives can be gained in terms of identifying epoxy glass as a more suitable substrate for the SERS detection of the assay, high, uncontrollable background SERS intensity is still an issue in terms of exposing bare gold nanoparticles to the surface for as long as an hour.

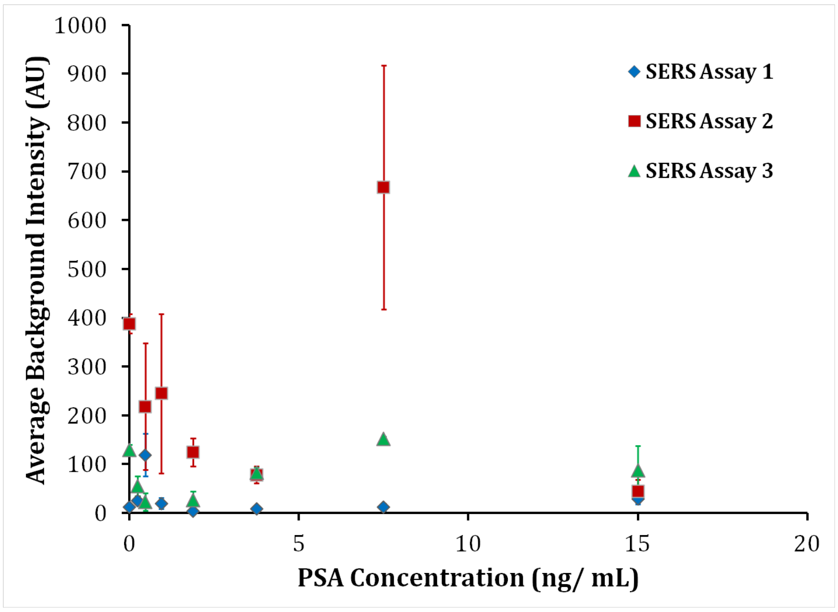

Figure 5.12: *Plot of average background intensity vs. PSA concentration comparing all 3 SERS PSA immunoassay array concentration studies. Plot generated from 1330 cm^{-1} peak of the NBT spectrum*

It is possible that the various biotin-streptavidin binding points that occur within the assay are also contributing to the poor nanoparticle correlation with PSA concentrations. Currently, the LbL assay has a biotinylated PSA Det Ab that binds to streptavidin and another biotin linker attachment is bound through the same streptavidin molecule, in order to immobilise the nanoparticles on the arrays. Fluorescent microarrays regularly utilised dye conjugated streptavidin which attaches through biotinylated antibodies for quantitative determination of a biomarker, as the binding is very strong between the two biomolecules. While streptavidin has 4 binding sites for biotin, by sandwiching a streptavidin with two biotins, it is possible to cause competition between the two streptavidin-biotin interactions, which could result in some cases where the streptavidin may get removed from the assay itself therefore, creating an ongoing equilibrium of breaking and forming of the biotin-streptavidin bond at the surface of the array. This would remove the proportionality on streptavidin present on the array spot that would be representative of the level of PSA contained within the sandwich assay spot. This would in turn give a disproportionate attachment of gold nanoparticles and could be the reason why poor linearity is found in the graphs produced for the concentration study. Additionally, all three assays showed non-specific nanoparticle binding in the control arrays, with two out of the three giving control average spot intensities higher than some of the arrays with PSA present in them. This again could be an issue related to the use of bare nanoparticles, as they are maybe more susceptible to interactions with the arrays regardless of the correct proteins in the assay being present, as opposed to if functionalised nanoparticles were used.

As a whole, the assay protocol for LbL nanoparticle assembly was proving unfavourable and unrealistic. While the intention of this method was used on the basis of it involving simply adding materials without any conjugate preparation beforehand, it resulted in not only poor results, but in fact it also proved impractical. When considering the fluorescent PSA immunoassay array preparation, from the moment the slide is removed from the overnight cooling at 4 °C, to carrying out the assay, it takes approximately 7 hours overall to prepare. In the case of LbL SERS PSA immunoassay array preparation, the additional steps required resulted in an assay preparation time of over 9 hours. In terms of creating a user friendly assay in a commercial sense, the assay preparation time would extend beyond a full working day. Considering that one of the main incentives for improving biomarker detection methods is efficiency, extending assay preparation time is highly unfavourable.

5.1.4 Concluding Remarks

The LbL assembly of a SERS based detection method was adopted with the initial idea that the raw materials that make up the final array could be added sequentially in order to gain a SERS response. Unfortunately this approach provided poor control over nanoparticle assembly at the arrays, with respect to non-specific binding in the control and poor signal to concentration correlation. Moreover, the method required a longer assay preparation time than that of the fluorescence set up, making it a user unfriendly method. As a result, a nanoparticle conjugate method was attempted.

5.2 SERS Active PSA Immunoassay Arrays Using Protein-Nanoparticle Conjugates

5.2.1 Adapting the Assay Format for SERS Detection

The protein nanoparticle conjugate system utilised in this assay was based on well established combinations of dye, linker and nanoparticle choices resulting in a highly intense SERS signal. The successful adaptation of the sandwich assay to array format for fluorescence detection that was discussed in chapter 4 utilised a fluorescent dye conjugated streptavidin. For SERS optimisation, the streptavidin Dylight™ 549 was replaced with a streptavidin-silver nanoparticle conjugate linked through a benzotriazole (BT) dye linker. For this conjugate system, a change from gold to silver nanoparticles was made as silver nanoparticles in this case are bigger and give a greater SERS enhancement with suitable dyes such as BT, more so than that of small gold used in the section 5.1. Furthermore, small gold was used for the purpose of good nanoparticle stability as they were added to the assay bare. In a conjugate system, the silver nanoparticles are pre-functionalised with streptavidin and therefore will be less sensitive to the assay surrounding in terms of aggregation risk upon addition to the assay. Figure 5.13 depicts this set up as it should be at the epoxy surface.

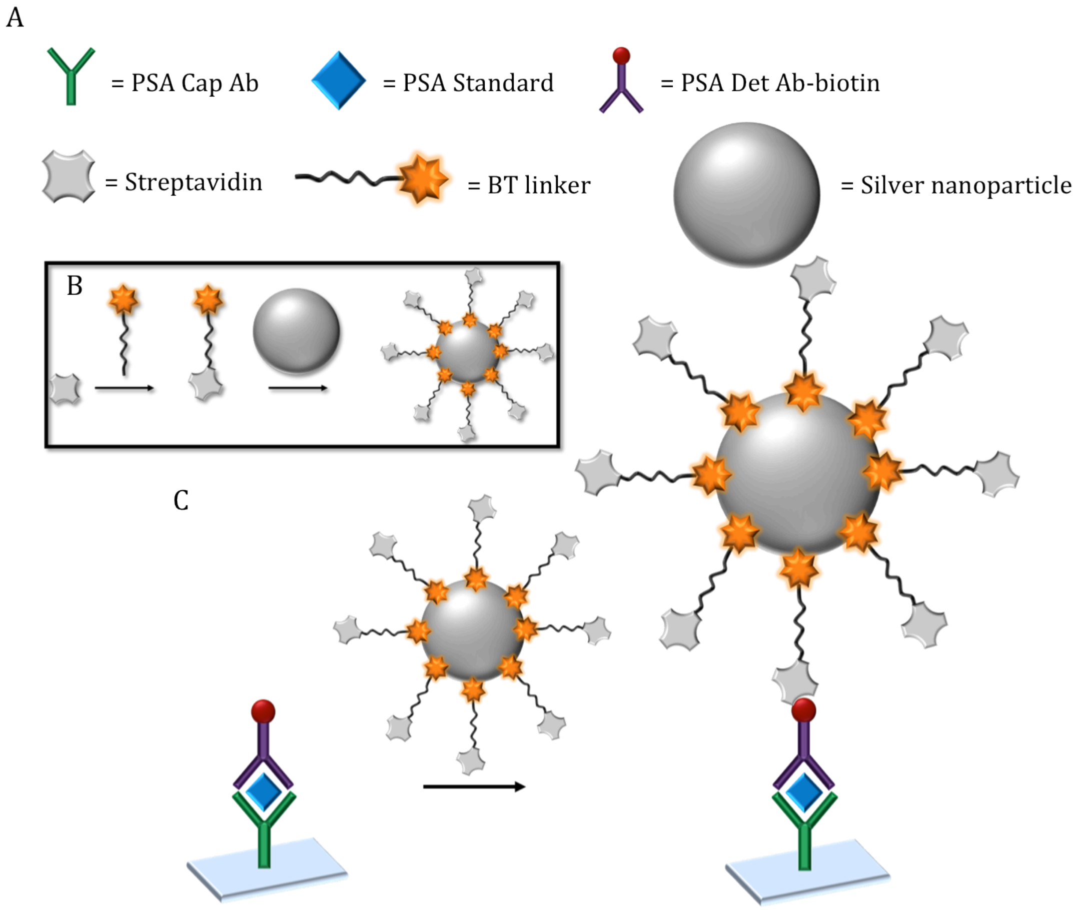

Figure 5.13: *Schematic of SERS immunoassay array format. Legend is given (A) along with steps required to prepare streptavidin dye nanoparticle conjugates (B) and application to sandwich assay on an array surface (C)*

5.2.2 Streptavidin-Nanoparticle Conjugate Preparation and Characterisation

Benzotriazoles are well established as effective SERS dyes.[175] Many derivatives and modified versions have been developed for the purpose of multiplexed SERS and enzyme-based applications.[176,177,178] The two advantages of pairing BT dyes with silver nanoparticles are the high affinity of the BT group for the silver surface as it is found to form a fixed orientation and strong polymeric Ag (I)–BT complex at the nanoparticle surface and also the intense SERS response found for the highly sensitive detection of analytes when immobilised on silver nanoparticles. It was for these reasons that a BT dye linker was used for conjugating streptavidin to the silver nanoparticle surface when preparing the streptavidin conjugated nanoparticles (figure 5.13B). The BT dye linker utilised was synthesised in-house by Anna Robson and its chemical structure is given in figure 5.14. The BT derivative used here was previously developed as part of a large SE(R)RS dye library that was published by Graham *et al.*,[175a] The linker applied in this case was similar to that applied for previous bio-conjugation studies using alternative cyanine based dyes, by McKenzie *et al.*[179] Attachment of the BT linker to streptavidin was done through EDC coupling via the carboxylic acid group available on the BT linker (details of method found in section 3.3.2).

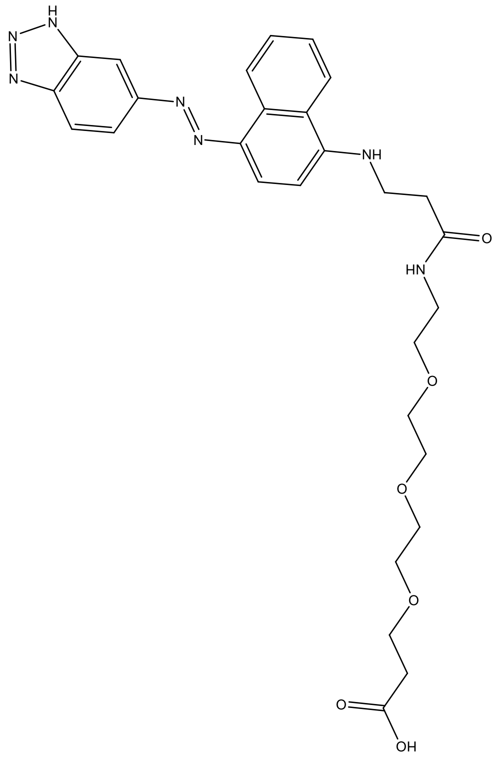

Figure 5.14: *Chemical structure of BT linker*

Once the streptavidin was coupled to the BT linker it was then assembled on silver nanoparticles, forming silver nanoparticle conjugates (method of conjugate preparation found in section 3.3.3). Silver citrate nanoparticles were prepared via the Lee and Meisel method as detailed in section 3.2.2. Figure 5.15 shows a UV/ vis absorbance spectrum for the batch of silver nanoparticles used in this body of work.

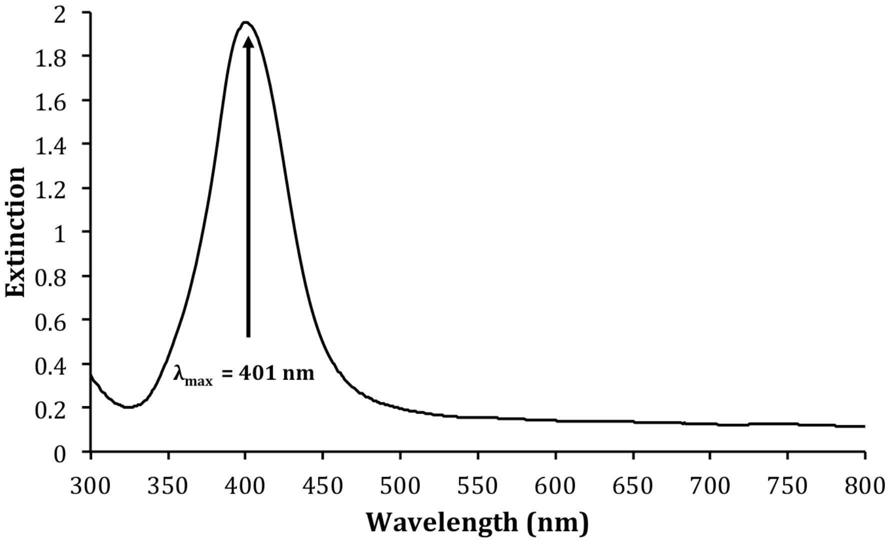

Figure 5.15: *UV/ vis spectrum of silver nanoparticles used in streptavidin-nanoparticle conjugate array application*

Ideally silver nanoparticles should give a UV/ vis absorption with a λ_{max} as close to 400 nm as possible. The Lee and Meisel method is found to prepare particles in the 40-50 nm range. The batch of silver nanoparticles prepared for this work was in good agreement with these parameters as the UV/ vis spectrum gave a λ_{max} of 401 nm and an average particle size of 45 ± 4.3 nm (determined by dynamic light scattering).

Particle size analysis was also carried out on the conjugates prepared for use in the assay. Addition of the streptavidin and BT linker gave an increase in average particle size to 52 ± 5.5 nm (determined by dynamic light scattering), giving an overall 7 nm increase. To further confirm that this increase was due to attachment of the streptavidin BT linker, the conjugates were analysed in solution using a 514 nm laser at 100 % power (37.3 mW) and an integration time of 5 seconds. The resulting SERS spectrum is given in figure 5.16. As can be seen, the BT dye itself produces very distinctive peaks that are found to match well with that reported by McAnally *et al.*[175a] As a result, when conjugates were added to the PSA immunoassay arrays, it was expected that a similar spectra should result from the array features.

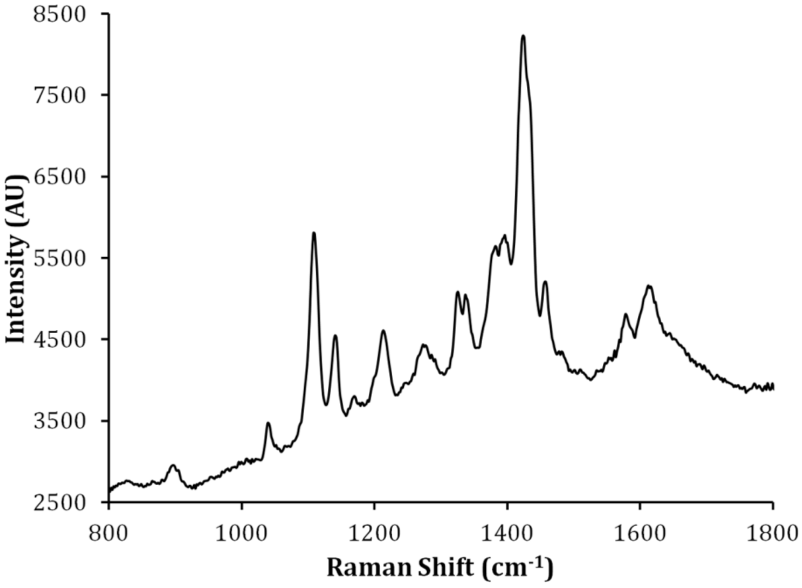

Figure 5.16: *SERS spectrum collected from streptavidin-nanoparticle conjugates in solution using a 514 nm laser and integration time of 5 seconds*

5.2.3 Application of Streptavidin-Nanoparticle Conjugates to PSA immunoassay Arrays for PSA Concentration Study

PSA immunoassay arrays were prepared using the NLP 2000, with the same pattern dimensions used as per section 5.1. Eight sets of arrays were printed on epoxysilane coated glass and PSA immunoassay arrays were developed. To each array set, a different PSA standard concentration was applied, covering the range of 15-0.24 ng/ mL, plus a control array set. Once the arrays were prepared as far as the biotinylated PSA Det Ab, streptavidin-nanoparticle conjugates were added to each array set for 1 hour (full details of protocol found in section 3.6.3). Conjugates were then removed from the arrays and the slide was washed, dried and fixed for analysis. Three SERS maps were collected for a 3 x 3 array from each of the 7 various PSA standard concentrations and the control arrays. All maps covered a 60 x 60 μm area with a 1 μm resolution and each spectrum taken using a 0.1 second integration time. Each map took approximately 8 minutes to create. An example SERS map with corresponding spectra and dark field image is shown in figure 5.17. The map shown was based on the intensity of the peak at 1420 cm^{-1} for the BT dye.

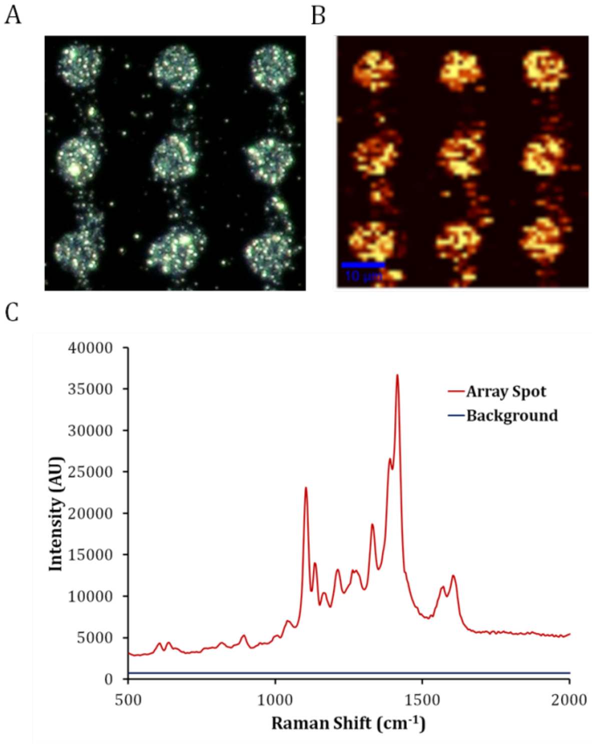

Figure 5.17: *Dark field image (A) and SERS map (B) of a 3 x 3 SERS active PSA immunoassay array developed using streptavidin-nanoparticle conjugates. SERS map generated from intensity given by BT dye at 1420 cm^{-1}, colour scale shows most intense peaks as yellow, lower intensity as red and lowest to negligible peak presence as black. A graph is plotted showing the difference in signal (C) for that of an area on the array feature (red) and the background surrounding the arrays (blue)*

The dark field and Raman map images show good attachment of the streptavidin-nanoparticle conjugates over the arrays with minimal background attachment (figure 5.17A and B), an issue encountered with the LbL nanoparticles assembly method. This is further proven by the plot comparing the background signal with that of the arrays, showing that the background signal is almost negligible compared with that of the PSA immunoassay arrays (figure 5.17C). This improvement is likely due to the silver nanoparticles being well coated and functionalised with streptavidin through the BT linker, giving them a high affinity for the arrays only. Further to this, the BT spectra produced by the arrays were well defined and highly intense, with many peaks showing an intensity of over 35000 counts, a far greater signal than that ever achieved using gold with NBT. The spectra from the arrays also gave good correlation to the spectrum found from the conjugates in solution (figure 5.16). An interesting observation was made in that the spectra from the arrays are more intense than that gained from the conjugate solution despite the integration times used being considerably lower, reduced from 5 to 0.1 seconds. This is likely due to the fact that when the streptavidin-nanoparticle conjugates orientate specifically on the arrays, this causes an aggregated state. Nanoparticles are forced into a fixed, closer proximity to each other giving a further enhanced SERS beyond that observed when the particles are freely moving around in solution.

The data collected from each of the array sets was then processed using WITech Project 2.02 software. The mean Raman peak intensity at 1105 cm^{-1} and 1420 cm^{-1} was used to calculate the mean intensity from 9 spots (3 spots chosen at random from each of the array maps) giving an average spot intensity for each array set of a specific PSA standard concentration. Background subtraction was also performed on each spot based on areas selected within the set Raman map. A plot of average spot intensity using peaks at 1105 cm^{-1} and 1420 cm^{-1} vs. PSA concentration is shown in figure 5.18. The figure gives a representative Raman map generated for each PSA concentration using the 1420 cm^{-1} peak.

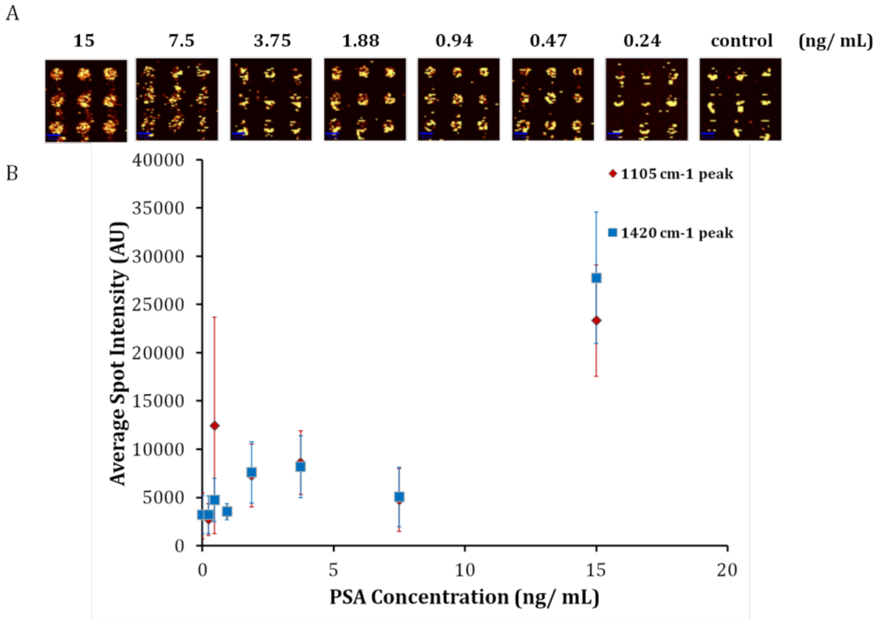

Figure 5.18: *SERS maps generated from the 1420 cm^{-1} peak of the BT dye for each PSA concentration (A), colour scale shows most intense peaks as yellow, lower intensity as red and lowest to negligible peak presence as black. SERS map colour scales are not relative to each other and are optimised for spot clarity in each case. Plot of average spot intensity vs. PSA concentration for SERS PSA immunoassay arrays using the peaks at 1105 cm^{-1} and 1420 cm^{-1} produced from the BT spectrum (B)*

The resulting graph from the processed SERS data shows poor linearity. There is no obvious pattern of decreasing intensity with PSA concentration meaning that no LOD could be calculated. Therefore, it was considered that the binding of the conjugates was not representative of the concentrations of PSA present and that a level of non-specific binding was occurring on the arrays. This is particularly evident in the case of the 0.24 ng/ mL and control arrays. Looking at the example SERS map images given for each PSA concentration (figure 5.18A), the majority of the maps show good bright signal coming from the whole spot, whereas 0.24 ng/ mL and control maps show only major signal occurring at the lower 'rim' of the spot. A closer observation of this phenomenon is given clarity in figure 5.19.

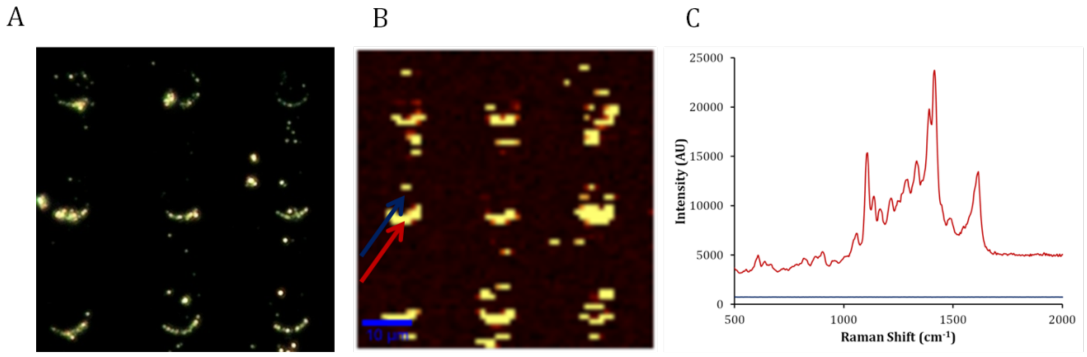

0.24 ng/ mL

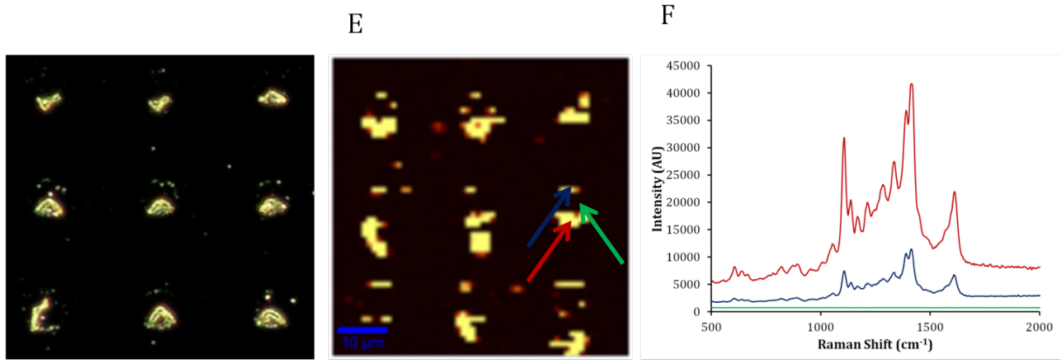

Control

Figure 5.19: *Dark field (A and D), SERS map images (B and E) and spectra for areas highlighted by colour co-ordinated arrows (C and F) for 0.24 ng/ mL (A-C) and control arrays (D-F)*

Dark field images are used to show clearly the reasoning for the signals given on the arrays in the manner that they are (figure 5.19A and D). SERS maps and correlating spectra for specific areas on the spot are also given to highlight the patterning of the signal on the spots. From the comparable images in figure 5.19, it is clear that this non-specific binding on the arrays results in nanoparticles gathering in a semi-circular way around the outer edge of part of the spots, or in the case of the control "squiggle" shapes have formed on the spots. While the quantity of nanoparticles found on the spot is likely to be greatly depleted compared with the other arrays of higher PSA concentration, their arrangement in the control and 0.24 ng/ mL array is not suitable. This is evidenced by the resulting SERS maps. As can be seen, the collection of nanoparticles in localised areas on the spot, give a highly intense SERS signal compared with that of areas that are within the spot. In some cases there is no SERS signal from within the spot area, which is what would be expected in the case of the control. This would suggest that in the hour that the conjugates are applied to the surface, it is possible that some interference causes clustering of nanoparticle conjugates in specific localised areas of the spots. As shown, this results in a highly excessive SERS response, manipulating the average spot intensity values and gives poor linearity in the PSA concentration study. However, it was considered that further data was required to back this result up.

5.2.4 Streptavidin Dylight™ 549 vs. Streptavidin BT Nanoparticle Conjugates: Are the Nanoparticles causing Non-specific Binding?

As both detection method choice and format of streptavidin delivery was altered for this assay, it is important to fully confirm that it is the presence of the nanoparticles that is causing the large signal due to non-specific binding and it is not due to an error in the processing or data collection of SERS from the arrays. To investigate this, silver nanoparticle conjugates of streptavidin Dylight™ 549 were prepared and added to a series of arrays using the same protocols for that of the fluorescence assay. The combination of silver conjugated to streptavidin Dylight™ 549 is an interesting pairing as the silver should enhance the resulting spot fluorescence intensity upon excitation of the TRITC filter in the microscope. Therefore, if successful, there should be an increased detection limit as a result of surface enhanced fluorescence (SEF).

Streptavidin Dylight™ 549-nanoparticle conjugates were prepared using similar methods used to prepare the streptavidin BT linker-nanoparticle conjugates, with different materials. As the streptavidin is already tagged with a fluorescence dye, the protein simply required a thiol group linker attached in order to bind with the silver nanoparticles. The linker used was MHA. No extra dye incorporation was required (full method detailed in section 3.3.1 and 3.3.3) as the dye was present on the streptavidin itself, this meant the dye would be further from the nanoparticle surface, however, it was thought that even with MHA as a spacer, the metal surface could still provide an enhancing effect on the dye.

Eight Sets of 24 x 8 arrays of PSA Cap Ab were printed using the NLP 2000, adopting the same print method as used in the fluorescent assay section, utilising a 33 µm pitch and a 0.1 second dwell time, single print. PSA immunoassay arrays were produced with each array set covering a PSA concentration range of 15-0.24 ng/ mL plus a control array. In order to mimic that of the original fluorescence assay, the streptavidin Dylight™ 549 conjugates were added to the arrays for 30 minutes before being removed and the slide washed and dried. Arrays were analysed using fluorescence microscopy with a TRITC filter. Data processing was performed via the same method as that for the fluorescence assay (details in section 4.3).

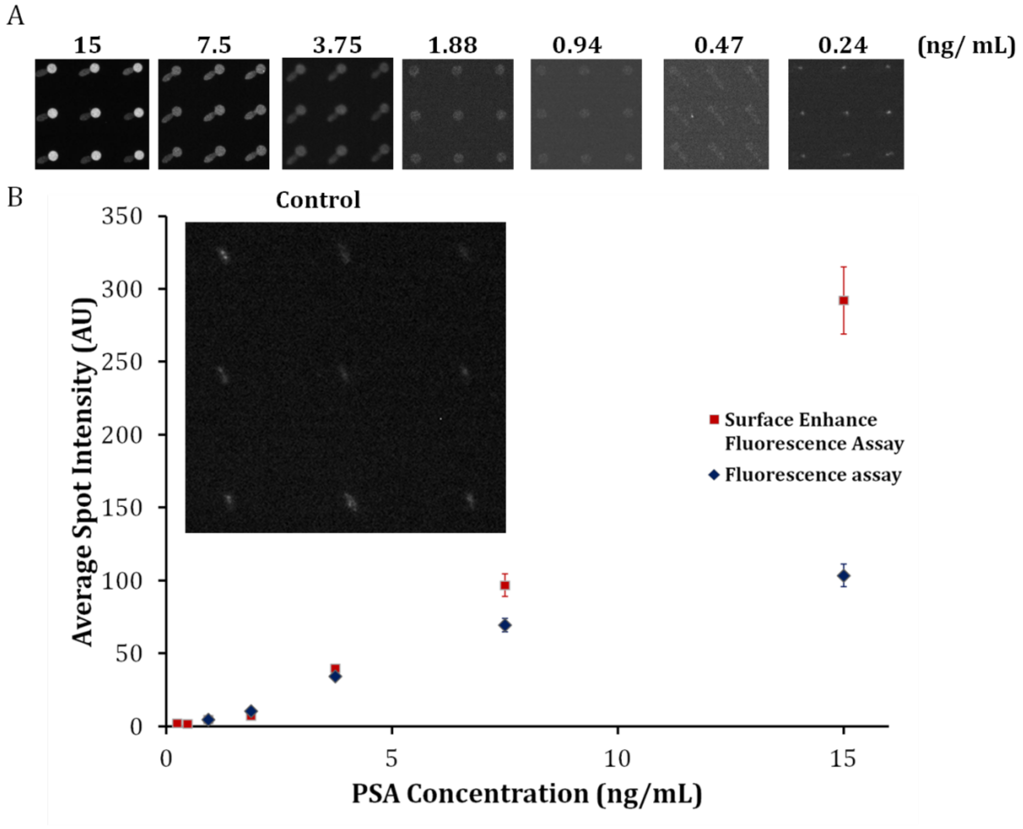

Figure 5.20: *Fluorescence images of a 3 x 3 array for each PSA concentration for the SEF assay (A) and a plot of average spot intensity vs. PSA concentration for SEF PSA immunoassay arrays compared with the fluorescence assay from figure 4.7 (B)*

The resulting SEF PSA concentration study was plotted against the fluorescence assay results (figure 4.7) in figure 5.20. Positives of utilising a SEF conjugate system is immediately recognised as spot intensities are higher than that of the fluorescence assay in the concentration range of 15-3.75 ng/ mL. Additionally arrays corresponding to 0.47 and 0.24 ng/ mL could be detected which was previously not possible with the fluorescence assay with no metal conjugate enhancement. However, the purpose of this comparison experiment was to recognise if non-specific binding could be recognised due to nanoparticle conjugate formats. Unfortunately this was the case. Use of streptavidin Dylight™ 549 in a non-conjugate nanoparticle system gave no fluorescent response from the control arrays, therefore minimal non-specific binding was achieved. In the case of the streptavidin Dylight™ 549 nanoparticle conjugate assay, some nonspecific binding was detected in the control arrays, as depicted in the image inset of figure 5.20B. The signal from the spots was less than that of the other PSA concentration arrays, however, this small level of signal in the control resulted in a calculated limit of detection of 0.123 ng/ mL, which compares poorly with the fluorescence assay LOD of 0.066 ng/ mL. Observation of the control array image highlights similar issues that were found with that of the SERS detection assay. The fluorescence signal is purely coming from a concentrated area within the spot, in a similar manner as before, where the signal comes from across the edges of the spots. Therefore, whatever it is that is causing this nucleation of conjugate formation, it results in a localised signal of fluorescence like it did for SERS. This confirmed that the nanoparticles were the cause of the non-specific binding in the control arrays and the lower PSA concentration arrays, giving bogus concentration study results.

One point of note is that a reduced conjugate addition time of 30 minutes was used in this study. Although a poor LOD was calculated due to signal in the control, an improved linearity of decreasing signal with PSA concentration was achieved on this occasion. While this could still be due to the alternative use of fluorescence over SERS detection of the arrays, another possibility could be the reduced time the conjugates were added. It seemed that in terms of optimising the assay for SERS detection, it was worth pursuing this possible alteration to the assay conditions.

5.2.5 Discovering Optimal Streptavidin-Nanoparticle Conjugate Addition Times

A time study was carried out in order to determine if reduced conjugate addition time to the arrays would combat the non-specific binding issues that occurred in previous attempts. For this, four reduced periods of conjugate addition times were investigated, comparing PSA standard concentration of 15 ng/ mL, against control arrays for each of the times. By using 15 ng/ mL, it was possible to determine what kind of intensity to expect at each varying time against that of no PSA.

For each concentration and time set, each tip produced a 3 x 3 array using 0.1 second dwell time and single print with a pitch of 20 μm. Four immunoassay arrays comprised a PSA concentration of 15 ng/ mL and the other four where control arrays. To each 15 ng/ mL and control array pair, varying conjugate addition times of 30, 20, 10 and 5 minutes were applied. Streptavidin-nanoparticle conjugates were prepared as per the previously mentioned methods. Once arrays were prepared, they were analysed with a 532 nm laser by Raman mapping as per previous SERS mapping experiments. The resulting plot of conjugate addition time vs. average spot intensity is shown in figure 5.21.

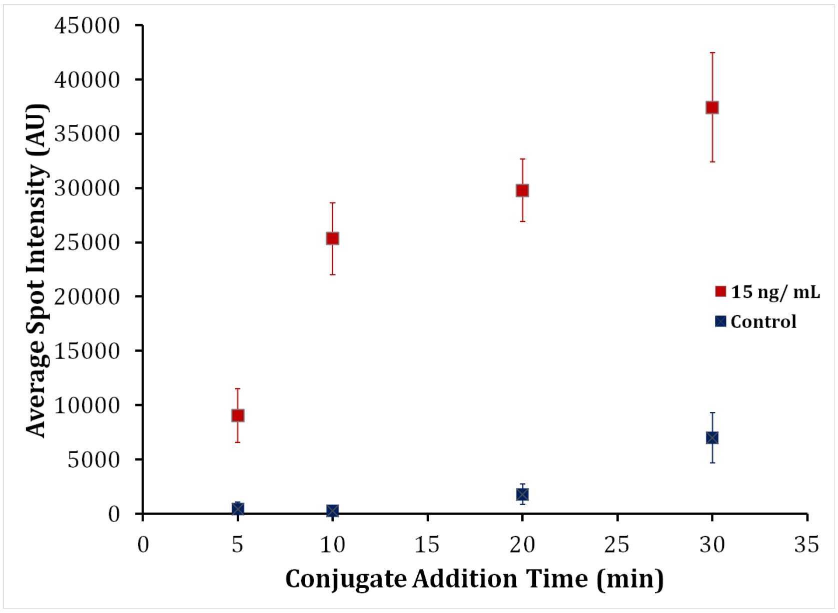

Figure 5.21: *Plot of average spot intensity (background corrected for BT peak at 1420 cm^{-1}) vs. conjugate addition time for 15 ng/ mL and control PSA immunoassay arrays. All data points are background corrected*

Analysis of the control arrays proved consistent with respect to the 30 minute conjugate addition. As seen with the streptavidin Dylight™ 549 conjugate study, 30 minutes of conjugate addition results in a considerable level of intensity given out by the control, due to non-specific binding. The average spot intensity of control arrays, however, decreases with reduced conjugate addition time. Suitably low signal is only achieved at addition times of 5 and 10 minutes.

The 15 ng/ mL arrays showed a reduced average spot intensity with decreasing conjugate addition time as expected, but importantly, there is still a considerable level of intensity being given out by the arrays at 5 and 10 minutes addition times. This proves promising in terms of the requirements needed for the assay to work effectively i.e. high level of SERS response from PSA immunoassay arrays and minimal signal from control immunoassay arrays.

A further advantage to reducing the time of conjugate addition to 10 minutes or less is the opportunity to shorten the assay time. Thus far, the main focus of the work carried out in this chapter has been solely devoted towards improving upon the current sensitivity of the PSA immunoassay arrays. However, as stated previously, researchers as a whole continue to investigate ways of improved disease diagnostic processes to result in cost reduction, improved efficiency through increase sample throughput and an overall decreased labour time, all while maintaining a level of sensitivity relevant to the biomarkers being analysed. Therefore, this reduction in conjugate addition time could be the answer to producing a good PSA concentration study by SERS giving a shorter assay time with good sensitivity.

5.2.6 Reduced Conjugate Addition Time for Improved SERRS PSA Immunoassay Concentration Study

Firstly a 10 minute conjugate addition time was investigated. Reasons being that it gave minimal signal in the control, with a higher signal for 15 ng/ mL arrays over that of a 5 minute addition time.

Adopting the usual standard PSA Cap Ab printing layout, PSA immunoassay arrays were once again developed for 15-0.24 ng/ mL concentration range, utilising only a 10 minute addition time for the streptavidin-nanoparticle conjugates. Usual slide SERS analysis and data processing was carried out, however one change made was the mapping resolution applied. A reduction to 2 μm resolution was used, as this shortened the mapping time for each 3 x 3 spot area from 8 minutes to just 3 minutes. This was decided for faster analysis of the arrays in order to compete with that of gathering fluorescence images. Further to this, the ability to visualise the spots easily in the maps was not compromised.

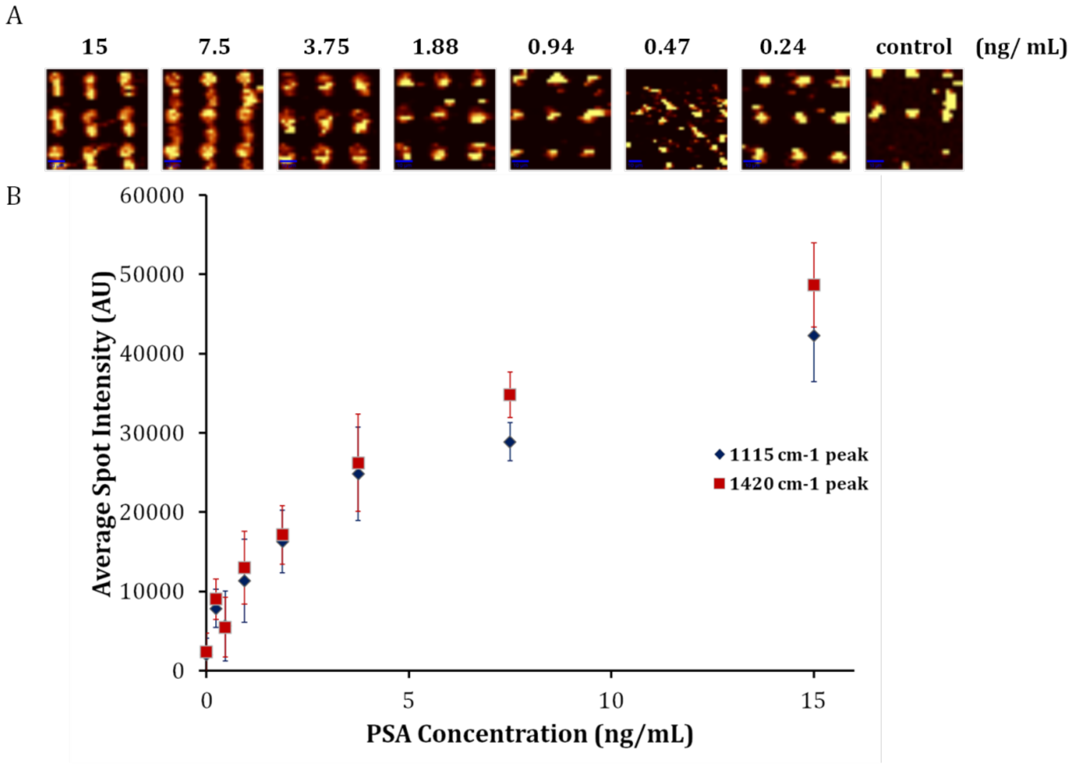

Figure 5.22: *SERS maps generated from a 3 x 3 array of SERS active PSA immunoassay for each PSA concentration applied using the peak at 1420 cm^{-1} from the BT spectrum (A), colour scale shows most intense peaks as yellow, lower intensity as red and lowest to negligible peak presence as black. SERS map colour scales are not relative to each other and are optimised for spot clarity in each case. Plot of average spot intensity vs. PSA concentration for BT peaks at 1420 cm^{-1} and 1105 cm^{-1}*

Figure 5.22B shows the plot of average spot intensity vs. PSA concentration for the 10 minute conjugate addition time. Example Raman maps produced from the 1420 cm^{-1} peak for each PSA concentration and control arrays are given in figure 5.22A. The above graph is thus far the best resulting concentration study produced in relation to using the SERS detection format. Overall, a decrease in spot intensity is achieved in terms of average spot intensity with decreasing PSA concentration. The 0.47 ng/ mL arrays proved to be hard to analyse, although it seems likely that experimental error in addition of conjugates to these arrays may have caused this. If this concentration is discarded, a linear portion of the graph is found from 3.75-0.24 ng/ mL range. A major issue is that non-specific binding has again occurred in the control, which, when values are used to calculate the LOD, it gives a poor value of 1.475 ng/ mL. In terms of the 10 minute conjugate addition assay, although the control signal is lower than that of the PSA array, the standard deviation varies considerably, giving a very poor LOD. Therefore, a lower 5 minute conjugate addition time was attempted.

5.2.7 Optimised SERS PSA Immunoassay Arrays using Conjugate Addition Time of 5 Minutes

Finally a successful PSA concentration study was achieved by reducing the conjugate addition time to only 5 minutes. Arrays were printed and PSA immunoassay developed using the same methodology as previous, simply reducing conjugate addition time to only 5 minutes. Resulting SERS maps and plot of average spot intensity vs. PSA concentration is given in figure 5.23.

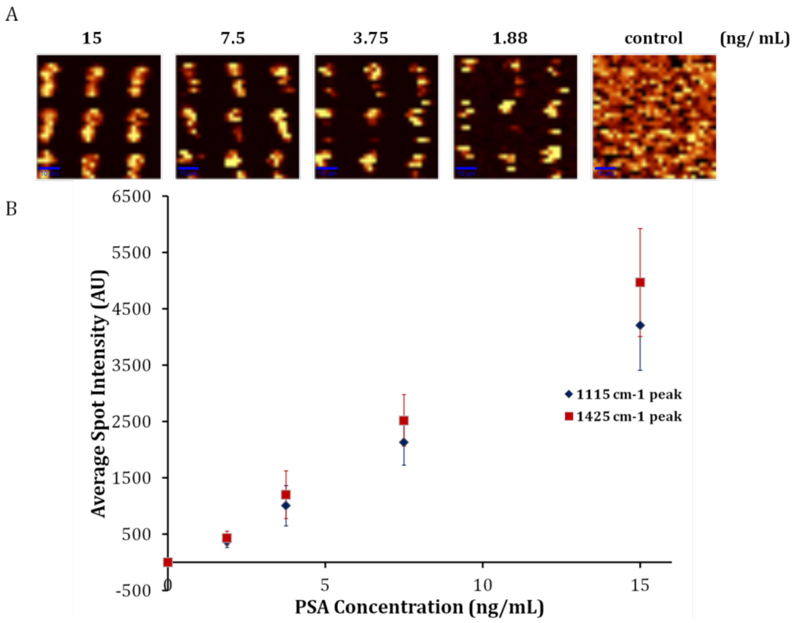

__Figure 5.23:__ SERS maps generated from a 3 x 3 array of SERS active PSA immunoassay for each PSA concentration applied using the peak at 1420 cm^{-1} from the BT spectrum (A), colour scale shows most intense peaks as yellow, lower intensity as red and lowest to negligible peak presence as black. SERS map colour scales are not relative to each other and are optimised for spot clarity in each case. Plot of average spot intensity vs. PSA concentration for BT peaks at 1420 cm^{-1} and 1105 cm^{-1}

Upon observation of the maps alone, the arrays are easily visible as far as 1.88 ng/ mL although, with given settings for SERS map collection (i.e. low integration time of 0.1 second), no arrays were detected at PSA concentrations lower than this. Further to this, no control arrays were detected proving minimal non-specific binding similar to that found with the fluorescence control array. As is plotted in the graph in figure 5.23B, the data produced a linear decrease in spot intensity. This assay was produced twice more giving similar results. Calculated LOD for the strongest peak at 1420 cm^{-1} was 22.8 pg/ mL, a 3 fold increase in sensitivity over that of the fluorescence assay. This suggests that due to the increased signal intensities achieved by SERS, a lower calculated LOD is possible over that of fluorescence detection methods. However, improved sensitivity in terms of visually detecting arrays with lower applied PSA concentrations using SERS was not possible.

5.2.8 Surface Analysis of Optimised SERS PSA Immunoassay Arrays

The optimised SERS assay produced an improved calculated LOD over that of the fluorescence assay due to increased overall intensities of the arrays. This was further exploited by the negligible SERS signal interference from the substrate. For both epoxysilane and nitrocellulose functionalised glass substrates, there was a level of interfering fluorescence background, reducing overall spot signal at each PSA concentration for the fluorescence assay.

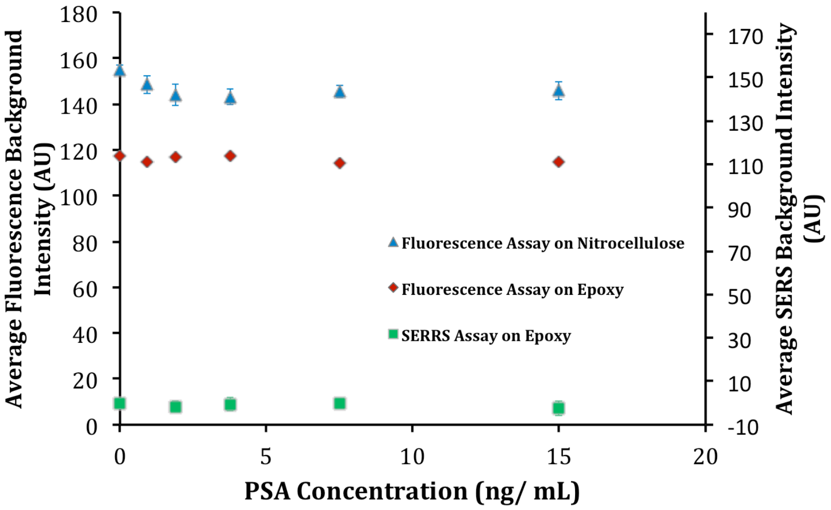

Figure 5.24: *Plot of average background intensity vs. PSA concentration for SERS assay and fluorescence assay on both epoxy and nitrocellulose*

As is clear in figure 5.24, the SERS background interference from the substrate is negligible compared with that of fluorescence methods. This is another advantage to the SERS approach over the popular choice of fluorescence, as substrates of varying functionality are often found to give varying fluorescence interference, a factor that does not need to be considered when using SERS based detection methods.

Despite the improved calculated LOD, the SERS assay arrays at 0.94 ng/ mL and lower were difficult to detect with the scanning methods used to create the SERS maps. It was possible that with such a minimal conjugate addition time of 5 minutes, it was not long enough for the streptavidin conjugates to bind to the arrays. Alternatively, it could be that the arrays were undetectable due to the current laser setting for the SERS maps. Upon preparing the SERS maps, the spectrometer only provides white light microscopy in order to find the arrays for which a user wishes to map, adding to the difficulty of finding the arrays at the surface, as with lower concentrations of PSA, lesse nanoparticles are formed on the spots, making locating the arrays more difficult.

Therefore an investigation into how the arrays form at the surface using 5 minutes conjugate addition time was carried out using the analysis techniques of dark field microscopy and AFM.

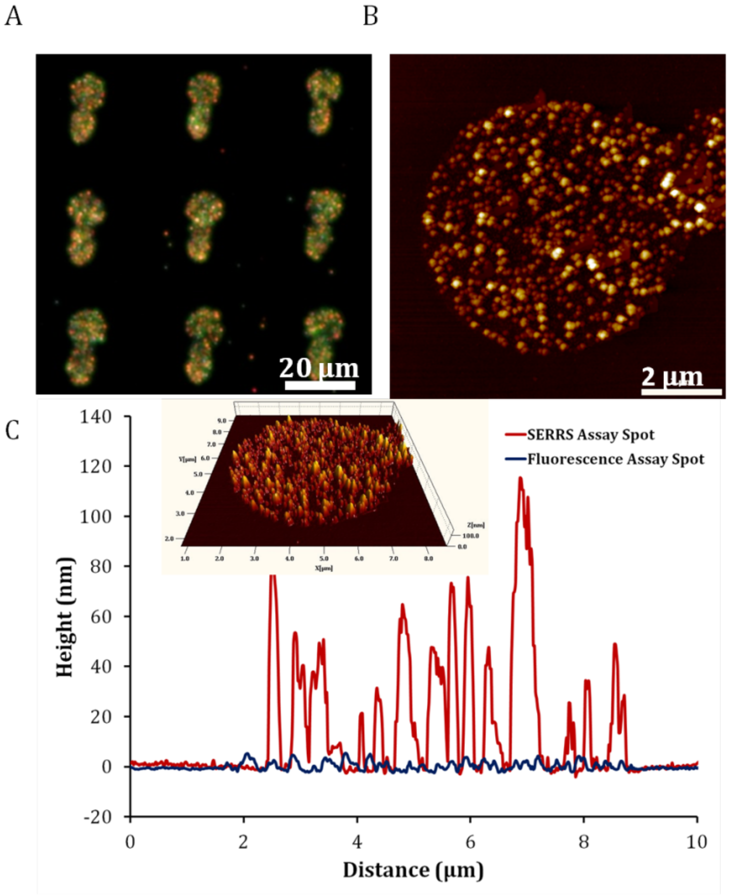

Figure 5.25: *Dark field image of a 3 x 3 spot area of a SERS PSA immunoassay array using 15 ng/ mL PSA concentration (A). Topography 2D AFM image of single spot from array shown (B) with corresponding 3D image inset to that of a cross section analysis compared against a fluorescence spot on epoxy glass (C)*

In terms of appearance at the surface, the use of nanoparticles creates a major difference between the fluorescence and SERS array formats. Figure 5.25 captures a sample dark field image and AFM data of the 15 ng/ mL arrays. It is clear that the arrays have selectively clustered across the array areas only. Tailing (signal found from area surrounding spot due to non specific binding from slide washing before block step) is quite prominent in theses arrays, an issue that fortunately does not affect the resulting spot intensity calculations, but should be reduced if such assays were to be commercialised. A high-resolution topography AFM image of a single spot from this region is shown in figure 5.25B along with a cross sectional graph giving a representative height analysis of the spot against that of the fluorescence arrays (figure 5.25C). As the streptavidin nanoparticle conjugates used in this assay are sized in the region of 57 nm, the large difference in height variation between the SERS and fluorescence array format can be attributed to them. In the case of the SERS PSA immunoassay spot, as 15 ng/ mL is one of the higher concentrations used, the conjugate coverage across the whole spot is higher including nanoparticle cluster areas that produced heights at the surface greater than that of a single nanoparticle conjugate layer. When considering the SERS maps that correlate with these arrays, it clarifies the nature of the SERS signal gained from the arrays. As would be expected, the diminishing SERS signal due to lower PSA concentrations being present result in a reduced nanoparticle population at the surface of the arrays. This pattern can be seen in figure 5.26, which gives dark field and topography AFM images of arrays ranging from 7.5-1.88 ng/ mL PSA concentration.

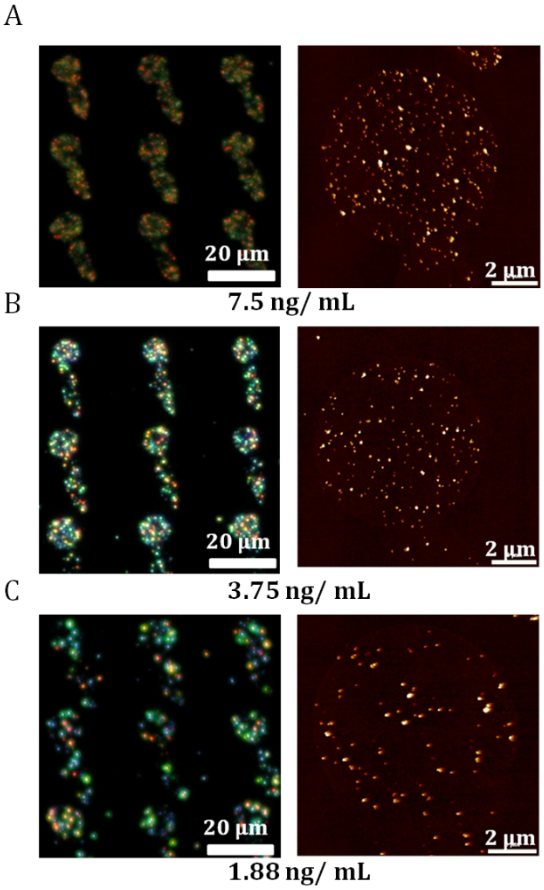

Figure 5.26: *Dark field image of 3 x 3 spot area of SERS active PSA immunoassay arrays with corresponding 2D topography AFM image of an individual spot for PSA concentrations of 7.5 (A), 3.75 (B) and 1.88 ng/ mL (C)*

As expected, a diminishing number of nanoparticles are collected at the array surface with decreasing PSA concentration. This is evidenced by AFM and dark field microscopy, where AFM shows the diminishing nanoparticle population at a single spot very clearly. Additionally, the dark field images show a reduced nanoparticle clustering effect when reaching PSA concentrations of 3.75 and more so for 1.88 ng/ mL. The dark field images show more defined green, blue and red individual colours at these lower concentrations, as opposed to yellow, which suggest nanoparticle clusters. The increased red, blue and green colours being scattered by the arrays represent the presence of single nanoparticles. As the amount of nanoparticle clusters reduced due to diminishing PSA concentration, an increase in single particles covering the spot surface will contribute to a further reduced SERS response from the arrays, due to the reduction of formed 'hot spots'.

Another observation was made in relation to the nanoparticle coverage pattern with reduced PSA concentrations. This is particularly evident in the 1.88 ng/ mL arrays. The dark field image in figure 5.26C shows some spots to have minimal nanoparticle deposition in the middle areas of the spot. This explains the nature of some of the SERS maps, where only spectra were recorded from the outer edges of the spot (seen in figure 5.23A for the 3.75 and 1.88 ng/ mL SERS map examples).

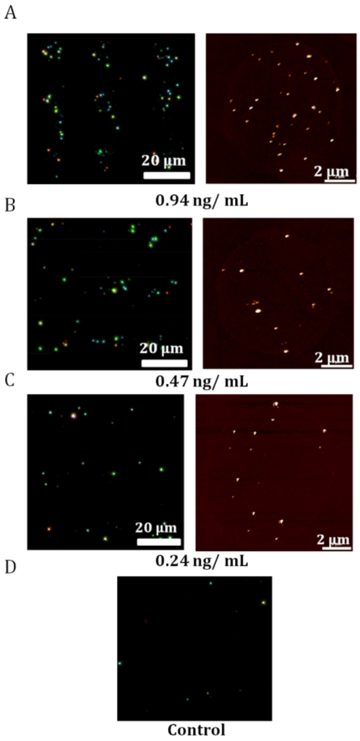

Figure 5.27: *Dark field image of 3 x 3 spots of SERS active PSA immunoassay arrays with corresponding 2D topography AFM image of an individual spot for PSA concentrations of 0.94 (A), 0.47 (B) and 0.24 ng/ mL. Dark field image on control only (D)*

This lack of nanoparticles in the centre of the spot becomes particularly prominent in the 0.94 ng/ mL arrays, which are pictured by dark field microscopy and AFM in figure 5.27A, alongside arrays with lower PSA concentrations of 0.47, 0.24 and control (figure 5.27B, C and D). The dark field image of the 0.94 ng/ mL arrays show that most nanoparticle formation occurs around the edge of the array spot. This is likely explained by the 'coffee ring' effect, often encountered in bulk droplets of liquids at a surface. Although this has not been encountered thus far in the case of fluorescence arrays, it is still a likely occurrence. Upon printing of the PSA Cap Ab, high concentrations of it are used and although we have miniaturised feature sizes used here, we are still printing on the low micro-scale. As in the case of many larger droplet based printing methods, the 'coffee ring effect' (marangoni effect)[180,181,182] is often encountered, where during the time that the droplet is present at the surface (i.e. arrays printed and left wet overnight at 4 °C), the antibodies will move around in solution, towards the surface and bind. However, as the droplet dries, it will dry from the edge first and then inwards, resulting in movement of the antibodies outwards to the drying area at the edge, giving more densely packed antibody coverage around the outer edge of the spot than in the centre. In the case of these SERS nanoparticle based arrays, with conjugate addition limited at only 5 minutes, it seems that due to higher concentrations of PSA Cap Ab depositions, the outer edge of the spot will result in the initial conjugate binding to occur there. This seems like a reasonable assumption as to why, with reduced concentrations of PSA, reduced conjugate formation at the centre of the spot occurs, as in the case of 0.94 ng/ mL arrays.

The images in figure 5.27 also give an idea as to why the arrays were unable to be detected by SERS with the current SERS map settings. The Raman maps are designed for fast scanning, using a low integration time of just 0.1 second and also by comprising map resolution to just 2 μm. However, as can be seen by the dark field images, the depleted presence of conjugates at the surface and low resolution mapping means that it is likely that signal from some spots would be missed when spectra are collected using 2 μm steps. It is likely that this was the issue in the case of the 0.94 ng/ mL arrays, as the maps produced for those arrays showed some signal, but not consistently enough to resolve 3 x 3 array spots. Further to this, as the Raman instrument is coupled with only a bright field microscope, this made it difficult to locate the arrays at lower concentrations; therefore, much of the data from the spots was lost due to lack of ability to scan the correct area. This is particularly notable in the case of these epoxy slides which are 2.54 x 7.62 cm in overall surface size and each area segmented by the incubation chamber is around 1 x 1 cm. Therefore, with such conditions upon analysis, an array of less than 0.8 mm in size needs to be located from within a whole 10 x 10 mm area. This is possible by bright field with the spots of higher concentration of PSA as there is a large presence of nanoparticles on the spots, but as this diminishes with lower PSA concentration, even with highly magnified objectives, it is hard to recognise the arrays for mapping.

Ideally to combat this issue, a 're-vamp' of our current microarray consumables and instruments would be required. As spot sizes are reduced, the sizes of epoxy slides used would be unnecessary. Miniaturised chip sizes and also a suitably altered microarray chamber compatible with such chip sizes would reduce the size of area available to print in the slide. This would make it easier to locate smaller arrays and gather SERS maps of the arrays quicker and more accurately. Additionally, in order to gain a SERS response from those lower concentration PSA immunoassay arrays, an alternative data collection process could be applied when gathering the SERS intensity of each spot. For example, instead of mapping the arrays at a resolution lower than that of the array spot, if the exact location of each spot was more easily identified (i.e. a Raman laser coupled with dark field microscope), it may be possible to defocus the laser and use longer integration times to essentially collect a single spectra that sums the intensity of each spot. However, for this to be better utilised, smaller feature sizes would be ideal as it would reduce how defocused the laser needed to be and thus give a more intense signal. Additionally, smaller feature sizes would localise the nanoparticles in a more clustered format giving further SERS enhancement.

5.2.9 Concluding Remarks

This chapter discussed methods used to adapt the PSA immunoassay arrays from a fluorescence-based detection to SERS. Despite the previous chapter proving that the proteins involved in the PSA immunoassay were easily adapted into an array format and ELISA based format, altering the array format from fluorescence detection and optimising for SERS analysis proved more difficult than expected. In an attempt to avoiding utilising nanoparticle conjugates, it was thought a more facile method to consider would be the LbL method, whereby adding a complementary linker, then nanoparticle followed by a dye to the assay array, in a stepwise manner, would be effective. In fact, this method was found to be both time consuming and gave unpredictable and inconsistent results, with the levels of SERS intensity produced by the arrays being in no way related to the level of PSA present in the arrays. As a result, using a nanoparticle protein conjugate system was a more suitable method, utilising streptavidin bound through a BT dye linker on silver nanoparticles. Initial results proved this system was already a better alternative to that of the LbL method, as conjugates were found to selectively bind to the arrays only. However, non-specific binding continued to be an issue in the control arrays. These issues were tackled by reducing nanoparticle conjugate addition times to only 5 minutes. Results from this assay format further proved effective as analysis gave a calculated LOD of 22.4 pg/ mL, a 3 fold improvement over that achieved by fluorescence microscopy. Finally AFM and dark field analysis of the SERS based assay proved that lower levels of PSA could be detected over that seen by fluorescence, but unfortunately due to time restrictions, the methods employed thus far were unable to reach these levels of detection using SERS.

It became clear that with the right modifications to instrumental analysis, even lower LOD's could be achieved for the PSA biomarker and the principle of this system could easily be adapted to a variety of other biomarkers for immunoassay array formats, proving a faster assay production, reduced array feature size and a possibility of increased sensitivity of detection.

6. Creating SERS-Active Substrates via DPN Templates

6.1 Role of Metal Structured Substrates in Biosensing

The use of alternative detection methods in biosensing such as SE(R)RS, are of great interest in research to find novel ways to improve diagnostic techniques. Nanoparticle conjugate methods are often adopted for SE(R)RS detection in order to gain further sensitivity in surface based assays. However, it is clear that due to the lack of control over nanoparticle assembly, uneven signal intensities are often produced, as the level of nanoparticle aggregation at a surface can greatly affect the level of the SE(R)RS response. Evidence of this is clear in the previous chapter as well as much of the work pursued by Porter *et al.*[161] In their work they functionalised flat gold and carried out a PSA immunoassay, finally capturing the biomarker with a PSA Det Ab conjugated to a gold nanoparticle with a Raman reporter molecule (RRM) attached. In the case of collecting signal from each varying PSA concentration, they found for the number of point spectra taken per concentration, 20% of the spectra collected had to be discarded, as the intensities gained were excessively higher than those gathered from other areas of the immunoassay surface. This need to discard data is unfavourable in terms of developing a consistent read out method for the detection of analytes.

An alternative approach is to use roughened metal substrates to contribute to the enhancement in a bottom-up format. In this case, a surface is treated by a variety of methods that can achieve a roughened metal state, giving it a SERS active quality. This surface is then used as the substrate in which the analyte or immunoassay is immobilised on and with the presence of an active dye, a SERS signal can be gained due to the enhancing properties of the substrate. The design of most SERS active substrates vary greatly, as some are based on nanoparticle assembly on a compatible substrate,[183,184] while others consist of nano pillars,[185,186] triangles[187] and spheres.[188] In most cases a generic consistent pattern is maintained throughout the whole of the surface resulting in a homogenous signal enhancement over the whole substrate.

Large interest in the use of SERS active substrates has resulted in numerous new metal nanostructures being developed for a variety of applications based around high sensitivity SERS detection. Such things as DNA,[94,189] protein[190] and analyte sensing applications have all be proven to work well upon utilising a SERS active substrate.[184,191]

6.2 Methods for Preparing SERS-active Substrates

Preparation of SERS-active substrates can be generally categorised into two different methods; a bulk self assembly method or a lithographic based approach. Many bulk methods involve the controlled self assembly of gold or silver nanoparticles or rods on a surface through use of compatible SAMs or polyelectrolyte layer in order to bind the nanoparticles to the surface.[183-184, 192,193] Parameters that contribute to the uniformity of the surface include size of nanoparticle and pH upon immobilisation. Other bulk coat methods involve a variety of techniques, which often involve a physical vapour deposition (PVD) of the metal at the surface. PVD is often applied to a surface that has been pre-treated to create the roughened structures, which are then coated by a metal of choice via PVD giving the substrate its enhancing feature shapes.[194] A common technique that uses this preparation method is nanoimprint lithography (NIL).[195,196] Alternatively the likes of nanosphere lithography (NSL) uses polystyrene beads as a mask to dictate feature shape at the surface. Etching of the spheres is carried out to control gap sizes which after PVD give a variety of shapes based on the size of sphere used and length of etching time.[173,197,198] Such methods as NSL and NIL give better uniformity than the surfaces produced from bulk depositions of nanoparticles.

Some of the mask based systems however, often require preparation via e-beam. Use of such a technique generates high precision features but it can be costly, therefore there is a large focus on techniques such as NSL where cheap polystyrene beads are used and there is a constant strive to find alternative methods that remain cheap and are easy to make in terms of substrate development.

6.3 The Role of DPN in Generating Metallic Structures

An alternative application for DPN of alkanethiols is their use as etch resists on flat metal surfaces so that upon wet etching, uniform metal nanostructures are achieved.[199,200,201] Alternative ways of creating metal nanostructures by DPN include liquid carrier inks to deposit metal directly,[95] printing the metal salt and post-printing, using various treatments to produce the metal on the surface[103] or using eDPN to deposit the metal structure from the oxide form used as the ink.[56] In most cases, these structures have been developed to either highlight the precision of DPN printing,[201] or for creating conductive nanowires.[95]

However, as stated before, in order to push the limits of sensitivity in biosensor technology, it is important to constantly seek new methods of detecting low levels of certain biomarkers. Detection techniques like SE(R)RS and SPR achieve optimal enhancement for low levels of analytes when they are bound to a roughened surface. Due to this, many different metal substrates have been fabricated in order to enhance and tune the localised plasmon suited to that of the analyte and detection method chosen.[202,203,204] Various fabrication methods have been used to create plasmonic surfaces for biosensing purposes but they have tended to be bulk coat methods that rely on various layer depositions and etching steps.[205,197] DPN based methods of producing metal nanostructures could have an advantage over current techniques in terms of its high patterning precision and flexibility in pattern design. Furthermore, large scale nanopatterning of metal nanostructures has been made possible by multi-pen probes with good tip to tip variability (figure 6.1).[66] As a result, there is an opportunity to explore the use of DPN in generating metal patterns as a basis for a SERS active substrate. The work carried out in this thesis thus far has shown the applicability of SERS for biosensing using nanoparticle conjugate methods but there is a large area to be explored in terms of using DPN to fabricate a substrate for detection of analytes by SERS.

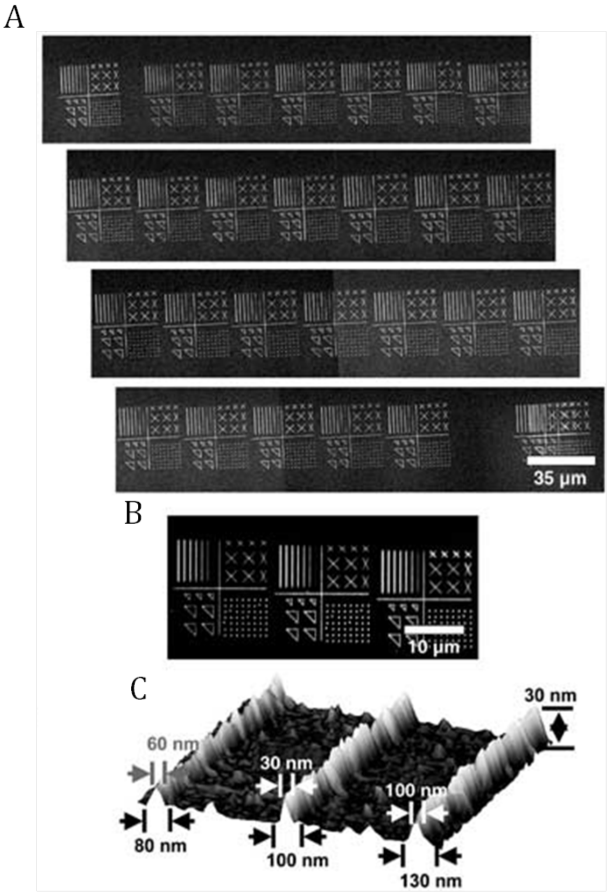

Figure 6.1: *An SEM image of 26 copies of gold line, triangle, dot, and cross structures on a Si/SiOx substrate produced from wet chemical etching (A). A dark-field micrograph of the same nanostructures (B)and representative AFM image of one of the line arrays (C)* [66]

6.4 EnzMet™: Enzymatically Produced Silver Crystals

EnzMet™ has emerged as a silver staining product within the last decade. Unlike many other silver staining kits, where the presence of gold nanoparticles are required, EnzMet™ selectively produces solid silver crystals in the presence of horseradish peroxidise (HRP). The solution itself is made up of three separately applied solutions, which are added sequentially and mixed together on the sample of choice. The HRP enzymatically produces Ag(0) from Ag^+ ions in the solution.

EnzMet™ has mostly found applications in immunohistochemistry (IHC) and the recognition of certain analytes such as HER2 in tissue samples,[206,207] once captured with a peroxidised conjugated antibody. Another application involved its use for monitoring DNA hybridisations.[208] In this case, DNA hybridisations were immobilised at an electrical chip junction. As the probe strand was conjugated to a peroxidase enzyme, application of the EnzMet™ solution produced silver across the junction of the electrode giving an electrical readout in the DNA reader.[208]

However, inspiration for the work carried out in this chapter was taken from the work of Dr. Jürgen Popp's group, where they immobilised microarrays of EnzMet™ using a peroxidase polymer and then attached DNA molecules conjugated to 3 Raman dyes. They successfully detected the DNA by SERRS and found it to be a more enhanced signal than that of nanoparticle enhancements, they assumed this was due to the sharpness of the silver crystals that the EnzMet™ produced.[209]

6.5 Combining EnzMet™ Application with DPN Based Techniques

The work discussed in chapters 3 and 4 found that the NLP 2000 could be used to produce protein arrays in a high throughput manner. Therefore, an opportunity was recognised in terms of producing various line and dot array formats of streptavidin HRP (strep-HRP) on epoxy, using similar methods as applied to the PSA Capture Ab.

The aim was to print and use strep-HRP arrays as templates that the EnzMet™ solution could be applied to, in order to produce silver arrays that give an enhancing SERS effect. Ultimately, these arrays could be created for the purpose of being used as a SERS-active substrate, which could be an alternative approach to gaining improved sensitivity of biomarker detection in future applications (schematic of this work given in figure 6.2).

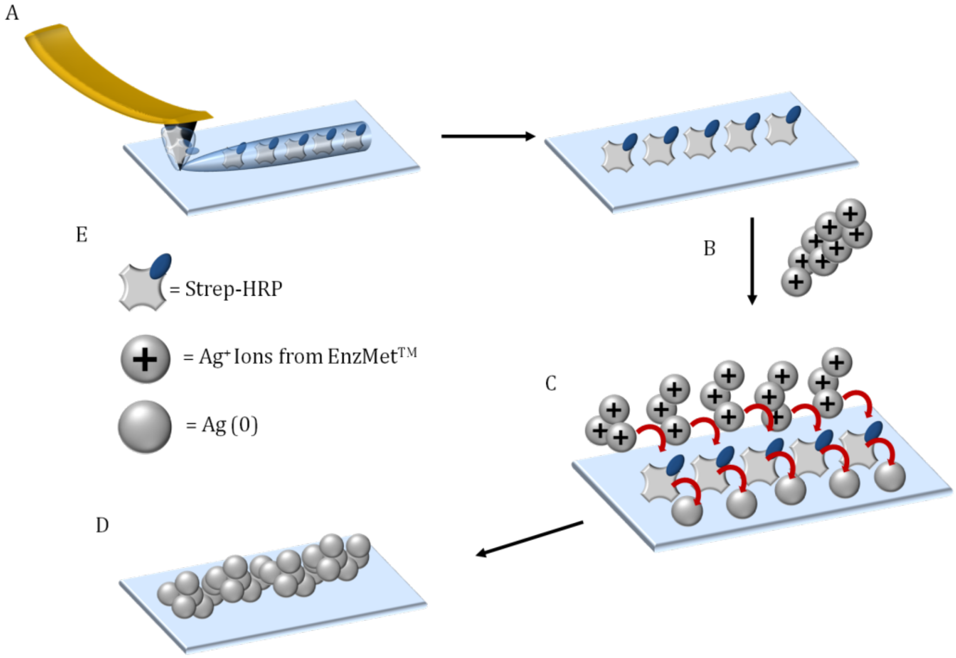

Figure 6.2: *Schematic for DPN-template EnzMet™ arrays. DPN of strep-HRP (A) is performed immobilising various strep-HRP patterns on epoxysilane glass. EnzMet™ solution is then added to the arrays (B) of which silver ions in solution react with the HRP groups on the arrays (C). This results in a silver metal layer immobilised on the area where the array template was printed (D). Legend for schematic is also given (E)*

6.6 Fabrication of Strep-HRP Arrays on Epoxysilane Coated Glass

6.6.1 Spot Array Fabrication

Initially, optimum conditions needed to be established for producing the most consistent silver substrate features. Strep-HRP had never been printed by DPN nor has EnzMet™ ever been applied to arrays in this format. Therefore, it was important to investigate various parameters that could affect production of the DPN based silver substrate. In terms of pattern control, both preparation of strep-HRP in protein print buffer (PPB) and style of array pattern were varied. As the inkwell arrays used for printing allow for up to six separate inks to be investigated simultaneously, the following solutions were prepared:

1. 5: 3 ratio of strep-HRP at 100 %: PPB
2. 5: 3 ratio of strep-HRP at 50 % in PBS: PPB
3. 5: 3 ratio of strep-HRP at 25 % in PBS: PPB
4. 1: 1 ratio of strep HRP at 100 %: PPB
5. 5: 2 ratio of Step HRP at 100 %: PPB
6. 5:1 ratio of Strep HRP at 100 %: PPB

Altering the concentration of strep-HRP added to the print solution could determine whether growth of EnzMet™ silver crystals at the surface was dictated by this variable. However, it would seem unlikely with such concentrations applied as a reasonably high concentration was still being delivered to the surface. Secondly the ratio of PPB to strep-HRP was varied. This was to investigate how the change in ratio of PPB would affect the printability of strep-HRP both in terms of spot size with dots and also line length achieved. In fact, the ability to print lines was of particular interest as this has not been performed using the NLP 2000 nor for inks that deposit through a liquid ink meniscus model. Once inks were added to the inkwell arrays, a multi pen M-type probe and epoxy slide were mounted on the NLP 2000 for printing the arrays as per standard protocols. Using single print methods, 3 sets of dot arrays were printed where each tip produced:

1. 3 x 3 array, 20 μm pitch 0.1 second dwell time
2. 6 x 6 array, 10 μm pitch, 0.1 second dwell time
3. 12 x 12 array, 5 μm pitch, 0.1 second dwell time

The basis of utilising these types of patterns was to investigate smaller array spots in order to see if nanoscale features of silver could be produced. Previous results from chapters 4 and 5, when printing proteins, found that each tip could only produce 16 spots before the spot size was greatly depleted. Figure 6.3 shows an image of the strep-HRP dot arrays which were captured immediately after printing using the NLP 2000 using a bright field microscope with a 20x objective.

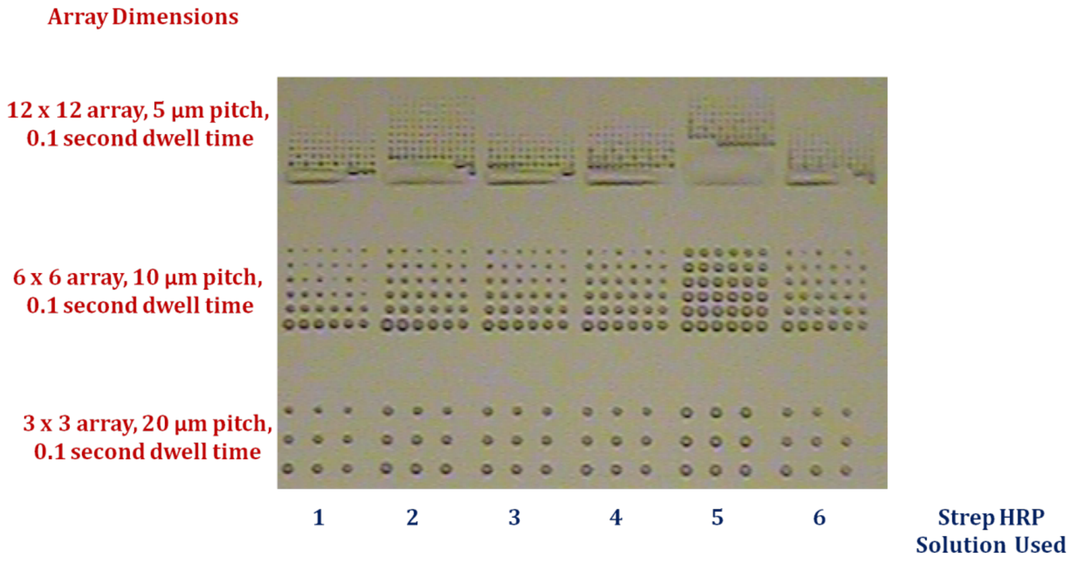

Figure 6.3: *Bright field microscopy image of strep-HRP dot arrays using various array dimensions and solution ratios as detailed on page 111*

As found with printing of PSA Cap Ab the 3 x 3 array parameters gave consistent spot sizes throughout the array, producing feature sizes of around 10 µm in diameter. This was found for all the strep-HRP printing solutions, which are identified for each array in figure 6.3. The difference in solution ratios becomes more obvious in the 6 x 6 arrays. The 5:3, 1:1 and 5:1 ratio solutions give patterns where spot sizes beyond the 2nd row deplete, as encountered with the PSA Cap Ab when determining optimal array printing conditions. However, the spot sizes of the features beyond the 3rd row reach the range of 1-3 µm diameter. Although this gave inconsistent feature sizes throughout the array, it will be useful to have this change in spot size to determine if feature sizes that small can produce silver EnzMet™ product and what conditions are required to achieve these features of silver. Further to this, the 5: 2 ratio of strep HRP: PPB has in fact maintained a fairly consistent low micro-feature size throughout the array. The closer pitch was of interest too as when EnzMet™ solution is applied, it is possible that minimised gaps between the silver spots may cause an enhanced SERS effect. As the 6 x 6 array in the majority of cases gave very low feature sizes, the 12 x 12 array format was utilised in order to form more densely packed arrays containing smaller feature sizes.

6.6.2 Line Array Printing

For the fabrication of lines, each tip was used to make a grid of lines, the parameters for these were:

1. 3 x 3, 40 μm length lines, 20 μm pitch, 10 μm/ second
2. 3 x 3, 40 μm length lines, 20 μm pitch, 20 μm/ second
3. 3 x 3, 40 μm length lines, 20 μm pitch , 30 μm/ second

These arrays were also captured by bright field microscopy after printing and are shown in figure 6.4

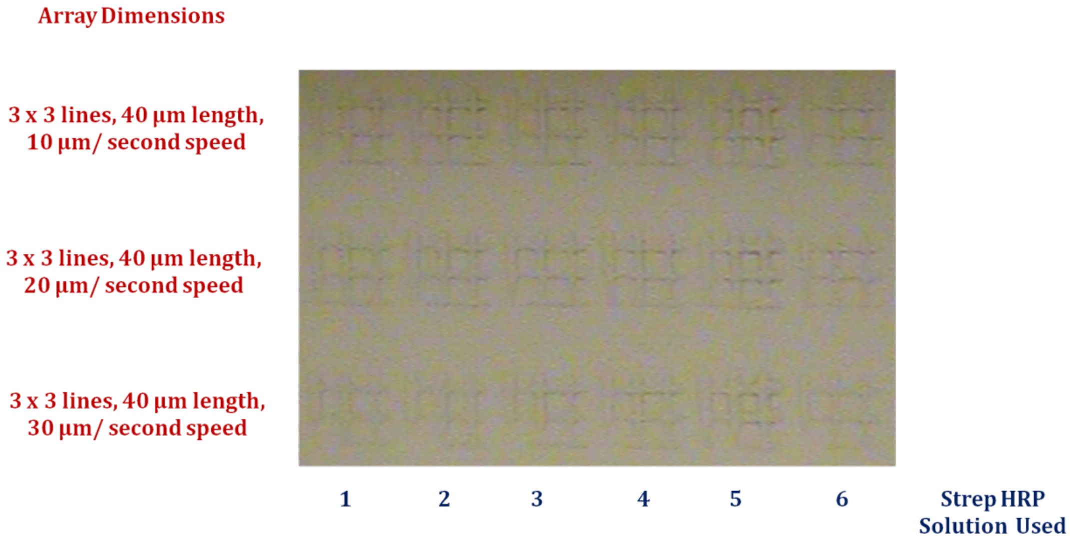

Figure 6.4: *Bright field microscopy image of strep-HRP line grid arrays using various array dimensions and solution ratios as detailed on page 111 and 113.*

Due to the transparency of the glass and the difference in the nature of the lines, it was difficult to capture them on the microscope, giving a poor image in figure 6.4. However, the only parameters of each of these arrays changed were the line patterning speed and solution ratios. In comparing both these parameters, none have any real influence over line widths or shape of the grids made. The only anomaly to this rule was the 3 arrays made by solution 5, where the lines do appear thicker than that of the others, a similar trend to what was found for the dot arrays.

However, during printing of the lines it was discovered that the nature of how line patterning is controlled in terms of a liquid meniscus model differs greatly from that of the water meniscus diffusion model. Further to this, no literature exists on DPN of line printing using the liquid ink meniscus model and therefore careful studying of this patterning was carried out.

6.7 Printing Lines of Proteins: A Liquid Ink Meniscus Model

There is a reasonable number of both theoretical and experimental publications showing the water meniscus model for producing nanometer width lines of inks such as thiols.[82,210] In the case of spot features, SAM molecules (thiols) push out from the tip and molecules seek out exposed areas of surface around the point of the tip contact through pushing other molecules out (push model) or transporting over molecules anchored closer to the tip (stepping out model).[211] For lines, as the tip is constantly moving, new areas of gold are constantly being exposed, meaning that ink transport is faster and the lines of ink are bound to the surface immediately as the tip travels across the surface.[210a] This is the likely reason for why lines of thiols were printed at the early stages of DPN in order to show minimum nano-scale line widths and thus the capabilities of DPN.

However, during printing of strep-HRP for grid like patterns, it was found that the strep-HRP mixed with the liquid carrier PPB behaved very differently from that of both spot depositions of the same liquid ink and the line printing for water meniscus model.

Figure 6.5 shows captured images gathered from a video taken of part of an M-type tip array printing strep-HRP in a grid like format. A 5:3 ratio of strep HRP (100 %): PPB was used to coat all tips via the inkwell array and each tip was programmed to print 2 x 2 lines of 66 μm length and a 33 μm pitch, using a 20 μm/ second tip speed.

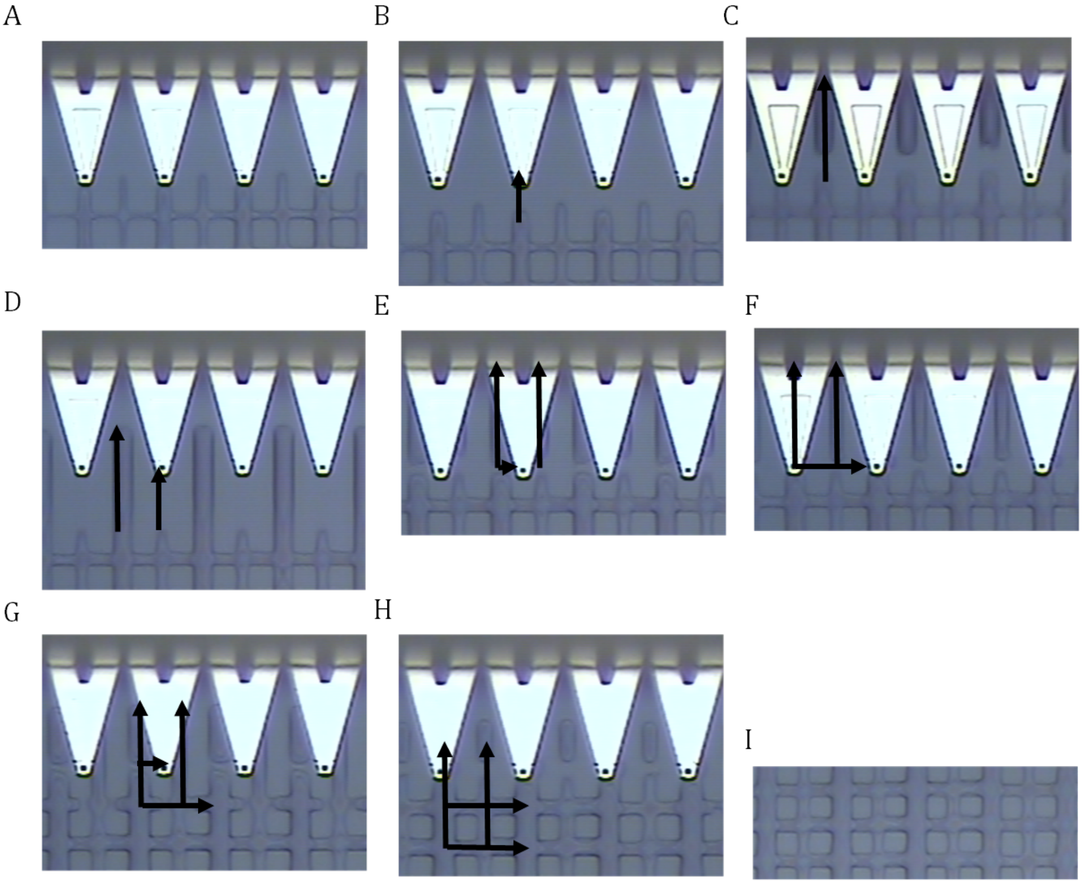

__Figure 6.5:__ Capture images taken from the NLP 2000 microscope of strep-HRP line grids being printed. In alphabetical order it captures each step and tip movement required for creating a 2 x 2, 66 μm long line per tip

Both X and Y coordinate line movements gave the same resulting printing based method. Figure 6.5 show the process of line fabrication in real time. When the tip first contacts the surface and begins printing, it appears as if nothing is depositing (figure 6.5A and B). However, upon closer inspection and high zoom of the NLP 2000 microscope (not shown due to the image resolution being too poor), it could be seen that a very thin line of ink was in fact being traced along the surface. It was only when the tip reached the end of the line being printed and upon lifting the tips from the surface that a small volume of the ink is released (figure 6.5C). The ink then continues to flow back along the area traced by the tip giving a fuller line of ink as part of the arrays. What seems to be happening is that the ink is trapped at the tip while printing due to the surface tension of the liquid meniscus at the tip location. As the tip is lifted from the surface, this disrupts the tension held at the tip-surface interface, allowing the ink remaining at the surface to spread. As the trail already traced out by the tip has been created throughout the printing process, instead of expanding outwards like a spot would, the ink travels back along the thin trail. By the time the tip has moved to the next location to print a new line as part of the array, the previous non-existent line had been filled with a line of strep-HRP printing solution of a low micro-scale thickness.

This was an unexpected and interesting discovering during the process of this work as it contributes to the little understanding of how liquid ink meniscus patterns are formed. It confirmed that the pattern is greatly manipulated by the tip-surface interface and for future work, it will allow researchers to consider how changing carrier molecule properties and choice of substrate will affect printing methods, with regards to liquid ink meniscus printing.

6.8 Identifying Optimal EnzMet™ patterns and Conditions

There are a variety of available EnzMet™ products for different applications. The kit used for this work was the EnzMet™ western blot kit. It comes with three solutions; A, B and C. The volumetric ratios of the solutions were 3:1:1 and the solutions were added to the surface sequentially for set times, except for solution C which is varied based on the level of silver production required.

5 sets of the dot and line arrays printed in section 6.5 were fabricated on an epoxysilane coated substrate. The slide was left overnight at 4 °C before treatment with EnzMet™.

Both the epoxy slide and the EnzMet™ kit were brought back to room temperature before experimental procedures were carried out. The epoxy slide was washed with wash buffer and water to remove any unbound strep-HRP from the array surface. Next the slide was placed in an incubation chamber and 60 µL of solution A was added to the surface of each array set for 4 minutes. 20 µL of solution B was then added to each well and mixed within the well with solution A for 4 minutes. Solution C (20 µL) was then added to each array set. For this, the time varied for each array set, with a time range of 5-25 minutes being used. For all stages of incubation, gentle agitation was applied to the slide and chamber. Once the incubation time with the EnzMet™ solutions ended, it was removed from the slide and the slide was washed 3 times with deionised water for 5 minutes each. Finally substrates on the slide were fixed by drying under nitrogen.

Although the arrays could be seen visually using bright field microscopy, dark field was used in order to gain a detailed analysis of silver crystal growth at the surface and to conclude what conditions provided the best silver substrate arrays. From observation of the arrays using dark field, it was easy to recognise how the length of time solution C was on the surface, affected the clarity of silver attached in place of the strep-HRP arrays.

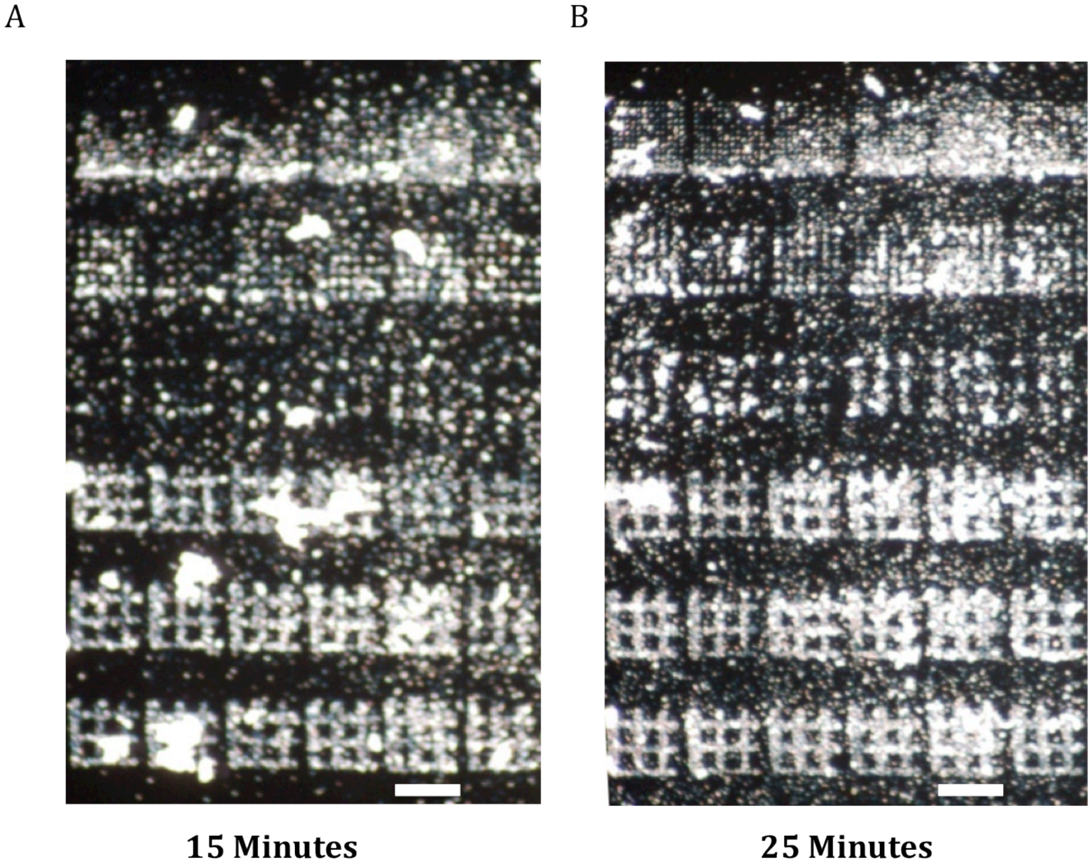

Figure 6.6: *Dark field microscopy images of dot and grid patterns produced from strep-HRP arrays using an EnzMet™ incubation time of 15 (A) and 25 (B) minutes. Scale bar represents 40 µm width and 20x objective used*

It was found that times beyond 15 minutes of EnzMet™ application resulted in excess deposition of silver, which occupied the areas surrounding the arrays. This can be seen in figure 6.6, which shows images of all dot and line arrays produced by 6 of the tips. It appears that due to the longer times EnzMet™ solution C was applied for, resulted in overproduction of silver, which has immobilised itself in and around the area of the arrays. This issue was reduced in the case of 5 and 10 minute application times of solution C, results of which are shown in figure 6.7.

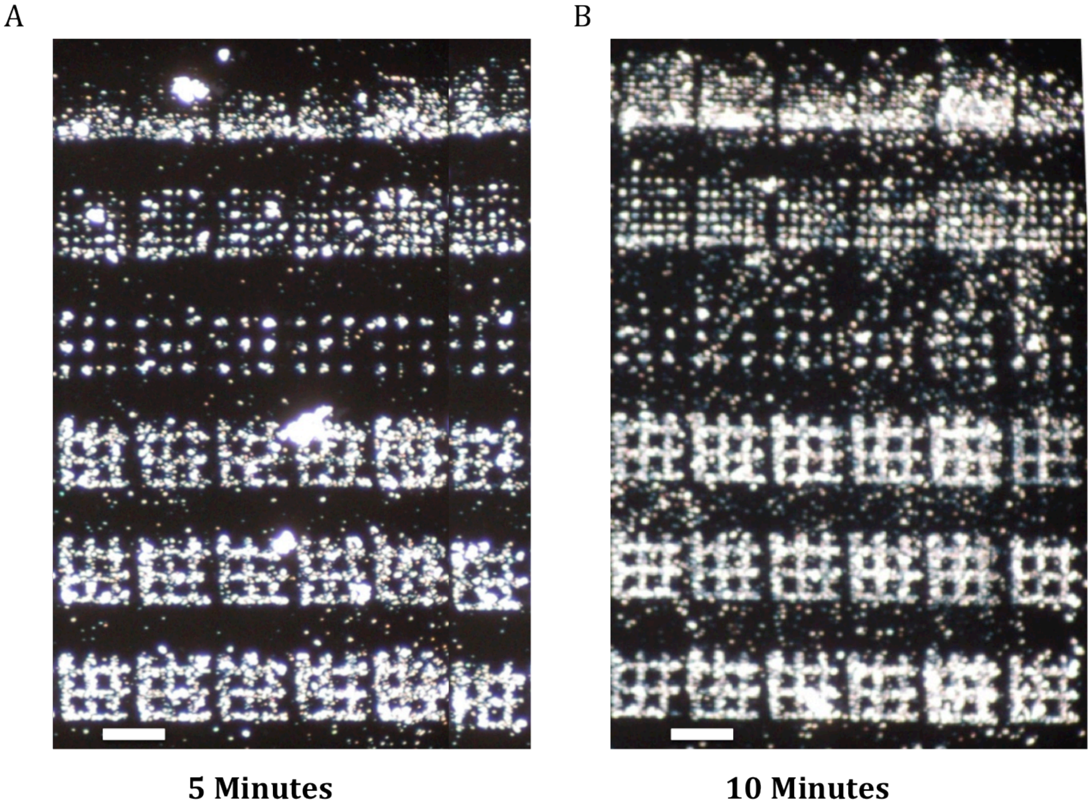

Figure 6.7: *Dark field microscopy images of dot and grid patterns produced from strep-HRP arrays using an EnzMet™ incubation time of 5 (A) and 10 (B) minutes. Scale bar represents 40 μm width and 20x objective used*

Both 5 and 10 min arrays have far less background silver deposition than those using longer EnzMet™ application times. The arrays of strep-HRP have produced silver substrates in their place and are very similar in feature size and shape (referring to figure 6.3 and 6.4). At this stage it is difficult to determine which time gave the optimal substrate without clarification of SERS enhancing properties. The 5 minute arrays show less background silver than that of the 10 minute arrays, however, in the case of the grid like structures, the 5 minute arrays appear slightly less bright and more broken up than those of the 10 minute arrays, which could result in a reduction of SERS intensity. In terms of the solution constitutions used for Strep-HRP prints, a few observations were made. The dot arrays made have produced silver spots; but show poor uniformity and have varying feature size and morphologies. While this could be expected for those spot arrays which showed a change in feature size with continuous printing, it also occurred with the 3 x 3 arrays, which from comparing with the printed arrays in figure 6.3, showed good feature size consistency. It is very clear from the dark field analysis that the micro-waffles (grid array format) are consistently coated with silver and show well-defined features. Variation in strep-HRP concentration made very little difference to the resulting levels of silver present in the line arrays and it is clear that the variation in ratio of strep-HRP to PPB has influenced line thickness slightly as can be seen in both figure 6.4 and 6.7 for the 5:2 ratio, where the lines are almost too thick, giving poor grid shapes. It appears as though optimal printing conditions should remain at a 5:3 ratio and instead of varying the strep-HRP concentration the time the EnzMet™ is applied to the arrays should be limited, in order to control silver production at the surface.

6.9 SERS Output from EnzMet™ Arrays

To determine if the silver EnzMet™ arrays were in fact SERS active, NBT was applied to the dot and micro-waffle based silver arrays produced after 5 and 10 minutes of EnzMet™ solution application (see section 3.7.3 for details). SERS maps of each of the arrays was carried out giving 1 μm resolution maps, generated from the 1565 cm^{-1} peak and using 0.1 seconds integration time. As found from the dark field images previously, the spot arrays appear to have created inconsistent silver features, both in size and morphology. Figure 6.8 shows an example of these results for the 5 minute EnzMet™ application, where the 3 x 3 dot array produced from solutions 1 and 4 of the strep-HRP solutions are shown for both dark field microscopy and corresponding SERS map. The SERS intensity of the NBT dye corresponds well the shapes that can be seen under dark field microscopy. However, the feature shapes and morphology have proven hard to control in the spot format as within a single array, the features vary in shape and size. This is of particular note for the 3 x 3 array format, as it was clear from figure 6.3 that the spots of strep-HRP for these arrays are very homogenous and consistent in size throughout the array.

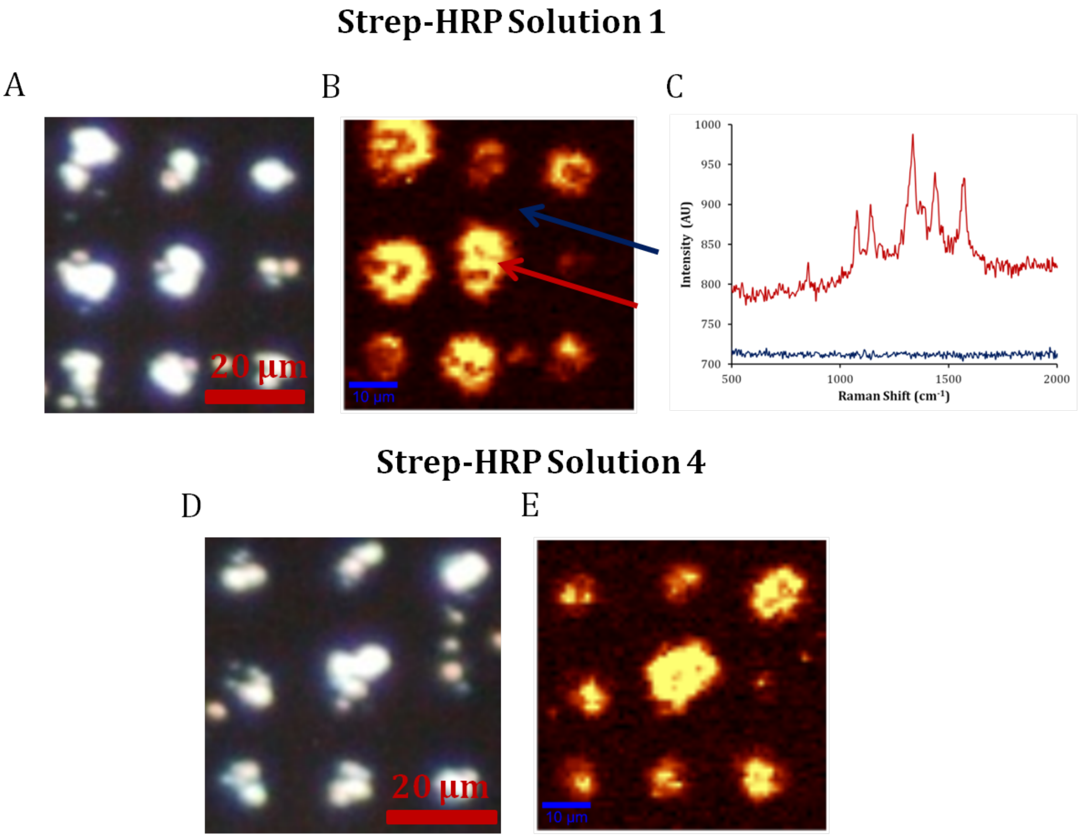

Figure 6.8: *Dark field image and corresponding SERS map for 3 x 3 dot arrays produced from 5 minutes EnzMet™ application to strep-HRP solutions 1 (A-C) and 4 (D an E). SERS maps generated from the 1565 cm^{-1} peak of the NBT spectra, which was added to the array surface*

The 6 x 6 dot array format also showed inconsistent features in terms of silver production at the array location. Dark field and SERS map images in figure 6.9 highlight the need for large features for effective SERS enhancement of the dye. The dark field image in figure 6.9A shows a mixture of larger and smaller features. When compared with the corresponding SERS map (figure 6.9B), only the larger spots produce a SERS enhancement and in fact the smaller features are not visible in the SERS map. Longer intergration times may have generated a SERS signal from these smaller silver features, however, this information is useful for determining the level of silver production required to gain significant SERS enhancement at the faster integration times used.

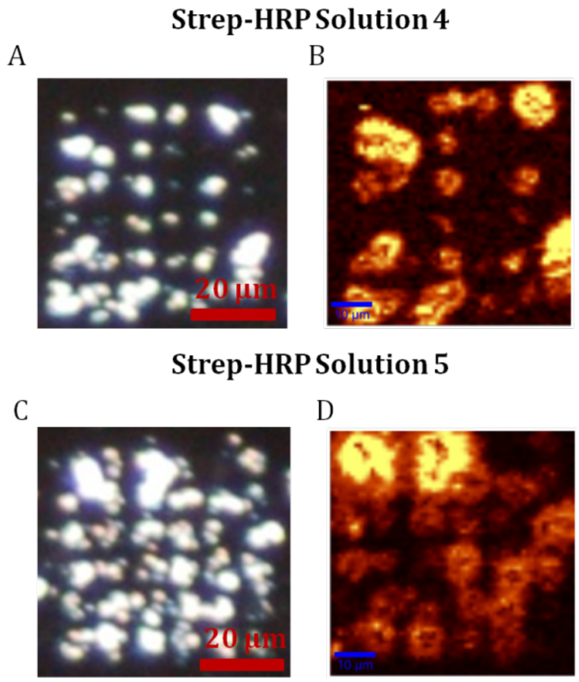

Figure 6.9: *Dark field image and corresponding Raman map for 6 x 6 dot arrays produced from 5 minutes EnzMet™ application to strep-HRP solutions 4 (A and B) and 5 (C and D). Maps generated from the 1565 cm^{-1} peak of the NBT spectra, which was added to the array surface*

The array captured in figure 6.9C and D was produced from strep-HRP solution 5, the solution that produced a denser but homogenous array feature size. It is clear from the Raman map, that the SERS enhancemnt gives poor resolution of these arrays and that the spot shape is barely visible in the Raman map, compared with that of the dark field image.

From these obstervations, the dot arrays of strep-HRP successfully activate a silver growth at the array surface upon reaction with EnzMet™ solution. However, in terms of producing a homogenous substrate with reproducible SERS enhancement, a dot format is not suitable.

The micro-waffles proved more promising for improved pattern consistency. Examples of resulting micro-waffles from the 5 minute EnzMet™ application are shown in figure 6.10. The grid shape of the mirco-waffles are well defined and give a good SERS reponse, spectra of which are shown in the graph in figure 6.10C. Both the original strep-HRP array, dark field and Raman map images all match well in terms of area of enhanced signal. Areas of highest SERS enhancement in figure 6.10B corresponds well with the dak field image, as it shows more scattering in those areas, which suggests a greater build up of silver and increased roughness. Figure 6.10D shows 5 other maps taken from the 5 minute EnzMet™ array set. The waffle shapes still resolve well in the maps, however, consistency throughout the array pattern in terms of SERS activity varies a great deal.

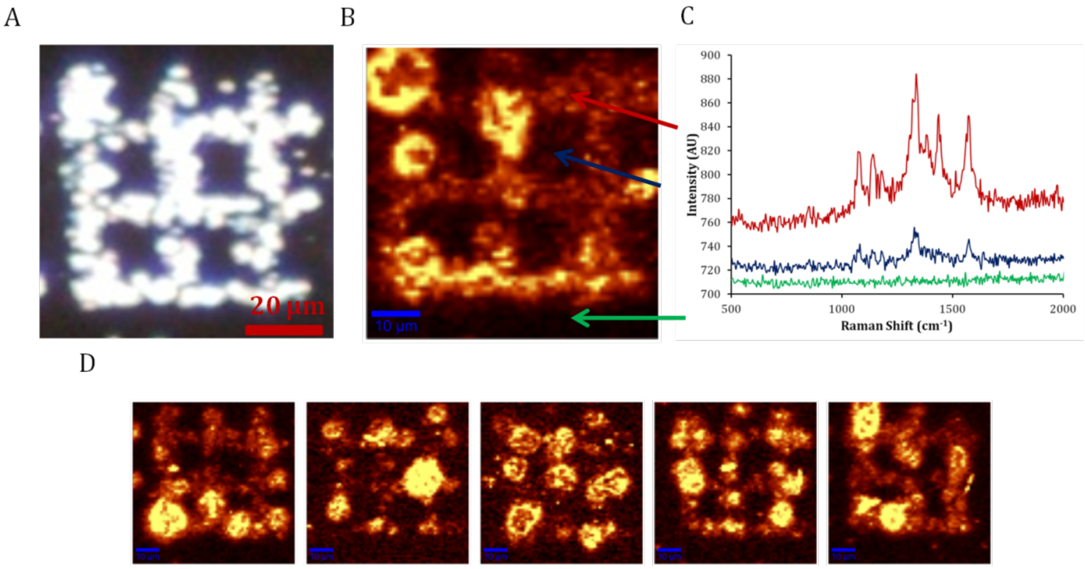

Figure 6.10: *Dark field microscopy image (A) and corresponding SERS map (B) of a micro-waffle array generated from 5 minute EnzMet™ solution application. SERS map taken after array was coated with NBT. SERS map was generated from the 1565 cm^{-1} peak of NBT and spectra from on and off the arrays are given and highlighted with colour co-ordinated arrows (C). Other examples of best micro-waffle SERS maps from this array set (D)*

Interestingly the micro-waffles produced by 10 minute EnzMet™ addition gave improved SERS signal homogeneity and also an overall increased enhancement over those produced from 5 minute EnzMet™ addition times. Figure 6.11 show much brighter SERS maps from these arrays, with vastly improved definition between the signal from the silver arrays and that of the epoxy substrate. Although it should be highlighted, that in all cases, the NBT signal is only given from the silver arrays, and no non-specific SERS NBT signal has occurred in the surrounding areas. Despite the improved signal enhancement, the 10 minute EnzMet™ array still gives areas that give more of a SERS enhancement that the rest of the areas on the micro-waffle. A pattern has emerged where the majority of these increased SERS active areas occur at the corners of the waffles or at junctions where an X and Y plane line have crossed. It is hard to determine the exact cause of the trend. If the areas are crossed by two lines, it could be increasing the density of Strep-HRP in those regions, giving a greater build up of silver crystal growth resulting in an increased SERS enhancement. Alternatively, junctions and corners within the waffle structure may offer a greater surface area, allowing more dye to immobilise in a denser area to that of the rest of the structure. If so, an increased packing density of the dye would also give an increased SERS enhancement.

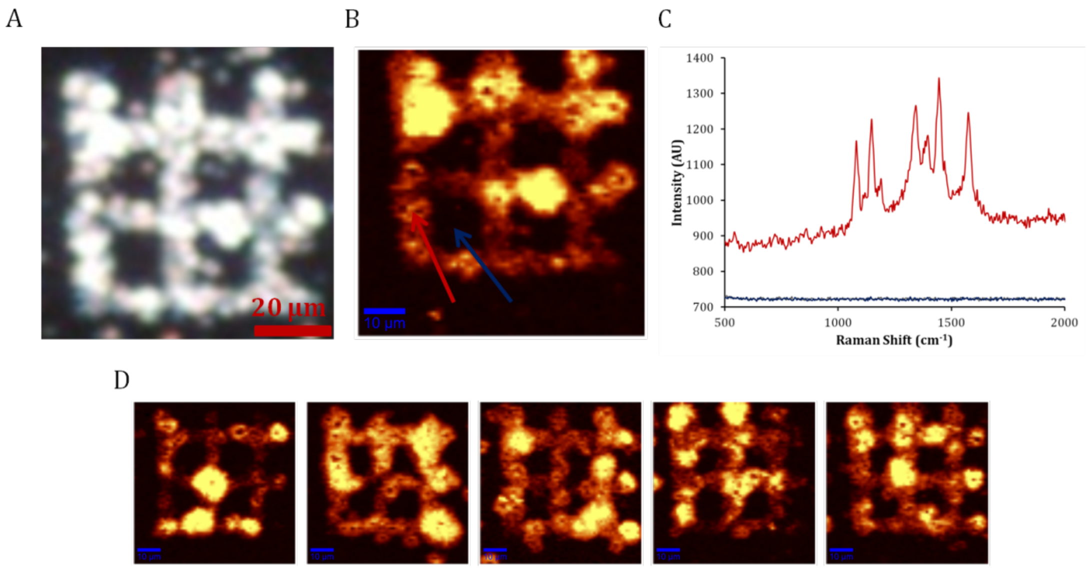

Figure 6.11: *Dark field microscopy image (A) and corresponding Raman map (B) of a micro-waffle array generated from 10 minute EnzMet™ solution application. Raman map taken after array was coated with NBT. Map was generated from the 1565 cm^{-1} peak of NBT and spectra from on and off the arrays are given and highlighted with colour co-ordinated arrows (C). Other examples of best micro-waffle Raman maps from this array set (D)*

From the results shown it is clear that use of the micro-waffle format and 10 minutes EnzMet™ solution on the strep-HRP arrays, produced the most consistent SERS active substrates, with good enhancement and little background signal from the surrounding areas, as overproduction of silver was minimised with these set conditions.

6.10 Concluding Remarks

This chapter explored the use of DPN techniques in order to generate a SERS active substrate for the first time. By adapting some of the fundamental optimisations of protein printing from the previous work carried out in this thesis, strep-HRP arrays were fabricated both in spot format and a series of crossing lines to give a micro-waffle shape. Use of liquid inks to form line features resulted in discovering more information about the nature of liquid inks due to the effects surface tension has over the successful deposition of inks, which abide by the liquid ink meniscus transport model. Strep-HRP array templates were used to enzymatically deposit silver at the surface of the arrays using EnzMet™ solution. Final optimised conditions gave irregular spot shapes but silver micro-waffles proved to give good SERS enhancement of the dye NBT, with accurate silver deposition that mimicked the original strep-HRP template printed.

These initial results show the potential use of DPN in the fabrication of SERS-active and plasmonic substrates, for an alternative approach to improved methods for biosensing.

7. Conclusion

The work detailed in this thesis, has utilised high-throughput DPN of protein arrays in two very different ways, with the aim for improved sensitivity in the field of biosensing.

High-throughput fabrication of protein arrays were achieved through the use of the NLP 2000, multi-pen probes and inkwells. Robust print methods were investigated and optimised giving a printing method that can be generically applied to potentially any surface or protein of interest. This body of work exemplifies how the evolution of DPN research has resulted in its use a high-throughput printing instrument, rivalling current direct-print methods such as ink jet and micro-contact printing, yet achieving miniaturised features sizes for microarrays.

The optimised fabrication methods were applied to development of a low micro-scale PSA immunoassay array study, in which relevant LOD's were achieved by fluorescence. Further research was carried out in determining if SERS could be applied in order to achieve an improved sensitivity for PSA immunoassay arrays. Improved calculated LOD was possible, however due to the use of nanoparticles, optimisation of this assay format proved difficult. To utilise SERS detection in combination with a DPN printing immunoassay array, further work must be carried out. An investigation into the SERS analysis method would result in an optimised SERS-based detection method. This could be highly beneficial in order to achieve detection of PSA at lower limits than found using fluorescence detection. It would also establish SERS as a DPN compatible detection method, further proving DPN flexibility in application.

Recognising the difficultly that occurred with the use of nanoparticles for SERS-based detections, an alternative approach was considered utilising both the optimised printing for protein arrays and the application of EnzMet™ solution to create the first ever SERS-active DPN fabricated substrate. While initial studies simply show the SERS capabilities based on the addition of a dye alone, it highlights the possible biosensing applications that these substrates could be used for, bypassing the use of nanoparticles for SERS detection. Again, future work is required in order to determine effective attachment of proteins/antibodies to these metal surfaces. Effective thiol/ protein linkers would have to be determined in order to maintain protein functionality at these surfaces. Furthermore, it would be of interest to determine what distance between the dye and the metal surface would result in losing the enhancing effect of the EnzMet arrays, in order to ensure the assay structure is optimised for this alternative approach to SERS detection of proteins.

Ultimately this work exploits the versatile use of DPN, using the technique in both a direct and indirect way to influence the future of biosensing. It is hoped that work emcompassed in this thesis shows the new alternative opportunities that researchers have with DPN and that it can be used beyond a proof of concept technique and could eventually be implemented in various commercial biosensing applications.

8. References

---

1. C. N. LaFratta and D. R. Walt, *Chem. Rev.*, 2008, **108**, 614.
2. T. O. Joos, M. Schrenk, P. Hopfl, K. Kroger, U. Chowdhury, D. Stoll, D. Schorner, M. Durr, K. Herick, S. Rupp, K. Sohn and H. Hammerle, *Electrophoresis*, 2000, **21**, 2641.
3. S. Lee, Y. H. Ko, H. Jung, J. D. Kim, J. M. Song, J. Chooe, S. K. Eo and S. H. Kang, *Talanta*, 2009, **78**, 608.
4. A. Sassolas, B. D. Leca-Bouvier and L. J. Blum, *Chem. Rev.*, 2008, **108**, 109.
5. C. A. K. Borrebaeck and C. Wingren, *J. Proteomics*, 2009, **72**, 928.
6. M. Cretich, F. Damin, G. Pirri and M. Chiari, *Biomol. Eng.*, 2006, **23**, 77.
7. S. Nishizuka, *Eur. J. Cancer*, 2006, **42**, 1273.
8. M. A. Walling and J. R. E. Shepard, *Chem. Soc. Rev.*, 2011, **40**, 4049.
9. S. Donthu, Z. X. Pan, B. Myers, G. Shekhawat, N. G. Wu and V. Dravid, *Nano Lett.*, 2005, **5**, 1710.
10. S. M. Huang, L. M. Dai and A. W. H. Mau, *Adv. Mater.*, 2002, **14**, 1140.
11. S. Q. Sun and G. J. Leggett, *Nano Lett.*, 2002, **2**, 1223.
12. H. Li, J. Zhang, X. Zhou, G. Lu, Z. Yin, G. Li, T. Wu, F. Boey, S. S. Venkatraman and H. Zhang, *Langmuir*, 2010, **26**, 5603.
13. J. C. Soo, J. Zhang, Q. He, S. Agarwal, H. Li, H. Zhang and P. Chen, *Integr. Biol.*, 2010, **2**, 250.
14. T. H. Patwa, C. Li, L. M. Poisson, H. Y. Kim, M. Pal, D. Ghosh, D. M. Simeone and D. M. Lubman, *Electrophoresis*, 2009, **30**, 2215.
15. L. R. Allain, D. N. Stratis-Cullum and T. Vo-Dinh, *Anal. Chim. Acta*, 2004, **518**, 77.
16. R. D. Piner, J. Zhu, F. Xu, S. H. Hong and C. A. Mirkin, *Science*, 1999, **283**, 661.

17. H. Jung, R. Kulkarni and C. P. Collier, *J. Am. Chem. Soc.*, 2003, **125**, 12096.

18. K. B. Lee, J. H. Lim and C. A. Mirkin, *J. Am. Chem. Soc.*, 2003, **125**, 5588.

19. W. M. Wang, R. M. Stoltenberg, S. Liu and Z. Bao, *ACS Nano*, 2008, **2**, 2135.

20. A. Hernandez-Santana, E. Irvine, K. Faulds and D. Graham, *Chem. Sci.*, 2011, **2**, 211.

21. S. Rozhok, R. Piner and C. A. Mirkin, *J. Phys. Chem. B.*, 2003, **107**, 751.

22. S. H. Hong, J. Zhu and C. A. Mirkin, *Science*, 1999, **286**, 523.

23. D. Nyamjav and A. Ivanisevic, *Adv. Mater.*, 2003, **15**, 1805.

24. R. A. Vega, D. Maspoch, K. Salaita and C. A. Mirkin, *Angew. Chem. Int. Ed.*, 2005, **44**, 6013.

25. H. Z. Jiang and S. I. Stupp, *Langmuir*, 2005, **21**, 5242.

26. J. M. Curran, R. Stokes, E. Irvine, D. Graham, N. A. Amro, R. G. Sanedrin, H. Jamil and J. A. Hunt, *Lab Chip*, 2010, **10**, 1662.

27. P. Samori, *Scanning Probe Microscopies Beyond Imaging: Manipulation of Molecules and Nanostructures* Wiley, 2006, pp. 141-171; 315-353.

28. I. Kopf, C. Grunwald, E. Bruendermann, L. Casalis, G. Scoles and M. Havenith, *J. Phys. Chem. C,* 2010**, 114***,* 1306.

29. L. G. Rosa, J. Jiang, O. V. Lima, J. Xiao, E. Utreras, P. A. Dowben and L. Tan, *Mater. Lett.,* 2009**, 63***,* 961.

30. S. Xu and G. Y. Liu, *Langmuir,* 1997**, 13** 127.

31. L. G. Rosa and J. Liang, *J. Phys.: Condens. Matter,* 2009**, 21**, 48.

32. S. Q. Sun, K. S. L Chong and G. J. Leggett, *J. Am. Chem. Soc.* 2002**, 124**, 2414.

33. N. P. Reynolds, J. D. Tucker, P. A. Davison, J. A. Timney, C. N. Hunter and G. J. Leggett, *J. Am. Chem. Soc.* 2009**, 131**, 896.

34. S. A. A. Ahmad, L. S. Wong, E. Ul-Haq, J. K. Hobbs, G. J. Leggett and J. Micklefield, *J. Am. Chem. Soc.* 2011**, 133**, 2749.

35. S. Sun and G. J. Leggett, *Nano Letters,* 2004, **4**, 1381.

36. G. Binnig, C. F. Quate and C. Gerber, *Phys. Rev. Lett.*, 1986, **56**, 930.

37. S. Alexander, L. Hellemans, O. Marti, J. Schneir, V. Elings, P. K. Hansma, M. Longmire and J. Gurley, *J. Appl. Phys.*, 1989, **65**, 164.

38. D. Rugar and P. Hansma, *Phys. Today*, 1990, **43**, 23.

39. G. Binnig and H. Rohrer, *IBM J. Res. Dev.*, 2000, **44**, 279.

40. T. R. Albrecht and C. F. Quate, *J Vac. Sci. Technol. A.*, 1988, **6**, 271.

41. O. Marti, B. Drake and P. K. Hansma, *Appl. Phys. Lett.*, 1987, **51**, 484.

42. J. L. Wilbur, H. A. Biebuyck, J. C. Macdonald and G. M. Whitesides, *Langmuir*, 1995, **11**, 825.

43. C. Bustamante and D. Keller, *Phys. Today*, 1995, **48**, 32.

44. J. Tamayo and R. Garcia, *Langmuir*, 1996, **12**, 4430.

45. M. Su, X. G. Liu, S. Y. Li, V. P. Dravid and C. A. Mirkin, *J. Am. Chem. Soc.*, 2002, **124**, 1560.

46. D. L. Wilson, R. Martin, S. Hong, M. Cronin-Golomb, C. A. Mirkin and D. L. Kaplan, *Proc. Natl. Acad. Sci. USA.*, 2001, **98**, 13660.

47. L. M. Demers, D. S. Ginger, S. J. Park, Z. Li, S. W. Chung and C. A. Mirkin, *Science*, 2002, **296**, 1836.

48. J. H. Lim, D. S. Ginger, K. B. Lee, J. Heo, J. M. Nam and C. A. Mirkin, *Angew. Chem. Int. Ed.*, 2003, **42**, 2309.

49. H. Jung, C. K. Dalal, S. Kuntz, R. Shah and C. P. Collier, *Nano Lett.*, 2004, **4**, 2171.

50. M. Su, M. Aslam, L. Fu, N. Q. Wu and V. P. Dravid, *Appl. Phys. Lett.*, 2004, **84**, 4200.

51. M. Lee, D. K. Kang, H. K. Yang, K. H. Park, S. Y. Choe, C. Kang, S. I. Chang, M. H. Han and I. C. Kang, *Proteomics*, 2006, **6**, 1094.

52. P. E. Sheehan, L. J. Whitman, W. P. King and B. A. Nelson, *Appl. Phys. Lett.*, 2004, **85**, 1589.

53. B. A. Nelson, W. P. King, A. R. Laracuente, P. E. Sheehan and L. J. Whitman, *Appl. Phys. Lett.*, 2006, **88**, 033104.

54. M. Yang, P. E. Sheehan, W. P. King and L. J. Whitman, *J. Am. Chem. Soc.*, 2006, **128**, 6774.

55. W. K. Lee, L. J. Whitman, J. Lee, W. P. King and P. E. Sheehan, *Soft Matter*, 2008, **4**, 1844.

56. Y. Li, B. W. Maynor and J. Liu, *J. Am. Chem. Soc.*, 2001, **123**, 2105.

57. Z. Zheng, M. Yang and B. Zhang, *J. Phys. Chem. C.*, 2010, **114**, 19220.

58. J. W. Jang, R. G. Sanedrin, D. Maspoch, S. Hwang, T. Fujigaya, Y. M. Jeon, R. A. Vega, X. Chen and C. A. Mirkin, *Nano Lett.*, 2008, **8**, 1451.

59. B. Garipcan, J. Winters, J. S. Atchison, M. D. Cathell, J. D. Schiffman, O. D. Leaffer, S. S. Nonnenmann, C. L. Schauer, E. Piskin, B. Nabet and J. E. Spanier, *Langmuir*, 2008, **24**, 8944.

60. L. Ding, Y. Li, H. B. Chu, X. M. Li and J. Liu, *J. Phys. Chem. B.*, 2005, **109**, 22337.

61. G. Agarwal, R. R. Naik and M. O. Stone, *J. Am. Chem. Soc.*, 2003, **125**, 7408.

62. S. H. Hong and C. A. Mirkin, *Science*, 2000, **288**, 1808.

63. G. MacBeath and S. L. Schreiber, *Science*, 2000, **289**, 1760.

64. M. Zhang, D. Bullen, S. W. Chung, S. Hong, K. S. Ryu, Z. F. Fan, C. A. Mirkin and C. Liu, *Nanotechnology*, 2002, **13**, 212.

65. K. Salaita, Y. H. Wang, J. Fragala, R. A. Vega, C. Liu and C. A. Mirkin, *Angew. Chem. Int. Ed.*, 2006, **45**, 7220.

66. K. Salaita, S. W. Lee, X. F. Wang, L. Huang, T. M. Dellinger, C. Liu and C. A. Mirkin, *Small*, 2005, **1**, 940.

67. A. Martinez-Otero, P. Gonzalez-Monje, D. Maspoch, J. Hernando and D. Ruiz-Molina, *Chem. Commun.*, 2011, **47**, 6864.

68. D. Bullen, S. W. Chung, X. F. Wang, J. Zou, C. A. Mirkin and C. Liu, *Appl. Phys. Lett.*, 2004, **84**, 789.

69. X. F. Wang, D. A. Bullen, J. Zou, C. Liu and C. A. Mirkin, *J. Vac. Sci. Technol. B.*, 2004, **22**, 2563.

70. J. Haaheim, R. Eby, M. Nelson, J. Fragala, B. Rosner, H. Zhang and G. Athas, *Ultramicroscopy*, 2005, **103**, 117.

71. http://www.nanoink.net.

72. J. Stettner, P. Frank, T. Griesser, G. Trimmel, R. Schennach, E. Gilli and A. Winkler, *Langmuir*, 2009, **25**, 1427.

73. J. Hyun, S. J. Ahn, W. K. Lee, A. Chilkoti and S. Zauscher, *Nano Lett.*, 2002, **2**, 1203.

74. R. Valiokas, A. Vaitekonis, G. Klenkar, G. Trinkunas and B. Liedberg, *Langmuir*, 2006, **22**, 3456.

75. R. McKendry, W. T. S. Huck, B. Weeks, M. Florini, C. Abell and T. Rayment, *Nano Lett.*, 2002, **2**, 713.

76. (a) V. Bindu and T. Pradeep, *Vacuum*, 1998, **49**, 63. (b) C. D. Bain, E. B. Troughton, Y. T. Tao, J. Evall, G. M. Whitesides and R. G. Nuzzo, *J. Am. Chem. Soc.*, 1989, **111**, 321.

77. P. V. Schwartz, *Langmuir*, 2002, **18**, 4041.

78. J. Y. Jang, G. C. Schatz and M. A. Ratner, *J. Chem. Phys.*, 2002, **116**, 3875.

79. E. J. Peterson, B. L. Weeks, J. J. De Yoreo and P. V. Schwartz, *J. Phys Chem. B.*, 2004, **108**, 15206.

80. P. E. Sheehan and L. J. Whitman, *Phys. Rev. Lett.*, 2002, **88**, 156104.

81. B. L. Weeks and J. J. DeYoreo, *J. Phys. Chem. B.*, 2006, **110**, 10231.

82. B. L. Weeks, A. Noy, A. E. Miller and J. J. De Yoreo, *Phys. Rev. Lett.*, 2002, **88**, 255505.

83. L. Huang, Y. H. Chang, J. J. Kakkassery and C. A. Mirkin, *J. Phys. Chem. B.*, 2006, **110**, 20756.

84. K. Salaita, A. Amarnath, D. Maspoch, T. B. Higgins and C. A. Mirkin, *J. Am. Chem. Soc.*, 2005, **127**, 11283.

85. O. A. Nafday and B. L. Weeks, *Langmuir*, 2006, **22**, 10912.

86. L. R. Giam, Y. Wang and C. A. Mirkin, *J. Phys. Chem. A.*, 2009, **113**, 3779.

87. K. Salaita, A. Amarnath, T. B. Higgins and C. A. Mirkin, *Scanning*, 2010, **32**, 9.

88. Y. Cho and A. Ivanisevic, *Langmuir*, 2006, **22**, 8670.

89. S. Li, S. Szegedi, E. Goluch and C. Liu, *Anal. Chem.*, 2008, **80**, 5899.

90. M. Lynch, C. Mosher, J. Huff, S. Nettikadan, J. Johnson and E. Henderson, *Proteomics*, 2004, **4**, 1695.

91. C. C. Wu, H. P. Xu, C. Otto, D. N. Reinhoudt, R. G. H. Lammertink, J. Huskens, V. Subramaniam and A. H. Velders, *J. Am. Chem. Soc.*, 2009, **131**, 7526.

92. S. Turri, L. Torlaj and M. Levi, *Macromol. Rapid Commun.*, 2010, **31**, 1373.

93. Y. H. Shin, S. H. Yun, S. Pyo, Y. Lim, H. J. Yoon, K. Kim, S. Moon, S. W. Lee, Y. G. Park, S.-I. Chang, K.-M. Kim and J.-H. Lim, *Angew. Chem. Int. Ed.*, 2010, **49**, 9689.

94. R. J. Stokes, J. A. Dougan and D. Graham, *Chem. Commun.*, 2008, **44**, 5734.

95. H. T. Wang, O. A. Nafday, J. R. Haaheim, E. Tevaarwerk, N. A. Amro, R. G. Sanedrin, C. Y. Chang, F. Ren and S. J. Pearton, *Appl. Phys. Lett.*, 2008, **93,** 143105.

96. A. J. Senesi, D. I. Rozkiewicz, D. N. Reinhoudt and C. A. Mirkin, *ACS Nano*, 2009, **3**, 2394.

97. J. W. Jang, A. Smetana and P. Stiles, *Scanning*, 2010, **32**, 24.

98. S. C. Hung, O. A. Nafday, J. R. Haaheim, F. Ren, G. C. Chi and S. J. Pearton, *J. Phys. Chem. C.*, 2010, **114**, 9672.

99. Q. Tang, S. Q. Shi, H. T. Huang and L. M. Zhou, *Superlattice. Microst.* 2004, **36**, 21.

100. J. H. Lim and C. A. Mirkin, *Adv. Mater.*, 2002, **14**, 1474

101. A. Hernandez-Santana, A. R. Mackintosh, B. Guilhabert, A. L. Kanibolotsky, M. D. Dawson, P. J. Skabara and D. Graham, *J. Mater. Chem.*, 2011, **21**, 14209.

102. K. S. Salaita, S. W. Lee, D. S. Ginger and C. A. Mirkin, *Nano Lett.*, 2006, **6**, 2493.

103. M. G. Sung, T. Y. Lee, B. Kim, T. H. Kim and S. Hong, *Langmuir*, 2010, **26**, 1507.

104. L. M. Demers, S. J. Park, T. A. Taton, Z. Li and C. A. Mirkin, *Angew. Chem. Int. Ed*, 2001, **40**, 3071.

105. K. B. Lee, S. J. Park, C. A. Mirkin, J. C. Smith and M. Mrksich, *Science*, 2002, **295**, 1702.

106. K. B. Lee, E. Y. Kim, C. A. Mirkin and S. M. Wolinsky, *Nano Lett.*, 2004, **4**, 1869.

107. H. Zhang, K. B. Lee, Z. Li and C. A. Mirkin, *Nanotechnology*, 2003, **14**, 1113.

108. C. Wingren and C. A. K. Borrebaeck, *Drug Discov. Today*, 2007, **12**, 813.

109. S. W. Lee, B. K. Oh, R. G. Sanedrin, K. Salaita, T. Fujigaya and C. A. Mirkin, *Adv. Mater.*, 2006, **18**, 1133.

110. D. P. Lomax, W. T. Roubal, J. D. Moore and L. L. Johnson, *Comp. Biochem. Physiol. Biochem. Mol. Biol.*, 1998, **121**, 425.

111. L. Al-Harthi, G. Marchetti, C. M. Steffens, J. F. Poulin, R. P. Sekaly and A. Landay, *J. Immunol. Methods*, 2000, **237**, 187.

112. S. Laing, A. Hernandez-Santana, J. Sassmannshausen, D. L. Asquith, I. B. McInnes, K. Faulds and D. Graham, *Anal. Chem.*, 2011, **83**, 297.

113. T. Rakickas, M. Gavutis, A. Reichel, J. Piehler, B. Liedberg and R. Valiokas, *Nano Lett.*, 2008, **8**, 3369.

114. M. Hirtz, R. Corso, S. Sekula-Neuner and H. Fuchs, *Langmuir*, 2011, **27**, 11605.

115. S. Lenhert, C. A. Mirkin and H. Fuchs, *Scanning*, 2010, **32**, 15.

116. S. Biswas, M. Hirtz and H. Fuchs, *Small*, 2011, **7**, 2081.

117. J. M. Collins and S. Nettikadan, *Anal. Biochem.*, 2011, **419**, 339.

118. D. Nyamjav, S. Rozhok and R. C. Holz, *Nanotechnology*, 2010, **21**, 235105.

119. P. W. Atkins, *Physical Chemistry*, Third edn., Oxford University Press, 1986.

120. J. W. Borst and A. J. W. G. Visser, *Meas. Sci. Technol.*, 2010, **21**, 102002.

121. J. M. Curran, R. Chen and J. A. Hunt, *Biomaterials*, 2006, **27**, 4783.

122. M. Abo, Y. Urano, K. Hanaoka, T. Terai, T. Komatsu and T. Nagano, *J. Am. Chem. Soc.*, 2011, **133**, 10629.

123. S. Cunningham, J. Q. Gerlach, M. Kane and L. Joshi, *Analyst*, 2010, **135**, 2471.

124. M. K. Wagner, F. Li, J. Li, X.-F. Li and X. C. Le, *Anal. Bioanal. Chem.*, 2010, **397**, 3213.

125. I. T. Li, E. Pham and K. Truong, *Biotech. Lett.*, 2006, **28**, 1971.

126. J. C. Pickup, F. Hussain, N. D. Evans, O. J. Rolinski and D. J. S. Birch, *Biosensors. Bioelectron.*, 2005, **20**, 2555.

127. H. Wang, E. Nakata and I. Hamachi, *Chembiochem*, 2009, **10**, 2560.

128. P. Ellmark, S. Ghatnekar-Nilsson, A. Meister, H. Heinzelmann, L. Montelius, C. Wingren and C. A. K. Borrebaeck, *Proteomics*, 2009, **9**, 5406.

129. E. Smith and G. Dent, *Modern Raman Spectroscopy: A Practical Approach*, Wiley, Chichester, West Sussex, 2005, **Chp. 4**, p. 93, **Chp. 5**, p. 113.

130. G. Sabatte, R. Keir, M. Lawlor, M. Black, D. Graham and W. E. Smith, *Anal. Chem.*, 2008, **80**, 2351.

131. R. J. Stokes, A. Macaskill, P. J. Lundahl, W. E. Smith, K. Faulds and D. Graham, *Small*, 2007, **3**, 1593.

132. F. McKenzie and D. Graham, *Chem. Commun.*, 2009, **38**, 5757.

133. A. MacAskill, D. Crawford, D. Graham and K. Faulds, *Anal. Chem.*, 2009, **81**, 8134.

134. R. Narayanan, R. J. Lipert and M. D. Porter, *Anal. Chem.*, 2008, **80**, 2265.

135. Y. C. Cao, R. C. Jin, J. M. Nam, C. S. Thaxton and C. A. Mirkin, *J. Am. Chem. Soc.*, 2003, **125**, 14676.

136. F. M. Campbell, A. Ingram, P. Monaghan, J. Cooper, N. Sattar, P. D. Eckersall and D. Graham, *Analyst*, 2008, **133**, 1355.

137. C. A. R. Auchinvole, P. Richardson, C. McGuinnes, V. Mallikarjun, K. Donaldson, H. McNab and C. J. Campbell, *ACS Nano*, 2012, **6**, 888.

138. J. Ando, K. Fujita, N. I. Smith and S. Kawata, *Nano Lett.*, 2011, **11**, 5344.

139. Z. Zhang, Y. Wen, Y. Ma, J. Luo, L. Jiang and Y. Song, *Chem. Commun.*, 2011, **47**, 7407.

140. K. Faulds, R. Jarvis, W. E. Smith, D. Graham and R. Goodacre, *Analyst*, 2008, **133**, 1505.

141. http://www.microscopyu.com/articles/stereomicroscopy/stereodarkfield.html.

142. Y. Li, C. Jing, L. Zhang and Y. T. Long, *Chem. Soc. Rev.*, 2012, **41**, 632.

143. C. S. Huang, V. Chaudhery, A. Pokhriyal, S. George, J. Polans, M. Lu, R. Tan, R. C. Zangar and B. T. Cunningham, *Anal. Chem.*, 2012**, 84**, 1126.

144. A. Mills, K. Lawrie, J. Bardin, A. Apedaile, G. A. Skinner, and C. O'Rourke, *Analyst,* 2012**, 137**, 106.

145. H. Ben-Yoav, P. H. Dykstra, W. E. Bentley and R. Ghodssi, *Biosensors Bioelectron.*, 2012**, 38**, 114.

146. G. J. Worsley, S. L. Attree, J. E. Noble, A. M. Horgan, *Biosensors Bioelectron.*, 2012**, 34**, 215.

147. H. Nagasaki, M. Watanabe, N. Komatsu, T. Kaneko, J. Y. Dube, T. Kajita, Y. Saitoh and Y. Ohta, *Clinical Chem.* 1999**, 45**, 486.

148. J. Turkevich, P. C. Stevenson and J. Hillier, *Discuss. Faraday Soc.*, 1951, **11**, 55.

149. P. C. Lee and D. Meisel, *J. Phys. Chem.*, 1982, **86**, 3391.

150. J. P. Bannantine, M. L. Paustian, W. R. Waters, J. R. Stabel, M. V. Palmer, L. L. Li and V. Kapur, *Infect. Immun.*, 2008, **76**, 739.

151. N. Karoonuthaisiri, R. Charlermroj, U. Uawisetwathana, P. Luxananil, K. Kirtikara and O. Gajanandana, *Biosens. Bioelectron.*, 2009, **24**, 1641.

152. M. S. Islam, H. G. Lee, J. Choo, J. M. Song and S. H. Kang, *Talanta*, 2010, **81**, 1402.

153. S. L. Seurynck-Servoss, A. M. White, C. L. Baird, K. D. Rodland and R. C. Zangar, *Anal. Biochem.*, 2007, **371**, 105.

154. I. Balboni, C. Limb, J. D. Tenenbaum and P. J. Utz, *Proteomics*, 2008, **8**, 3443.

155. E. Kopf, D. Shnitzer and D. Zharhary, *Proteomics*, 2005, **5**, 2412.

156. B. Kersten, T. Feilner, A. Kramer, S. Wehrmeyer, A. Possling, I. Witt, M. I. Zanor, R. Stracke, A. Lueking, J. Kreutzberger, H. Lehrach and D. J. Cahill, *Plant Mol. Biol.*, 2003, **52**, 999.

157. S. Oehler, R. Alex and A. Barker, *Anal. Biochem.*, 1999, **268**, 330-336.

158. J. M. Gershoni and G. E. Palade, *Anal. Biochem.*, 1983, **131**, 1.

159. N. R. Thirumalapura, R. J. Morton, A. Ramachandran and J. R. Malayer, *J. Immunol. Methods*, 2005, **298**, 73.

160. U. H. Stenman, J. Leinonen, H. Alfthan, S. Rannikko, K. Tuhkanen and O. Alfthan, *Cancer Res.*, 1991, **51**, 222.

161. D. S. Grubisha, R. J. Lipert, H. Y. Park, J. Driskell and M. D. Porter, *Anal. Chem.*, 2003, **75**, 5936.

162. T. Steuber, P. Helo and H. Lilja, *World J. Urol.*, 2007, **25**, 111.

163. R. Riffenburgh and C. L. Amling, *Prostate Cancer Prostatic Dis.*, 2003, **6**, 39.

164. W. J. Ellis, R. L. Vessella, J. L. Noteboom, P. H. Lange, R. L. Wolfert and H. G. Rittenhouse, *Urology*, 1997, **50**, 573.

165. Y. F. Chang, S. H. Hung, Y. J. Lee, R. C. Chen, L. C. Su, C. S. Lai and C. Chou, *Anal. Chem.*, 2011, **83**, 5324.

166. A. Gokarna, L. H. Jin, J. S. Hwang, Y. H. Cho, Y. T. Lim, B. H. Chung, S. H. Youn, D. S. Choi and J. H. Lim, *Proteomics*, 2008, **8**, 1809.

167. S. Xu, Y. Liu, T. Wang and J. Li, *Anal. Chem.*, 2011, **83**, 3817.

168. L. Huang, G. Reekmans, D. Saerens, J. M. Friedt, F. Frederix, L. Francis, S. Muyldermans, A. Campitelli and C. Van Hoof, *Biosens. Bioelectron.*, 2005, **21**, 483.

169. M. Yue, J. C. Stachowiak, H. Lin, R. Datar, R. Cote and A. Majumdar, *Nano Lett.*, 2008, **8**, 520.

170. G. H. Wu, R. H. Datar, K. M. Hansen, T. Thundat, R. J. Cote and A. Majumdar, *Nat. Biotechnol.*, 2001, **19**, 856.

171. K. J. Yoon, H. K. Seo, H. Hwang, D. Pyo, I. Y. Eom, J. H. Hahn and Y. M. Jung, *Bull. Korean Chem. Soc*, 2010, **31**, 1215.

172. R. Stevenson, A. Ingram, H. Leung, D. C. McMillan and D. Graham, *Analyst*, 2009, **134**, 842.

173. J.-F. Masson, K. F. Gibson and A. Provencher-Girard, *J. Phys. Chem. C.*, 2010, **114**, 22406.

174. M. E. Abdelsalam, *Cent. Eur. J. Chem.*, 2009, **7**, 446.

175. (a) G. McAnally, C. McLaughlin, R. Brown, D. Robson, K. Faulds, D. Tackley, W. Smith and D. Graham, *Analyst*, 2002, **127**, 838; (b) A. Enright, L. Fruk, A. Grondin, C. McHugh, W. Smith and D. Graham, *Analyst*, 2004, **129**, 975.

176. C. McHugh, F. Docherty, D. Graham and W. Smith, *Analyst*, 2004, **129**, 69.

177. A. Ingram, K. Stirling, K. Faulds, B. Moore and D. Graham, *Org. Biomol. Chem.*, 2006, **4**, 2869.

178. A. Ingram, L. Byers, K. Faulds, B. Moore and D. Graham, *J. Am. Chem. Soc.*, 2008, **130**, 11846.

179. F. McKenzie, A. Ingram, R. Stokes and D. Graham, *Analyst*, 2009, **134**, 549.

180. D. Pesach and A. Marmur, *Langmuir*, 1987, **3**, 519.

181. C. V. Sternling and L. E. Scriven, *AIChE J.*, 1959, **5**, 514.

182. H. Hu and R. G. Larson, *J. Phys. Chem. B.*, 2006, **110**, 7090.

183. S. Li, L. Liu and J. Hu, *Spectrochim. Acta A. Mol. Biomol. Spectrosc.*, 2012, **86**, 533.

184. W. W. Yu and I. M. White, *Analyst*, 2012, **137**, 1168.

185. J. D. Caldwell, O. Glembocki, F. J. Bezares, N. D. Bassim, R. W. Rendell, M. Feygelson, M. Ukaegbu, R. Kasica, L. Shirey and C. Hosten, *ACS Nano*, 2011, **5**, 4046.

186. A. J. Chung, Y. S. Huh and D. Erickson, *Nanoscale*, 2011, **3**, 2903.

187. F. Yaghobian, T. Weimann, B. Guettler and R. Stosch, *Lab Chip*, 2011, **11**, 2955.

188. J. P. Camden, J. A. Dieringer, J. Zhao and R. P. Van Duyne, *Acc. Chem. Res.*, 2008, **41**, 1653.

189. S. Sun, D. Thompson, U. Schmidt, D. Graham and G. J. Leggett, *Chem. Commun.*, 2010, **46**, 5292.

190. C. W. Chang, J. D. Liao, A. L. Shiau and C. K. Yao, *Sens. Actuators B. Chem.*, 2011, **156**, 471.

191. W. Xie, P. Qiu and C. Mao, *J. Mater. Chem.*, 2011, **21**, 5190.

192. J. Ferreira, F. S. Teixeira, A. R. Zanatta, M. C. Salvadori, R. Gordon and O. N. Oliveira, Jr., *Phys. Chem. Chem. Phys.*, 2012, **14**, 2050.

193. X. G. Hu, W. L. Cheng, T. Wang, Y. L. Wang, E. K. Wang and S. J. Dong, *J. Phys. Chem. B.*, 2005, **109**, 19385.

194. J. M. Oran, R. J. Hinde, N. Abu Hatab, S. T. Retterer and M. J. Sepaniak, *J. Raman Spectrosc.*, 2008, **39**, 1811.

195. S. Krishnamoorthy, S. Krishnan, P. Thoniyot and H. Y. Low, *ACS Appl. Mat. Interfaces*, 2011, **3**, 1033.

196. W. Wu, M. Hu, F. S. Ou, Z. Li and R. S. Williams, *Nanotechnology*, 2010, **21**, 255502.

197. J. F. Masson, M. P. Murray-Methot and L. S. Live, *Analyst*, 2010, **135**, 1483.

198. E. M. Hicks, O. Lyandres, W. P. Hall, S. Zou, M. R. Glucksberg and R. P. Van Duyne, *J. Phys. Chem. C.*, 2007, **111**, 4116.

199. D. A. Weinberger, S. G. Hong, C. A. Mirkin, B. W. Wessels and T. B. Higgins, *Adv. Mater.*, 2000, **12**, 1600.

200. H. Zhang, S. W. Chung and C. A. Mirkin, *Nano Lett.*, 2003, **3**, 43.

201. H. Zhang and C. A. Mirkin, *Chem. Mater.*, 2004, **16**, 1480.

202. I. A. Larmour and D. Graham, *Analyst*, 2011, **136**, 3831.

203. T. Chung, S. Y. Lee, E. Y. Song, H. Chun and B. Lee, *Sensors*, 2011, **11**, 10907.

204. E. Petryayeva and U. J. Krull, *Anal. Chim. Acta*, 2011, **706**, 8.

205. K. F. Gibson, D. Correia-Ledo, M. Couture, D. Graham and J. F. Masson, *Chem. Commun.*, 2011, **47**, 3404.

206. R. Tubbs, J. Pettay, R. Powell, D. G. Hicks, P. Roche, W. Powell, T. Grogan and J. E. Hainfeld, *Appl. Immunohistochem. Mol. Morphol.*, 2005, **13**, 371.

207. R. Tubbs, J. Pettay, D. Hicks, M. Skacel, R. Powell, T. Grogan and J. Hainfeld, *J. Mol. Histol.*, 2004, **35**, 589.

208. R. Moller, R. D. Powell, J. F. Hainfeld and W. Fritzsche, *Nano Lett.*, 2005, **5**, 1475.

209. K. K. Hering, R. Moeller, W. Fritzsche and J. Popp, *Chemphyschem*, 2008, **9**, 867.

210. (a) S. K. Saha and M. L. Culpepper, *App. Phys. Lett.*, 2010, **96**, 243105; (b) S. K. Saha and M. L. Culpepper, *J. Phys. Chem. C.*, 2010, **114**, 15364.

211. (a) J. Y. Jang, S. H. Hong, G. C. Schatz and M. A. Ratner, *J. Chem. Phys.*, 2001, **115**, 2721; (b) H. Kim and J. Jang, *J. Phys. Chem. A.*, 2009, **113**, 4313; (c) D. M. Heo, M. Yang, H. Kim, L. C. Saha and J. Jang, *J. Phys. Chem. C.*, 2009, **113**, 13813.

Appendix: Publications

EDGE ARTICLE www.rsc.org/chemicalscience | Chemical Science

Rapid prototyping of poly(dimethoxysiloxane) dot arrays by dip-pen nanolithography†

Aaron Hernandez-Santana, Eleanore Irvine, Karen Faulds and Duncan Graham*

Received 9th August 2010, Accepted 1st November 2010
DOI: 10.1039/c0sc00420k

We report the first direct patterning of elastomeric PDMS structures by dip-pen nanolithography (DPN). This method involves the use of a cantilever tip to transfer a PDMS ink onto a silicon dioxide surface to create dot array patterns which are then cross-linked and bonded irreversibly to the substrate. The chemical composition of the PDMS structures deposited by DPN was characterised by Raman microspectroscopy to provide an insight into the ink transfer process. This technique offers a significant advance in the ability to rapidly and easily produce programmable surface features from a widely used polymer for use in a variety of applications.

Introduction

Poly(dimethoxysiloxane) (PDMS) is one of the most widely used silicon based organic polymers. In fact, it is a common component in lubricants, sealants, foodstuffs, implants, and health and beauty products.[1] PDMS is relatively inexpensive, readily available, nontoxic, chemically inert, transparent and odourless. Soft-lithography techniques such as microcontact printing (μCP) employ PDMS to create micro- and nanoscale structures.[2] It is usually patterned by a moulding process and used as a master for pattern transfer. Firstly, a mask is generated using photo or electron beam lithography, which can be expensive and time-consuming. PDMS is then poured over the master, cured and removed to obtain a negative structure. Unlike photoresists, PDMS may be cured at room temperature and does not require ultraviolet light to cross-link. The patterned elastomeric stamp can then be used to transfer chemical inks onto a surface. PDMS is also a popular material of choice in the fabrication of microfluidic systems for flow delivery and biomedical diagnostics.[3]

Dip-pen nanolithography (DPN) is a versatile and powerful nano and micro fabrication technique capable of patterning a wide range of materials on an equally extensive variety of surfaces.[4] A number of review articles have been reported in this field of research.[5,6] In this technique, a sharp cantilever tip (AFM tip) is used to transport chemical "inks" when placed in contact with a suitable surface. However, this is not strictly a requisite and close-contact (tapping mode) has been proposed as a method for material deposition.[7] In the context of DPN, PDMS has been used to develop techniques such as scanning probe contact printing (SP-CP), where a commercial scanning probe microscope (SPM) with an integrated elastomeric PDMS tip was used to transfer chemicals onto a substrate.[8] Further work by Mirkin and co-workers led to the development of polymer-pen lithography (PPL) in which a 2D array containing thousands to millions of elastomeric tips are used to pattern surfaces in a high-throughput manner.[9]

In this work, however, we have used DPN to produce the first direct patterning of a PDMS-based ink onto silicon dioxide surfaces. Once patterned, the structures are cured and bonded irreversibly to the substrate. PDMS has been printed on paper using a dot plotter to produce hydrophilic barriers as channels for fluid containment but the minimum size of the printed features was ~1 mm.[10] The direct-write method of DPN allows the fast and controlled fabrication of PDMS structures of micrometer dimensions with piezo-controlled placement capability and registry.

Results and discussion

One of the key initial steps in our method involved the formulation of a suitable PDMS ink composition for use in DPN. PDMS is normally supplied as a two-part kit, composed of a pre-polymer base and a curing agent which are then mixed in a 10 : 1 ratio (wt/wt), respectively. Once combined, the mixture has a pot-life (time taken for viscosity to double) of approximately 2 h. Nevertheless, this mixture will take ~48 h at room temperature to form a solid crosslinked polymer and will remain in the liquid state throughout the patterning process.

The DPN tip may be coated with a "chemical ink" in a variety of ways including dip-coating, vapour coating, and through the use of microfluidic inkwells. We opted for the latter approach for a number of practical reasons including the ability to coat different tips with multiple inks at once when using a one dimensional (1D) 12-tip array and the possibility to re-ink the tips when required.[11] The main drawback of this method was that PDMS is a viscous liquid, with a viscosity resembling that of a syrup (3900 cP), which prevented it from flowing in the microfluidic channels. However, it can be easily diluted in hexane and other organic solvents in order to decrease its viscosity.[12] Hexane is considered to be a good, compatible solvent for diluting the PDMS prepolymer in applications such as spin casting of thin films.[13,14,15] We determined the appropriate dilution of the PDMS mixture in hexane by varying their proportions. Different PDMS dilutions 0–40% hexane (wt/wt) were loaded into the inkwells and the most consistent results were

---

Centre for Molecular Nanometrology, WestCHEM, Department of Pure and Applied Chemistry, University of Strathclyde, 295 Cathedral Street, Glasgow, G1 1XL, UK. E-mail: duncan.graham@strath.ac.uk; Fax: +44 (0)141 548 4787; Tel: +44 (0)141 548 4701

† Electronic supplementary information (ESI) available: Information on the patterning of PDMS lines. See DOI: 10.1039/c0sc00420k

obtained when the base PDMS mixture was diluted with hexane at 30% (wt/wt). This ink formulation was used throughout our experiments and was observed to remain "wet" inside the microfluidic inkwell during the patterning process.

The fabrication process for PDMS structures deposited by DPN is illustrated in Fig. 1. The tip was first coated with the PDMS ink by submerging it into the inkwell for five seconds, after which the polymer was immediately patterned on a silicon dioxide surface. Tip-surface position was controlled by computer software and a piezoelectric (x-y-z) scanner stage, which allows the fabrication of custom designed patterns.

Unlike other traditional DPN-based experiments found in the literature, patterning was performed without force-feedback (AFM), where a laser reflecting off the probe ensures that constant force is applied with respect to the substrate surface. Tip-surface contact and array levelling was accomplished through visual observation of the tip deflection, characterised by a sharp change in tip reflectivity upon contact with the surface. Under this condition, the DPN deposition process is regarded to be effectively force independent.[16]

The PDMS arrays were heat cured at 60 °C for one hour to finalise the crosslinking process. Once cured, PDMS can be easily bonded either reversibly or irreversibly to a range of materials including glass, silicon and PDMS itself.[17] When exposed to an oxygen plasma, Si–CH_3 groups along the PDMS backbone are transformed into hydrophilic Si–OH groups by the reactive oxygen species. However, hydrophobicity is recovered soon after when placed back in air.[18] If desired, surface silanisation may be achieved by immediately exposing the silanol surface to alkoxysilanes containing functional headgroups to obtain surface properties and functionalities of choice.[17] Oxygen-plasma treatment of PDMS can lead to the formation of a smooth oxidised surface layer of >100 nm in thickness[19] and we used this method to permanently bond the PDMS structures patterned by DPN to the underlying silicon dioxide substrate. The bonding mechanism is poorly understood but it is considered to involve breaking of bonds on each surface during treatment followed by the formation of Si–O–Si bonds.

DPN was used to pattern custom designed PDMS spot arrays with excellent control and high throughput (Fig. 2). The contact time between the PDMS coated tip and the substrate surface, also known as the dwell time, was alternated between 0.25 and 0.1 s to produce the features illustrated in Fig. 2 (b).

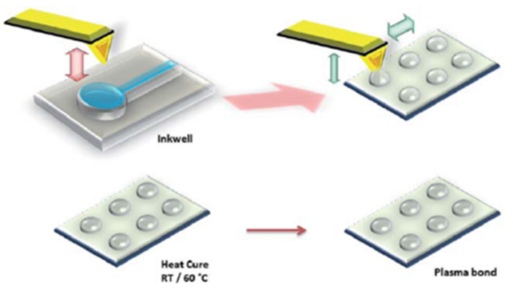

Fig. 1 Schematic representation of the DPN procedure used to pattern PDMS on a silicon dioxide substrate.

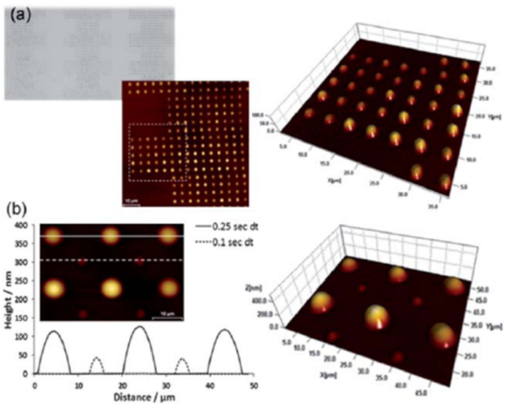

Fig. 2 (a) Optical image and overlaid AFM topography images of programmable patterning of PDMS structures by DPN. (b) Overlaid height profile of PDMS spots created by using alternating dwell times of 0.25 and 0.1 s (first two rows). *Inset and adjacent image*: AFM topography image of PDMS spots used in (b).

Close-contact AFM analysis was used to determine the size of the features, which showed a difference in both spot diameter and feature height depending on the dwell time used, with the longer dwell time producing larger features. AFM topographical analysis did not show delamination or deformation at the edges of the features after oxygen-plasma treatment, suggesting successful bonding to the underlying substrate.

The deposition process was examined in more detail by systematically varying the dwell time from 0.1 to 1 s. Ink transport is assumed to occur due to 2-D surface diffusion from the tip to the substrate, where the dot diameter of the features should follow a square root dependence on dwell time.[20] Fig. 3 shows plots of changes in spot diameter and height as a function of dwell time (plotted as $\sqrt{t}$) from AFM analysis data. The smallest features achieved by this method were 2.7 µm in diameter and only 18.6 nm in height when using a dwell time of 0.1 s. The deposition process follows a linear increase in spot diameter for dwell times up to 0.75 s but did not seem to increase with longer dwell times. This non-linear phenomenon at longer dwell times has been observed for other liquid inks used in DPN, where further contact time with the surface will not increase feature size.[21,22] We observed a linear increase ($R^2 = 0.99$) in feature height for the dwell time range used in this study. The largest features obtained in this study produced features of about 13.96 µm in diameter and 376.4 nm in height at 1 s dwell time. We have shown that it is effectively possible to generate PDMS features with a range of dimensions (2.7–13.9 µm diameter, 18.6–376.4 nm height) by simply varying the tip-substrate contact time. Furthermore, the use of 1D arrays containing 12 individual tips makes it possible to pattern large areas in a very short period of time.

Traditionally, DPN experiments have been centred on the patterning of thiols on Au surfaces. This combination of ink-surface is characterised by chemisorption of the thiol molecules on the Au surface to form Au–S bonds. Mercaptohexadecanoic

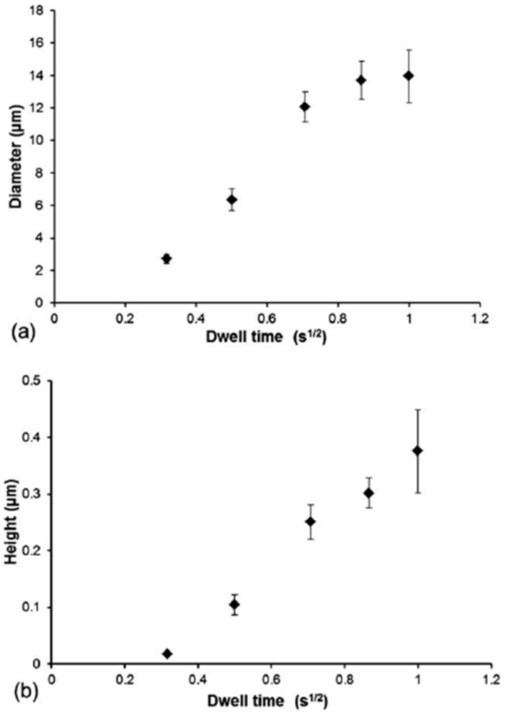

Fig. 3 (a) Plot of dwell time *vs.* spot diameter and (b) plot of dwell time *vs.* feature height.

acid (MHA) and octadecanethiol (ODT) are common examples of alkanethiols that have been studied under ambient conditions.[20] Unlike the liquid ink used in this study, the ink is chemisorbed onto the tip in a dry state by dip-coating or vapour coating. It has been suggested that the water meniscus found at the tip-surface interface is then used as a medium for ink transport, where the ink deposition rate is influenced by parameters such as humidity and temperature.[23,24] In this regard, some studies suggest that ink transfer is related to the solubility of the ink in water.[25] However, the transport rate of MHA and ODT as model molecular inks was examined under atmospheres of different organic vapours and it was found that this increased deposition rate and feature size by up to one order of magnitude.[26] This suggests that the exact mechanism of ink transport is still not fully understood and that other mechanisms can take place apart from bulk meniscus transfer. A number of models have been proposed but unfortunately they have been centred almost exclusively on thiol/Au systems involving a water meniscus.[27,28]

Several examples in literature have used aqueous based additives such as Tween-20,[29] glycerol,[21] agarose,[22] poly(ethylene glycol),[30] to carry biomolecules and nanomaterials. The role of these additives range from preventing biomolecule denaturation to increasing the wettability of the substrate and the viscosity of the ink formulation. Alternatively, the surface properties of the cantilever tip itself may be chemically modified to control transfer of materials.[31] The PDMS ink used in this study is already in the liquid phase and is immiscible with water, so this process might not require a water meniscus for transport. PDMS is hydrophobic and viscous so this facilitates ink adsorption onto the hydrophobic silicon nitride tip. The ink transfer behaviour of the PDMS ink appears to be in relative agreement with other viscous liquid inks reported in literature, where ink transfer seems to be dominated at two key points of the writing process: (a) wetting/loading of the tip with the ink, (b) transfer of the ink from the tip onto the substrate surface. It has been recognized that feature size of liquid inks deposited by DPN is dictated by factors such as physisorption (unlike thiols on Au where chemisorption is involved) and surface tension between the ink and the substrate surface.[21,32] For instance, a non-wetting surface can present an additional activation barrier for ink transport. The use of surfactants as additives in ink formulations provide a means of controlling ink transfer by increasing the wettability of the substrate.[29] Viscosity plays an important role in the DPN process of various liquid inks.[21,22,33] Studies based on thiol inks patterned on Au by DPN have shown that the ink transport properties can be greatly affected by the hydrophobicity of the substrate. For instance, ink transport of ODT deposited over an existing MHA layer was almost twice as fast as when compared to the bare gold surface.[34] Although we did not carry out an extensive study of different surfaces, we support that the surface properties of the substrate will play an important role in dictating liquid PDMS ink transport and ultimately feature size.

In most cases, the actual composition and relative concentrations of the components present in the bulk ink preparation compared to that of the ink ultimately deposited on the substrate is unknown. When patterning binary mixtures of MHA and ODT alkanethiols, phase separation has been reported, where the more hydrophilic alkanethiol always forms the interior phase, while the hydrophobic alkanethiol will form the outer phase.[35] This report described phase separation at the substrate surface but this is also likely to occur at the liquid-tip interface during the tip coating procedure. In order to establish whether phase separation of the different PDMS ink components occurred when using DPN as the deposition method, a small drop (∼1 μL) of the same PDMS ink formulation was placed with a micropipette onto the silicon dioxide surface. The droplet was then cured and bonded to the substrate in the same manner as done for the DPN-based arrays. Raman spectroscopy was our chosen method of chemical analysis.

Raman spectroscopy is a non-invasive method of chemical analysis that enables real-time reaction monitoring and characterisation of compounds.[36] In a typical measurement, the sample is illuminated with a laser and the scattered light is collected and analysed. The wavelengths and intensities of the scattered light can be used to identify functional groups in a molecule. The integration of a microscope with Raman systems provides access to confocal techniques, which allow spectra to be collected from a very small volume (<1 μm in diameter). Confocal Raman spectroscopy allowed us to carry out non-destructive analysis of the elastomeric materials deposited by DPN.

A microscope was used to focus the laser beam and obtain chemical characterisation of single PDMS droplets and microspots. Fig. 4 shows a sample Raman spectrum of the PDMS material deposited as a droplet using a micropipette, which was

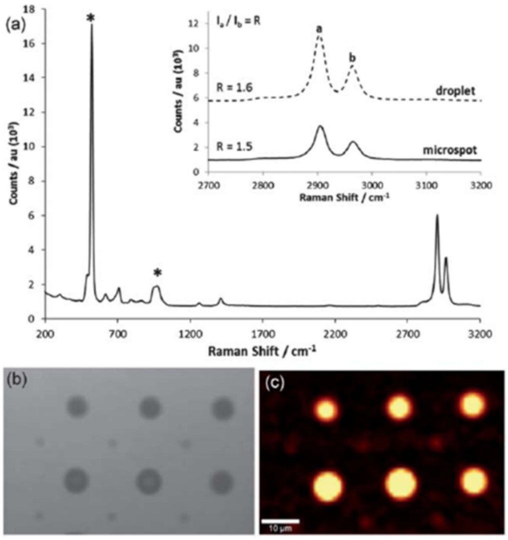

Fig. 4 (a) Raman spectrum of PDMS spot cured onto the silicon dioxide substrate. Raman bands originating from the silicon substrate are marked with a star. Inset: Comparison of the relative intensity of the Raman bands found in the methyl stretch region for the PDMS drop and microspot. (b) Bright-field image of PDMS structures deposited by DPN using alternating dwell times of 0.25 and 0.1 s and (c) Raman map (CH_3 stretch region) of the same alternating features.

typical of Raman spectra obtained previously by others.[37] Si–O–Si stretching vibrations appear at 492 cm^{-1}, Si–CH_3 rocking vibrations appear at 708 cm^{-1}, CH_3 bending vibrations appear at 1263 and 1412 cm^{-1}, and CH_3 stretching vibrations appear at 2905 and 2965 cm^{-1}. The peak vibration frequencies obtained for the PDMS droplet were in agreement with the corresponding microspot deposited by DPN (Table 1). The relative intensity of the methyl stretch vibrations of PDMS have been shown to be sensitive to the polymer conformation and can be used to assess changes in molecular structure.[37] The inset in Fig. 4 compares the relative intensity of the Raman bands in the methyl stretch region (symmetric and asymmetric carbon–hydrogen stretch at 2905 cm^{-1} and 2965 cm^{-1}) for each type of preparation, which show a similar peak ratio intensity. Further to this, we were able to generate chemical composition maps of PDMS microspots based on the Raman intensity of a relevant vibration of choice (symmetric methyl stretch, Fig. 4 (b & c)), confirming the chemical identity of the structures and their relative spatial positions on the surface.

Table 1 Raman frequencies and assignments for PDMS drop and microspot deposited by DPN ($\lambda_{EX} = 532$ nm)

Band assignment	PDMS droplet	PDMS microspot
Si–O–Si symmetric stretching	492 cm^{-1}	491 cm^{-1}
Si–C asymmetric rocking	708 cm^{-1}	709 cm^{-1}
CH_3 bending		
Symmetric	1263 cm^{-1}	1262 cm^{-1}
Asymmetric	1412 cm^{-1}	1412 cm^{-1}
CH_3 stretching		
Symmetric	2905 cm^{-1}	2905 cm^{-1}
Asymmetric	2965 cm^{-1}	2964 cm^{-1}

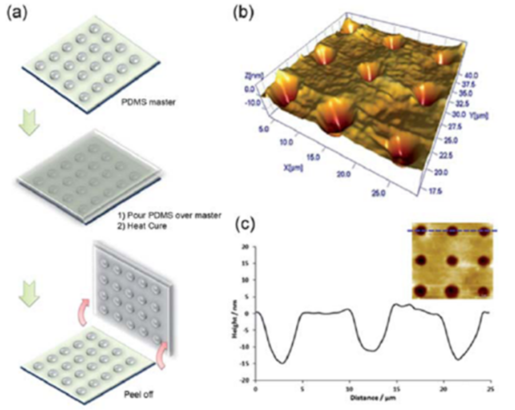

Fig. 5 (a) Schematic representation of the procedure to fabricate a PDMS negative replica from a PDMS master prepared by DPN. (b) 3D AFM topography image of negative features transferred onto the PDMS replica and (c) height profile for three negative structures showing voids in the surface.

DPN has been previously used to generate nanostructures on gold for use as lithographic masters.[38] To further demonstrate the versatility of our approach we used a PDMS array deposited on silicon dioxide by DPN as a master for replication in soft lithography (Fig. 5). In fact, it has been shown that PDMS masters reinforced with silicon dioxide plates can reduce residual and deflecting deformations encountered during pattern transfer.[39] In this particular example, PDMS arrays were first patterned using a 0.1 s dwell time and a 10 µm pitch onto a silicon dioxide surface to create a master. Freshly prepared PDMS prepolymer (10 : 1 mixture, no hexane) was then poured over the master and left to cure at room temperature over 48 h. The crosslinked PDMS replica was then peeled off and analysed by AFM. Feature transfer was readily observed under a light microscope. In practice, the master is left intact and ready to produce more replicas. Masks made using photoresists would normally require a larger amount of polymer to pattern a given area, with unexposed material removed and going to waste during the developing process.

Conclusions

We have demonstrated the first direct-write method for patterning PDMS structures with micrometer dimensions and arbitrary geometries using DPN. The PDMS prepolymer was dissolved in hexane in order to allow flow into a microfluidic inkwell and ink transfer onto a silicon dioxide surface. Silicon dioxide was used as a substrate due to its wide availability and the possibility to permanently bond the structures to the surface through plasma treatment. PDMS structures with dimensions ranging from 2.7–13.9 µm in diameter and 18.6–376.4 nm in height were fabricated using dwell times of less than 1 s, illustrating the flexibility with regards to feature size control provided by this method. The use of short dwell times and 1D arrays of DPN probes (12 tips) allow for an increase in overall patterning throughput and rapid prototyping of PDMS structures. Raman microspectroscopy was used to analyse and compare the chemical composition of the PDMS arrays against the bulk preparation and it was concluded that phase separation of the ink components was not apparent under the conditions used. This advance provides a massive step forward in terms of the ability to develop PDMS structures for BioMEMS applications and the example given of a PDMS array fabricated by DPN used as a replication master indicates the potential for many other applications.

Experimental section

Materials and methods

Hexane was purchased from Sigma-Aldrich, UK. The elastomeric kit used in this work (Sylgard 184, Dow Corning Corporation) is composed of a two-component heat curing system, consisting of a pre-polymer (base) and a cross-linker (curing agent). In this study, pre-polymer (1.0 g) was mixed thoroughly with the curing agent in the weight ratio of 10 : 1. The PDMS mixture was then diluted with n-hexane to give a 30% (wt/wt) mixture.

PDMS array fabrication

DPN was performed on an NLP 2000™ nanolithography platform (NanoInk, Inc., Skokie, IL). A 1-D tip-array containing 12 tips with a 66 micron pitch between tips (M-type, NanoInk, Inc., Skokie, IL) was used to pattern the PDMS arrays. Tips were cleaned in an oxygen plasma (Diener Electronic, Germany) prior to use. This instrument was also used to plasma bond the PDMS arrays to the silicon dioxide surfaces as part of the fabrication process. Ink delivery to the tip array was carried out by placing the array in a 6-channel micro-inkwell (DNA inkwell, NanoInk, Inc., Skokie, IL).

DPN deposition of the PDMS inks was carried out on silicon dioxide surfaces (thermally grown over silicon) containing registration marks (NanoInk, Inc., Skokie, IL). Surfaces were thoroughly cleaned with acetone, IPA and deionised water prior to use. All DPN experiments were carried out at room temperature (19–21 °C) and a relative humidity of 45–55%. AFM topography images (close-contact) were recorded on a DPN 5000™ desktop nanofabrication system (NanoInk, Inc., Skokie, IL).

Raman spectroscopy

Confocal Raman microscopy images were recorded on a Witec Alpha 300 R microscope (Ulm, Germany) equipped with a 532 nm Ar-Ion laser (~40 mW) and a ×100 objective (NA = 0.9). Spectra were processed using Witec Project v2.0 software.

Acknowledgements

We would like to acknowledge Nanoink Inc. for funding.

Notes and references

1 V. Bergeron, P. Cooper, C. Fischer, J. Giermanska-Kahn, D. Langevin and A. Pouchelon, *Colloids Surf., A*, 1997, **122**, 103.
2 A. Kumar and G. M. Whitesides, *Appl. Phys. Lett.*, 1993, **63**, 2002.
3 J. C. McDonald, D. C. Duffy, J. R. Anderson, D. T. Chiu, H. Wu, O. J. A. Schueller and G. M. Whitesides, *Electrophoresis*, 1999, **21**, 27.
4 R. D. Piner, J. Zhu, F. Xu, S. Hong and C. A. Mirkin, *Science*, 1999, **283**, 661.
5 K. Salaita, Y. Wang and C. A. Mirkin, *Nat. Nanotechnol.*, 2007, **2**, 145.
6 D. S. Ginger, H. Zhangand and C. A. Mirkin, *Angew. Chem., Int. Ed.*, 2004, **43**, 30.
7 G. Agarwal, L. A. Sowards, R. R. Naik and M. O. Stone, *J. Am. Chem. Soc.*, 2003, **125**, 580.
8 X. Wang, K. S. Ryu, D. A. Bullen, J. Zou, H. Zhang, C. A. Mirkin and C. Liu, *Langmuir*, 2003, **19**, 8951.
9 F. Huo, Z. Zheng, G. Zheng, L. R. Giam, H. Zhangand and C. A. Mirkin, *Science*, 2008, **321**, 1658.
10 D. A. Bruzewicz, M. Reches and G. M. Whitesides, *Anal. Chem.*, 2008, **80**, 3387.
11 J. W. Jang, A. Smetana and P. Stiles, *Scanning*, 2010, **32**, 24.
12 J. N. Lee, C. Park and G. M. Whitesides, *Anal. Chem.*, 2003, **75**, 6544.
13 A. L. Thangawng, R. Ruoff, M. A. Swartz and M. R. Glucksberg, *Biomed. Microdevices*, 2007, **9**, 587.
14 J. J. Lange, M. M. Collinson, C. T. Culbertson and D. A. Higgins, *Anal. Chem.*, 2009, **8**, 10089.
15 A. Goyal, A. Kumar, P. K. Patra, S. Mahendra, S. Tabatabaei, P. J. J. Alvarez, G. John and P. M. Ajayan, *Macromol. Rapid Commun.*, 2009, **30**, 1116.
16 J. Haaheim, V. Val, J. Bussan, S. Rozhok, J. W. Jang, J. Fragala and M. Nelson, *Scanning*, 2010, **32**, 49.
17 J. Zhou, A. V. Ellis and N. H. Voelcker, *Electrophoresis*, 2010, **31**, 2.
18 A. Mata, A. Fleischman and S. Roy, *Biomed. Microdevices*, 2005, 7, 281.
19 H. Hillborg, J. F. Ankner, U. W. Gedde, G. D. Smith, H. K. Yasuda and K. Wikström, *Polymer*, 2000, **41**, 6851.
20 S. Rozhok, R. Piner and C. A. Mirkin, *J. Phys. Chem. B*, 2003, **107**, 751.
21 H. T. Wang, O. A. Nafday, J. R. Haaheim, E. Tevaarwerk, N. A. Amro, R. G. Sanedrin, C.-Y. Chang, F. Ren and S. J. Pearton, *Appl. Phys. Lett.*, 2008, **93**, 143105.
22 A. J. Senesi, D. I. Rozkiewicz, D. N. Reinhoudt and C. A. Mirkin, *ACS Nano*, 2009, **3**, 2394.
23 O. A. Nafday, M. W. Vaughn and B. L. Weeks, *J. Chem. Phys.*, 2006, **125**, 144703.
24 E. J. Peterson, B. L. Weeks, J. J. De Yoreo and P. V. Schwartz, *J. Phys. Chem. B*, 2004, **108**, 15206.
25 P. V. Schwartz, *Langmuir*, 2002, **18**, 4041.
26 K. Salaita, A. Amarnath, T. B. Higgins and C. A. Mirkin, *Scanning*, 2010, **32**, 9.
27 J. Y. Jang, S. H. Hong, G. C. Schatz and M. A. Ratner, *J. Chem. Phys.*, 2001, **115**, 2721.
28 H. Kim, G. C. Schatz and J. Jang, *J. Phys. Chem. C*, 2010, **114**, 1922.
29 H. Jung, C. K. Dalal, S. Kuntz, R. Shah and C. P. Collier, *Nano Lett.*, 2004, **4**, 2171.
30 L. Huang, A. B. Braunschweig, W. Shim, L. Qin, J. K. Lim, S. J. Hurst, F. Huo, C. Xue, J. W. Jang and C. A. Mirkin, *Small*, 2010, **21**, 1077.
31 K. B. Lee, J. H. Lim and C. A. Mirkin, *J. Am. Chem. Soc.*, 2003, **125**, 5588.
32 R. G. Sanedrin, L. Huang, J.-W. Jang, J. Kakkassery and C. A. Mirkin, *Small*, 2008, **4**, 920.
33 S.-C. Hung, O. A. Nafday, J. R. Haaheim, F. Ren, G. C. Chi and S. J. Pearton, *J. Phys. Chem. C*, 2010, **114**, 9672.
34 J. R. Hampton, A. A. Dameron and P. S. Weiss, *J. Am. Chem. Soc.*, 2006, **128**, 1648.
35 K. Salaita, A. Amarnath, D. Maspoch, T. B. Higgins and C. A. Mirkin, *J. Am. Chem. Soc.*, 2005, **127**, 11283.
36 E. Smith and G. Dent. *Modern Raman spectroscopy: a practical approach.*, 2005, Chichester, Wiley, UK.
37 S. C. Bae, H. Lee, Z. Lin and S. Granick, *Langmuir*, 2005, **21**, 5685.
38 K. S. Salaita, S. W. Lee, D. S. Ginger and C. A. Mirkin, *Nano Lett.*, 2006, **6**, 2493.
39 C. Luo, F. Meng, X. Liu and Y. Guo, *Microelectron. J.*, 2006, **37**, 5.

Introducing dip pen nanolithography as a tool for controlling stem cell behaviour: unlocking the potential of the next generation of smart materials in regenerative medicine†

Judith M. Curran,*[a] **Robert Stokes,**[b] **Eleanore Irvine,**[b] **Duncan Graham,**[b] **N. A. Amro,**[c] **R. G. Sanedrin,**[c] **H. Jamil**[c] **and John A. Hunt**[a]

Received 10th March 2010, Accepted 29th March 2010
First published as an Advance Article on the web 14th April 2010
DOI: 10.1039/c004149a

Reproducible control of stem cell populations, regardless of their original source, is required for the true potential of these cells to be realised as medical therapies, cell biology research tools and *in vitro* assays. To date there is a lack of consistency in successful output when these cells are used in clinical trials and even simple *in vitro* experiments, due to cell and material variability. The successful combination of single chemistries in nanoarray format to control stem cell, or any cellular behaviour has not been previously reported. Here we report how homogenously nanopatterned chemically modified surfaces can be used to initiate a directed cellular response, particularly mesenchymal stem cell (MSC) differentiation, in a highly reproducible manner without the need for exogenous biological factors and heavily supplemented cell media. Successful acquisition of these data should lead to the optimisation of cell selective properties of materials, further enhancing the role of nanopatterned substrates in cell biology and regenerative medicine. The successful design and comparison of homogenously molecularly nanopatterned surfaces and their direct effect on human MSC adhesion and differentiation are reported in this paper. Planar gold surfaces were patterned by dip pen nanolithography (DPN®) to produce arrays of nanodots with optimised fixed diameter of 70 nanometres separated by defined spacings, ranging from 140 to 1000 nm with terminal functionalities of simple chemistries including carboxyl, amino, methyl and hydroxyl. These nanopatterned surfaces exhibited unprecedented control of initial cell interactions and subsequent control of cell phenotype and offer significant potential for the future.

Introduction

Within the fields of regenerative medicine and cell biology significant research endeavour is focused on using minimally invasive methods to induce a specific cellular response. One way in which this could be achieved is by controlling the direct contact and interaction between a given cell type and a well defined material; for this strategy to prove successful the material must be homogenous. Also in addition to playing a role in controlling initial cell adhesion, the stimulus presented to the cells must be sufficient to control the cellular response over a prolonged period. This can either be by controlling what factors cells release, or by ensuring the long term stability and continuation of the spatial stimulus.

As research in this field develops it is clear that an array of material and *in vitro* factors can be utilised to induce a cellular response *i.e.* roughness, topography (micro and nano), surface energy, interactions, flow and bulk chemistry. To date research into the effect of isolated single variables has been limited as material production and modification methods have lacked the control required to produce surfaces that will allow investigations into specific interactions between cells and isolated variables *i.e.* a precisely defined chemical modification in a defined space with control over the induced change in topography and associated changes to surface energy. Therefore due to the phenomenological nature of current studies, at the single cell scale, the responses achieved have been heterogenous at both single cell and cell population levels;[1–8] therefore tissue resulting from these studies may have inherent weakness as it is not structurally correct. The nature of cellular interaction also inhibits advances in the research area as the heterogenous response of cells is amplified between research groups due to experimental variables introduced by local protocols and practice and the cells themselves. For certain applications *i.e.* bone contacting applications, this phenomenological response does provide a significant enhancement of the *status quo*, and so simple roughening of a surface (alumina blasted titanium) produces an implantable device that provides a significant improvement to the patient *i.e.* a stable hip replacement. In contrast for other tissue applications *i.e.* neurogenic,

---

[a] *UKCTE, The Division of Clinical Engineering, School of Clinical Sciences, LINSET, The University of Liverpool, Ground Floor Duncan Building, Daulby Street, Liverpool, UK. E-mail: j.curran@liv.ac.uk; Fax: +44 (0)151 7064915; Tel: +44 (0)151 7064913*
[b] *Centre for Molecular Nanometrology, WestCHEM, Department of Pure and Applied Chemistry, University of Strathclyde, 295 Cathedral Street, Glasgow, UK; Fax: +44 (0)141 552 0876; Tel: +44 (0)141 548 4701*
[c] *NanoInk Inc., 8025 Lamon Ave, Skokie, IL, 60077, USA*

† Electronic supplementary information (ESI) available: Time lapse microscopy videos taken when cells were cultured in contact with; 1. –CH_3 patterned surfaces, 2. and 3. –NH_2 patterned surfaces. See DOI: 10.1039/c004149a

chondrogenic and myogenic, if the definition of a complete cell population cannot be provided then the potential of stem cells in regenerative medicine may not be realised.

MSCs are by definition heterogenous and it is now widely accepted that stem cells are often made up of a number of discrete sub-populations of committed progenitor cells.[9,10] Therefore to combat this inherent level of heterogeneity and utilise materials that will act efficiently and drive stem cells in one uniform behaviour, the stimulus from the material is required to be well defined and homogenous. Ultimately the material should also display cell selective properties that can further refine the heterogenous nature of the generic MSC population. This is particularly important for stem cells, as control over the initial attachment could dictate the ultimate function of the stem cell and result in the formation of *de novo* tissue that is far superior to any results that are currently achievable.

One way of controlling cell adhesion and subsequent morphology is by nanotopography, and research has proven that cells can detect and respond to an array of topographies and can be affected by the level of order of an induced topography, with clear effects on cell functionality.[11–15] Cell adhesion can also be controlled *via* manipulation of integrin/ligand binding.[16,17] These studies proved that control over integrin spacing and clustering dictated the formation and stability of focal adhesions and dictated the levels of cellular adhesion. RGD dots separated by a distance of 58 nm induced cell spreading, whilst RGD dots separated by a distance of 110 nm resulted in weakly attached cells due to the induced stability of focal contacts caused by the initial integrin/ligand interactions. The hypothesis tested in this research was that surface modification using chemical nanoarrays can efficiently control stem cell behaviour *via* control of focal contact formation and distribution; furthermore that there are optimum patterns of chemical arrays that will control cell function.

Previous research has demonstrated a strong correlation between protein adsorption onto a surface, focal contact formation and subsequent MSC differentiation that is directly related to surface chemistry.[18,19] Modifying surfaces using bulk surface techniques with $-CH_3$, $-NH_2$, –OH and –COOH groups can induce stem cell differentiation,[18–20] but these results were heterogenous for the total area in terms of cell differentiation, largely due to the method of introducing the groups to the surface and the lack of control regarding spacing between groups and their distribution pattern. However, using both glass and polymer surfaces as the material substrate $-CH_3$ groups have been shown to enhance the MSC phenotype, whilst $-NH_2$ groups directed stem cells to become osteogenic *i.e.* bone forming. –OH and –COOH groups directed stem cells towards a cartilaginous tissue phenotype. These specific cellular effects were attributed to the chemical groups on the surfaces. The interaction between the surfaces and the cells drives the cellular response, eliminating the need for the use of additional biological factors, *i.e.* growth factors and cytokines or other cell culture supplements. Optimisation of these interactions could result in the development of highly defined, reproducible therapies in regenerative medicine and cell biology as a whole.

In parallel with advances in chemically defined material driven cell responses there is a wide body of emerging research evidence which has demonstrated that cells, more specifically MSC, can detect and respond to stimuli at the nanoscale *i.e.* nanotopography,[4,5,12] therefore the potential to combine a wide array of chemistries and defined nanoarrays is an area of research that is novel and previously unreported. Additionally the ability to control and enhance initial cell interactions to this degree using simple chemistries could result in the formation of new cost effective, stable surfaces that could offer an alternative technique for control of cell functionality. Dip pen nanolithography (DPN®) is an emerging technology that has an increasing use in the development of surfaces that can be used to investigate biological responses from the sub-micron level and upwards.[21,22] Within this study DPN® was used to produce a range of different and precisely defined large areas of chemically homogenous surface using four different chemical functionalities deposited at the nanometre scale using thiolated molecules on gold (which is an ideal flat, chemically appropriate surface to form nano-structured self-assembled monolayers (SAMs)). DPN® provides a suitable technique for the controlled deposition of a wide range of materials ranging from small organic molecules such as alkyl thiols, silazanes, Au(III) complexes, to large systems such as bio-molecules and nanoparticles by using a scanning probe microscope tip to deliver defined molecules in the form of an "ink" onto a surface *via* a water meniscus. The size of the feature being written is related to the interaction between the coated tip, surface, and DPN® conditions such as dwell time, temperature and humidity and these were optimised in this study. Areas of introduced modification were optimised to allow the formation of 1 focal contact on one area of modification *i.e.* dot size, dβ, was limited to 70–80 nm and focal contacts have been reported to be 60 nm.[23] DPN® allowed a top-down nanoscale deposition of a number of molecules that presented distinctly different chemical functionalities ($-CO_2H$, $-NH_2$, $-CH_3$, –OH) and as previously stated have a role in triggering MSC differentiation. Careful selection of the materials allowed deposition in the form of isolated nano-areas of SAMs onto gold surfaces *via* thiol linkages under low temperature and humidity conditions.

Preliminary screening experiments highlighted combinations of chemical nanoarrays that had a role in controlling cell adhesion, focal contact formation and cytoskeletal organization. In addition to highlighting the necessity to control material modifications at the nanometre scale for enhanced cell adhesive properties, this study also demonstrated the ability of specifically selected and homogenously modified surfaces to control MSC differentiation and phenotype and demonstrated a clear role for nanoarrays in the development of more efficient cell culture technologies. The study also proved that optimal spacing of chemical groups was dependent on the exact interaction induced by the chemical group, therefore enhancing the current perceptions of material mediated integrin responses.

Results and discussion

In order to investigate the effect of both the nanopattern and the terminating chemical functionality, a series of nanopatterned gold surfaces were prepared. Each nanopattern comprised a series of parallel dots spaced by a fixed distance (pitch, dα) and fixed diameter (dβ ≈ 65–70 nm) (Fig. 1). Preliminary studies tested an array of dβ values, ranging from 40–80 nm, these parameters were chosen based upon system limitations in terms

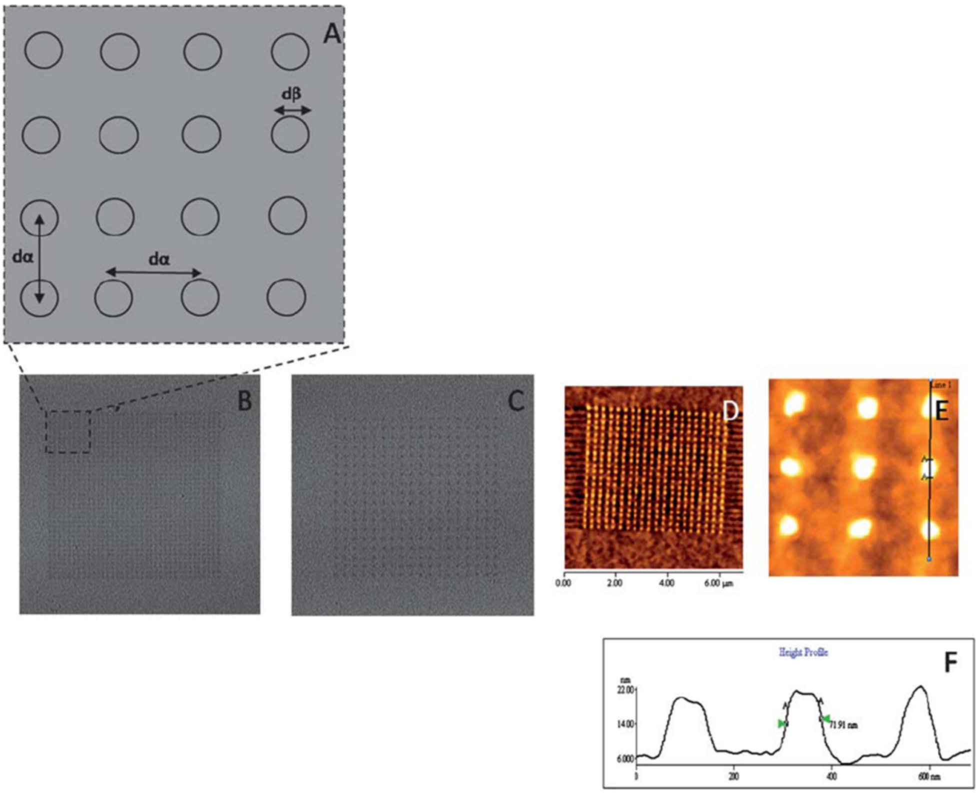

Fig. 1 (A) Nanopatterned surfaces used for MSC control and differentiation showing dot to dot pitch (dα) and dot diameter (dβ), (B) LFM image of small area 280 nm pitch array, (C) LFM image of 140 nm pitch array. (D–F) AFM topographical image of an alkanethiol resist array fabricated on gold surface after chemical etching. The cursor profile shows an average diameter feature (dβ) of 70 nm.

of large scale production and accurate deposition of the pattern for all inks. These results showed no difference in initial focal contact formation and cellular response (data not shown) between 40 and 80 nm dot sizes, therefore to enable successful scale up and correlation between all inks a dot size of 70 nm was chosen for subsequent studies. Focal adhesions have previously been reported to be 60–67 nm in size, therefore this dot size provided for the formation of one focal contact per dot.[24] Spatial distribution of inks and the resultant effect on MSC adhesion were also compared using both square and hexagonal arrays. Nanopatterns using each ink were prepared using differing values for dα (140, 280, 1000 nm) with dot diameter and spacing confirmed by lateral force microscopy (LFM). These initial pitches were chosen for preliminary proof of concept studies based on published data regarding cellular response to various nanofeatures.[11–13,16,24–29] Stability of the nanostructures under standard tissue culture conditions was established prior to cell seeding, therefore ensuring that material induced cell responses were not inhibited by degradation or desorption of the materials/molecules from the surface (Fig. 1). For this study into the use of DPN technologies in cell culture applications, the range of pitches were chosen based upon dimensions used in studies that focused on nanotopography and its role in controlling cell adhesion and focal adhesions,[15,23,25] and the workable dimensions of the DPN® systems ensuring the accurate deposition of each ink with the defined parameters. DPN® conditions were optimised to produce close to identical dot diameters for each ink.

Well characterised human MSCs were cultured in contact with the model surfaces and the effects of the chemical functionality and nanometre pitch and distribution on focal contact formation and cytoskeletal organisation were determined after 24 hours. Three nanopatterns were prepared for each of the four inks and the direct contact stem cell experiments repeated 4 times. Based on data received from these preliminary experiments combinations of chemistry and pitch that demonstrated a significant effect on initial cell adhesion were investigated further in terms of cellular responses over a prolonged period of time in basal conditions using a combination of qualitative (Flow Cytometry) and quantitative methods (immunohistochemistry, analysis of an array of markers associated with MSC differentiation).

Previously we have reported on the use of bulk coated –CH_3 surfaces as promoters of the MSC phenotype, a hypothesis that was supported by the results obtained in this study. Additionally results obtained also proved that combinations of chemistry and pitch can control initial cell attachment by dictating the distribution of initial focal contact formation. When cultured in contact with $-CH_3$ presenting surfaces hexadecane thiol (HDT) (Fig. 2) only supported viable cell attachment at a 280 nm pitch. Within the area of modification, cells attached and formed dense cell clusters with focal contacts evident throughout the bulk of the cell cluster indicative that the cell cluster was well attached to the surface. The distribution of cell contacts and differences in cell contact shape and density were dictated by the underlying nanopattern and closer observation proved that dense mature focal contacts[23] were directly associated with the nanopatterned area. Focal contacts associated with the edge of the cell cluster and the outer extremities of the area of nanopatterning were more immature, less dense and elongated in shape, and associated with individual stress fibres, associated with motile and less well attached areas of the cells (Fig. 2G). Evaluation of the distribution of F-actin throughout the cells was indicative of highly motile cells, subsequent cell migration assays proved that cells preferentially attached and moved into the $-CH_3$ 280 nm pitch patterned area from adjacent unmodified areas and cells that were initially attached in the modified area were highly active in terms of lamellipodia formation and contraction, well attached to the surface and did not move out of the area of modification, confirming the chemotactic properties of the surface (Fig. 2H and ESI Video S1†).

Material characterisation data, LFM images in Fig. 1B and C, demonstrated the change in surface features between a pitch of 280 nm and 140 nm. At 280 nm the individual features will be easily recognisable to the cells, as the outer extremities of each field of modification will be separated by at least 210 nm, whilst at a pitch of 140 nm, where pitch refers to a centre-to-centre spacing, the dots will have a separation value of just 70 nm. Stable focal contact formation relies on integrin formation and clustering, a lack of integrin clustering results in weakly attached cells, which in the case of MSC would lead to non-viable cells. Previous studies based on integrin spacing on RGD patterned surfaces have demonstrated that on ordered surfaces a spacing of approximately 70 nm is essential for determining the ability of a material to support cell adhesion.[27–29] At distances greater than

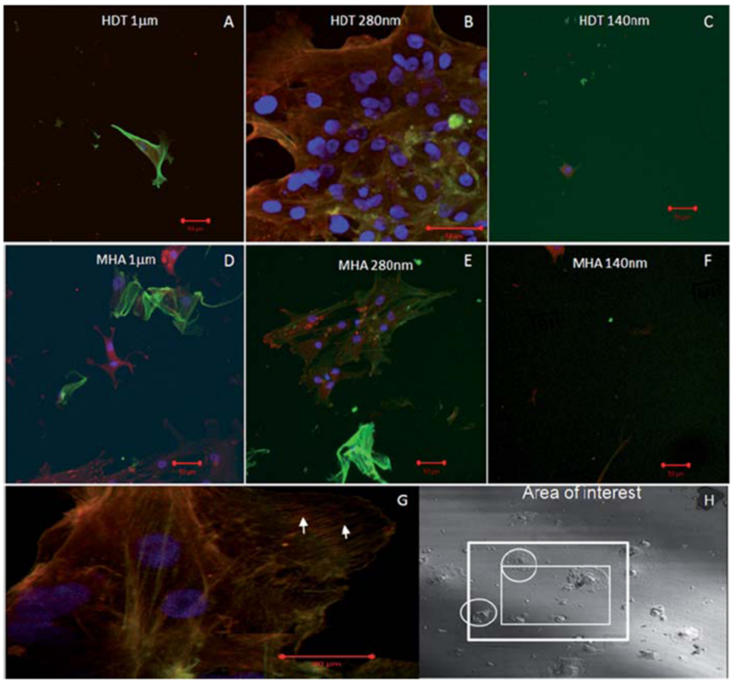

Fig. 2 (A–F) MSC cultured in contact with HDT and MHA modified surfaces for 24 hours and stained with Oregon Green Phalloidin (green-stress fibres), vinculin (red-focal contacts) and DAPI (blue-nuclei). Only 280 nm pitch modified surfaces supported viable cell adhesion. (G) High magnification image of cells clustered on ODT 280 nm pitch, arrow heads show motile focal adhesions associated with the periphery of the patterned area, whilst focal adhesions inside the cell cluster are dense and well established, depicting the strong binding of the cell *via* focal adhesions to the underlying nanoarray. (H) Single frame from time lapse microscopy experiment demonstrating the chemotactic nature of the modified surface. Over a 12 hour time period highlighted cells moved from the periphery of the modified area (where cell bodies were in contact with control and modified areas) into the centre of the modified area (CH_3 280 nm pitch, inside the smaller white square) from the adjacent unmodified areas, full time lapse analysis is available in ESI Video S1†. The images collected were from low cell density experiments to allow investigation into single cell interactions with the surface, the same chemotactic properties were observed when the cell density was increased.

and equal to 67 nm, focal contact formation is inhibited, a phenomena observed on the 140 nm pitch HDT substrates, which in turn have an end-to-end spacing of approximately 70 nm. Fitting well with previous data the surface control and definition used in this research could be used to inhibit focal contact formation *via* the controlled spacing of integrin clustering at a critical level. Furthermore these data were indicative that control of cell adhesion by $-CH_3$ presenting surfaces was similar to RGD induced cell adhesion *i.e.* the cells preferentially bound to the $-CH_3$ presenting areas, a response that was also replicated by –COOH presenting surfaces. At a pitch of 1 micron spacing between individual focal contacts would have been too great to support cell adhesion, once again indicating that when cultured in contact with $-CH_3$ presenting surfaces, focal contacts preferentially form on the $-CH_3$ areas of modification.

When cultured in contact with mercaptohexadecanoic acid (MHA), –COOH presenting nanopatterns viable cell adhesion was only observed at the 280 nm pitch. Levels of cell adhesion associated with MHA 280 nm pitch were far less than previously observed with the HDT surfaces, but the distribution of focal contacts was similar within the areas of viable cell adhesion *i.e.* at the centre of the area of interest there was evidence of dense mature focal contacts, whilst evidence of more motile immature focal contacts was found at the periphery of the cells, once again these focal contacts were associated directly with individual stress fibres, Fig. 2E. Closer examination of the MHA 1 μm patterned area showed evidence of very weakly attached cells, with no evidence of focal contacts formation or subsequent organised actin networks, Fig. 2D. The inability to form stable focal contacts on these surfaces ultimately leads to the lack of viable cell adhesion.

Previously we have reported on the ability of bulk coated –OH groups to trigger chondrogenic differentiation *via* their ability to induce minimal focal contact formation on a surface whilst maintaining viable cell adhesion. It is widely accepted that optimal chondrogenic culture conditions minimise cell contact formation to a surface, ultimately chondrocyte attachment to a substrate can lead to dedifferentiation, characterised by the loss of collagen II expression and an increase in collagen I expression. More recently it has been proven that changes in stem cell shape can optimise the potential of chondrogenic differentiation in combination with exogenous biological factors.[30] Results obtained in this study regarding control of focal adhesion formation were amplified when combining the introduction of –OH groups at specific pitches and arrays, Fig. 3A–C. When cultured in contact with the mercaptoundecanol (MUO), –OH presenting surfaces, viable cell adhesion was observed at all pitches, but patterns of focal contact formation and actin distribution were affected by changes in pitch, Fig. 3. At a phenomenological level these data were indicative that –OH group induced cell binding was controlled by a different mechanism than the previously discussed "RGD" hypothesis and associated integrin clustering, as cells could adhere and form actin networks at all pitches. When cultured in contact with 280 nm and 140 nm pitches actin fibre formation was evident throughout the entirety of the cell body, and the cells appeared more well spread on the 280 nm pitch, Fig. 3B. When cultured in contact with the 140 nm pitch there was evidence of concentrated areas of actin associated with the periphery of cell bodies, and areas of concentrated dense focal contact formation at distinct areas under the cell body. Overall the number of individual focal contact formations was less than previously observed on octadecanethiol (ODT) and mercaptoundecylamine (AUT) surfaces, but there was evidence of focal contact clustering, resulting in viable cell adhesion. When cultured in contact with 1 μm pitch MUO surfaces, in addition to the previously described actin budding, there was also evidence of actin ring formation at the periphery of individual cells (Fig. 3A), a response that has been previously observed when MSCs are actively undergoing chondrogenic differentiation.[18] Focal contacts were reduced on the 1 μm surface compared to the 280 nm and 140 nm pitches, but there was evidence of focal contact clustering which anchored the cells to the surface, minimising parallel stress fibre formation throughout the body of the cell and supporting viable cell adhesion with a morphology representative of chondrogenic differentiation at a very early time point.

When cultured in contact with AUT (amino groups) viable cell adhesion was recorded with well orientated cytoskeletons and focal contact formation at all pitches. Changing the pitch between the dots of the amino functionality controlled cell spreading and orientation (Fig. 3D–F). The formation and distribution of focal contacts on the AUT at 280 nm and 140 nm pitches were reflective of highly motile cells on the surface, for the 280 nm pitch this was accompanied by elongated cells that showed evidence of polarisation and alignment, Fig. 3E. When cultured in contact with the 1 μm AUT pitch there was a mixture of stable mature focal contacts, associated with cell nuclei and immature focal contacts associated with individual stress fibres, Fig. 3D. No evidence of cell alignment was observed on the AUT 1 μm or 140 nm pitches. Additional cell migration assays (time lapse microscopy, ESI Video S2†) confirmed the cell elongation properties of the $-NH_2$ 280 nm pitch surfaces (Fig. 3G) and the importance of pitch. Cell migration assays proved that cells attached well to the 280 nm AUT surface, initially cell clusters were formed but cells were highly motile on the surface and resulted in polarisation and elongation of the cell clusters (ESI Video S2†). When the pitch was increased to 395 nm (Fig. 3H and ESI Video S3†) there was a profound effect on cell adhesion and behaviour. When cultured in contact with the 395 nm array initial cell attachment in the modified area was much reduced compared to the 280 nm pitch. Cells remained rounded and were not able to spread out, there was no evidence of lamellipodia formation or contraction on the surface resulting in weakly attached cells, after a prolonged time in culture there was a minimal level of attachment that was not sufficient to support viable cell adhesion after 24 hours *in vitro*. Overall the phenomena observed on the 395 nm pitch surfaces followed the previously discussed "RGD" binding phenomena, where critical distances between sites of integrin clustering and subsequent focal contact formation determined the stability of the cell on the surface. The data collected within this research have proven that both chemistry and pitch play a role in determining the initial integrin binding and subsequent focal adhesion formation.

Results from the AUT modified surfaces proved that both chemistry and pitch play a role in determining the focal contact formation and distribution throughout a cell body, subsequent adhesion and spreading. The combination of control of focal contact formation with material induced cell signalling,

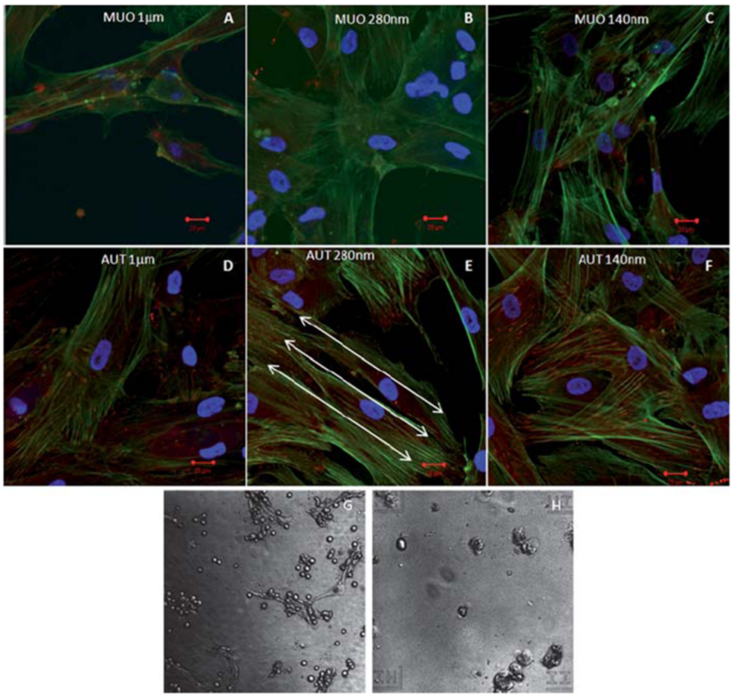

Fig. 3 (A–C) MSC cultured in contact with MUO (–OH) and with AUT (–NH_2) modified surfaces for 24 hours and stained for F-actin (green), vinculin (red) and cell nuclei (blue). When cultured in contact with 1 μm spaced MUO groups, there was evidence of rounded cell morphology and concentrated clusters of focal adhesions. Cells cultured in contact with 280 nm and 140 nm pitched surfaces showed parallel fibres of F-actin and an elongated cell morphology with minimal focal contact formation. There was also evidence of concentrated buds of actin on these surfaces. When MSCs were cultured in contact with –NH_2 modified (D–F) surfaces for 24 hours cells were elongated and aligned when cultured in contact with 280 nm pitch surfaces (E), cells in the upper right and left corners are at the outer extremities of the patterned area, therefore show signs of polarisation but are not as strong as cells in the centre of the pattern where the entirety of the cell body receives the same stimulus. Time lapse microscopy (G–H) confirmed the –NH_2 280 nm pitch surfaces ability to induce elongation. (G) Single frame from 280 nm pitch –NH_2, all of the field of view is patterned with –NH_2, there is clear evidence of cell clustering and elongation of the well attached cell clusters, single frame taken from ESI Video S2†. When the pitch was increased by 100 nm (H) the effect on cell adhesion and morphology was significant, at a pitch of 395 nm the cells could not attach properly or elongate and resulted in rounded poorly attached cells, the area of modification is located within the four marker points, double letters contained within a square bracket, located at the corners of the field of view, single frame taken from ESI Video S3†.

attributed to a specific surface chemistry, provides a unique way to amplify previous material induced differentiation, *via* control of focal contact formation.

As stated previously the role of specific nanoarrays and their effect on MSC phenotype were evaluated further over a prolonged culture period *in vitro*. Novel DPN® systems were incorporated to produce homogenous nanopatterned surfaces, with no edge effects, therefore ensuring that every cell in a given test received the same spatial stimulus, minimizing uncontrolled cell surface interaction and enhancing the effect of the chemical nanoarrays on a cell response. More specifically optimum –CH_3 presenting nanoarrays were evaluated in terms of promoting/maintaining the MSC phenotype for prolonged periods of time *in vitro*. MSCs were cultured in contact with –CH_3 280 nm square array surfaces for up to 28 days on modified and control surfaces. The expression of a panel of MSC markers was quantified by fluorescent activated cell sorting (FACS) analysis. To maximise the relevance of the results MSCs isolated from 4 separate donors (data provided by Lonza, UK) were used in the experiments. Results obtained after 28 days proved that –CH_3 modified surfaces maintained and enhanced the expression of CD29, CD73, CD90, CD105 and CD166 compared to unmodified substrates. Of significance was the fact that the –CH_3 modified surfaces maintained an enhanced expression of the phenotypic markers compared to traditional TCPS (tissue culture polystyrene), this was statistically significant for CD29, 73, 90 and 166. The expression of CD34 (hematopoietic stem cell marker and negative for MSC) was significantly lower on –CH_3 surfaces compared with TCPS controls, proving that chemical nanoarrays can be used to produce surfaces that can enhance current protocols used for the maintenance and purification of MSC phenotypes *in vitro* (Fig. 4). The maintenance of the panel of markers associated with the MSC phenotype was solely attributable to the combination of –CH_3 at a 280 nm square array, as when cultured in contact with –NH_2 280 nm square array patterns the expression of CD29, CD73, CD90, CD105 dropped

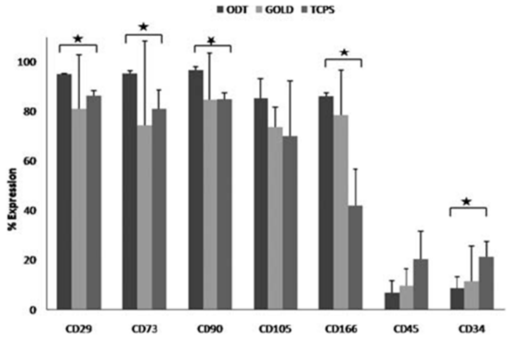

Fig. 4 Human MSCs were cultured in contact with ODT (CH_3 nanoarray), plain gold and standard TCPS substrates for 28 days in basal conditions, $n = 4$. FACS analysis showed a significant increase in expression of CD29, CD73, CD90 and CD166 on ODT compared to standard TCPS substrates. Expression of CD34 on ODT substrates was also significantly reduced on ODT substrates compared to TCPS.

to below 70% by day 14 (data not shown), also there was a loss of STRO-1 expression from as early as day 7. Therefore whilst no distinct pattern of differentiation was observed on the $-NH_2$ patterned surfaces the surfaces did not maintain the MSC phenotype. Correlation of the data supported the original hypothesis that $-CH_3$ chemical modifications could be used to promote and maintain the MSC phenotype *in vitro*, combining the introduction of this group with chemical patterning resulted in surfaces that performed more efficiently than TCPS in MSC culture, in addition to being chemotactic to MSC.

Experimental section

Materials and methods

Creation of homogenous small area nanopatterned surfaces *via* DPN for initial cell culture studies. DPN patterning of the surface was achieved using an NScriptor (NanoInk, Skokie, IL) system in contact mode. The AFM cantilever probes were coated by dipping the chip into a saturated solution of thiol molecules (3–5 mM). For the 1 μm pitch arrays an A-type cantilever with spring constant of 0.1 N m^{-1} was used (NanoInk) to fabricate an area equivalent to the full range of the scanner (~90 × 90 μm^2). Optical alignment with surface marks allowed patterning over larger areas. For the smaller pitch patterns ($d\alpha = 140$ and 280 nm) multiple pen arrays consisting of 24 tips (D type with a 35 μm tip to tip pitch) were used to pattern areas of 700 × 700 μm^2. Calibration and determination of the diffusion coefficient for each ink were carried out prior to array fabrications. The diffusion coefficient was checked again at the end of each deposition cycle to ensure that homogeneous arrays were fabricated. Dwell times varied according to ink type. Typically tip dwell times of 0.1 s (HDT and MHA) or 0.2 s (MUO and AUT) were used to produce dots of $d\beta = 65$–70 nm. Small quality control areas were deposited on the same substrate and examined using lateral force mode (LFM) scanning. Samples were rejected prior to cell deposition if array characteristics were varied significantly or if non-specific deposition of ink occurred *via* airborne diffusion from the non-tip portion of the cantilever to the substrate surface during the DPN experiment.

Creation of homogenous nanopatterened surfaces for long term cell culture studies. For higher throughput and large area fabrication of nanosized features a two-dimensional pen array (2D nano PrintArray™) was used. The 2D NPA consists of 55 000 tips in a 1 cm^2 chip. The chip was vapour-coated under vacuum with thiol molecules under 300 motors and 80 °C for 3 hours, followed by gradual cooling to 25 °C for 6 hours. This was done to lower the melting point of the thiol molecules to facilitate the evaporation of the thiol compounds into the gas phase. This process was repeated twice to ensure homogeneous coating of the tips. The coated chip is then loaded into an NScriptor and levelled with respect to the substrate surface, thereby providing uniform contacts between the cantilevers and the surface which lead to reproducible, accurate, and homogeneous edge-to-edge patterning of nanostructures on surfaces across large areas. In order to achieve uniform patterning across the surface several DPN parameters were controlled, such as homogeneous tip coating, temperature and humidity. In addition, the substrate was heated or cooled depending on the thiol ink.[31] The substrate temperature was controlled to control the dot sizes, several substrates were prepared with different dot sizes ranging from 50 to 200 nm. These substrates were characterized and tested, the best results were obtained for the 70 nm dot diameters. For every three substrates one was used as a quality control to ensure homogeneous edge-to-edge nanostructures fabrication with 70 nm spot diameters (Fig. 1E) using chemical wet-etching.

Cell culture. Well characterised ($CD29^+$, $CD73^+$, $CD90^+$ and $CD105^+$) Human MSCs (Lonza, UK) were introduced to the surface at a cell concentration of 5 × 10^4 cells ml^{-1}, 1 ml of cell suspension (basal medium Lonza, UK) was added to each material in a 24 well plate. As a screening process to determine optimum combinations of chemistry and pitch cells were cultured for 24 hours at 37 °C, 5% CO_2 at which time samples were washed and fixed and stained for focal adhesions and F-actin. Selected surfaces that supported viable cell adhesion were progressed through to long term culture and analysis experiments.

Focal adhesion and F-actin staining. Samples were dual labelled with vinculin (focal adhesions) and F-actin (stress fibres) using previously described methods.[18] Briefly samples were removed from culture, washed with PBS and fixed with 4% formaldehyde and 2% sucrose. After washing samples were permeabilised, 0.05% Triton ×100 solution, washed and incubated with primary mouse anti-human vinculin, 0.22 mg ml^{-1} (Sigma UK), followed by a rhodamine-conjugated IgG goat anti-mouse secondary antibody, 10 μg ml^{-1} (ICN). Samples were washed with a 0.1% Tween 20 solution in PBS and incubated with 0.005 mg ml^{-1} Oregon Green Phalloidin (Invitrogen), 30 minutes at 4 °C. Samples were mounted with Vectashield (Vector) and visualised using Confocal Laser Scanning Microscopy (CLSM 510, Zeiss).

Time lapse microscopy. Human MSCs were resuspended in basal medium (Lonza, UK) and labelled with DiI (Vybrant cell-labelling, Invitrogen) according to the manufacturers guidelines. Labelled cells were introduced to the substrate in suspension and monitored over a 12 hour period using confocal laser microscopy (Zeiss). Images were taken at 60 second intervals.

Quantitative FACS analysis. Human MSCs from 4 different donors were purchased from Lonza, UK and expanded to 4P.

Cells were stained with CD29 (Cy5-PE conjugated, BD), CD90 (FITC conjugated BD), CD73 (PE conjugated, BD), CD105 (FITC conjugated, BD), CD166 (PE conjugated, BD), CD34 (FITC conjugated, BD) and CD45 (FITC conjugated, BD) prior to introduction to the test substrates to confirm the MSC phenotype of the cells. MSCs were cultured in contact with the 5 mm^2 test substrates surfaces in 48 well plates at an optimised concentration of 2×10^4 cells per well in basal medium (Lonza, UK) for 28 days. Cells were fed twice weekly and the expression of the panel of CD markers was quantified at the end of the test period. Statistical Analysis, ANOVA Tukey models, were incorporated to establish the statistical significance of the results, $p = 0.05$.

Materials and abbreviations.

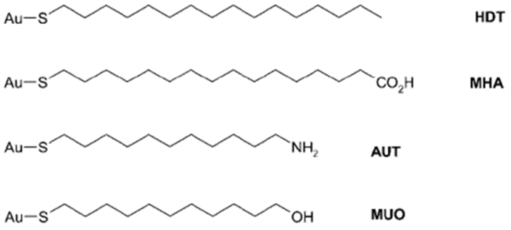

Conclusion

The data presented in this study provided evidence that direct functional chemical modifications can themselves control the mechanism of focal contact formation; with one of the mechanisms being through controlling specific integrin clustering. This control of initial cell signalling events can then be used to direct the cellular response *i.e.* controlling phenotype and function. Chemistry can control specific integrin binding; this is dependent on the type of integrin interaction and the spacings between integrin clusters, as this is critical in determining the nature of the cell adhesion and subsequent cell signalling events.

It has been proven that the combination of specific chemistry with defined positioning and density had a direct effect on cell adhesion and function. For –CH_3 and –COOH groups it was established that the cell responses followed the previously published research data for RGD nanopatterns. –NH_2 chemistries initiated different cellular responses in terms of pitch induced cellular adhesion, this effect was most notable on the –NH_2 modified surfaces for which increasing the pitch by 100 nm essentially inhibited good cell attachment and spreading on the surface, such a pronounced effect will ultimately control cell function. The weak level of attachment associated with the 395 nm pitch would limit the use of these surfaces in a number of applications *i.e.* osteogenic and for any surfaces that require cells to withstand a shear force.

Control is provided by controlling initial adhesion, integrin formation and clustering, focal contact formation, distribution and spreading of cells on surfaces. There are many important subtle variations in adhesion between well adhered and fully spread to non-adherent cells within which cells can be directed to the desired phenotype and function. Even significant inhibition of cell adhesion using chemistry and spacing to inhibit focal contact formation can be utilised to control cell populations, for example –OH chemistry can provide the optimal chemistry for chondrogenic and possibly adipogenic applications, –NH_2 for bone formation and possibly neurogenesis due to cellular elongation. This range of functional chemistries provide the proof that cell growth can be controlled using substrate definition by defined nanopatterns through the use of specific chemical functionalities which can be chosen for different cell phenotypes and functions for both *in vitro* assays and *in vivo* cell based therapies.

It has been demonstrated that surfaces modified using DPN® provided the required resolution and definition for these chemical functionalities. This approach was highly reproducible and provided for the control of MSC adhesion. There are potentially an almost unlimited number of inks that can be delivered to a surface using this approach, unlocking a vast array of options for the production of materials that can be used both *in vivo* and *in vitro* in cell biology, clinical diagnostics and cell therapies, by applying the production of surfaces that not only control cell function but also have the ability to act as cell selection agents. In parallel the new generation of DPN systems and the increasing availability of compatible “inks” have provided the successful scale up of materials and prolonged cell culture, unlocking the potential of these materials in all areas of cell biology and regenerative medicine.

References

1 G. Balasundaram and T. J. Webster, *J. Biomed. Mater. Res., Part A*, 2007, **80a**, 602–611.
2 R. Barbucci, D. Pasqui, A. Wirsen, S. Affrossman, A. Curtis and C. Tetta, *J. Mater. Sci.*, 2003, **14**, 721–725.
3 J. Blümmel, N. Perschmann, D. Aydin, J. Drinjakovic, T. Surrey, M. Lopez-Garcia, H. Kessler and J. P. Spatz, *Biomaterials*, 2007, **28**, 4739–4747.
4 A. S. Curtis, M. J. Dalby and N. Gadegaard, *J. R. Soc. Interface*, 2006, **3**, 393–398.
5 M. J. Dalby, N. Gadegaard, R. Tare, A. Andar, M. O. Riehle, P. Herzyk, C. D. Wilkinson and R. O. Oreffo, *Nat. Mater.*, 2007, **6**, 997–1003.
6 M. J. Ernsting, R. S. Labow and J. P. Santerre, *J. Biomed. Mater. Res., Part A*, 2007, **83a**, 759–769.
7 K. Kimura, A. Hattori, Y. Usui, K. Kitazawa, M. Naganuma, K. Kawamoto, S. Teranishi, M. Nomizu and T. Nishida, *Invest. Ophthalmol. Visual Sci.*, 2007, **48**, 1110–1118.
8 J. Salber, S. Grater, M. Harwardt, M. Hofmann, D. Klee, J. Dujic, H. Jinghuan, J. Ding, S. Kippenberger, A. Bernd, J. Groll, J. P. Spatz and M. Moller, *Small*, 2007, **3**, 1023–1031.
9 I. Majore, P. Moretti, R. Hass and C. Kasper, *Cell Communication and Signaling*, 2009, **7**, 6.
10 M. Kucia, R. Reca, V. R. Jala, B. Dawn, J. Ratajczak and M. Z. Ratajczak, *Leukemia*, 2005, **19**, 1118–1127.
11 M. J. Dalby, *Nanomedicine*, 2009, **4**, 247–248.
12 M. J. Dalby, A. Andar, A. Nag, S. Affrossman, R. Tare, S. McFarlane and R. O. Oreffo, *J. R. Soc. Interface*, 2008, **5**, 1055–1065.

13 M. J. Dalby, M. J. Biggs, N. Gadegaard, G. Kalna, C. D. Wilkinson and A. S. Curtis, *J. Cell. Biochem.*, 2007, **100**, 326–338.
14 M. J. Dalby, N. Gadegaard, A. S. Curtis and R. O. Oreffo, *Curr. Stem Cell Res. Ther.*, 2007, **2**, 129–138.
15 M. J. Dalby, N. Gadegaard, R. Tare, A. Andar, M. O. Riehle, P. Herzyk, C. D. Wilkinson and R. O. Oreffo, *Nat. Mater.*, 2007, **6**, 997–1003.
16 E. A. Cavalcanti-Adam, D. Aydin, V. C. Hirschfeld-Warneken and J. P. Spatz, *HFSP J.*, 2008, **2**, 276–285.
17 E. A. Cavalcanti-Adam, T. Volberg, A. Micoulet, H. Kessler, B. Geiger and J. P. Spatz, *Biophys. J.*, 2007, **92**, 2964–2974.
18 J. M. Curran, R. Chen and J. A. Hunt, *Biomaterials*, 2005, **26**, 7057–7067.
19 J. M. Curran, R. Chen and J. A. Hunt, *Biomaterials*, 2006, **27**, 4783–4793.
20 Y. J. Ren, H. Zhang, H. Huang, X. M. Wang, Z. Y. Zhou, F. Z. Cui and Y. H. An, *Biomaterials*, 2009, **30**, 1036–1044.
21 D. K. Hoover, E. J. Lee, E. W. Chan and M. N. Yousaf, *ChemBioChem*, 2007, **8**, 1920–1923.
22 K. Salaita, Y. Wang and C. A. Mirkin, *Nat. Nanotechnol.*, 2007, **2**, 145–155.
23 B. Wehrle-Haller and B. Imhof, *Trends Cell Biol.*, 2002, **12**, 382–389.
24 K. Poole, K. Khairy, J. Friedrichs, C. Franz, D. A. Cisneros, J. Howard and D. Mueller, *J. Mol. Biol.*, 2005, **349**, 380–386.
25 E. A. Cavalcanti-Adam, A. Micoulet, J. Blummel, J. Auernheimer, H. Kessler and J. P. Spatz, *Eur. J. Cell Biol.*, 2006, **85**, 219–224.
26 E. A. Cavalcanti-Adam, I. M. Shapiro, R. J. Composto, E. J. Macarak and C. S. Adams, *J. Bone Miner. Res.*, 2002, **17**, 2130–2140.
27 J. Huang, S. V. Grater, F. Corbellini, S. Rinck, E. Bock, R. Kemkemer, H. Kessler, J. Ding and J. P. Spatz, *Nano Lett.*, 2009, **9**, 1111–1116.
28 C. Selhuber-Unkel, T. Erdmann, M. Lopez-Garcia, H. Kessler, U. S. Schwarz and J. P. Spatz, *Biophys. J.*, 2010, **98**, 543–551.
29 C. Selhuber-Unkel, M. Lopez-Garcia, H. Kessler and J. P. Spatz, *Biophys. J.*, 2008, **95**, 5424–5431.
30 L. Gao, R. McBeath and C. S. Chen, *Stem Cells*, 2010, **28**(3), 564–572.
31 R. G. Sanedrin, N. A. Amro, J. Rendlen and M. Nelson, Temperature controlled dip-pen nanolithography, *Nanotechnology*, 21((11)), DOI: 10.1088/0957–4484/21/11/115302.

Analyst

Dynamic Article Links

Cite this: *Analyst*, 2011, **136**, 2925

www.rsc.org/analyst

PAPER

Fabricating protein immunoassay arrays on nitrocellulose using Dip-pen lithography techniques

Eleanore Jane Irvine, Aaron Hernandez-Santana, Karen Faulds and Duncan Graham*

Received 4th March 2011, Accepted 23rd May 2011
DOI: 10.1039/c1an15178a

Advancements in lithography methods for printing biomolecules on surfaces are proving to be potentially beneficial for disease screening and biological research. Dip-pen nanolithography (DPN) is a versatile micro and nanofabrication technique that has the ability to produce functional biomolecule arrays. The greatest advantage, with respect to the printing mechanism, is that DPN adheres to the sensitive mild conditions required for biomolecules such as proteins. We have developed an optimised, high-throughput printing technique for fabricating protein arrays using DPN. This study highlights the fabrication of a prostate specific antigen (PSA) immunoassay detectable by fluorescence. Spot sizes are typically no larger than 8 μm in diameter and limits of detection for PSA are comparable with a commercially available ELISA kit. Furthermore, atomic force microscopy (AFM) analysis of the array surface gives great insight into how the nitrocellulose substrate functions to retain protein integrity. This is the first report of protein arrays being printed on nitrocellulose using the DPN technique and the smallest feature size yet to be achieved on this type of surface. This method offers a significant advance in the ability to produce dense protein arrays on nitrocellulose which are suitable for disease screening using standard fluorescence detection.

Introduction

The ability to bind biomolecules to a surface whilst retaining their functionality has proven beneficial to the understanding of protein-protein interactions,[1] with the focus to develop protein arrays for medical diagnostics.[2] Capture antibodies or functional inks are often printed in an array format to control protein attachment steps and produce features of full immunoassays for the purpose of detecting specific biomolecules that correspond to a disease or condition.[3–5] Over the past decade, there has been great interest in developing effective protein micro- and nano-arrays as a replacement for the more common disease screening method; enzyme-linked immunosorbent assay (ELISA).[4–6] Protein arrays have many advantages over standard ELISA, including the ability to multiplex,[4,7] higher through-put of samples[8] and far less sample and reagent consumption.[6]

Substrate surface chemistry plays a vital role in both retaining protein activity and efficacy of assay detection. It is essential that the activity of the initially attached antibody or protein is retained to allow binding of target proteins and detection molecules to create functional assays. There are a variety of surface chemistries which can be used for microarrays including epoxy, aldehyde and NHS-activated glass surfaces which have been reviewed extensively in literature.[9,10] Nitrocellulose is a polymer matrix often coated on glass slides and has been used as a platform for fabricating protein microarrays for various applications.[6,11,12] It is a common surface of choice in protein array applications due to its protein binding properties and high capacity. However, the exact mechanism which provides the ability to retain protein functionality is not completely understood.[13]

Protein microarrays may be fabricated using a number of different printing techniques, including non-contact methods, such as ink jet printing,[7,14] and contact methods like micro-contact printing[15,16] and microarray printers utilizing micro-sharp pins.[4,11,12,17,18] Microarray features achieved by these methods is considered to be in the range of 100–200 μm.[19] Miniaturisation of feature size can prove advantageous since high-density arrays allow for increased experimental parameters to be tested per chip. Other benefits include a reduction in reagent consumption and increased sensitivity.[8] Furthermore, smaller volumes of protein solutions deposited at the surface should allow for faster kinetics and reaction times with the surface and other proteins.[20]

Dip-pen nanolithography (DPN) is a fast emerging technique successfully utilised in printing protein arrays on the low micron scale.[21,22] It involves the use of a sharp atomic force microscope (AFM) style cantilever being coated with a chemical ink or biomolecule. The tip is then brought into contact with a surface and through the formation of a water or ink meniscus, the ink

Centre for Nanometrology, Department of Pure and Applied Chemistry, WestCHEM, University of Strathclyde, 295 Cathedral Street, Glasgow, UK. E-mail: duncan.graham@strath.ac.uk; Fax: +0141552 0876; Tel: +01415484701

diffuses from the tip onto the surface. Numerous papers have highlighted the capabilities of the technique including its flexibility in application and more importantly, its ability to produce features on the micro/nanoscale whilst maintaining mild conditions suitable for biomolecules.[23–28] Much of the earlier work published on protein arrays printed using DPN requires tip modification,[29] surface modification[1,5,30] or thiol arrays printed for protein attachment.[31,32] This additional surface and tip preparation prior to printing can result in increased overall assay development time and extra steps where possible protein denaturation can occur. Wingren *et al.*[19,33] further highlighted the fact that despite the excellent attempts to produce protein nanoarrays by DPN, its major disadvantages include long printing time (especially when only single tips are used) and incompatibility with printing reagents.

Previous research found that changing various conditions such as humidity, temperature and tip-to-surface contact time (also known as dwell time), can affect feature size with respect to water meniscus transport for diffusion of thiols across a surface.[1,32,34] When printing chemical inks like thiols by DPN, the tip is coated either by dissolving the chemical in an appropriate solvent and immersing the tip in the solution,[21] or by vapour coating the tip with the solid ink using high temperatures.[35] Both methods result in the chemical being dried onto the tip, therefore ink transport is possible due to the humidity in the air forming a water meniscus at the interface of the tip and surface contact. This allows for the ink to flow from the tip to the surface. In more recent publications where DPN is used to directly print biomolecules the ink is of liquid composition and may not need to rely on a water meniscus for transport onto the surface.[36] Alternatively, as tip to surface contact occurs, the liquid ink naturally forms a meniscus itself and therefore the potential for the biomolecule to be transferred through the liquid ink and bind to a surface will depend on different conditions. Hydrophobic and hydrophilic interactions between the ink, tip and surface play an important role in influencing ink deposition onto a substrate. Furthermore, as opposed to dry chemical ink coated tips, where the water meniscus diffusion model allows for deposition through chemisorption,[37] it is thought that liquid ink transfer to a surface is dominated initially by physical adsorption. This concept was first coined by Wang *et al.* where they used silver nanoparticle ink and glycerol as a carrier for nanoscale arrays of silver nanoparticles on a silicon oxide surface.[36] Thus far, successful liquid ink printing and control of spot homogeneity and size has been possible through using additives such as glycerol, agarose, tricine and even hexane for PDMS polymer printing.[36,38,39] These can influence viscosity, wettability, and the hydrophobic interactions of the ink to give successful array printing and favourable ink-surface interactions. It is clear that liquid-ink deposition for active biomolecules like proteins, is becoming the favoured method of printing using DPN.

Finally, expensive, high resolution technologies are required to acquire data from nano-arrays since common conventional fluorescence scanners tend to have a limited resolution down to only 1 μm. This can be a major drawback. Therefore, a more ideal miniaturised printing scale would be 1–10 μm which is more compatible with lower cost, more accessible, fluorescence scanners.

Herein, we report the fabrication of a prostate-specific antigen (PSA) immunoassay array on spin-coated nitrocellulose slides using DPN.

Experimental

Chemicals, materials and instrumentation

Bovine serine albumin (BSA), phosphate buffered saline (PBS) and Tween 20 was all purchased from Sigma Aldrich (Dorset, UK). Monoclonal mouse anti-human 3/PSA capture antibody, recombinant human PSA and detection antibody biotinylated goat anti-human PSA in PBS were obtained from Research & Diagnostics (R&D) systems (Abingdon, UK). Streptavidin Dylight™ 549 was acquired from Thermo Scientific (Northumberland, UK).

Nitrocellulose PATH® slides were purchased from Gentel® Biosciences (Madison, WI, USA) and the Nexterion® 16 well incubation chamber from Schott (Jena, Germany). Array printing by DPN was performed on a NLP 2000™ nanolithography platform (NanoInk Inc., Skokie, IL, USA) using Inkwell arrays (M-6MW) and 12-probe 1D probe arrays (type M-ED). AFM analysis (close-contact) was carried out on a DPN 5000™ nanofabrication system (NanoInk Inc., Skokie, IL, USA). A Leica Leitz DMRB fluorescence microscope was used for the immunoassay fluorescence analysis.

Fabrication of PSA capture antibody arrays

12-probe 1D arrays (66 μm pitch) were cleaned using an oxygen plasma for 40 s (50% power, 72 $cm^3 min^{-1}$) prior to use. Capture antibody print solution was prepared by reconstituting the lyophilized protein in 5 parts phosphate buffered saline (PBS) and 3 parts protein carrier buffer (supplied by NanoInk Inc, Skokie, IL) with an antibody concentration of 2 mg/ml. Ink delivery to the tip array was carried out by placing the array in a 6-channel microfluidic inkwell containing the capture antibody print solution. Excess ink was removed by "bleeding" the ink outside the designated printing area. All DPN experiments were carried out at room temperature (19–21 °C) and a relative humidity of 40–60%. Once desired arrays were fabricated, the nitrocellulose slides were left to incubate overnight at 4 °C.

PSA immunoassay protocol

The printed nitrocellulose slide, after overnight incubation, was washed in wash buffer (WB, 0.05% Tween 20 in PBS) before being blocked with reagent diluent (RD, 1% BSA in PBS) and left to incubate for 1 h. The slide was placed in a microarray slide incubator at this stage to ensure different concentrations of PSA could be applied to corresponding arrays. A range of standard dilutions from 60 ng ml^{-1} to 0.94 ng ml^{-1} of PSA in RD were then added to the designated set of arrays. A control array was prepared by adding only reagent diluent to one set of arrays. The slide was then incubated on a sample shaker for two hours. Arrays were washed (×3) with WB before adding biotinylated detection antibody in RD (200 ng ml^{-1}) to the arrays. The slide was once again incubated for two hours with agitation.

Fluorescence detection

Following wash steps (×3), streptavidin Dylight™ 549 (5 µg ml^{-1} in RD) was added to the arrays and incubated for 30 min whilst agitating. Finally, the slide was washed in WB for 10 min followed by de-ionised water and then blown dry with nitrogen. The processed slides were analysed by fluorescence microscopy using a TRITC filter ($\lambda_{Ex.}$ 543/40, $\lambda_{Em.}$ 593/40) and a 40× objective. Gain and exposure times remained constant for all images taken using Leica QWin software. Images were processed using Image J software.

Results and discussion

Fig. 1 shows the schematic representation of the immunoassay format used in this study. The tip is first coated with the capture antibody by submerging it in a solution contained within a microfluidic inkwell. Once coated, the capture antibody is deposited onto nitrocellulose by placing the tip in contact with the surface by using the NLP 2000™. The tip-substrate contact is controlled through a series of plane calculations where the tip is lowered down and contact can be visualised through a white light microscope. Furthermore, the NLP 2000™ has the ability to print over a larger area range and at higher speeds than conventional DPN as the tips are held stationary while the stage movement is controlled by a series of piezoelectric stacks located under the platform which the substrate is placed on. Finally, the use of micron scale inkwells and chips with multiple cantilevers gives further advantages to DPN's flexibility in application since more features can be printed faster and the use of inkwells gives an opportunity to ink each cantilever with a different biomolecule adding multiplexing capabilities.[40]

Effect of dwell time on feature size and spot homogeneity

The protein carrier buffer used in this study had two main functions. It has a low vapour pressure that prevents drying out of the ink in the inkwells, whilst it also adds viscosity to the ink aiding good uptake of protein onto the tip to allow efficient transfer to the surface. More importantly, it retains the activity of the antibody during the printing process.

Firstly, we investigated how dwell time (the length of time the tip contacts with the surface to produce an array spot) would affect the feature size as it is usually one of the most influential factors when printing an ink by DPN. Five arrays were printed with the dimensions of 24 × 8 features and a pitch (distance between spots) of 33 µm. This meant that each pen on the probe contributed 2 × 8 spots within the overall array with the order of patterning for each pen working from left to right (i.e two spots side by side) followed by the pens moving in an upwards direction to print the next row. A 33 µm pitch was used because the distance between each pen was 66 µm so it produced even distances between each feature. Only 16 spots per pen were printed since the ink volume and the consistency of the spot size depleted greatly beyond this point. The dwell times used for the array printing ranged from 0.01 to 1 s for each feature per array. Secondly, these various dwell times were repeated again, however in this case repeat deposition over the same array was carried out by re-inking. This method of fabrication was of interest to investigate if further inking of the spot would improve signal intensity or influence the feature shape. Standard immunoassay protocols were then carried out on the arrays using a PSA concentration of 30 ng/ml. Immunoassay arrays were fluorescently labelled with Dylight™ 549 and images of the arrays were captured using fluorescence microscopy with a TRITC filter ($\lambda_{Ex.}$ 543/40, $\lambda_{Em.}$ 593/40). Average spot size per array was determined by measuring the diameter of 32 spots. A plot of average spot diameter against the square root of the dwell time for both single and repeat print arrays and are shown in Fig. 2 (A). A decrease in dwell time results in a reduction of feature size for both printing methods, the smallest being 5.4 ± 0.7 µm (0.01 s dwell time) and the largest being 7.4 ± 0.8 µm (1 s dwell time).

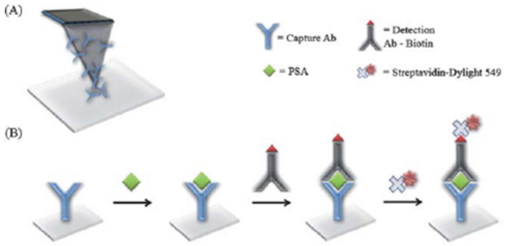

Fig. 1 Schematic of PSA immunoassay development on nitrocellulose (NC). DPN is used to pattern the NC surface with anti-PSA capture antibody (A) followed by the exposure to PSA, a biotinylated anti-PSA detection antibody and finally fluorescently-tagged streptavidin Dylight 549™ (B).

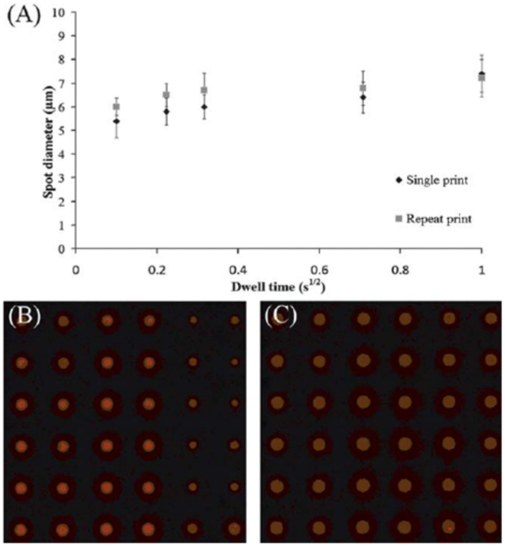

Fig. 2 Plot of average spot diameter against square root of dwell time for single print and repeat print (A) and fluorescence image of a 6 × 6 feature area (scale bar represents 33 µm) of single (B) and repeat (C) print array of PSA immunoassay arrays with 30 ng ml^{-1} PSA concentration using Dylight™ 549 dye.

However, the reduction is minimal as there is less than a 2 µm difference between using the longest and shortest contact time. The factors that influence the lack of reduction are likely to be the viscous nature of the protein carrier buffer and the nitrocellulose surface chemistry. The nature of nitrocellulose is thought to be 'sponge like' therefore it is likely that the nitrocellulose encourages spreading of the spot, regardless of the dwell time, once the ink is deposited. This correlates with the idea that the antibody in the ink has an affinity for the nitrocellulose. Furthermore, since the protein carrier buffer has a low vapour pressure, the spots will take time to dry at the surface, so continued spreading of the features can occur while the spot is still hydrated *i.e.* whilst they dry slowly overnight.

Repeat printing of the arrays influenced both the feature size and homogeneity of the features. Comparing the data in Fig. 2 (A), it is clear that the decrease in spot diameter for the repeat print arrays is less than that of the single print arrays. This is due to the repeat printing adding more liquid to the spot and the repeat contact spreading the spot wider resulting in larger feature sizes. Again, these increases are not significant. Interestingly, the repeated print does not increase the fluorescence intensity of the spots; however, it does improve the spot size consistency and shape. An example of this is shown in Fig. 2 which shows a 6 × 6 spot area of the single (Fig. 2(B)) and double print (Fig. 2(C)) arrays, both using 0.1 s contact time.

The fabrication of each array made use of all twelve pens printing simultaneously, therefore issues of feature size variation from pen to pen are possible. Reasons for this occurring include bending of the pens to produce variable contact points with the surface from pen to pen, surface plane shifts whilst printing and defects or tip damage. This variability is shown in Fig. 2(B) and where single printing has been used, resulting in the two columns of spots to the right of the image being different in size to the other columns. This means that the tip used to print those two columns was contacting differently with the surface compared to the two tips used to print the other four columns. However, this is less prone to happening when repeat printing is performed (Fig. 2(C)) as the process re-deposits extra ink and therefore gives the area a fuller spot and improving any poor printing that may have occurred from the first deposition. The lack of increase in intensity for the repeat print is likely due to the high concentration of capture antibody used in the inkwells. At 2 mg ml^{-1} concentration, large quantities of antibody will be deposited onto the nitrocellulose in the small volume of ink. Therefore, unless the first deposition was unsuccessful, there will be no available binding sites in the area as the high concentration of antibody from the first deposition will saturate the surface. It is likely that any excess capture antibody within the feature array is removed in the first wash step.

Analysis of nitrocellulose surface chemistry

Nitrocellulose substrates are readily available and often a popular choice of surface for protein microarray research. However available knowledge on how the matrix works to retain protein activity at the surface is limited. Various publications have drawn conclusions about its non-covalent binding nature, stating that nitrocellulose is 'sponge like' and electrostatic interactions play a role, alongside the material being hydrophobic in character.[13,41] Nitrocellulose can be coated onto glass in the form of a 3D porous matrix and in the case of the PATH® slides used here, it is spin-coated into a film of only 200 nm in thickness. This was ideal for the scale of the arrays printed, using DPN, since the surface is flat and claims to be non-porous. However, it appears that a porous matrix re-forms upon hydration as shown in Fig. 3(A). Here, the nitrocellulose PATH® slide was hydrated with wash buffer then dried under nitrogen before being analysed by AFM. Pores can be seen in the AFM image in Fig. 3(A) and the example used in the surface profile (Fig. 3(B)) shows that the pores are roughly 144 ± 21 nm in width. This suggests that spin coated nitrocellulose becomes porous upon hydration which allows for the matrix to absorb protein into the surface to bind and retain protein function.

AFM studies are often carried out on protein micro/nano arrays printed by DPN when working with flat surfaces such as glass or gold which show increasing heights that correlate with the size of the proteins present on the surface.[1] Our aim here was to determine how the PSA immunoassay arrays appeared on the absorbent nitrocellulose surface and to gain a better understanding of how the nitrocellulose maintains protein function. To this end, the assay was inspected at different stages to observe how each additional step affected surface topography. Seven sets of arrays were printed using 24 × 8 features layout with 33 µm pitch and a 0.1 s dwell time. Five of the arrays were printed with capture antibody solution and each array was developed to various stages of the immunoassay. One array was simply washed with wash buffer (0.05% Tween 20 in PBS), the next was washed and blocked with reagent diluent (1% BSA in PBS). The other three arrays were treated as per the assay protocol with one being the full fluorescent assay, another lacking the streptavidin Dylight™ 549 and the final one had both streptavidin Dylight™ 549 and the biotinylated detection antibody absent. To further test that spots were present due to the presence of protein in the ink, another two set of arrays were printed simply with PBS and protein carrier buffer combined. One array was washed with wash buffer whilst the other was blocked with reagent diluent.

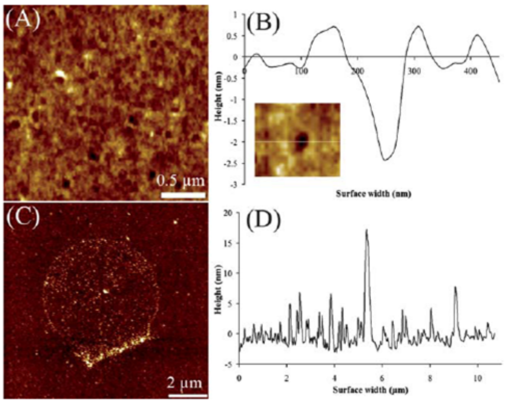

Fig. 3 AFM topography image of a hydrated nitrocellulose surface with no protein present (A) and height profile across a pore (B). AFM topography image of single spot from PSA immunoassay array (C) and surface profile through middle of the spot (D).

References

1 M. Lee, D. K. Kang, H. K. Yang, K. H. Park, S. Y. Choe, C. Kang, S. I. Chang, M. H. Han and I. C. Kang, *Proteomics*, 2006, **6**, 1094.

2 L. Belov, P. Huang, J. S. Chrisp, S. P. Mulligan and R. I. Christopherson, *J. Immunol. Methods*, 2005, **305**, 10.

3 J. P. Bannantine, M. L. Paustian, W. R. Waters, J. R. Stabel, M. V. Palmer, L. L. Li and V. Kapur, *Infect. Immun.*, 2008, **76**, 739.

4 T. O. Joos, M. Schrenk, P. Hopfl, K. Kroger, U. Chowdhury, D. Stoll, D. Schorner, M. Durr, K. Herick, S. Rupp, K. Sohn and H. Hammerle, *Electrophoresis*, 2000, **21**, 2641.

5 S. Lee, Y. H. Ko, H. Jung, J. D. Kim, J. M. Song, J. Chooe, S. K. Eo and S. H. Kang, *Talanta*, 2009, **78**, 608.

6 N. Karoonuthaisiri, R. Charlermroj, U. Uawisetwathana, P. Luxananil, K. Kirtikara and O. Gajanandana, *Biosens. Bioelectron.*, 2009, **24**, 1641.

7 T. H. Patwa, C. Li, L. M. Poisson, H. Y. Kim, M. Pal, D. Ghosh, D. M. Simeone and D. M. Lubman, *Electrophoresis*, 2009, **30**, 2215.

8 M. S. Islam, H. G. Lee, J. Choo, J. M. Song and S. H. Kang, *Talanta*, 2010, **81**, 1402.

9 S. L. Seurynck-Servoss, A. M. White, C. L. Baird, K. D. Rodland and R. C. Zangar, *Anal. Biochem.*, 2007, **371**, 105.

10 I. Balboni, C. Limb, J. D. Tenenbaum and P. J. Utz, *Proteomics*, 2008, **8**, 3443.

11 E. Kopf, D. Shnitzer and D. Zharhary, *Proteomics*, 2005, **5**, 2412.

12 B. Kersten, T. Feilner, A. Kramer, S. Wehrmeyer, A. Possling, I. Witt, M. I. Zanor, R. Stracke, A. Lueking, J. Kreutzberger, H. Lehrach and D. J. Cahill, *Plant Mol. Biol.*, 2003, **52**, 999.

13 S. Oehler, R. Alex and A. Barker, *Anal. Biochem.*, 1999, **268**, 330.

14 L. R. Allain, D. N. Stratis-Cullum and T. Vo-Dinh, *Anal. Chim. Acta*, 2004, **518**, 77.

15 H. Li, J. Zhang, X. Zhou, G. Lu, Z. Yin, G. Li, T. Wu, F. Boey, S. S. Venkatraman and H. Zhang, *Langmuir*, 2010, **26**, 5603.

16 J. Soo, J. Zhang, Q. He, S. Agarwal, H. Li, H. Zhang and P. Chen, *Integr. Biol.*, 2010, **2**, 250.

17 N. R. Thirumalapura, R. J. Morton, A. Ramachandran and J. R. Malayer, *J. Immunol. Methods*, 2005, **298**, 73.

18 G. MacBeath and S. L. Schreiber, *Science*, 2000, **289**, 1760.

19 C. A. K. Borrebaeck and C. Wingren, *J. Proteomics*, 2009, **72**, 928.

20 P. Ellmark, S. Ghatnekar-Nilsson, A. Meister, H. Heinzelmann, L. Montelius, C. Wingren and C. A. K. Borrebaeck, *Proteomics*, 2009, **9**, 5406.

21 R. D. Piner, J. Zhu, F. Xu, S. H. Hong and C. A. Mirkin, *Science*, 1999, **283**, 661.

22 D. S. Ginger, H. Zhang and C. A. Mirkin, *Angew. Chem., Int. Ed.*, 2004, **43**, 30.

23 H. Zhang, S. W. Chung and C. A. Mirkin, *Nano Lett.*, 2003, **3**, 43.

24 L. M. Demers, D. S. Ginger, S. J. Park, Z. Li, S. W. Chung and C. A. Mirkin, *Science*, 2002, **296**, 1836.

25 K. B. Lee, J. H. Lim and C. A. Mirkin, *J. Am. Chem. Soc.*, 2003, **125**, 5588.

26 Y. Li, B. W. Maynor and J. Liu, *J. Am. Chem. Soc.*, 2001, **123**, 2105.

27 H. Li, Q. He, X. Wang, G. Lu, C. Liusman, B. Li, F. Boey, S. S. Venkatraman and H. Zhang, *Small*, 2011, **7**, 226.

28 X. Zhou, Y. Chen, B. Li, G. Lu, F. Boey, J. Ma and H. Zhang, *Small*, 2008, **4**, 1324.

29 C. C. Wu, H. P. Xu, C. Otto, D. N. Reinhoudt, R. G. H. Lammertink, J. Huskens, V. Subramaniam and A. H. Velders, *J. Am. Chem. Soc.*, 2009, **131**, 7526.

30 M. Lynch, C. Mosher, J. Huff, S. Nettikadan, J. Johnson and E. Henderson, *Proteomics*, 2004, **4**, 1695.

31 K. B. Lee, E. Y. Kim, C. A. Mirkin and S. M. Wolinsky, *Nano Lett.*, 2004, **4**, 1869.

32 S. W. Lee, B. K. Oh, R. G. Sanedrin, K. Salaita, T. Fujigaya and C. A. Mirkin, *Adv. Mater.*, 2006, **18**, 1133.

33 C. Wingren and C. A. K. Borrebaeck, *Drug Discovery Today*, 2007, **12**, 813.

34 K. B. Lee, S. J. Park, C. A. Mirkin, J. C. Smith and M. Mrksich, *Science*, 2002, **295**, 1702.

35 P. E. Sheehan and L. J. Whitman, *Phys. Rev. Lett.*, 2002, **88**, 1561041.

36 H. T. Wang, O. A. Nafday, J. R. Haaheim, E. Tevaarwerk, N. A. Amro, R. G. Sanedrin, C. Y. Chang, F. Ren and S. J. Pearton, *Appl. Phys. Lett.*, 2008, **93**.

37 O. A. Nafday, M. W. Vaughn and B. L. Weeks, *J. Chem. Phys.*, 2006, **125**, 1447031.

38 A. J. Senesi, D. I. Rozkiewicz, D. N. Reinhoudt and C. A. Mirkin, *ACS Nano*, 2009, **3**, 2394.

39 A. Hernandez-Santana, E. Irvine, K. Faulds and D. Graham, *Chem. Sci.*, 2011, **2**, 211.

40 J. W. Jang, A. Smetana and P. Stiles, *Scanning*, 2010, **32**, 24.

41 J. M. Gershoni and G. E. Palade, *Anal. Biochem.*, 1983, **131**, 1.